Studies of Organic Semiconductor Nanostructures and Their Photovoltaic Applications

Guoqiang Ren

A dissertation

submitted in partial fulfillment of the

requirements for the degree of

Doctor of Philosophy

University of Washington

2013

Reading Committee:

Samson A. Jenekhe, Chair

David S. Ginger

Qiuming Yu

Program Authorized to Offer Degree:

Chemical Engineering

University of Washington

Abstract

Studies of Organic Semiconductor Nanostructures and Their Photovoltaic Applications

Guoqiang Ren

Chair of the Supervisory Committee:
Professor Samson A. Jenekhe
Department of Chemical Engineering

Organic solar cells are promising by virtue of their low-cost production, mechanical flexibility of plastics, and the range of possible applications. Although progress has been made in developing organic solar cells in the past decade, the power conversion efficiency now about 8-10% is still substantially lower than silicon-based devices. It has been recognized that the photovoltaic conversion process in organic solar cells is dependent on the morphology of the photoactive layer which consists of a binary blend of donor and acceptor materials. This work explores different approaches to controlling the morphology of bulk heterojunction polymer solar cells towards improving the photovoltaic efficiency, including diblock copolymer assemblies, organic semiconductor nanowires, and the use of processing additives. In addition, we explore a new method of characterizing the nanoscale morphology of polymer solar cells.

Investigation of the photovoltaic properties, charge transport, and morphology of a series of diblock conjugated copolymers as a function of block composition showed that the highest efficiency was achieved at the 50% block composition. Nanowires assembled from diblock

copolythiophenes of different compositions showed a tunable average aspect ratio (length/width) of 50−260, which revealed an increase of efficiency with increasing aspect ratio. All-nanowire solar cells comprising a polymer nanowire donor and a small-molecule nanowire acceptor were found to have enhanced photovoltaic efficiency. The use of a processing additive was found to give optimum device performance in benzobisthiazole-based donor–acceptor copolymer/fullerene and poly(3-hexylthiophene)/non-fullerene photovoltaic blend systems. The performance of non-fullerene polymer solar cells was enhanced 10-fold by using only 0.2 vol% additive and the mechanism of enhancement in efficiency was explained in terms of the optimized nanoscale morphology. Scanning transmission electron microscopy coupled with energy dispersive X-ray spectroscopy was successfully used for the first time to image the nanoscale morphology of all-polymer bulk heterojunction solar cells, demonstrating high spatial resolution with chemical specificity.

Table of Contents

LIST OF FIGURES

List of Tables

List of Schemes

Acknowledgements

First of all, I would like to acknowledge my advisor, Professor Samson A. Jenekhe, for his guidance, encouragement, and offering me the opportunity to pursue research in the exciting field of organic photovoltaics. His valuable comments and patience have been indispensable to the completion of the various research projects and this dissertation. I am most grateful to him for great opportunity and resources to interact with the scientific community at professional meetings and conferences as well as through collaborative efforts.

I would like to thank Professor David S. Ginger, Professor Qiuming Yu, and Professor David H. Cobden for taking time to serve on my committee and providing valuable comments.

I also would like to express my gratitude to my collaborators, Professor David S. Ginger and Dr. Cody W. Schlenker at UW Department of Chemistry, and Professor Antoine Kahn and Dr. Selina Olthof at Princeton University. Without their help and insightful discussions, the study on charge photogeneration would not be possible.

The former and present members of Professor Jenekhe's group – Dr. Hao Xin, Dr. Eilaf Ahmed, Dr. Haiyan Li, Dr. Selvam Subramaniyan, Dr. Felix S. Kim, Dr. Nishit Murari, Ye-Jin Hwang, and Taeshik Earmme, are acknowledged for their help and collaboration.

This research would not have been possible without the financial support provided by the UW Department of Chemical Engineering, the U.S. Department of Energy, Office of Naval Research, the National Science Foundation, and a UIF fellowship from the UW Center for Nanotechnology.

Finally, I would like to express my gratitude toward my family in China. Without their encouragement and support, everything would have not been possible.

Chapter 1 Introduction

1.1 Organic Semiconductors

Organic semiconductors represent an important class of materials that have been widely and extensively studied due to their interesting and fundamental physics, as well as their great promise in device applications, such as organic light emitting diodes (OLEDs), organic field effect transistors (OFETs), and organic solar cells (organic photovoltaic devices, OPVs). These molecules usually contain delocalized π-electrons in the form of monocyclic or polycyclic aromatic compounds. They can be classified into small molecule or polymer semiconductors according to their molecular weight, or p-type, n-type, and ambipolar semiconductors according to their charge transport properties.

The research on organic semiconductors can be traced back to 1977, when Alan J. Heeger, Hideki Shirakawa, and Alan MacDiarmid discovered that the electrical conductivity of a conjugated polymer – *trans*-polyacetylene can be increased by 10^7 times by chemical doping.[1-4] This pioneering research won them the 2000 Nobel Prize in Chemistry, and has triggered increasing efforts in the development and applications of organic semiconductors in academia and industry. The device applications of such organic semiconductors have brought in a new era of organic electronics, as contrasted to the traditional electronic devices based on inorganic semiconductors, silver or copper.

1.2 Organic Semiconductor Nanostructures

Organic semiconductor nanostructures emerged recently as a confluence of research on organic semiconductors and nanoscience/nanotechnology.[5] Among the many advantages organic semiconductor nanostructures offer, the most prominent one is the ability to control the morphology of such nanostructures to achieve enhanced or even novel properties. For example,

tuning of the nanostructures of the active layer of organic solar cells by either self-assembled nanowires[6] or adding processing additives[7] has both resulted in enhanced photovoltaic properties of the same photovoltaic blend materials. The use of organic semiconductor nanowires has been proven effective in achieving high charge carrier mobility in organic field-effect transistors as well.[8]

The primary driving force for the formation of organic semiconductor nanostructures is the stacking of π-electrons of the molecular backbones due to their planar framework and the highly delocalized π-systems.[5] Take the most-studied regioregular poly(3-alkylthiophene) (P3AT) nanowires for example.[9] The nanowire axis is formed by the stacking of π-electrons of polythiophene backbones along the (010) direction, and the side-chains interdigitate along the (100) direction to form the height. Nanowires with well-defined geometry, i.e. ~15 nm in width, 3-5 nm in height and several μm in length, are usually obtained for this particular polymer semiconductor.[9]

Diverse methods for synthesis of organic semiconductor nanostructures have been demonstrated and reviewed.[5] Some of the well-developed techniques for the sysnthesis of inorganic nanostructures are readily applied to the synthesis of organic semiconductor nanostructures, which include the templated methods, nanolithography, and physical vapor transport and deposition. In addition, various other techniques have been employed for the synthesis of organic nanostructures,[5] such as the solution-phase self-assembly approach, electrospinning, and controlled polymerization. The geometry and dimension of nanostructures vary with different synthetic routes, and their suitable applications differ as well.

1.3 Organic Solar Cells

Solar cells based on organic semiconductors are attracting increasing attention around the globe because they have shown great promise as solar-to-electric power conversion devices with recent power conversion efficiencies (PCEs) approaching 10%.[10-14] As an alternative for conventional solar cells based on inorganic semiconductors, organic solar cells offer advantages such as low-cost, light-weight, high flexibility, ease of fabrication, and short energy payback period.[15-17] For example, the synthesis of organic semicondcutors is usually environmentally friendly and the devices can be fabricated using solution processing, including simple spin-coating or inkjet printing methods.

1.3.1 Device Schematics and Characterization

An organic solar cell is usually built layer-by-layer using solution processing or thermal evaporation.[15] A typical structure of organic solar cell is schematically shown in Figure 1.1. A glass or plastic substrate coated with transparent and conductive indium tin oxide (ITO) is used as anode. A thin layer of poly(3,4-ethylenedioxythiophene):poly(styrenesulfonate) (PEDOT:PSS) is spin-coated on top of ITO from an aqueous solution to improve the surface quality of ITO and facilitate hole injection from anode to the active layer above. The photoactive layer where the photoenergy conversion takes place can be deposited by solution-processing or thermal deposition. The cell is completed by thermal deposition of a cathode composed of a low work function metal, e.g. Al or Ca. A very thin (~1 nm) underlayer of LiF is usually deposited before cathode material to reduce the cathode work function,[18] and protect the surface of active layer from damage by hot metal ions. Devices with enhanced fill factors and stabilized high open-circuit voltages are usually obtained with LiF underlayer. [19]

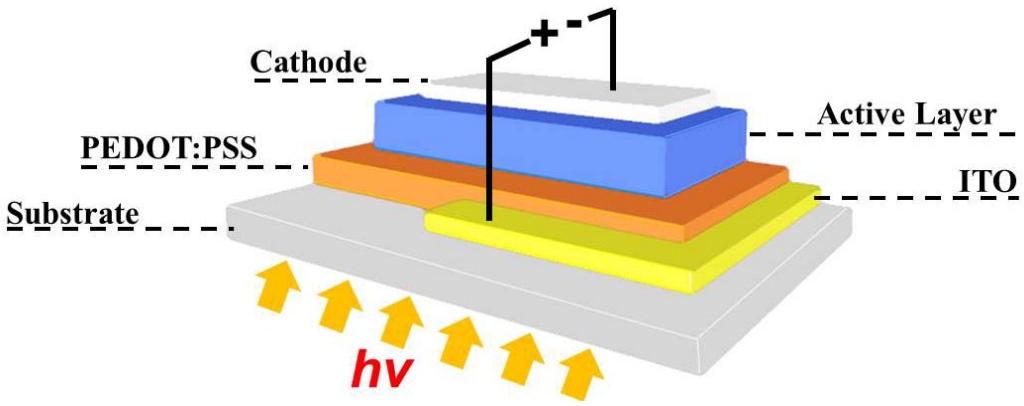

Figure 1.1 Schematic illustration of organic solar cells.

The performance of an organic solar cell is evaluated using current (J) – voltage (V) characterisics obtained under simulated light source with a light intensity of 100 mW/cm^2 and a spectral intensity distribution matching that of the AM1.5 solar spectrum.[20] Key photovoltaic parameters, including the open-circuit voltage (V_{oc}), short-circuit current density (J_{sc}), fill factor (FF), are then derived and the power conversion efficiency (PCE, η) is calculated: $\eta = \frac{P_{out}}{P_{in}} = FF \times \frac{J_{sc} \times V_{oc}}{P_{in}}$ (Figure 1.2a). The incident photon-to-current efficiency (IPCE) or external quantum efficiency (EQE) represents the number of electrons collected per absorbed photon under short-circuit condition, and can provide insight into the factors limiting the photovoltaic processes (Figure 1.2b). The J_{sc} can also be calculated by integration of the IPCE spectrum over the AM1.5 solar spectrum.

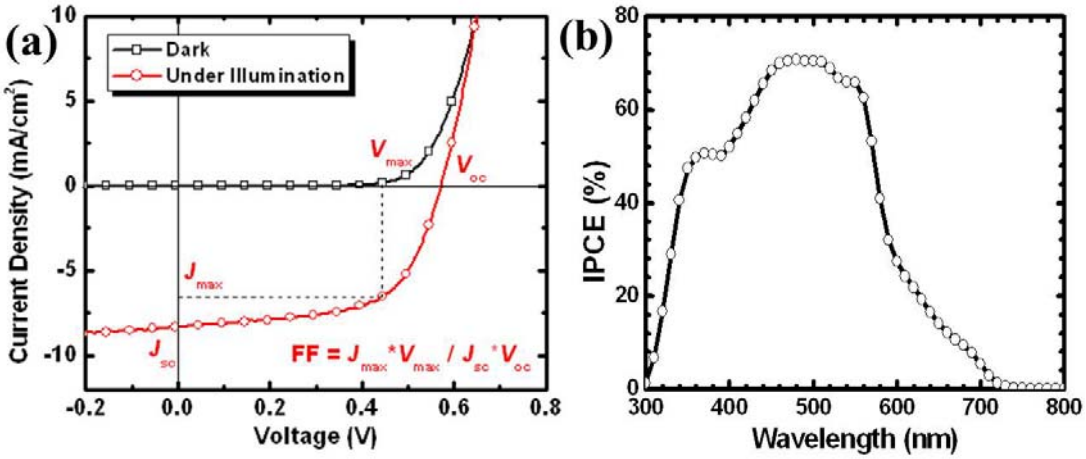

Figure 1.2 (a) Typical current density (J) – voltage (V) characteristics of an organic solar cell in dark and under illumination. (b) IPCE spectrum of an organic solar cell.

Depending on the structure of active layer, organic solar cells can be classified as single-layer, bilayer, and bulk heterojunction (BHJ) devices (Figure 1.3). The Schottky-type single-layer solar cell is fabricated by sandwiching an organic semiconductor layer between two metal electrodes with different work functions, which create a built-in field. The V_{oc} of single-layer solar cells is dependent on the metal electrodes used, and is usually equal to the difference of electrode work function divided by the basic charge.[17] The achieved efficiency is usually very low (<0.1% PCE) due to low J_{sc} and FF, attributable to inefficient exciton dissociation and charge generation at the metal/polymer semiconductor interface, and high charge recombination as indicated by the low external quantum efficiency (EQE).[21,22] The bilayer device, realized by sequential deposition of p-type and n-type semiconductors with offset energy bands, has shown increased EQE and PCE.[23] The improved performance is attributed to the enhanced exciton dissociation at p/n interface. However, limited by exciton diffusion and interfacial area, only excitons generated within the exciton diffusion length (5-20 nm) of the p/n heterojunction can reach the interface and be effectively dissocitated into charge carriers. Loss of photoinduced

excitons results in decrease in photocurrent, and fill factor. PCEs of up to 1.5% have been observed.[23-25] The bulk heterojunction (BHJ) device,[26] in which the active layer is made of a blend composed of p-type donor and n-type acceptor materials, has been the most effective architecture in achieving high photovoltaic efficiency and up to 10% PCE has been reported.[10-12,14,27,28] The enhanced photovoltaic efficiency in BHJ devices is attributed to the enhanced exciton dissotiation and charge photogeneration, enabled by a bicontinuous, interpenetrated donor/acceptor network with microscale phase separation and large interfacial areas. However, the blend morphology of BHJ films is highly dependent on the device fabrication conditions and nanoscale control of the morphology is still hard to achieve.

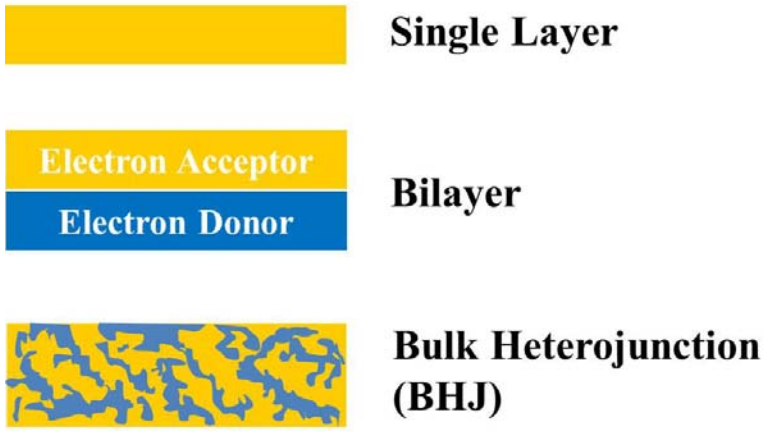

Figure 1.3 Schematic illustration of structure of active layer.

1.3.2 Operating Mechanism

Different from inorganic solar cells, organic solar cells belong to excitonic solar cells which, upon absorption of a photon, generate a mobile excited state (a Coulombically bound electron-hole pair, called an exciton), rather than a free electron-hole pair as happened in inorganic solar cells. The solar-to-electrical energy conversion in organic solar cells involves the following elementary steps and their effects on the photovoltaic efficiency of solar cells are illustrated in Figure 1.4 and are discussed below in details.

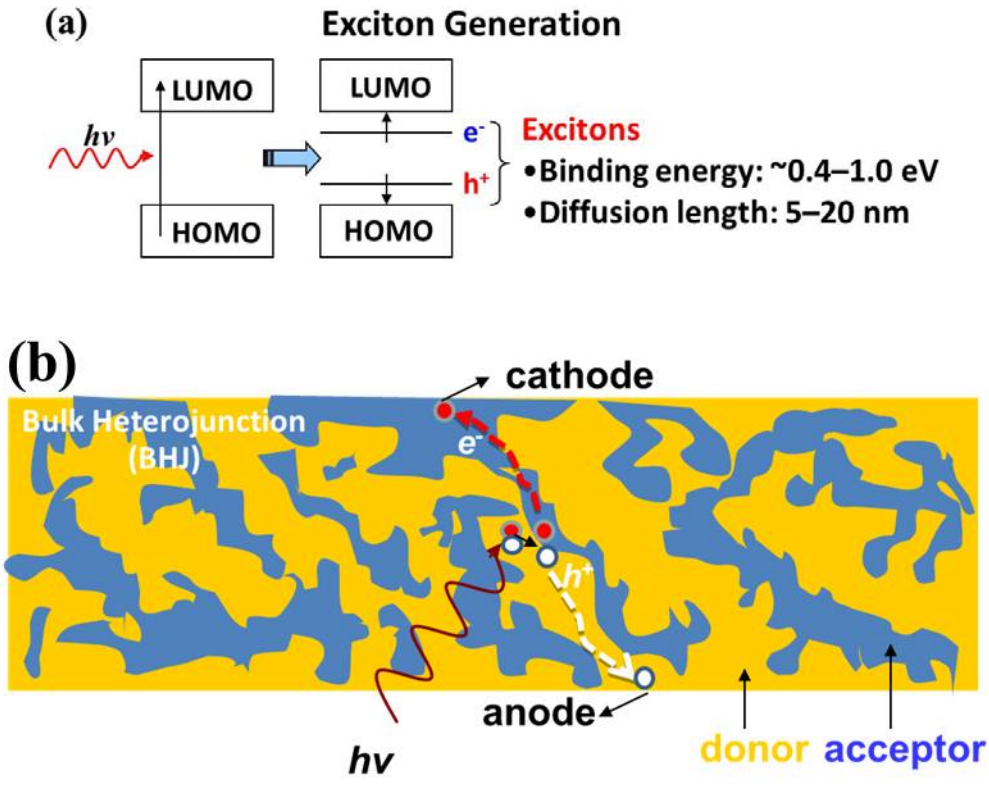

Figure 1.4 Schematic illustrations of (a) exciton generation and (b) photovoltaic process in bulk heterojunction (BHJ) organic solar cells.

(1) Light absorption and exciton generation: upon light incidence, photons with energy larger than the bandgap of organic semiconductors in the active layer are absorbed and bound electron-hole pairs are generated by exciting electrons from HOMO to LUMO bands. These excitons are paired by an exciton binding energy of ~0.4-1.0 eV, and have limited, finite lifetime. Due to the large absorption coefficient of conjugated organic materials (> 1×10^5 cm^{-1}), a thin film of several hundred nanometers is usually sufficient to absorb all of the photons at absorption maximum. However, due to the large bandgap in organic semiconductors, only a small region of the solar spectrum is captured by organic solar cells. For example, the mostly studied polymer semiconductor, poly(3-hexylthiophene) (P3HT) with a bandgap of 1.9 eV, is able to cover only 30% of solar photons, while silicon with a bandgap of 1.1 eV can capture >70% of these

photons.[29] Meanwhile, although a film with high thickness is favorable with respect to optical absorption, increasing the thickness of the film will significantly increase the serial resistance of solar cells, resulting in decreased photocurrent. Additonally, the low charge carrier mobility in organic semicondcutors also puts a limitation on the thickness of active layer, and a ~100 nm thick film is usually found to give the best photovoltaic efficiency.

(2) Exciton diffusion: the photogenerated excitons travel in donor or acceptor phases through diffusion. The effective width of the area an exciton can travel, called exciton diffusion length (L_D), is experimentally determined to be in the range of 5-20 nm for various organic semiconductors.[15-17,29,30] Ideally, the characteristic size of donor and acceptor phases (morphology of the active layer) should be optimized so that all the excitons can be generated within the exciton diffusion length from the donor/acceptor interfaces. Due to various recombination processes,[29,31] a portion of the excitons will be lost during diffusion, lowering the device performance.

(3) Exciton dissociation and charge generation: because of the low relative dielectric constants (e.g. $\varepsilon = 3$ for P3HT),[32] the electrostatic forces exerted on electron and hole in an exciton when exposed to an internal field are usually strong enough to break the mutual attraction within an electron-hole pair, generating free charge carriers. This internal field exists at the donor/acceptor interfaces, where the intrinsic electronic structures of donor/acceptor materials differ. The energetic requirements for photoinduced electron transfer in organic solar cells are empirically represented by the energy offset between the lowest unoccupied molecular orbitals (LUMOs) between donor and acceptor, and a minimum offset of 0.3 eV is considered necessary to enable the electron transfer.[16] However, a recent study has proven that a LUMO

offset as low as 0.12 eV is sufficient in certain polymeric bulk heterojunction solar cells,[33] which indicates the ongoing debate for the energy requirements in excitonic solar cells.

(4) Charge transport: after exciton dissociation and charge formation, holes and electrons are localized in respective donor and acceptor phases. To generate photocurrent, the free holes and electrons must be transported through the donor/acceptor phases to anode and cathode of a solar cell, respectively. Several processes are involved in charge transport in organic semiconductors, such as conduction along the polymer backbones, hopping between molecular chains, and tunneling between conducting segments.[34] In order to achieve efficient charge transport, it is highly desirable that connected and continuous donor and acceptor phases be present in the active layer. In addition, a critical parameter that characterizes how fast a charge carrier (hole and electron) can move in media is the mobility. Charge carrier mobility can be determined using experimental techniques[34-36] such as field-effect transistors (FETs),[37] space-charge limited current (SCLC),[38-40] time-of-flight (TOF),[41] etc, and achieving high charge carrier mobility in organic semiconductors is another hot topic in organic electronics. Since there are two types of charge carriers (electrons and holes) in organic solar cells, a balanced charge transport is usually required to achieve maximal photovoltaic efficiency.[42]

(5) Charge collection: Holes and electrons are transported to and collected by the anode and cathode, respectively. In order to maximize the charge extraction from the active layer, electrodes with proper work function are required to maintain Ohmic contacts to minimize the contact resistance. A general rule is that the work functions of cathode and anode need to match LUMO level of acceptor and HOMO level of donor, respectively. Besides, the modification of electrodes also affects the solar cell performance,[43,44] as the work function of electrodes is

varied.[45] For example, when the work function of the cathode was varied from 5.1 eV to 2.9 eV using different metals, a 160 mV change in open-circuit voltage was observed.[43]

1.3.3 Morphology of Organic Solar Cells

Due to the excitonic nature of organic solar cells, morphology plays a critical role in the optimization of photovoltaic properties, as it dictates the physical interaction between donor and acceptor phases (Figure 1.4b).[46,47] It is evident that dramatic enhancement in photovoltaic efficiency can be achieved when optimized morphology is achieved during device fabrication process.[27,28,48,49] Gerenally speaking, a bicontinuous, percolated donor/acceptor pathway with nanoscale phase-separation and maximal donor/acceptor interfacial areas for efficient exciton dissociation and charge transport constitutes an ideal morphology. The scale of phase separation between donor and acceptor phases must match that of the exciton diffusion length (5 – 20 nm) to maximize the charge photogeneration. Continuous pathways for donor and acceptor phases are needed to transport charge carriers (holes and electrons) to respective electrodes (anodes and cathodes) for charge collection.

Although the idea of optimized nanoscale morphology looks simple, it is nontrivial to achieve such morphology in bulk heterojunction structured solar cells because various intrinsic and extrinsic factors can affect the morphology of the BHJ active layer. Intrinsic factors are properties inherent to the donor/acceptor materials, such as their molecular shape, crystallinity, and miscibility. Extrinsic factors are related to the processing conditions during device fabrication. Such factors include the choice of solvent,[49,50] blend composition,[51] concentration, deposition techniques (spin-coating, doctor blading, inject printing, etc), post-processing conditions (drying, aging, annealing, etc). [27,52] As a result, non-ideal morphology with micron-sized donor/acceptor phase separation usually forms, causing reduction in photovoltaic

efficiency. Therefore, there is an urgent need to develop strategies to optimize the nanoscale morphology in organic solar cells in order to maximize the photovoltaic properties of given materials.

To manipulate the nanoscale morphology of active layer in BHJ solar cells, several approaches have been developed and widely used. Such approaches include, but are not limited to, using thermal/solvent annealing, block copolymers, organic semiconductor nanowires, and mixed solvent (processing additives).[53,54] While there are many available techniques, the applicability is selective and dependent on the materials system, and the detailed processing conditions also vary in a case-by-case situation.

1.4 Literature Review of Morphology Control in Organic Solar Cells

1.4.1 Thermal/Solvent Annealing

Annealing refers to a process which usually involves heat treatment and slow cooling in order to remove internal stresses and change the morphology of a material. In organic solar cells, annealing includes both thermal and solvent annealing and has been extensively studied as an effective approach to enhance the photovoltaic properties of a given blend. During annealing, the fast evaporation (thermal annealing) or excessively slow evaporation (solvent annealing) of solvent leads to favorable microscopic domains of donor/acceptor phases, a dramatic increase in the crystallinity and the charge carrier mobility.[16]

Thermal annealing is typically carried out by heating the active layer of the device on a hotplate to a temperature higher than the glass transition temperature (T_g) of the polymer.[27,28,55-58] For example, P3HT has a T_g of 110 ℃ and devices made from blends of P3HT:PCBM have been optimized at a thermal annealing temperature of ~150 ℃.[27,56] The role of thermal annealing has been found to affect both the polymer chain organization and the PCBM diffusion in the polymer

matrix which lead to the formation a thermodynamically favorable two-phase morphology.[16] However, thermal annealing at much higher temperature than T_g or for extended time periods will cause deterioration of device performance.[56] The negative effect of thermal annealing has been attributed to the increased level of mixing between polymer and PCBM to a extent that charge transport will deteriorate.[56] Proper selections of temperature and time period of thermal annealing treatment are the key to achieve optimized device performance in BHJ solar cells.

Solvent annealing, or sometimes refered to as film aging,[59] facilates the slow-evaporation of residual solvent in the blend films to allow better organization of the blend films.[28,52,60] It is usually performed by leaving the just-spun device in a covered Petri dish for a desired period of time. During solvent annealing, not only the polymer side chain will reorganize, but also the PCBM molecules will diffuse to the top of the active layer with the evaporation of solvent.[61] Studies of the solvent annealing effect on the morphology of P3HT:PCBM blend devices showed that a solvent annealing time of 1 min is enough to achive optimal ordering of P3HT and PCBM in the blend films.[52] We note that although thermal annealing and solvent annealing are usually conducted in different ways, it has been proposed that these techniques all result in a common arrangement of the blend components by controlling the vertical and lateral phase separation of donor/acceptor phases.[61] Similar optimized power conversion efficiency (4-5%) has been reported in devices treated with either annealing technique.[61]

1.4.2 Block Copolymer Semiconductors

Block copolymers have been well known for their ability to achieve versertile nanostructures.[62-65] By covalently incorporating blocks with different properties into one polymeric material and controlling the thermodynamic parameters, the interaction between these blocks can be tuned to drive for different microscale phase separations. A block copolymer with

two different blocks, refered to as a diblock copolymer, has been observed to form body-centered cubic spheres, hexagonally packed cylinders, and lamellae morphology. A vast variety of morphologies can be obtained for block copolymers with more than two blocks.

The use of block copolymer semiconductors in solar cells has been exploited in two different directions. (1) Block copolymer semiconductors are used as active materials in organic solar cells. For example, by incorporating blocks with donor and acceptor moieties into a donor-acceptor-type block copolymer, the single photoactive material can be used to replace the polymer/polymer or polymer/fullerene blends in the fabrication of BHJ solar cells.[66,67] The advantage of this approach is that the nanoscale morphology in the active layer can be fine tuned at the nanoscale, but the power conversion efficiency achieved to date is still low. (2) Block copolymers are used as compatibilizers to stabilize the nanoscale morphology in polymer/fullerene blend films of BHJ solar cells.[68] For example, using a compatibilizer of P3HT-*b*-poly(fullerene) block copolymer, the photovoltaic properties of P3HT:fullerene blend solar cells were enhanced. The role of the block copolymer compatibilizer was demonstrated to attenuate, or even prevent, the large scale phase separation by lowering the interfacial energy between polymer and fullerene. Along the two lines, various block copolymer semiconductors have been demonstrated in enhancing the photovoltaic properties of organic solar cells; however, a systematic understanding of how the molecular structure/block ratios of block copolymer semiconductors affects the nanomorphology of the active layer and thus the photovoltaic properties of solar cells is still missing.

1.4.3 Self-Assembled Nanostructures

Self-assembly of organic semiconductors has been extensively researched because of their unique, well-defined 1D nanostructures, high crystallinity, and high charge carrier mobility.[5] The

self-assembly of organic semiconductor nanowires is usually driven by efficient π-π stacking between polymer backbones. In the case of poly(3-alkylthiophene)s (P3ATs), stacking of π-electrons forms the nanowire axis along the (010) direction, and interdigitation of side-chains along the (100) direction forms the height of nanowires. Polymer backbones usually fold to accommodate for the width of the nanowires. Self-assembled polymer semiconductor nanowires, as exemplified by P3BT[6,59,69] and P3HT,[70] have been effective in enhancing the photovoltaic efficiency of organic solar cells. For example, P3BT nanowires with ~15 nm width and several μm length are blended with PCBM to form the nanowire-BHJ blend films. The dimension of nanowires matches the exciton diffusion length (~5-20 nm) required for efficient exciton dissociation and charge transport.[15] In addition, these nanowires are highly crystalline, and their morphology can be retained in the blend films during spin-coating, which enabled rational control of blend morphology. As a result, photovoltaic efficiency of 3% PCE was achieved in P3BT-nw:PCBM BHJ solar cells, representing a factor of at least three in enhancement compared with 0.5-1% PCE obtained in non-nanowire BHJ blend films. However, the effect of nanowire dimension on the photovoltaic properties of polymer nanowire/fullerene BHJ solar cells is still not fully understood. Furthermore, the use of self-assembled small molecule semiconductor nanostructures in organic BHJ solar cells is yet to be well developed and studied.

1.4.4 Processing Additive Approach

The use of processing additives has been demonstrated to be effective in many fullerene-based BHJ blends, including P3HT/PCBM,[71,72] and low bandgap polymers/PCBM.[7,10,73] In the case of P3HT/PCBM blends, the processing additive appears to enhance the photoresponsivity in the blend films, increase the hole mobility by two orders of magnitude,[72] and increase the crystallinity of the P3HT phase as indicated by the increased number and size of P3HT

crystalline domains in the blend films.[71,72] The underlying mechanism originated from the relatively lower solubility of PCBM in processing additive than in host solvent which facilitated PCBM aggregation to make room for P3HT crystallization.[71] In the case of low bandgap polymers/PCBM blends, the enhancement in photovoltaic properties is attributed to the increased charge carrier generation efficiency as a result of the formation of a bicontinuous, interpercolated nanomorphology.[7,73-75] However, the use of processing additives has not been investigated in the optimization of non-fullerene polymer solar cells.

1.5 Major Challenges

Although significant achievements (up to ~10%) have been made in enhancing the power conversion efficiency of organic solar cells, there are still many remaining challenges in the field. More specifically, several major challenges to tackle include increasing the power conversion efficiency, rational control of the nanoscale morphology of the BHJ active layer, and assembly of organic semiconductor nanowires with novel properties and applications.

The power conversion efficiency of the most efficient organic solar cells is still much lower compared with that of their inorganic counterparts based on crystalline silicon (over 20% PCE).[76] To further increase the efficiency of organic solar cells, new materials, device architecture, and processing methods are absolutely necessary. Among these new approaches, the key of optimization of device performance to a given material is how to rationally control the nanoscale morphology of the active layer to achieve an optimal bicontinuous, percolated network for efficient exciton generation and dissociation. This requires a good understanding of the physical interaction of donor-acceptor in the blend films and the development of universal approaches to fine-tune the interactions to optimize their morphology towards high photovoltaic efficiency.

π-Conjugated organic semiconductors as molecular building blocks for the assembly of functional 1D nanostructures (nanorods, nanowires, etc) are of special interest because of their various novel electronic and optoelectronic properties emerged with tunable nanostructures. However, only a small number of conjugated polymers and small molecules have been investigated as nanowires, most notably poly(3-alkylthiophene)s and perylene diimides. Considering the potential for enhanced performance of organic semiconductor nanowire-based organic electronics (e.g., field-effect transistors, solar cells), it is necessary that nanowires from other existing p-type and n-type conjugated molecules be made and studied. The use of nanowires of novel conjugated molecules can ultimately result in an increase in the photovoltaic efficiency of given materials and clarify the nanostructure – photovoltaic property relationship in organic solar cells.

1.6 Research Objectives and Significance

The primary goal of this research is to optimize the photovoltaic properties of various organic semiconductors by synthesizing and controlling their nanostructures in BHJ solar cells. The objectives of this research focus on addressing several current issues in the field.

1. Synthesize, characterize and control the morphology of organic semiconductor nanostructures;
2. Understand morphology – photovoltaic property relationship in organic BHJ solar cells;
3. Develop efficient nanostructured organic BHJ solar cells.

The synthesis and control of nanostructures of organic semiconductors includes the use of block copolymers, self-assembled nanostructures, processing additive approach, and all-polymer blends. The obtained nanostructures will be characterized by various techniques, such as microscope (TEM, AFM, STEM) and spectroscope (UV-vis, XRD), to reveal their

morphological and optical properties. These organic semiconductor nanostructures will then be used in the construction of bulk heterojunction solar cells and their charge transport and photovoltaic properties will be studied. The relationship between the morphology of nanostructures and their photovoltaic properties will be investigated, and the obtained knowledge will be applied towards the optimization of the photovoltaic properties of organic semiconductors by tuning the morphology of their nanostructures. Nanostructures from a variety of organic semiconductors, including small molecules and polymers, will be studied, and results from this study will help us better understand how the nanostructures affect the photovoltaic properties of organic semiconductors, and eventually, lead a way to enhance the photovoltaic properties of organic solar cells by rationally controlling the nanostructures in the active layer.

1.7 References

1. Shirakawa, H.; Louis, E. J.; MacDiarmid, A. G.; Chiang, C. K.; Heeger, A. J. *J. Chem. Soc., Chem. Commun.* **1977**, 578-580.
2. Shirakawa, H. *Angew. Chem. Int. Ed.* **2001**, *40*, 2574-2580.
3. MacDiarmid, A. G. *Angew. Chem. Int. Ed.* **2001**, *40*, 2581-2590.
4. Heeger, A. J. *Angew. Chem. Int. Ed.* **2001**, *40*, 2591-2611.
5. Kim, F. S.; Ren, G.; Jenekhe, S. A. *Chem. Mater.* **2011**, *23*, 682-732.
6. Xin, H.; Kim, F. S.; Jenekhe, S. A. *J. Am. Chem. Soc.* **2008**, *130*, 5424-5425.
7. Peet, J.; Kim, J. Y.; Coates, N. E.; Ma, W. L.; Moses, D.; Heeger, A. J.; Bazan, G. C. *Nat. Mater.* **2007**, *6*, 497-500.
8. Briseno, A. L.; Mannsfeld, S. C. B.; Jenekhe, S. A.; Bao, Z.; Xia, Y. *Mater.Today* **2008**, *11*, 38-47.
9. Ihn, K. J.; Moulton, J.; Smith, P. *J. Polym. Sci., Part B* **1993**, *31*, 735-742.
10. Liang, Y.; Xu, Z.; Xia, J.; Tsai, S. T.; Wu, Y.; Li, G.; Ray, C.; Yu, L. *Adv. Mater.* **2010**, *22*, E135−E138.

11. Zhou, H.; Yang, L.; Stuart, A. C.; Price, S. C.; Liu, S.; You, W. *Angew. Chem. Int. Ed.* **2011**, *50*, 2995-2998.

12. Small, C. E.; Chen, S.; Subbiah, J.; Amb, C. M.; Tsang, S.-W.; Lai, T.-H.; Reynolds, J. R.; So, F. *Nat. Photon.* **2012**, *6*, 115-120.

13. Dou, L.; You, J.; Yang, J.; Chen, C.-C.; He, Y.; Murase, S.; Moriarty, T.; Emery, K.; Li, G.; Yang, Y. *Nat. Photon.* **2012**, *6*, 180-185.

14. He, Z.; Zhong, C.; Su, S.; Xu, M.; Wu, H.; Cao, Y. *Nat. Photon.* **2012**, *6*, 593-597.

15. Gunes, S.; Neugebauer, H.; Sariciftci, N. S. *Chem. Rev.* **2007**, *107*, 1324-1338.

16. Thompson, B. C.; Fréchet, J. M. J. *Angew. Chem. Int. Ed.* **2008**, *47*, 58-77.

17. Coakley, K. M.; McGehee, M. D. *Chem. Mater.* **2004**, *16*, 4533-4542.

18. Jong, D.; Friedlein, M. P.; Osikowicz, R. W.; Salaneck, W. R.; Fahlman, M. *Mol. Cryst. Liq. Cryst.* **2006**, *455*, 193-203.

19. Brabec, C. J.; Shaheen, S. E.; Winder, C.; Sariciftci, N. S.; Denk, P. *Appl. Phys. Lett.* **2002**, *80*, 1288-1290.

20. Shrotriya, V.; Li, G.; Yao, Y.; Moriarty, T.; Emery, K.; Yang, Y. *Adv. Funct. Mater.* **2006**, *16*, 2016-2023.

21. Marks, R. N.; Halls, J. J. M.; Bradley, D. D. C.; Friend, R. H.; Holmes, A. B. *J. Phys. Condens. Matter* **1994**, *6*, 1379-1394.

22. Antoniadis, H.; Hsieh, B. R.; Abkowitz, M. A.; Jenekhe, S. A.; Stolka, M. *Synth. Met.* **1994**, *62*, 265-271.

23. Tang, C. W. *Appl. Phys. Lett.* **1986**, *48*, 183-185.

24. Alam, M. M.; Jenekhe, S. A. *Chem. Mater.* **2004**, *16*, 4647-4656.

25. Sariciftci, N. S.; Braun, D.; Zhang, C.; Srdanov, V. I.; Heeger, A. J.; Stucky, G.; Wudl, F. *Appl. Phys. Lett.* **1993**, *62*, 585-587.

26. Yu, G.; Gao, J.; Hummelen, J. C.; Wudl, F.; Heeger, A. J. *Science* **1995**, *270*, 1789-1791.

27. Ma, W.; Yang, C.; Gang, X.; Lee, K.; Heeger, A. J. *Adv. Funct. Mater.* **2005**, *15*, 1617-1622.

28. Li, G.; Shrotriya, V.; Huang, J.; Yao, Y.; Moriarty, T.; Emery, K.; Yang, Y. *Nat. Mater.* **2005**, *4*, 864-868.

29. Blom, P. W. M.; Mihailetchi, V. D.; Koster, L. J. A.; Markov, D. E. *Adv. Mater.* **2007**, *19*, 1551-1566.

30. Moliton, A.; Nunzi, J.-M. *Polym. Int.* **2006**, *55*, 583-600.

31. Pivrikas, A.; Neugebauer, H.; Sariciftci, N. S. *IEEE J. Sel. Top. Quant. Electron.* **2010**, *16*, 1746-1758.

32. Mihailetchi, V. D.; Xie, H.; de Boer, B.; Koster, L. J. A.; Blom, P. W. M. *Adv. Funct. Mater.* **2006**, *16*, 699-708.

33. Gong, X.; Tong, M.; Brunetti, F. G.; Seo, J.; Sun, Y.; Moses, D.; Wudl, F.; Heeger, A. J. *Adv. Mater.* **2011**, *23*, 2272-2277.

34. Tiwari, S.; Greenham, N. *Opt. Quant. Electron.* **2009**, *41*, 69-89-89.

35. Bredas, J.-L.; Beljonne, D.; Coropceanu, V.; Cornil, J. *Chem. Rev.* **2004**, *104*, 4971-5004.

36. Shirota, Y.; Kageyama, H. *Chem. Rev.* **2007**, *107*, 953-1010.

37. Sze, S. M. *Physics of Semiconductor Devices (2nd ed.)*; Wiley: New York, 1981.

38. Mihailetchi, V. D.; Wildeman, J.; Blom, P. W. M. *Phys. Rev. Lett.* **2005**, *94*, 126602-4.

39. Murgatroyd, P. N. *J. Phys. D: Appl. Phys.* **1970**, *3*, 151.

40. Domercq, B.; Yu, J. S.; Kaafarani, B. R.; Kondo, T.; Yoo, S.; Haddock, J. N.; Barlow, S.; Marder, S. R.; Kippelen, B. *Mol. Cryst. Liq. Cryst.* **2008**, *481*, 80-93.

41. Haber, K. S.; Albrecht, A. C. *J. Phys. Chem. C* **1984**, *88*, 6025-6030.

42. Sirringhaus, H. *Adv. Mater.* **2005**, *17*, 2411-2425.

43. Brabec, C. J.; Cravino, A.; Meissner, D.; Sariciftci, N. S.; Fromherz, T.; Rispens, M. T.; Sanchez, L.; Hummelen, J. C. *Adv. Funct. Mater.* **2001**, *11*, 374-380.

44. Mihailetchi, V. D.; Blom, P. W. M.; Hummelen, J. C.; Rispens, M. T. *J. Appl. Phys.* **2003**, *94*, 6849-6854.

45. Gomez, E. D.; Loo, Y.-L. *J. Mater. Chem.* **2010**, *20*, 6604-6611.

46. Nagarjuna, G.; Venkataraman, D. *J. Polym. Sci. B: Polym. Phys.* **2012**, *50*, 1045–1056.

47. Liu, F.; Gu, Y.; Jung, J. W.; Jo, W. H.; Russell, T. P. *J. Polym. Sci. B: Polym. Phys.* **2012**, *50*, 1018–1044.

48. Ren, G.; Ahmed, E.; Jenekhe, S. A. *Adv. Energy. Mater.* **2011**, *1*, 946-953.

49. Shaheen, S. E.; Brabec, C. J.; Sariciftci, N. S.; Padinger, F.; Fromherz, T.; Hummelen, J. C. *Appl. Phys. Lett.* **2001**, *78*, 841-843.

50. Chen, L. M.; Hong, Z.; Li, G.; Yang, Y. *Adv. Mater.* **2009**, *21*, 1434-1449.

51. Mayer, A. C.; Michael, F. T.; Shawn, R. S.; Jonathan, R.; Christoph, J. B.; Marcus, S.; Marcus, K.; Martin, H.; Iain, M.; Michael, D. M. *Adv. Funct. Mater.* **2009**, *19*, 1173-1179.

52. Li, G.; Yao, Y.; Yang, H.; Shrotriya, V.; Yang, G.; Yang, Y. *Adv. Funct. Mater.* **2007**, *17*, 1636-1644.

53. Xu, T.; Qiao, Q. *Energy Environ. Sci.* **2011**, *4*, 2700-2720.

54. Oosterhout, S. D.; Wienk, M. M.; van Bavel, S. S.; Thiedmann, R.; Jan Anton Koster, L.; Gilot, J.; Loos, J.; Schmidt, V.; Janssen, R. A. J. *Nat. Mater.* **2009**, *8*, 818-824.

55. Padinger, F.; Rittberger, R. S.; Sariciftci, N. S. *Adv. Funct. Mater.* **2003**, *13*, 85-88.

56. Kim, Y.; Choulis, S. A.; Nelson, J.; Bradley, D. D. C.; Cook, S.; Durrant, J. R. *Appl. Phys. Lett.* **2005**, *86*, 063502-3.

57. Savenije, T. J.; Kroeze, J. E.; Yang, X.; Loos, J. *Adv. Funct. Mater.* **2005**, *15*, 1260-1266.

58. Bertho, S.; Janssen, G.; Cleij, T. J.; Conings, B.; Moons, W.; Gadisa, A.; D'Haen, J.; Goovaerts, E.; Lutsen, L.; Manca, J.; Vanderzande, D. *Sol. Energy Mater. Sol. Cells* **2008**, *92*, 753-760.

59. Xin, H.; Ren, G.; Kim, F. S.; Jenekhe, S. A. *Chem. Mater.* **2008**, *20*, 6199-6207.

60. Shrotriya, V.; Yao, Y.; Li, G.; Yang, Y. *Appl. Phys. Lett.* **2006**, *89*, 063505-3.

61. Campoy-Quiles, M.; Ferenczi, T.; Agostinelli, T.; Etchegoin, P. G.; Kim, Y.; Anthopoulos, T. D.; Stavrinou, P. N.; Bradley, D. D. C.; Nelson, J. *Nat. Mater.* **2008**, *7*, 158-164.

62. Bates, F. S.; Fredrickson, G. H. *Physics Today* **1999**, *52*, 32-38.

63. Bates, F. S.; Fredrickson, G. H. *Annu. Rev. Phys. Chem.* **1990**, *41*, 525-57.

64. Darling, S. B. *Energy Environ. Sci.* **2009**, *2*, 1266-1273.

65. Segalman, R. A.; McCulloch, B.; Kirmayer, S.; Urban, J. J. *Macromolecules* **2009**, *42*, 9205-9216.

66. Lindner, S. M.; Huttner, S.; Chiche, A.; Thelakkat, M.; Krausch, G. *Angew. Chem., Int. Ed.* **2006**, *45*, 3364-3368.

67. Zhang, Q.; Cirpan, A.; Russell, T. P.; Emrick, T. *Macromolecules* **2009**, *42*, 1079-1082.

68. Sivula, K.; Ball, Z. T.; Watanabe, N.; Frechet, J. M. J. *Adv. Mater.* **2006**, *18*, 206-210.

69. Xin, H.; Reid, O. G.; Ren, G.; Kim, F. S.; Ginger, D. S.; Jenekhe, S. A. *ACS Nano* **2010**, *4*, 1861-1872.

70. Berson, S.; Bettignies, R. D.; Bailly, S.; Guillerez, S. *Adv. Funct. Mater.* **2007**, *17*, 1377-1384.

71. Chen, H.-Y.; Yang, H.; Yang, G.; Sista, S.; Zadoyan, R.; Li, G.; Yang, Y. *J. Phys. Chem. C* **2009**, *113*, 7946-7953.

72. Peet, J.; Soci, C.; Coffin, R. C.; Nguyen, T. Q.; Mikhailovsky, A.; Moses, D.; Bazan, G. C. *Appl. Phys. Lett.* **2006**, *89*, 252105.

73. Lee, J. K.; Ma, W. L.; Brabec, C. J.; Yuen, J.; Moon, J. S.; Kim, J. Y.; Lee, K.; Bazan, G. C.; Heeger, A. J. *J. Am. Chem. Soc.* **2008**, *130*, 3619-3623.

74. Peet, J.; Senatore, M. L.; Heeger, A. J.; Bazan, G. C. *Adv. Mater.* **2009**, *21*, 1521-1527.

75. Peet, J.; Heeger, A. J.; Bazan, G. C. *Acc. Chem. Res.* **2009**, *42*, 1700-1708.

76. The National Center for Photovoltaics (NCPV) at the National Renewable Energy Laboratory, http://www.nrel.gov/ncpv/images/efficiency_chart.jpg, accessed May 2013.

Chapter 2 Solar Cells Based on Block Copolymer Semiconductor Nanostructures

2.1 Bulk Heterojunction Solar Cells Based on Block Copolymer Semiconductors: Effects of Block Composition

2.1.1 Introduction

Polymer solar cells are of world-wide research interest due to their potential as low-cost and easy-to-fabricate solar energy-to-electric power conversion devices.[1-19] Bulk heterojunction (BHJ) devices,[8, 9] in which a donor polymer is blended with a fullerene derivative or other acceptor material, have emerged as the most efficient polymer solar cells to date. Among donor polymers in fullerene-based BHJ solar cells, regioregular poly(3-hexylthiophene) (P3HT) has been the most widely investigated and has resulted in some of the highest power conversion efficiencies (3 - 5 % PCE).[1, 2, 10, 11] However, BHJ solar cells similarly made from related regioregular poly(3-alkylthiophene)s (P3ATs), such as poly(3-butylthiophene) (P3BT), poly(3-octylthiophene) (P3OT), and poly(3-decylthiophene) (P3DT), have very poor efficiencies (< 0.5 – 1 % PCE).[12] Although recent efforts, such as nanowire-based BHJ solar cells[18] and extensive materials processing and device optimization,[19] have pushed the power conversion efficiency above 3.0 % for P3BT-based BHJ solar cells, the inferior photovoltaic properties of other P3ATs compared to P3HT remain to be fully explored and addressed. In addition to the greatly reduced photovoltaic properties of P3ATs with alkyl chain length greater or shorter than hexyl, the intrinsic carrier mobility of thin films of P3ATs is known to similarly vary with alkyl chain length.[20] Although not fully understood, the underlying mechanism for this large dependence of the photovoltaic and charge transport properties of P3ATs on alkyl chain length appears to include differences in

solubility, self-assembly/crystallization and molecular packing of chains, dilution effect of the insulating alkyl chain on π-electron density, and the absorption spectra and coefficients. Of major current interest in the field is the development of new approaches that can improve the BHJ materials and associated solar cells.

In the search of novel materials for improving the performance of polymer photovoltaic devices, block copolymers have recently attracted interest because of their intrinsic ability to form nanoscale domains by self-assembly.[21-32] Block copolymers have been explored in the fabrication of solar cells along three directions. First, BHJ devices free of fullerene have been made from diblock copolymers that incorporate electronically active donor and acceptor blocks; this is exemplified by poly(4-vinyltriphenylamine)-*b*-poly(perylene bisimide acrylate) from which an efficiency of 0.07 % PCE was achieved.[24,25] Another example along this line is the diblock copolymer poly(3-hexylthiophene-*b*-perylene diimide) from which a 0.49 % PCE was observed.[26] Second, diblock copolymers have been used as compatibilizers to stabilize the nanoscale morphology of poly(3-hexylthiophene) (P3HT)/fullerene and P3HT/perylene diimide blends. The nanoscale morphology and overall performance of P3HT:$PC_{61}BM$ and P3HT:perylene diimide BHJ solar cells were improved by using a P3HT-*b*-poly(fullerene) diblock[27] and a P3HT-*b*-poly(perylene diimide) diblock,[28] respectively. Third, diblock copolymers have been used as templates to fabricate devices with a 3D-bicontinuous morphology.[29-31] This is exemplified by the use of poly(4-fluorostyrene)-*b*-poly(D, L-lactide) as a bicontinuous gyroid network template to fabricate titania-based dye-sensitized solar cells.[29, 30]

In this chapter, we report an alternative block copolymer strategy towards improvement of BHJ polymer solar cells. By using a crystalline-crystalline diblock copoly(3-alkylthiophene) as the donor component in fullerene-based BHJ polymer solar cells, we have found a strong

dependence of device performance on block composition and observed a substantial enhancement of the photovoltaic properties compared to those of the parent homopolymers. BHJ solar cells fabricated from blends of diblock poly(3-butylthiophene)-*b*-poly(3-octylthiophene) with fullerene ($PC_{71}BM$) were found to have efficiency of up to 3.0 % PCE, which represents factors of 1.6 – 9 improvements in the efficiencies of the homopolymer (P3BT:$PC_{71}BM$ and P3OT:$PC_{71}BM$) devices. Our results demonstrate that by virtue of the unique capability of block copolymers to integrate multiple or even conflicting functionalities (e.g. solubility, self-assembly, interlayer/intermolecular distances, etc) into one polymeric material, they offer a promising approach to advanced materials for polymer solar cells.

The molecular structures of the diblock copoly(3-alkylthiophene)s, poly(3-butylthiophene)-*b*-poly(3-octylthiophene) (P3BT-*b*-P3OT, denoted as BO*x*, where x is the mol % of the P3BT block), the two parent homopolymers (P3OT and P3BT), and [6,6]-phenyl C_{71}-butyric acid methyl ester ($PC_{71}BM$) are shown in Scheme 2.1. The diblock copolymer P3BT-*b*-P3OT by design carries one block (P3BT) with short insulating butyl side groups and thus poor solubility, enhanced self-assembly and efficient π-stacking of chains and the other block (P3OT) has good solubility, retarded self-assembly and π-stacking of chains, and long insulating octyl side groups. We seek to use the different side chains incorporated into the diblock P3BT-*b*-P3OT to balance and optimize the solubility, self-assembly and π-stacking, effects of the insulating side groups and thus the electronic and optoelectronic properties. Our studies included the optical and charge transport properties, fabrication and evaluation of BHJ solar cells, and investigation of the morphology of binary blends of $PC_{71}BM$ with each diblock copolymer BO*x*.

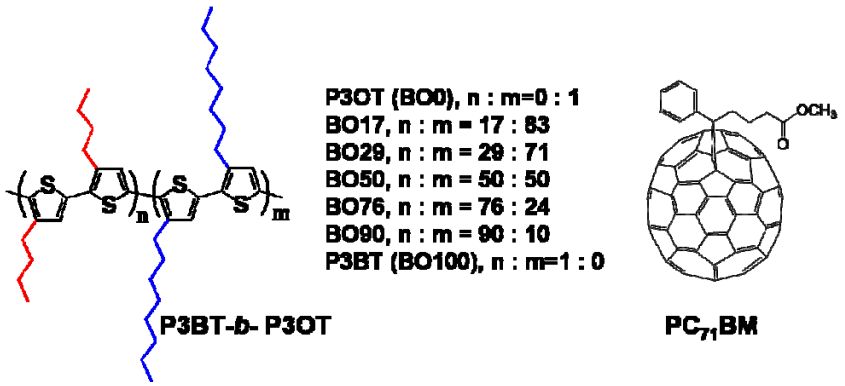

Scheme 2.1 Structures of the diblock copolythiophenes, P3BT-*b*-P3OT (denoted BO*x*), and $PC_{71}BM$.

2.1.2 Experimental Section

2.1.2.1 Materials. Samples of P3BT (M_n = 107 900 g/mol, PDI = 3.61) and $PC_{71}BM$ (> 99.0 %) were obtained from American Dye Sources Inc. (Quebec, Canada). The as-received P3BT sample was subjected to Soxhlet extraction by hexane, dichloromethane, tetrahydrofuran (THF), and then chloroform. The THF-soluble fraction denoted P3BT-1 was collected and precipitated into methanol. The P3BT-1 sample had a M_n of 13 900 g/mol and a PDI of 1.07 as characterized by GPC. A sample of P3OT (M_n = 330 000 g/mol, PDI = 1.37) was synthesized using $Ni(dppe)Cl_2$ as catalyst, following the literature method.[33] A lower molecular weight sample of P3OT (denoted P3OT-1) was also synthesized by the literature method using $Ni(dppe)Cl_2$ as catalyst.[33] The resulting purple solid (P3OT-1) was purified by Soxhlet extraction using methanol, acetone, hexane, and finally dichloromethane. The P3OT-1 sample (dichloromethane-soluble fraction) precipitated into methanol and dried had a M_n of 21 600 g/mol with a PDI of 2.21 as characterized by GPC. The synthesis of some of the diblock P3BT-*b*-P3OT samples (BO50, BO76) by quasi-living polymerization was previously reported.[34] The synthesis of BO17, BO29, and BO90 was carried out using the same reagents and conditions.[34,35] In the diblock copolymer P3BT-*b*-P3OT , denoted BO*x* (x = 17, 29, 50, 76, and 90), the composition variable x

is the percent mole fraction of P3BT segment in the diblock copolythiophene. BO17, BO29, and BO90 were similarly characterized by GPC (120 °C, eluent: 1,2,4-trichlorobenzene).[35] **BO17**: M_n = 17 400, PDI = 1.76; **BO29**: M_n = 33 800, PDI = 1.62; **BO90**: M_n = 15 800, PDI = 2.84. The series of BO*x* copolymers all have a comparable M_n in the range of 11 400 - 17 400,[34] corresponding to about 75-110 thiophene units in the main chains, except BO29 which has about a factor of 2 higher molecular weight.

Blend (1:1, wt:wt) solutions of BO*x*, P3OT or P3BT with $PC_{71}BM$ were prepared by dissolving and stirring them together in N_2-degassed ortho-dichlorobenzene (ODCB, Aldrich) until complete dissolution. For P3OT, BO17, BO29 and BO50, 40 mg mL^{-1} blend solutions were prepared at room temperature; for BO76, BO90 and P3BT, 40, 30 and 30 mg mL^{-1} blend solutions were prepared at 80 °C. All the blend solutions were passed through a 0.45 μm filter except P3BT (1.0 μm filter).

2.1.2.2 Device Fabrication and Characterization. Solar cells used for photovoltaic and incident photon-to-current efficiency (IPCE) measurements were prepared on ITO-coated glass (10 Ω/□, Shanghai B. Tree Tech, China). The substrates were cleaned sequentially with acetone, deionized water and isopropyl alcohol in an ultrasonic bath. A 50 nm PEDOT:PSS (Baytron P VP AI 4083) layer was spin-coated on top of ITO and dried at 150 °C for 10 min under vacuum. Each blend was spin-coated on top of the PEDOT:PSS layer for 30 s in a glovebox to make the active polymer blend layer of 80 – 110 nm. The devices were treated under one of three conditions: dried at 60 °C in vacuum for 2 h (condition 1), or aged in a Petri dish for 5 min (condition 2) or 30 min (condition 3) followed by drying at (110 ±10) °C on a hot plate for 5 min. The devices were loaded in a thermal evaporator (BOC Edwards, 306), where a cathode consisting of 1.0 nm LiF and 80 nm Al was deposited through a shadow mask under high

vacuum (8×10^{-7} torr) to produce 5 solar cells with an active area of 3.57 mm^2 each, per substrate. Space-charge limited current (SCLC) devices were fabricated in a similar way, except that Au electrode was deposited instead of LiF/Al, to facilitate hole-only injection and transport. The current density – voltage (*J-V*) curves of both solar cells and SCLC devices were measured using a HP4155A semiconductor parameter analyzer under laboratory ambient air condition.[36] AM1.5 illumination at 100 mW/cm^2 was provided by a filtered Xe lamp and calibrated by using an NREL-calibrated Si diode.[36] Incident photon-to-current efficiency (IPCE) measurement was done by using an Oriel xenon lamp (450 W) with an Oriel Cornerstone 130 1/8 m monochrometer. The signal was measured with a calibrated standard silicon solar cell and KG5 filter which was calibrated at NREL using a SR830 DSP lock-in amplifier at a chopping frequency of 400 Hz. SCLC characteristics were measured on the devices processed under condition 2 in dark condition. The zero-field SCLC hole mobility was obtained by using nonlinear least-square fitting of the *J-V* data according to the Mott-Gurney equation (Equation 1):

$$J=\frac{9}{8}\varepsilon\varepsilon_0\mu\frac{V^2}{L^3}\exp(\frac{0.89\beta}{\sqrt{L}}\sqrt{V}) \quad [1]$$

where J is the current density, V is the applied voltage, L is the active layer thickness, μ is the mobility, ε is the relative permittivity, ε_0 is the permittivity of free space, and β is the field-activation factor.[37]

2.1.2.3 Characterization of Morphology. X-ray diffraction (XRD) was performed on the actual solar cells, whose photovoltaic properties are reported, using a Bruker F8 Focus Powder X-ray Diffractometer with Cu K_α beam (40kV, 40 mA; λ = 0.15418 nm). Atomic force microscopy (AFM) imaging was performed on the same solar cell devices by using a Dimension 3100 SPM (Veeco) instrument operating in tapping mode. Thin films of the active layers were obtained by scratching edges of the thin films, soaking with water, and peeling them off from the device

substrates, and they were then supported on TEM grids (Electron Microscopy Sciences) for bright-field transmission electron microscopy (BF-TEM) imaging. An FEI Tecnai G^2 F20 TEM at 200 kV was employed, with a 0.031 mm^2 aperture for selected area electron diffraction (SAED). TEM images were acquired with a CCD camera and recorded with Gatan DigitalMicrograph™ software. SAED for $PC_{71}BM$ was obtained from a film drop-casted from ODCB solution. UV-vis absorption spectra were recorded with a Perkin-Elmer model Lambda 900 UV/vis/near-IR spectrophotometer on the blend films spin-coated on top of PEDOT/ITO substrates, following the same drying conditions as the solar cells.

2.1.3 Results and Discussion

The absorption spectra of the BO*x*:$PC_{71}BM$ blend thin films and those of P3BT:$PC_{71}BM$ and P3OT:$PC_{71}BM$ are shown in Figure 2.1. The lineshape of the spectra, absorption maxima, and absorption coefficients of the diblock copolymer blends are seen to vary slightly with the block composition. P3OT and P3BT blend thin films have absorption maxima at 513 nm and 462 nm, respectively. The absorption spectrum of P3BT:$PC_{71}BM$ blend thin films is similar to that previously reported based for P3BT:PCBM blends,[12] but is significantly blue shifted compared to that reported for self-assembled P3BT nanowires.[18] The blue shift and less structure in the spectrum of P3BT are likely a result of the high polydispersity (PDI = 3.61) of this sample and its poor assembly into highly crystalline domains within the P3BT:$PC_{71}BM$ blend. The absorption maxima of the BO*x*:$PC_{71}BM$ blends all fall between those of P3OT and P3BT. Enhanced absorption in the 550 – 650 nm region with vibronic shoulders at 560 and 600 nm, indicative of improved interchain π-stacking and crystalline domains in some of the BO*x* phase are observed (Figure 2.1).[38] The peak absorption coefficients are in the range of $3.8 \times 10^4 – 6.0 \times 10^4$ cm^{-1} for BO*x*:$PC_{71}BM$ blend thin films with x = 50 – 90 mol % P3BT, which are larger than

the peak absorption coefficient of P3OT:$PC_{71}BM$ blend. The higher peak absorption coefficients of blend thin films of some of the diblock copolymers, compared to those of the homopolymers, in some spectra regions suggest enhanced harvesting of the solar spectrum in BHJ devices. The enhanced absorption coefficient in some of the diblock copolymers can be understood in terms of a higher degree of crystallinity in those samples.

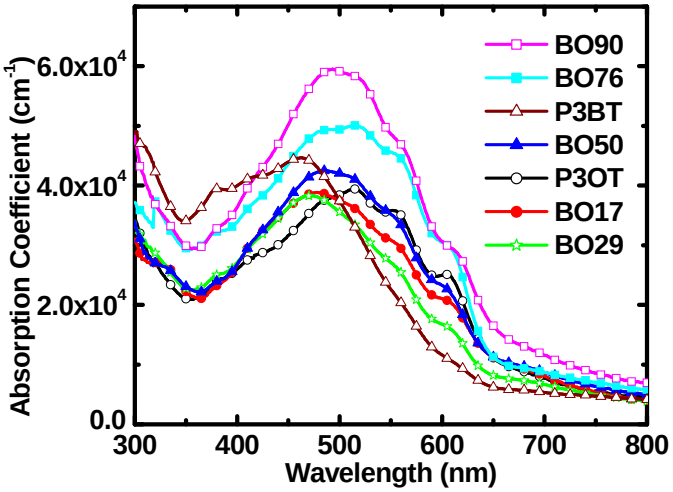

Figure 2.1 Absorption spectra of BOx:$PC_{71}BM$ (1:1, wt:wt) blend thin films dried at 60 °C in vacuum.

The photovoltaic properties of BHJ solar cells using the diblock copolythiophenes as the donor component and $PC_{71}BM$ as the acceptor were investigated in comparison with those of the parent homopolymer (P3BT and P3OT) solar cells. The BHJ devices were of the basic structure ITO/PEDOT:PSS/active layer/LiF/Al, where the active layer is a BO*x*:$PC_{71}BM$ or a P3OT:$PC_{71}BM$ or a P3BT:$PC_{71}BM$ blend thin film. All the solar cells were characterized under AM1.5 solar irradiation at 1 sun (100 mW/cm^2) in ambient air. The current density (*J*) – voltage (*V*) curves for BO50:$PC_{71}BM$ blend thin film solar cells processed under three conditions are shown in Figure 2.2a. A slight improvement in the photocurrent and overall device efficiency was observed by going from vacuum drying of the blend thin films at 60 °C (condition 1) to film

aging and thermal annealing (conditions 2 and 3). The photovoltaic parameters derived from Figure 2.2a and similar plots for BO*x*:$PC_{71}BM$ blend devices, including the short-circuit current density (J_{sc}), the open circuit voltage (V_{oc}), the fill factors (*FF*), and the maximum PCE for each polymer are summarized in Table 2.1. The observed open circuit voltage (0.56 – 0.65 V) in solar

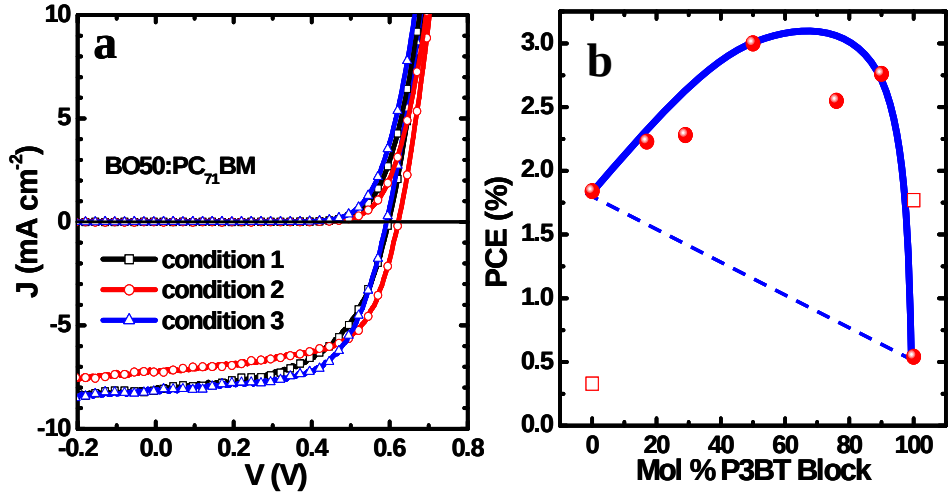

Figure 2.2 (a) Current density – voltage characteristics of BO50:$PC_{71}BM$ solar cells processed at different conditions: Condition 1, dried at 60 °C in vacuum; Condition 2, 5 min film aging in a Petri dish and 5 min thermal annealing at 110 °C; Condition 3, 30 min film aging in a Petri dish and 5 min thermal annealing at 110 °C. (b) Compositional dependence of the highest efficiency of solar cells with BO_x active layers. The trend line is drawn as a guide to eye. The PCE of P3BT-1 and P3OT-1 devices are indicated by open square (□).

Table 2.1 Summary of charge transport and photovoltaic properties of BO*x*:$PC_{71}BM$ blend thin films.

BOx:$PC_{71}BM$ [1:1 wt:wt]	μ_h [$cm^2\ V^{-1}\ s^{-1}$] [a]	J_{sc} [$mA\ cm^{-2}$]	V_{oc} [V]	FF	PCE [%]
P3OT	3.64×10^{-5}	5.81	0.66	0.48	1.84 [a]
P3OT-1	2.31×10^{-8}	1.58	0.65	0.33	0.33 [a]
BO17	1.53×10^{-5}	7.05	0.65	0.49	2.23 [a]
BO29	2.38×10^{-4}	7.06	0.62	0.52	2.28 [a]
BO50	2.50×10^{-4}	8.09	0.59	0.63	3.00 [b]
BO76	8.04×10^{-5}	7.41	0.61	0.57	2.55 [b]
BO90	2.76×10^{-4}	7.90	0.56	0.63	2.76 [b]
P3BT	5.32×10^{-6}	2.24	0.54	0.45	0.54 [b]
P3BT-1	1.15×10^{-7}	4.91	0.64	0.57	1.77 [b]

Processing conditions: [a] Condition 2; [b] Condition 3. Spin coated thin films of BOx:$PC_{71}BM$ (1:1, wt:wt) blends had thickness in the 80 to 110 nm range.

cells incorporating the series of block copolymers are comparable to those of the homopolymers, P3BT (0.54 V) and P3OT (0.66 V). However, there is a significant increase of both the photocurrent and fill factor of the block copolymer devices compared to those of either P3BT or P3OT. Indeed, these improvements in J_{sc} and *FF* translate to a large enhancement in the power conversion efficiency (PCE) of the BO*x*:$PC_{71}BM$ solar cells compared to the two homopolymers as shown in Figure 2.2b. The strong nonlinear dependence of solar cell efficiency (PCE) on block composition, showing enhancement relative to the homopolymers, suggest that the block composition could be an attractive variable for optimization of polymer solar cells. Among the block copolymer solar cells, BO50:$PC_{71}BM$ devices have the highest efficiency of 3.0 % PCE and this represents factors of 6 and 1.6 enhancement relative to P3BT and P3OT homopolymers, respectively. The 1.84 % PCE obtained for P3OT:$PC_{71}BM$ blends is the highest reported to date for P3OT-based solar cells; it is higher than 0.91 % PCE previously reported for this polymer.[12] In the case of the P3BT homopolymer, our observed 0.54 % PCE is higher than 0.27 % PCE reported earlier by others[12] for similar BHJ (P3BT:PCBM) devices. BHJ devices made from P3OT-1 homopolymer, whose molecular weight is comparable to those of the block copolythiophenes, gave an efficiency of 0.33 % PCE. This photovoltaic efficiency is significantly lower for the low molecular weight P3OT-1 compared to its higher molecular weight P3OT. In the case of P3BT-1, whose M_n value is also in the range of those of the BO*x* block copolymers, the photovoltaic efficiency of P3BT-1:$PC_{71}BM$ devices was 1.77 % PCE which is significantly higher than that of its higher molecular weight P3BT (0.54 %) or literature values (0.27 %)[12]. Thus, the highest efficiency of 3.0 % PCE seen in solar cells based on one of the BO*x* block copolythiophenes represents a factor of 1.6-9.1 enhancement compared to P3OT homopolymer and a factor of 1.7 – 5.6 enhancement compared to P3BT homopolymer. We note

that the efficiency (3.0 % PCE) observed for BO50:$PC_{71}BM$ is also in the range of those observed for P3HT/fullerene BHJ solar cells[1, 2, 10, 11] and is comparable to those reported for the best P3BT nanowire-based devices.[18, 19]

The photoaction or incident photon-to-current efficiency (IPCE) spectrum of the BO50:$PC_{71}BM$ blend solar cell is shown in Figure 2.3. The photoresponse of this BHJ diode turns on at about 730 nm and peaks at ~490 nm, giving a maximum IPCE of 67 % electrons/photon. It is interesting that this IPCE value is very close to those reported for P3HT/fullerene BHJ solar cells.[39, 40]

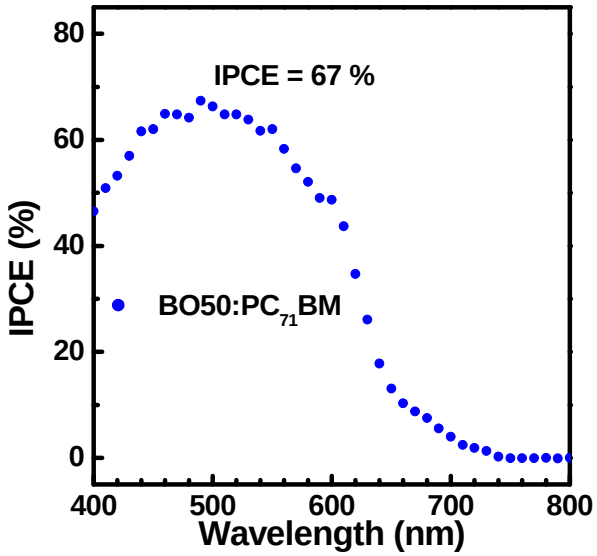

Figure 2.3 IPCE spectrum of a BO50:$PC_{71}BM$ (1:1) device prepared by condition 3 above.

To better understand the photovoltaic properties of these diblock copolythiophenes compared with their parent homopolymers, we studied the surface and bulk morphologies of the blend thin films by atomic force microscopy (AFM) and transmission electron microscopy (TEM). The AFM phase images of BO*x*:$PC_{71}BM$ (x = 0, 17, 29, 50, 76, 90 and 100) blend thin films are shown in Figure 2.4. Nanoscale mixing between BO*x* and $PC_{71}BM$ is seen in the

surface morphology of the blend thin films with x = 0 and 50 – 100, and small $PC_{71}BM$ domains are distributed among the polymer matrices. In the case of BO17:$PC_{71}BM$ and BO29:$PC_{71}BM$ blend thin films, macrophase separation was visually observed immediately after spin-coating.

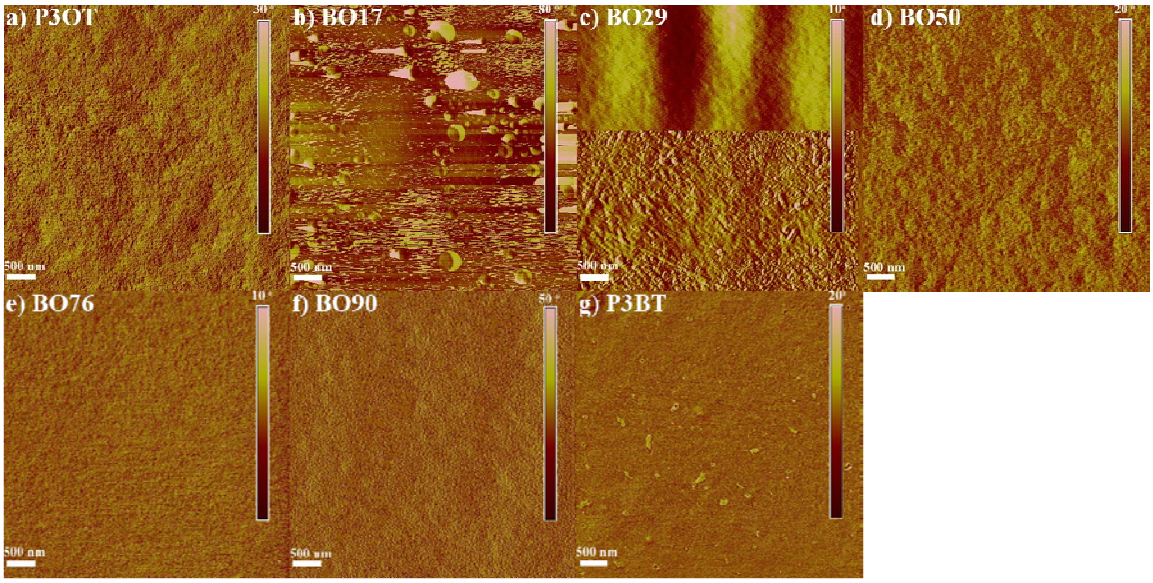

Figure 2.4 AFM phase images of BO*x*:$PC_{71}BM$ blend thin films. The thin films were prepared by 5 min film aging in a Petri dish and 5 min thermal annealing at 110 °C (condition 2).

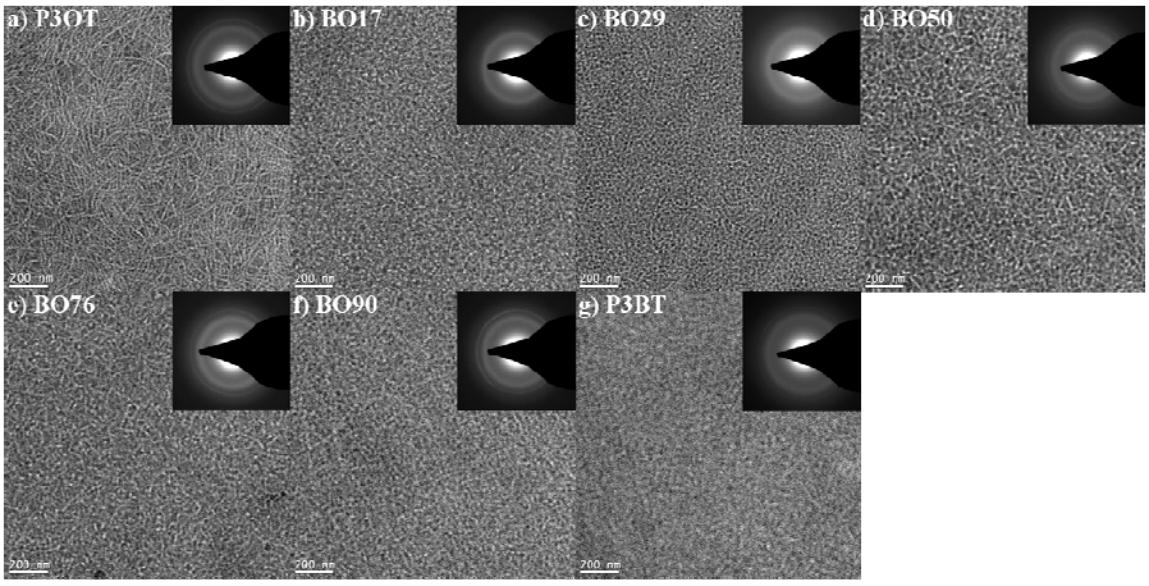

Figure 2.5 TEM images (inset: SAED pattern) of BO*x*:$PC_{71}BM$ blend thin films. The thin films were prepared by 5min film aging in a Petri dish and 5 min thermal annealing at 110 °C (condition 2).

This phase separation is also evidenced by the distinct two phases identified in BO17:$PC_{71}BM$ blend thin film (Figure 2.4b) and the two different surface morphologies seen in BO29:$PC_{71}BM$ (Figure 2.4c). Bright-field TEM imaging of the BO*x*:$PC_{71}BM$ blend thin films under a slightly defocused condition provided good phase contrast between polymer and $PC_{71}BM$ domains, as exemplified by the micrographs shown in Figure 2.5. A network of fibrilar nanostructures observed in all the BO*x*:$PC_{71}BM$ blend thin films is characteristic of the polymer domains while the $PC_{71}BM$ domains are distributed around the polymer networks. The width of these nanostructures is about 11 - 18 nm in all the BO*x*:$PC_{71}BM$ blend thin films, but the length of the nanowires varies, for example, 500 - 2500 nm in BO50:$PC_{71}BM$. These polymer nanostructures are reminiscent of those formed by solution-phase self-assembly of P3BT or BO50.[18, 34, 41] The interpenetrating, quasi-bicontinuous, polymer/fullerene network revealed by TEM imaging of BO*x*:$PC_{71}BM$ blend thin films clearly facilitates charge carrier photogeneration and transport.

Selected area electron diffraction (SAED) was performed on the same BO*x*:$PC_{71}BM$ blend thin films used for TEM imaging to obtain a measure of their crystallinity. The SAED pattern of pure $PC_{71}BM$ film acquired as a reference (Figure 2.6) showed two distinct Debye-Scherrer diffraction rings, corresponding to *d*-spacings of 0.49 and 0.33 nm.[42, 43] The SAED patterns of the BO*x*:$PC_{71}BM$ blend thin films are shown in the insets of Figure 2.5. The diffraction peaks around q = 2.5 – 2.9 nm^{-1} in reciprocal space agree with the (020) reflections of P3AT crystals with random orientations, indicating that the π-π stacking distances are within the range of 0.35 – 0.40 nm and in good agreement with a previously reported value of 0.38 nm.[42, 44] The peaks around q = 1.99 – 2.23 nm^{-1} are due to the diffraction of $PC_{71}BM$, with a *d*-spacing around 0.45 – 0.50 nm.[42, 43] These SAED results mean that the block copolymers form crystalline domains in the blend thin films, and that the $PC_{71}BM$ aggregates observed in AFM and TEM are

nanocrystallites. The formation of crystalline donor and acceptor phases in the blend thin films is important for charge transport.

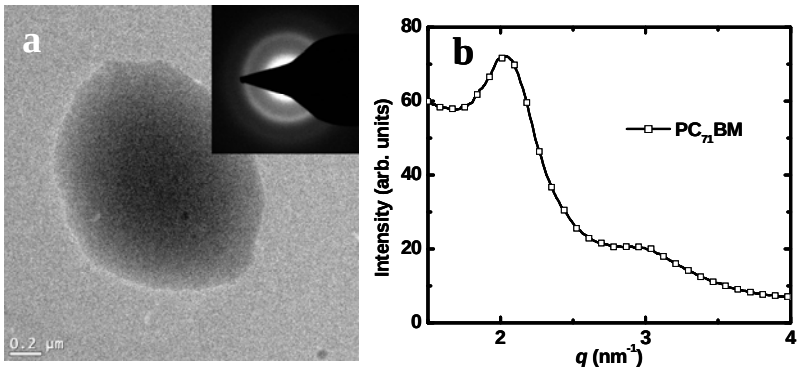

Figure 2.6 (a) TEM image of a $PC_{71}BM$ aggregate and the corresponding SAED; (b) 1-D plot of SAED.

The crystallinity and molecular packing of the BO*x*:$PC_{71}BM$ thin films were further confirmed by X-ray diffraction (XRD) conducted on the same solar cells as characterized in Figures 2.2 and 2.3 and the XRD spectra are shown in Figure 2.7. In P3OT:$PC_{71}BM$ and P3BT:$PC_{71}BM$ blends, interchain spacings (d_{100}) of 1.91 nm and 1.24 nm were observed, respectively. In the case of the BO*x*:$PC_{71}BM$ blends, they are expected to show two distinct crystalline domains with different *d*-spacings, due to the different interlayer distances of d_{P3OT} and d_{P3BT}.[34] However, except for BO50 in which two distinct reflections at 1.95 nm (d_{P3OT}) and 1.46 nm (d_{P3BT}) with nearly equal relative intensities were detected, only the dominant reflection was revealed in the other BO*x* blends. This observation can be understood considering the small film thickness (80 – 110 nm) and the varying copolymer composition. The d_{P3OT} values seen in BO17 and BO29 are 2.22 nm and 2.14 nm, while the d_{P3BT} values observed in BO76 and BO90 are 1.43 nm and 1.24 nm, respectively. Compared with P3OT, the larger d_{P3OT} values in BO17 and BO29 indicate that molecular packing of these two block copolymers is significantly modified by $PC_{71}BM$. All the other BO*x* show decreased interlayer distances in the P3OT

domains and increased interlayer distances in the P3BT domains.[34] The average interlayer distance in BO50 is 1.71 nm, which is close to that of P3HT (1.65 nm).[12] This interlayer distance seems to yield the best photovoltaic properties of solar cells based on P3AT:fullerene binary blends, since it maintains a reasonable polymer/fullerene phase separation, while maximizing the volume density of light absorbing backbone which leads to a higher photocurrent.

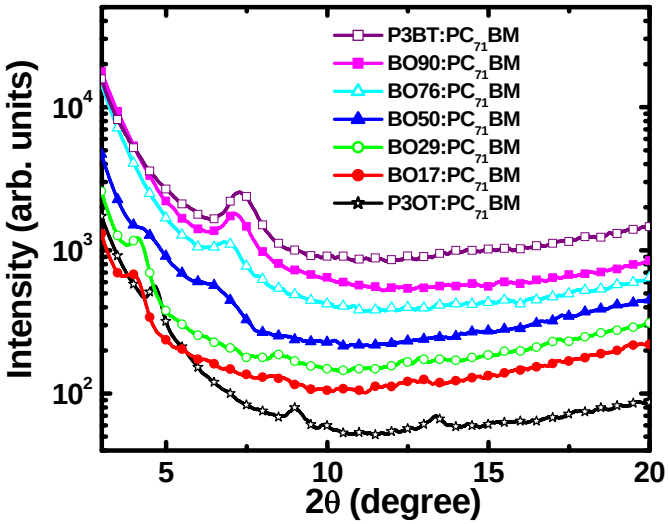

Figure 2.7 XRD spectra of BO*x*:$PC_{71}BM$ blend films obtained directly from the solar cell devices.

To gain insights into charge transport in the block copolythiophene solar cells, we used the space charge limited current (SCLC) method to evaluate the mobility of holes using ITO/PEDOT:PSS/active layer/Au as the hole-only devices. Figure 2.8a shows the dark-current density (*J*) - voltage (*V*) characteristics of these BO*x*:$PC_{71}BM$ devices and these data were analyzed by using the Mott-Gurney equation[37] and prior procedures.[41] The zero-field mobility (μ_h) of holes in BO*x*:$PC_{71}BM$ blends are summarized in Table 2.1. The hole mobility varies from 2.3×10^{-8} cm^2 V^{-1} s^{-1} in P3OT-1:$PC_{71}BM$ to 2.8×10^{-4} cm^2 V^{-1} s^{-1} in BO90:$PC_{71}BM$ (Table 2.1). The block compositional dependence of the SCLC hole mobility, $\mu(x)$, in BO*x*:$PC_{71}BM$ blend films is shown in Figure 6b. We note that the hole mobility of both homopolymers and

homopolymer/PCBM blends varies significantly with molecular weight. Compared with the P3OT and P3BT homopolymers, almost all of the diblock copolymers show enhanced hole transport (Figure 2.8). The μ_h values for BO29, BO50 and BO90 blend thin films are orders of magnitude higher than those of P3OT and P3BT, respectively. The enhanced charge transport in the block copolythiophene/fullerene blends can be understood in terms of the facile self-assembly of highly crystalline nanostructures in the spin-coated thin films (Figure 2.4 and 2.5) as observed by TEM/SAED and XRD.

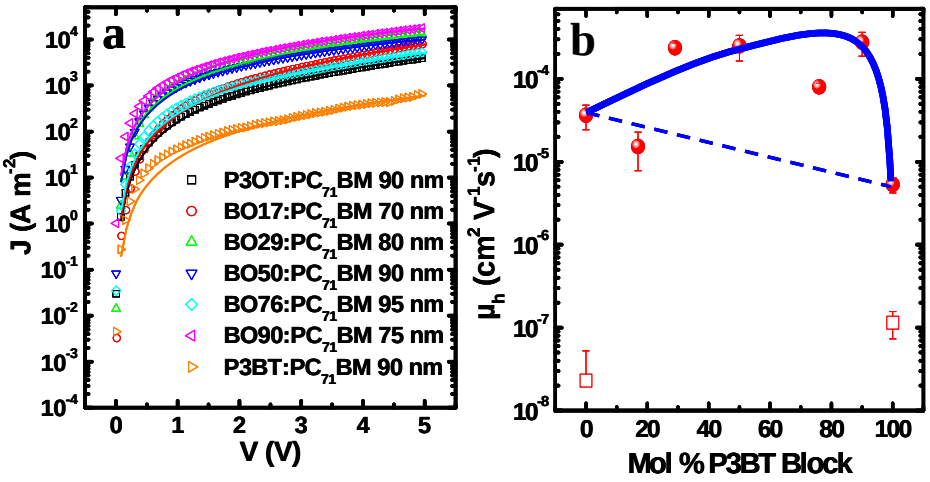

Figure 2.8 (a) The dark current density – voltage (*J-V*) characteristics of ITO/PEDOT:PSS/BO*x*:$PC_{71}BM$/Au for SCLC measurement of mobility and model fitting of the data. (b) Block compositional dependence of SCLC hole mobility of BOx:$PC_{71}BM$ blend thin films. The trend line is drawn as a guide to eye. The SCLC hole mobility of P3BT-1:$PC_{71}BM$ and P3OT-1:$PC_{71}BM$ blends are indicated by open square (□).

The SCLC mobility of holes in pure BO*x* thin films was also measured for comparison with the BO*x*:$PC_{71}BM$ BHJ films. Figure 2.9a shows the *J* – *V* characteristics of the ITO/PEDOT:PSS/BO*x*/Au devices and the SCLC hole mobility is plotted as a function of block composition (Mol % P3BT) in Figure 2.9b. The block composition dependence of hole mobility observed in BO*x* thin films is very similar to that seen in the BHJ BO*x*:$PC_{71}BM$ blends. Most of the block copolymers have SCLC hole mobilities that are comparable for both blend thin films

and the pure BO*x* thin films. The lower hole mobility in BO17:$PC_{71}BM$ thin films, compared to the other BO*x* diblock copolymers and pure BO17 thin films, is an anomaly due to macrophase separation between BO17 and $PC_{71}BM$. Overall, the SCLC hole mobility of the block copolymers (BO29, BO50 and BO90) is comparable with that reported for annealed P3HT:$PC_{61}BM$ (1:1) blend films exhibiting high photovoltaic efficiencies, which is 2×10^{-4} cm^2 V^{-1} s^{-1}.[45] The observed dependence of carrier mobility on block composition (Figure 2.9b) is remarkably similar to the previously discussed dependence of the power conversion efficiency of solar cells on block copolymer composition. This suggests that enhanced charge transport is a major contribution to the observed improvement in the efficiency of BHJ solar cells based on the diblock copolythiophenes.

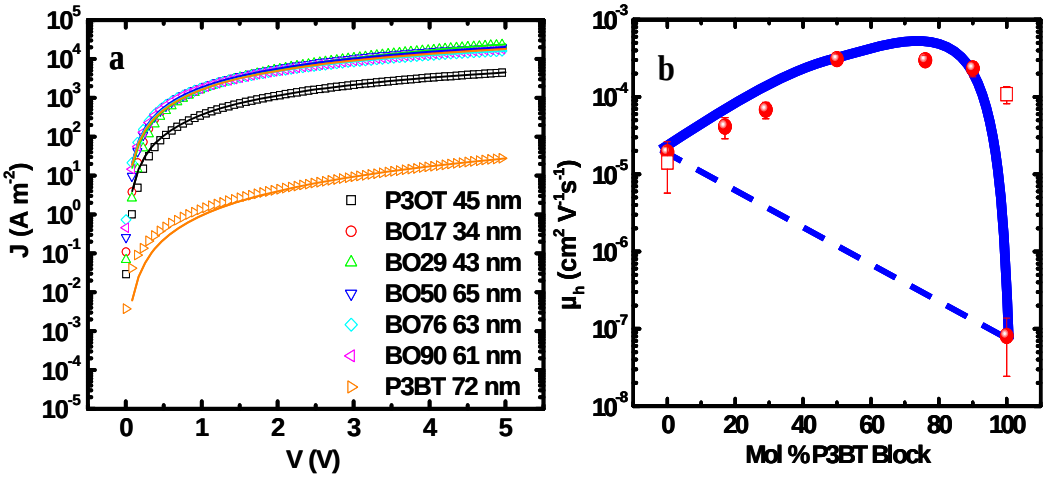

Figure 2.9 (a) The dark current density – voltage (*J-V*) characteristics of ITO/PEDOT:PSS/BO*x*/Au for SCLC measurement of mobility and model fitting of the data. (b) Block compositional dependence of the SCLC mobility of holes in pure block copolymer (BO*x*) thin films. The trend line is drawn as a guide to eye. The SCLC hole mobility of P3BT-1 and P3OT-1 thin films are indicated by open square (□).

2.1.4 Conclusions

We have investigated the photovoltaic and charge transport properties and morphology of bulk heterojunction solar cells based on a series of diblock copoly(3-alkylthiophene)s. Our results have showed that crystalline block copoly(3-alkylthiophene)s have substantially enhanced photovoltaic properties compared to the parent homopolymers. AFM and TEM imaging in conjunction with XRD/SAED showed that the P3BT-*b*-P3OT/$PC_{71}BM$ blends had an interpenetrating morphology with crystalline polymer domains (11 – 18 nm). Studies of BHJ solar cells based on poly(3-butylthiophene)-*b*-poly(3-octylthiophene) and fullerene derivative ($PC_{71}BM$) showed that the power conversion efficiency strongly depends on the block composition, reaching a maximum value of 3.0 % PCE at 50 mol % P3BT. This efficiency is about a factor of 1.6 – 9 times higher than the corresponding homopolymer devices made under similar conditions. The observed enhancement of carrier mobility of holes in the BHJ devices largely accounts for the large improvement in photovoltaic efficiency and its dependence on block copolythiophene composition. These results demonstrate that block conjugated copolymers represent a promising strategy in the design and optimization of polymer semiconductors for low cost solar energy conversion devices.

2.1.5 References and Notes

1. Gunes, S.; Neugebauer, H.; Sariciftci, N. S. *Chem. Rev.* **2007,** *107*, 1324-1338.
2. Thompson, B. C.; Frechet, J. M. J. *Angew. Chem. Int. Ed.* **2008,** *47*, 58-77.
3. Blom, P. W. M.; Mihailetchi, V. D.; Koster, L. J. A.; Markov, D. E. *Adv. Mater.* **2007,** *19*, 1551-1566.
4. Chen, L.-M.; Hong, Z.; Li, G.; Yang, Y. *Adv. Mater.* **2009,** *21*, 1434-1449.
5. Dennler, G.; Scharber, M. C.; Brabec, C. J. *Adv. Mater.* **2009,** *21*, 1323-1338.
6. Alam, M. M.; Jenekhe, S. A. *Chem. Mater.* **2004,** *16*, 4647-4656.

7. Kim, Y.; Cook, S.; Tuladhar, S. M.; Choulis, S. A.; Nelson, J.; Durrant, J. R.; Bradley, D. D. C.; Giles, M.; McCulloch, I.; Ha, C.-S.; Ree, M. *Nat. Mater.* **2006,** *5*, 197-203.

8. Yu, G.; Gao, J.; Hummelen, J. C.; Wudl, F.; Heeger, A. J. *Science* **1995,** *270*, 1789-1792.

9. Halls, J. J. M.; Walsh, C. A.; Greenham, N. C.; Marseglia, E. A.; Friend, R. H.; Moratti, S. C.; Holmes, A. B. *Nature* **1995,** *376*, 498-500.

10. Li, G.; Shrotriya, V.; Huang, J.; Yao, Y.; Moriarty, T.; Emery, K.; Yang, Y. *Nat. Mater.* **2005,** *4*, 864-868.

11. Ma, W.; Yang, C.; Gang, X.; Lee, K.; Heeger, A. J. *Adv. Funct. Mater.* **2005,** *15*, 1617-1622.

12. Nguyen, L. H.; Hoppe, H.; Erb, T.; Gunes, S.; Gobsch, G.; Sariciftci, N. S. *Adv. Funct. Mater.* **2007,** *17*, 1071-1078.

13. Zhou, E.; Yamakawa, S.; Tajima, K.; Yang, C.; Hashimoto, K. *Chem. Mater.* **2009,** *21*, 4055-4061.

14. Liang, Y.; Wu, Y.; Feng, D.; Tsai, S.-T.; Son, H.-J.; Li, G.; Yu, L. *J. Am. Chem. Soc.* **2009,** *131*, 56-57.

15. Bull, T. A.; Pingree, L. S. C.; Jenekhe, S. A.; Ginger, D. S.; Luscombe, C. K. *ACS Nano* **2009,** *3*, 627-636.

16. Wu, P.-T.; Bull, T.; Kim, F. S.; Luscombe, C. K.; Jenekhe, S. A. *Macromolecules* **2009,** *42*, 671-681.

17. Blouin, N.; Michaud, A.; Gendron, D.; Wakim, S.; Blair, E.; Neagu-Plesu, R.; Belletete, M.; Durocher, G.; Tao, Y.; Leclerc, M. *J. Am. Chem. Soc.* **2008,** *130*, 732-742.

18. Xin, H.; Kim, F. S.; Jenekhe, S. A. *J. Am. Chem. Soc.* **2008,** *130*, 5424-5425.

19. Gadisa, A.; Oosterbaan, W. D.; Vandewal, K.; Bolsee, J.-C.; Bertho, S.; D'Haen, J.; Lutsen, L.; Vanderzande, D.; Manca, J. V. *Adv. Funct. Mater.* **2009**, *19*, 3300-3306.

20. Babel, A.; Jenekhe, S. A. *Synth. Met.* **2005,** *148*, 169-173.

21. Eckert, J.-F.; Nicoud, J.-F.; Nierengarten, J.-F.; Liu, S.-G.; Echegoyen, L.; Barigelletti, F.; Armaroli, N.; Ouali, L.; Krasnikov, V.; Hadziioannou, G. *J. Am. Chem. Soc.* **2000,** *122*, 7467-7479.

22. Jenekhe, S. A.; Chen, X. L. *Science* **1998,** *279*, 1903-1907.

23. Chen, X. L.; Jenekhe, S. A. *Macromolecules* **1996,** *29*, 6189-6192.

24. Lindner, S. M.; Huttner, S.; Chiche, A.; Thelakkat, M.; Krausch, G. *Angew. Chem. Int. Ed.* **2006,** *45*, 3364-3368.

25. Sommer, M.; Huttner, S.; Wunder, S.; Thelakkat, M. *Adv. Mater.* **2008,** *20*, 2523-2527.

26. Zhang, Q.; Cirpan, A.; Russell, T. P.; Emrick, T. *Macromolecules* **2009,** *42*, 1079-1082.

27. Sivula, K.; Ball, Z. T.; Watanabe, N.; Frechet, J. M. J. *Adv. Mater.* **2006,** *18*, 206-210.

28. Rajaram, S.; Armstrong, P. B.; Kim, B. J.; Frechet, J. M. J. *Chem. Mater.* **2009,** *21*, 1775-1777.

29. Crossland, E. J. W.; Kamperman, M.; Nedelcu, M.; Ducati, C.; Wiesner, U.; Smilgies, D. M.; Toombes, G. E. S.; Hillmyer, M. A.; Ludwigs, S.; Steiner, U.; Snaith, H. J. *Nano Lett.* **2009**, *9*, 2807-2812.

30. Crossland, E. J. W.; Nedelcu, M.; Ducati, C.; Ludwigs, S.; Hillmyer, M. A.; Steiner, U.; Snaith, H. J. *Nano Lett.* **2009**, *9*, 2813-2819.

31. Botiz, I.; Darling, S. B. *Macromolecules* **2009**, *42*, 8211-8217.

32. Wu, P.-T.; Ren, G.; Kim, F. S.; Li, C.; Mezzenga, R.; Jenekhe, S. A. *J. Polym. Sci. A: Polym. Chem.* **2010**, *48*, 614-626.

33. Heeny, M.; Zhang, W.; Duffy, W.; McCulloch, I.; Koller, G. *World Patent Application* **2007**, WO2007/059838.

34. Wu, P.-T.; Ren, G.; Li, C.; Mezzenga, R.; Jenekhe, S. A. *Macromolecules* **2009,** *42*, 2317-2320.

35. Characterization details. **BO17**: purple solid, yield: 1.87 g, 75.6 %. Regioregularity: 93.9%. ^{1}H NMR ($CDCl_3$), (ppm): 7.0 (1H), 2.82-2.60 (2H), 1.77-1.67 (2H), 1.52-1.31 (8.64H), 1.03 (0.51H), 0.88 (2.49H). GPC: M_n = 17 400, PDI = 1.76. **BO29**: purple solid, yield: 1.29 g, 86.7 %. Regioregularity: 95.5%. ^{1}H NMR ($CDCl_3$), (ppm): 7.0 (1H), 2.86-2.58 (2H), 1.71-1.67 (2H), 1.54-1.32 (7.68H), 1.00 (0.87H), 0.88 (2.13H). GPC: M_n = 33 800, PDI = 1.62. **BO90**: purple solid, yield: 1 g, 59.2 %. Regioregularity: 94.1%. ^{1}H NMR ($CDCl_3$), (ppm): 7.0 (1H), 2.86-2.59 (2H), 1.76-1.63 (2H), 1.52-1.31 (2.8H), 1.00 (2.7H), 0.88 (0.3H). GPC: M_n = 15 800, PDI = 2.84.

36. Xin, H.; Guo, X.; Kim, F. S.; Ren, G.; Watson, M. D.; Jenekhe, S. A. *J. Mater. Chem.* **2009,** *19*, 5303-5310.

37. Murgatroyd, P. N. *J. Phys. D: Appl. Phys.* **1970,** *3*, 151-156.

38. Erb, T.; Zhokhavets, U.; Hoppe, H.; Gobsch, G.; Al-Ibrahim, M.; Ambacher, O. *Thin Solid Films* **2006,** *511-512*, 483-485.

39. Li, G.; Yao, Y.; Yang, H.; Shrotriya, V.; Yang, G.; Yang, Y. *Adv. Funct. Mater.* **2007,** *17*, 1636-1644.

40. Padinger, F.; Rittberger, R. S.; Sariciftci, N. S. *Adv. Funct. Mater.* **2003,** *13*, 85-88.

41. Xin, H.; Ren, G.; Kim, F. S.; Jenekhe, S. A. *Chem. Mater.* **2008,** *20*, 6199-6207.

42. van Bavel, S. S.; Sourty, E.; de With, G.; Loos, J. *Nano Lett.* **2009,** *9*, 507-513.

43. Yang, X.; van Duren, J. K. J.; Rispens, M. T.; Hummelen, J. C.; Janssen, R. A. J.; Michels, M. A. J.; Loos, J. *Adv. Mater.* **2004,** *16*, 802-806.

44. Ihn, K. J.; Moulton, J.; Smith, P. *J. Polym. Sci. B* **1993,** *31*, 735-742.

45. Mihailetchi, V. D.; Xie, H.; de Boer, B.; Koster, L. J. A.; Blom, P. W. M. *Adv. Funct. Mater.* **2006,** *16*, 699-708.

2.2 Solar Cells Based on Block Copolymer Semiconductor Nanowires: Effects of Nanowire Aspect Ratio

2.2.1 Introduction

Solar cells made from organic/polymer semiconductors are promising low cost alternative to conventional photovoltaic devices based on inorganic semiconductors.[1-4] However, because photogenerated excitons in polymer solar cells have relatively small diffusion lengths (5 – 20 nm)[1-3, 5, 6] and a large binding energy (~ 0.4 – 1.0 eV),[3, 4] the multicomponent organic/polymer active layer in bulk heterojunction (BHJ) cells[7] must necessarily be structured on the same scale as the exciton diffusion length to be highly efficient.[1-5, 8, 9] Among the new approaches to realizing the two-phase nanostructured morphology in such polymer/fullerene BHJ solar cells are: the use of a processing additive during the spin coating of the BHJ thin film;[10, 11] the use of self-assembled polymer semiconductor nanowires (NWs);[12-17] and the use of the microphase separation of a diblock copolymer containing one or both conjugated polymer blocks.[18-27] Block copolymers containing one or more π – conjugated polymer blocks are of increasing interest as an approach to the two-phase BHJ thin film morphology with nanoscale domain sizes for application in solar cells.[19-22, 28]

In the case of NWs of conjugated homopolymers, the primary focus has been on regioregular poly(3-alkylthiophene)s and especially poly(3-hexylthiophene) (P3HT),[16, 29-34] poly(3-pentylthiophene) (P3PT)[15, 30] and poly(3-butylthiophene) (P3BT).[12-14, 30, 31, 35] Highly crystalline NWs of ~ 8 – 30 nm widths, 3 – 5 nm thickness, and lengths of up to 1 – 10 μm have been assembled from solutions of P3BT,[12-14] P3PT[15] and P3HT[16] and exploited in the

construction of efficient BHJ solar cells. Although the width and thickness of self-assembled NWs of poly(3-alkylthiophene)s fall in the range comparable to the exciton diffusion length, their lengths and thus aspect ratios are difficult to control,[13] precluding a full understanding of the effects of the nanowire morphology on charge transport and photovoltaic properties of polymer semiconductor NWs. Indeed, we know of no literature report on any method to control the length or aspect ratio of solution-phase assembled conjugated polymer NWs nor of a study of effects of the aspect ratio on their properties and device applications.

In this chapter, we report the solution-phase self-assembly, morphology, charge transport, and photovoltaic properties of diblock copoly(3-alkylthiophene) NWs. We show that the copolymer composition provides a means to tune the aspect ratio (length/width, L/d) of NWs assembled from the block copolythiophenes. The vertical charge transport through the copolymer NWs/fullerene BHJ thin films was characterized by space charge limited current measurement and found to be independent of aspect ratio of the NWs. In contrast, the power conversion efficiency of the copolymer NWs/fullerene BHJ solar cells varied with the aspect ratio of the NWs. The molecular structures of the diblock copoly(3-alkylthiophene)s investigated in this study, poly(3-butylthiophene)-*block*-poly(3-octylthiophene) (BO*x*, where *x* refers to the percent molar fraction of P3BT segment in the diblock copolymers), and [6,6]-phenyl-C_{71} butyric acid methyl ester ($PC_{71}BM$) are shown in Scheme 2.2.

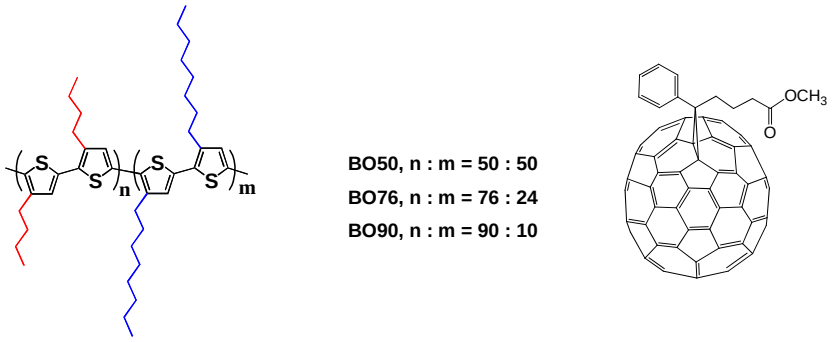

Scheme 2.2 Structures of the diblock copoly(3-alkylthiophene)s, BO*x*, and $PC_{71}BM$.

2.2.2 Experimental Section

2.2.2.1 Materials and Assembly of Nanowires. The synthesis of the series of block copoly(3-alkylthiophene)s was previously reported.[19] The molecular weight, regioregularity, and thermal properties of BO*x* are summarized in Table 2.2. The assembly of BO50, BO76 and BO90 NWs was done in *ortho*-dichlorobenzene (ODCB, Sigma-Aldrich, anhydrous, 99%) solution, following our previously reported methods.[12, 19] In general, a 10 mg sample (BO*x*) was dissolved in 1 mL N_2-degassed ODCB and magnetically stirred at a selected temperature until complete dissolution. Because of the difference in solubility, BO50, BO76, and BO90 were prepared at room temperature (20 °C), 50 °C and 80 °C, respectively. Each of the resulting solution was passed through a 0.45 μm filter, cooled to room temperature, and allowed to grow NWs undisturbedly for two days. Thus, a 10 mg/mL (1 wt %) suspension each of BO50, BO76, and BO90 NWs was obtained.

Table 2.2 Molecular Weight, Regioregularity, and Thermal Properties of BO*x*.

Copolymer	M_w (g/mol)	M_n (g/mol)	PDI	r.r (%)	T_m (^oC)	T_c (^oC)
BO50	29300	17300	1.69	94.1	190, 246	149, 204
BO76	18200	11400	1.60	93.7	263	223
BO90	44900	15800	2.84	94.1	278	234

2.2.2.2 Preparation of BO*x* Nanowire:Fullerene Nanocomposites. A 60 mg/mL [6,6]-phenyl-C_{71} butyric acid metyl ester ($PC_{71}BM$) solution in ODCB was prepared at room temperature and passed through a 0.45 μm filter. Nanocomposites were prepared by blending a suspension of BO*x* NWs with a $PC_{71}BM$ solution at desired weight ratios and stirred well before spin-coating to fabricate devices.

Device Fabrication and Characterization. Solar cells were fabricated on indium tin oxide (ITO) glass substrates. ITO substrates (10 Ω/□, Shanghai B. Tree Tech. Consult Co., Ltd, Shanghai, China) were cleaned sequentially with acetone, deionized water and isopropyl alcohol in an ultrasonic bath, and blown with nitrogen until they were dried. A 50 nm PEDOT:PSS (Baytron P VP AI 4083) layer was spin-coated on top of the ITO and dried at 150 °C for 10 min under vacuum. Each BO*x* NWs:$PC_{71}BM$ suspension was spin-coated on top of PEDOT:PSS layer for 30 s in a glovebox to make a BHJ active layer. The thickness of each BO*x* NWs:$PC_{71}BM$ (x = 50, 76, 90) thin film was 105 nm, 95 nm, and 100 nm, respectively. The photovoltaic properties of the BO*x* NWs:$PC_{71}BM$ nanocomposites were optimized by first testing several BO*x* NWs:$PC_{71}BM$ ratios (1:0.5, 1:0.75, 1:1, and 1:1.25) followed by further device optimization (thermal annealing, film aging) at the composition that gave the best PCE. Device optimization

techniques, such as film aging in a Petri dish and thermal annealing (at (110 ±10) °C for 5 min), were carried out. The substrates were then loaded in a thermal evaporator (BOC Edwards, 306) to deposit a cathode composed of 1.0 nm LiF and 80 nm Al under high vacuum (8×10^{-7} torr). Five solar cells, each with an active area of 4 mm^2, were fabricated per ITO substrate. Devices for space-charge limited current (SCLC) measurement were fabricated with the same device structure, except that a Au top electrode was deposited instead of LiF/Al, to facilitate hole-only transport.

Current – Voltage characteristics of the solar cells and SCLC devices were obtained using an HP4155A semiconductor parameter analyzer in laboratory ambient air. We note that our solar cell devices were not encapsulated, and thus to minimize the impact of ambient conditions (oxygen, water, etc) on the performance of the solar cells, they were kept in a desiccator before testing in air. 1 Sun illumination (AM1.5 at 100 mW/cm^2) was provided by a filtered Xe lamp and calibrated by using a calibrated Si diode from the National Renewable Energy Lab (NREL, USA). $J - V$ characteristics for SCLC were measured under dark condition. Zero-field mobilities of holes were extracted from the J–V curves by non-linear least-square fit to the modified Mott-Gurney equation [1].[36]

$$J=\frac{9}{8}\varepsilon\varepsilon_0\mu\frac{V^2}{L^3}\exp(\frac{0.89\beta}{\sqrt{L}}\sqrt{V}) \qquad [1]$$

where J is the current density, V is the applied voltage, L is the active layer thickness, μ is the mobility, ε is the relative permittivity, ε_0 is the permittivity of free space (8.85×10^{-12} F/m), and β is the field-activation factor (also called the electric field coefficient). The solid lines in Figure

2.17 represent the fitting curves based on this model. The electric field dependent value of charge carrier mobility can be calculated accordingly.[37, 38]

Measurement of the incident photon to current efficiency (IPCE) was made using an Oriel xenon lamp (450 W) with an Oriel Cornerstone 130 1/8 m monochrometer. The signal was measured with a calibrated standard silicon solar cell and KG5 filter which was calibrated at NREL using a SR830 DSP lock-in amplifier at a chopping frequency of 400 Hz.

2.2.2.3 Characterization of Morphology and Absorption Spectra. X-ray Diffraction (XRD) of the neat BO*x* NWs was done on films drop-casted onto clean silicon wafer and dried in vacuum. A Bruker F8 Focus Powder X-ray Diffractometer with Cu K_α beam (40 kV, 40 mA; $\lambda = 0.15418$ nm) was employed to obtain the XRD spectra. XRD spectra of the BHJ BO*x*:$PC_{71}BM$ blends were acquired on the actual solar cells, whose photovoltaic properties are reported. Imaging by atomic force microscopy (AFM) was done within an area of 5×5 μm with a Dimension 3100 SPM (Veeco) instrument operating in tapping mode. For transmission electron microscopy (TEM) imaging, each nanowire suspension was diluted with ODCB, drop-casted onto a TEM grid (300 mesh, carbon coated copper grids, Electron Microscopy Sciences, Inc.), dried and examined under bright-field TEM (BF-TEM). In the case of the nanocomposites, a thin film of the BO*x* NWs:$PC_{71}BM$ active layer was first scratched, and soaked in deionized water. The active layer was then peeled-off the substrate, supported on a TEM grid, and dried for imaging. An FEI Tecnai G^2 F20 TEM operated at 200 kV was employed for BF-TEM imaging. Selected area electron diffraction (SAED) was done on the same TEM, with a 0.031 mm^2 aperture. Images were acquired with a CCD camera and recorded with Gatan DigitalMicrograph^{TM} software.

UV-vis absorption spectra were recorded with a Perkin-Elmer model Lambda 900 UV/vis/near-IR spectrophotometer on BO*x* NWs:$PC_{71}BM$ thin films spin-coated on top of PEDOT:PSS/ITO substrates, following the same processing conditions for the solar cells. The film thickness was determined by using an Alpha-Step 500 profilometer (KLA-Tencor).

2.2.3 Results and Discussion

2.2.3.1 Assembly and Morphology of Block Copolythiophene NWs. The solution-phase self-assembly of NWs from the diblock copolythiophenes BO*x* is similar to our previously described methods for the assembly of NWs from poly(3-butylthiophene) homopolymer.[12, 14] We note that although five different block compositions of BO*x* (x = 17, 29, 50, 76, and 90) were synthesized and previously studied,[19, 21] here we focused on BO50, BO76, and BO90 nanowire growth by solution-phase self-assembly in *ortho*-dichlorobenzene (ODCB). Under similar conditions, NWs could not be assembled from BO17 and BO29. By maintaining the concentration of each BO*x* (BO50, BO76, and BO90) in ODCB at 10 mg/mL (1 wt %) while varying the temperature from room temperature (20 $^{\circ}$C) to 80 $^{\circ}$C, we were able to tune the morphology of the NWs. Figure 2.10 shows the morphology of the diblock copolythiophene NWs revealed by TEM and AFM images. The TEM images show that NWs obtained from the three diblock copolymers, BO50, BO76, and BO90, had widths of 13.3 ± 1.1, 15.8 ± 1.5 and 14.5 ± 1.0 nm, respectively, based on 100 measurements of the width and length of NWs in TEM images. Although the width (*d*) of the NWs (13 - 16 nm) is relatively narrow in distribution across the different block compositions, the length (*L*) distribution and thus aspect ratio (*L*/*d*) was quite broad. The aspect ratio varied from 15 – 75 in BO50[19] and 25 – 115 in BO76 to 125 – 350 in BO90. The average

aspect ratio of these diblock copolythiophene NWs were 48 ± 13, 80 ± 27 and 263 ± 46 for the BO50, BO76 and BO90 NWs, respectively. The observed morphology of BO50 NWs corresponds well with our previous report.[19] However, the NWs of BO76 and BO90, investigated here for the first time, have significantly higher aspect ratios compared to BO50. Since the BO*x* samples have comparable molecular weights, the huge difference in aspect ratio is attributable to the variation in block composition and perhaps also the dissolution temperature. On the other hand, we note that when BO50 solution was heated above 50 °C, assembly of NWs became difficult and only spherical aggregates of BO50 then result, suggesting that temperature is not a significant factor controlling the aspect ratio of BO*x* NWs. The AFM images (Figure 2.10) confirmed the morphology of NWs observed in TEM images.

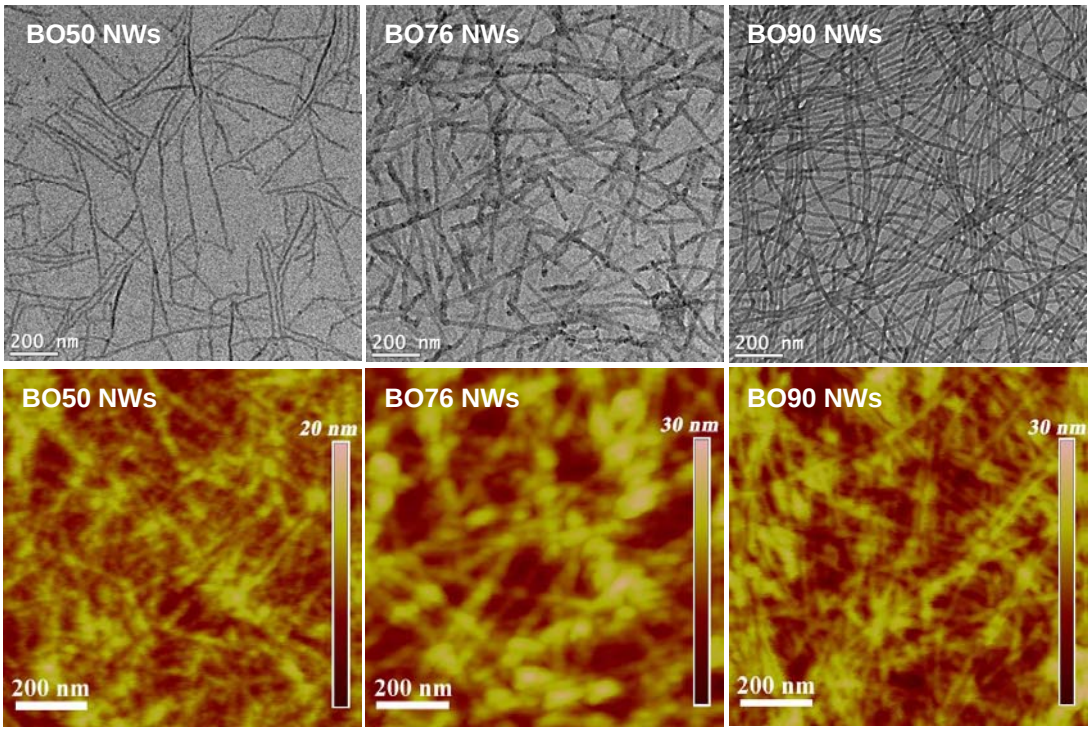

Figure 2.10 BF-TEM and AFM topographical images of NWs assembled from diblock copolythiophenes of different compositions: BO50, BO76, and BO90.

Figure 2.11 shows the TEM images of spin-coated thin films of the BO*x* NWs. It is obvious that the nanofiber morphology is maintained in the films, and even without any thermal annealing, these NWs show high crystallinity as indicated by the selected area electron diffraction (SAED) patterns shown in the inset of Figure 2.11. The fact that in SAED, diffraction signals are only collected from a small angle[39] up to 3 – 5^{o} makes the detection of reflections from π - π stacking in polymers possible.[40, 41] The bright outer rings in all the SAED patterns corresponds to (020) diffraction peak in the *q*-vector range of 2.5 – 2. 6 nm^{-1}, indicating that the π - stacking distance in films of BO*x* NWs is 0.38 – 0.40 nm. This π – stacking distance in films of diblock copolythiophene NWs is comparable to that in films of poly(3-alkylthiophene) homopolymers.[29] The observed SAED rings for BO50 and BO76 NWs are isotropic, indicating that these NWs arrange themselves randomly since there is no control over the orientation of the NWs. However, the SAED pattern for BO90 NWs appears to be anisotropic, which may be a result of oriented NWs in the small area sampled.

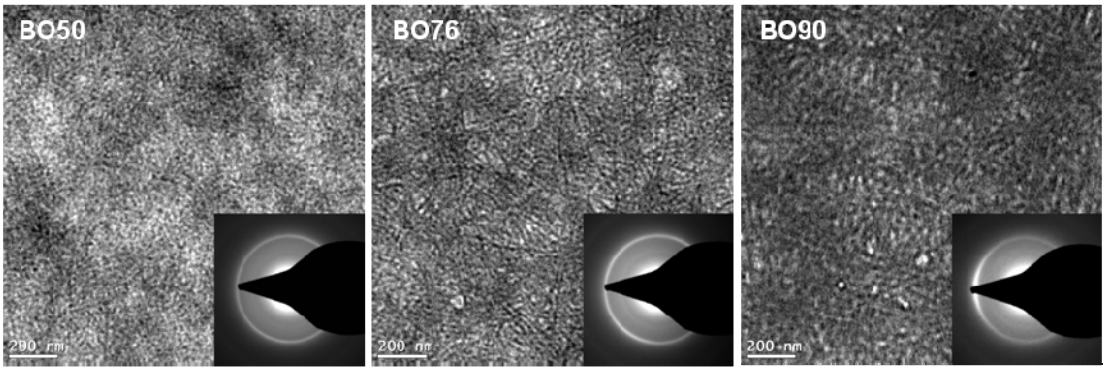

Figure 2.11 TEM images of pure block copolymer nanowire films.

The crystallinity and molecular packing in the diblock copolythiophene NWs were further confirmed by the X-ray diffraction (XRD) spectra shown in Figure 2.12a. The NWs of BO50, BO76, and BO90 show diffraction peaks that are characteristic of P3OT and P3BT blocks. In BO50 NWs, the observed interchain spacing (d_{100}) of 2.00 nm corresponds to that in P3OT block, while a shoulder that appears at a $2\theta = 6.10^{o}$ is characteristic of P3BT block (d_{100} = 1.45 nm).[42] In NWs of BO76 and BO90, a prominent peak corresponding to the P3BT block was observed with a d_{100} spacing of 1.36 nm and 1.38 nm, respectively. A shoulder at $2\theta = 5.19^{o}$ is visible in the XRD spectrum of BO76 NWs, corresponding to a *d*-spacing of 1.70 nm. It is obvious that in the assembly of the BO*x* NWs, the constituent P3OT and P3BT blocks organize in such a way that the lamellar spacings (d_{P3OT} and d_{P3BT}) are modified compared with the parent homopolymers (P3OT, P3BT). Combining information from both SAED and XRD, the molecular packing in these diblock copolythiophene NWs is proposed and schematically illustrated[19] in Figure 2.12b. The axis of the NWs is extended along the (010) or the π – stacking direction. In the (100) direction, the NWs are stacked by side-chain organization.

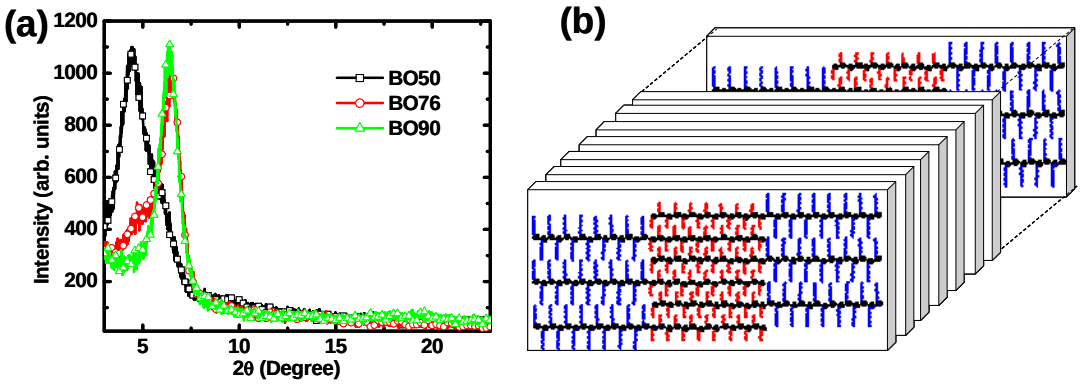

Figure 2.12 (a) X-ray diffraction spectra of films of BO50, BO76, and BO90 NWs. (b) Schematic illustration of molecular packing in a single BO*x* nanowire.

2.2.3.2 Bulk Heterojunction Solar Cells. The width of these copolythiophene NWs (13 – 16 nm) is comparable to the exciton diffusion length in polymer semiconductors (5 - 20) [1-3, 5, 6] and thus falls into the optimum distance for exciton dissociation in polymer solar cells. The crystalline nature of the copolymer NWs and their varying aspect ratios also suggest the possibility of tuning the charge transport and nanoscale morphology of BHJ solar cells.[12, 14] We have thus explored BHJ solar cells based on these diblock copolythiophene NWs.

The photovoltaic properties of BO*x* NWs in BHJ solar cells were studied by blending the NWs with an electron acceptor, [6,6]-phenyl-C_{71} butyric acid methyl ester ($PC_{71}BM$), using the device structure: ITO/PEDOT:PSS/active layer/LiF/Al, where the active layer is a BO*x* NWs:$PC_{71}BM$ nanocomposite. The solar cells were characterized under AM1.5 solar illumination at 1 sun (100 mW/cm^2) in laboratory air. Typical current density (J) – voltage (V) curves for BO50 NWs:$PC_{71}BM$, BO76 NWs:$PC_{71}BM$, and BO90 NWs:$PC_{71}BM$ thin film solar cells are shown in Figure 2.13a. The photovoltaic parameters calculated from the J-V curves are summarized in Table 2.3. The observed open circuit voltage (V_{oc}) was 0.53 - 0.59 V, which is comparable to BHJ solar cells from the homopolymers, P3BT and P3OT.[21] The short-current density (J_{sc}) increased from 8.31 mA/cm^2 in BO50 NWs to 9.85 mA/cm^2 in devices based on BO90 NWs. The fill factor of 0.58 – 0.65 is comparable to, and even higher than values found in P3BT NWs:$PC_{61}BM$ devices.[12,14] These photovoltaic parameters translate to a maximum power conversion efficiency (PCE) of 2.91, 3.14, and 3.38 %, and an average PCE of 2.86, 2.99, and 3.32% for BO50 NWs, BO76 NWs, and BO90 NWs BHJ devices, respectively. We note that the larger standard deviation in the average PCE of BO76 NW:$PC_{71}BM$ solar cells may be due to the higher polymer content in

this composite, which could have slowed the drying of the film and caused local heterogeneity. We also note that the small difference in PCEs between BO50 NWs:$PC_{71}BM$ and BO76 NWs:$PC_{71}BM$ solar cells arise from the small difference in their aspect ratios (48 ± 13 vs. 80 ± 27). Compared with the best BHJ devices based on P3BT:$PC_{71}BM$ blends (3.0 – 3.2 % PCE),[12] the BO*x* NW devices have a comparable efficiency, and in the case of 3.4 % PCE obtained for BO90 NWs, is even slightly higher.

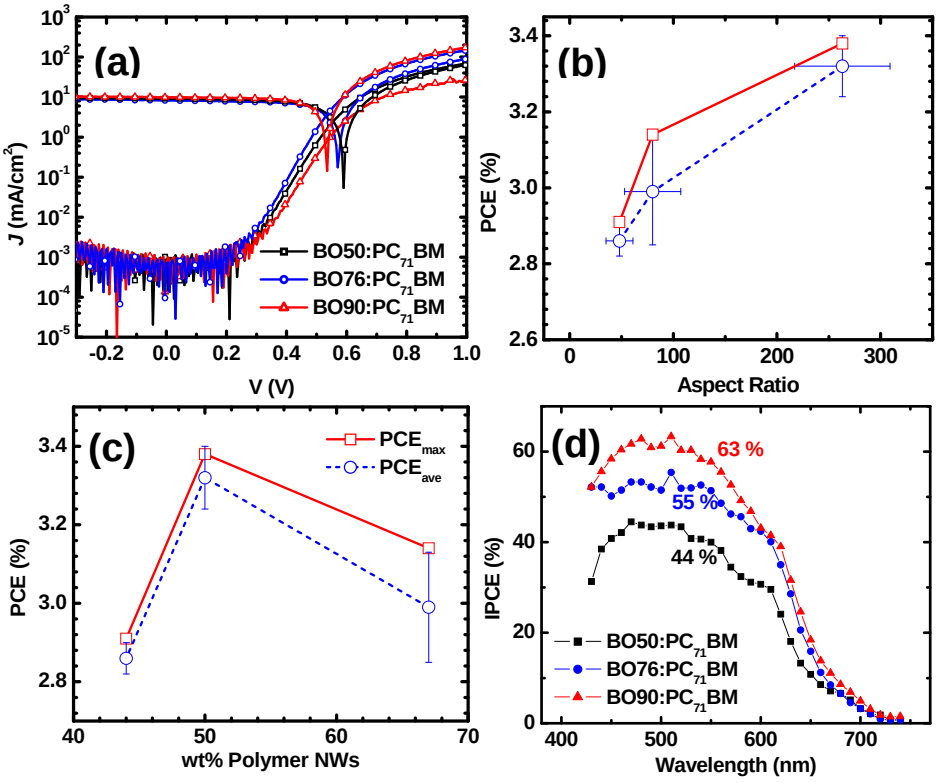

Figure 2.13 (a) Semi-logarithmic plot of the dark current density (*J*) – voltage (*V*) curves and the photocurrent density – voltage curves of solar cells made from BO*x* NWs:$PC_{71}BM$. (b) Plot of maximum (□) and average (○) PCEs vs. average aspect ratio of NWs. (c) Plot of maximum (□) and average (○) PCEs as a function of BO*x* NWs:$PC_{71}BM$ composition. (d) IPCE of BO*x* NWs:$PC_{71}BM$ solar cells at optimal blend ratios and processing conditions. BO50 NWs:$PC_{71}BM$ (1:1.25), BO76 NWs:$PC_{71}BM$ (1:0.5) and BO90 NWs:$PC_{71}BM$ (1:1) thin films were processed by 30 min, 120 min, 90 min film aging, respectively, followed by 5 min thermal annealing at 110 ^{o}C.

Table 2.3 Charge Transport and Photovoltaic Properties of BO*x* NWs:$PC_{71}BM$ Solar Cells.

Blends	Processing Condition[a]	μ_h[b] (cm^2/V s)	r_s (Ω cm^2)	r_p (Ω cm^2)	J_{sc} (mA/cm^2)	V_{oc} (V)	FF	PCE_{max} (%)	PCE_{ave}[c] (%)
BO50:$PC_{71}BM$ (1:1.25)	30 min FA 5 min TA	2.22 × 10^{-4}	10.3	449	8.31	0.57	0.62	2.91	2.86 ± 0.04
BO76:$PC_{71}BM$ (1:0.5)	120 min FA 5 min TA	7.03 × 10^{-5}	12.2	867	9.20	0.59	0.58	3.14	2.99 ± 0.14[d]
BO90:$PC_{71}BM$ (1:1)	90 min FA 5 min TA	1.72 × 10^{-4}	7.5	903	9.85	0.53	0.65	3.38	3.32 ± 0.08

[a] FA: film aging, TA: thermal annealing. [b] β values for BO*x*:$PC_{71}BM$ (x=50, 76, 90) are -1.70 × 10^{-4} $(m/V)^{1/2}$, -1.06 × 10^{-4} $(m/V)^{1/2}$, and -1.84 × 10^{-4} $(m/V)^{1/2}$, respectively. [c] Average based on 5 devices with standard deviation. [d] Average based on 10 devices with standard deviation.

The maximum and average efficiencies of BO*x* NW solar cells are plotted as a function of the average aspect ratio (*L*/*d*) of NWs, as shown in Figure 2.13b. A significant increase of both maximum and average PCEs with aspect ratio is observed, demonstrating that nanowires with high aspect ratio are beneficial in BHJ polymer solar cells. In contrast, the dependence of average and maximum efficiencies on the BO*x* NWs:$PC_{71}BM$ composition is non-monotonic as shown in Figure 2.13c. The incident photon-to-electron efficiency (IPCE) or action spectrum of each BO*x* NW solar cell is shown in Figure 2.13d. The photoresponse of these BHJ diodes turns on at about 730 nm and peaks at ~510 nm. Compared with solar cells based on blend thin films of the same block copolymers,[21] the IPCE maxima in the nanowire devices are red-shifted by 20 nm, an indication that more photons in the solar spectrum can be harvested and transformed to electrical current. The maximum IPCE was 44 % for BO50 NWs:$PC_{71}BM$, 55 % for BO76 NWs:$PC_{71}BM$, and 63 % for BO90 NWs:$PC_{71}BM$ devices. The IPCE thus increases with increasing aspect ratio of the diblock copolymer NWs, similar to the trend of PCE with aspect ratio. We note that the IPCE

value of BO90 NWs/$PC_{71}BM$ devices (63 %) is close to those reported for P3HT/fullerene BHJ solar cells.[43,44]

The electrical parameters of the copolythiophene NW solar cells were evaluated. The BO*x* NWs-based solar cells had good diode characteristics as indicated by the very high rectification ratios (680 – 2300 in the dark at ±0.60 V), and the large shunt resistance (r_p ~ 450 – 900 Ω cm^2) derived from the inverse of the slope at open-circuit conditions. On the other hand, the series resistance (r_s) obtained from the inverse of the slope at short-circuit conditions is in the range of 7.5 – 12.2 Ω cm^2, which is decreased compared with 13.5 – 21.1 Ω cm^2 observed in P3BT NWs:$PC_{61}BM$ solar cells.[14] The decreased series resistance of BO*x* NWs:$PC_{71}BM$ thin films (95 – 105 nm) is attributed to the decreased thickness compared with P3BT NWs:PC61BM thin films (200 – 230 nm). We also note that the series resistance observed in these BO*x* NWs:$PC_{71}BM$ solar cells is comparable to those of annealed P3HT:$PC_{61}BM$ blends with typical series resistance of 8 Ω cm^2 or less.[45, 46]

To gain further insight into the dependence of the performance of BHJ solar cells on nanowire aspect ratio, we investigated the photophysics, charge transport, and morphology of the same BO*x* NWs:$PC_{71}BM$ BHJ films. The thin film absorption spectra of BO50:$PC_{71}BM$ (1:1.25), BO76:$PC_{71}BM$ (1:0.5), and BO90:$PC_{71}BM$ (1:1), which gave the best power conversion efficiency, are shown in Figure 2.14. The lineshape of the spectra, absorption maxima, and absorption coefficient vary with the morphology of the NWs. All the spectra show distinct vibronic shoulders at 560 nm and 610 nm, indicative of improved interchain π - stacking and crystalline polymer domains in the BHJ thin films. The films of BO50 and BO90 NWs/$PC_{71}BM$

nanocomposites show a similar maximum absorption coefficient of 5×10^4 cm^{-1}, whereas BO76 NWs:$PC_{71}BM$ thin films had a higher value of 6.5×10^4 cm^{-1}. This trend can be explained by the fact that a lower amount of $PC_{71}BM$ is present in the BO76 nanocomposite, which also causes less disruption in the crystalline polymer NW phase. Comparing the absorption spectrum with the IPCE spectrum (Figure 2.13d) for each BO*x* NWs:$PC_{71}BM$ thin film, the two spectra have similar lineshapes and the same peak position. On the basis of the similar absorption spectra, the higher device efficiency of BO90 NWs:$PC_{71}BM$ solar cells compared to BO50 NWs:$PC_{71}BM$ cannot be fully understood and thus other factors must be considered.

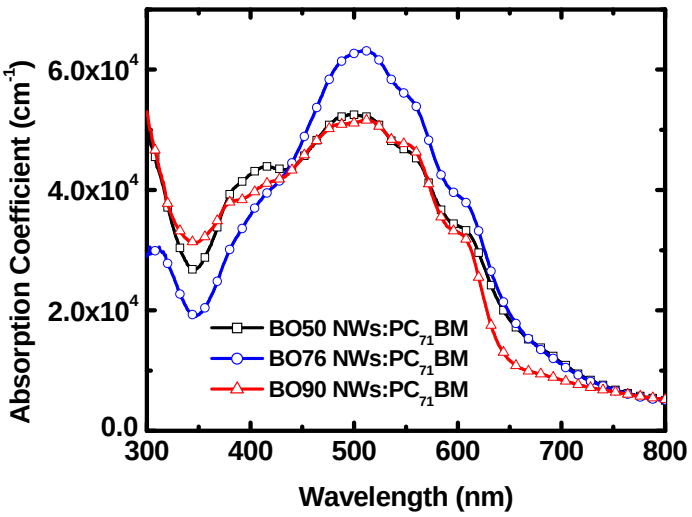

Figure 2.14 The absorption spectra of BO*x* NWs:$PC_{71}BM$ thin films measured directly from solar cells.

X-ray diffraction (XRD) was used to investigate the morphology and molecular packing in the BO*x* NWs:$PC_{71}BM$ BHJ thin films (80 – 100 nm). The XRD data were collected directly from the BHJ thin films without the LiF/Al cathode (Figure 2.15). BO50 NWs:$PC_{71}BM$ film shows two distinct reflections with 2θ angles of 4.39° and 6.29°, corresponding to *d*-spacings of

2.01 nm and 1.40 nm, respectively. In the case of BO76 and BO90 NWs, only one dominant reflection from the P3BT blocks was detected at 6.67° and 6.43°, with corresponding *d*-spacings of 1.32 nm and 1.37 nm, respectively. These *d*-spacings indicate that the interchain distances between polymer backbones are in good agreement with the *d*-spacing values for the pure BO50 and BO76 NWs.[19] This means that the molecular packing in the NWs is not significantly affected by $PC_{71}BM$ in the nanocomposites, or the processing conditions (film aging and thermal annealing).

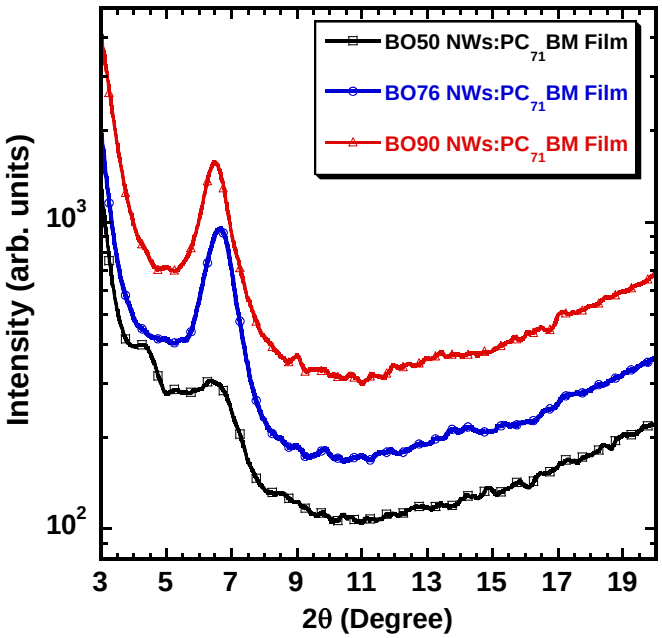

Figure 2.15 X-ray diffraction of BO*x* NWs:$PC_{71}BM$ thin films on solar cells without cathode deposition.

The morphology of BO*x* NWs:$PC_{71}BM$ films peeled directly from the solar cells were investigated by BF-TEM. The images were taken at slightly defocused conditions to enhance the contrast between crystalline and amorphous phases (Figure 2.16). The polymer phase is presumably the brighter phase and $PC_{71}BM$ is the darker phase due to density difference.[40] NWs

are present in the BO*x* NWs:$PC_{71}BM$ films as interconnected networks of the block copolymer donor phases. The darker phase in the images represents the distribution of $PC_{71}BM$ and it can be seen that these $PC_{71}BM$ domains are interconnected with sizes less than 50 nm. SAED was employed to probe the changes of crystallinity in the BHJ thin films and the results are shown in the insets of Figure 2.16. The bright outer rings in the SAED patterns indicate that the π - stacking distances of the diblock copolythiophene NWs in the blend films are 0.38 – 0.40 nm, which means that the π - stacking in the NWs is not destroyed by the presence of $PC_{71}BM$. The inner rings in the SAED patterns are $PC_{71}BM$ diffractions positioned at around 2.0 – 2.1 nm^{-1}, as confirmed by the pure $PC_{71}BM$ reflection peak at 2.04 nm^{-1} in Figure 2.16. The *d*-spacing for the $PC_{71}BM$ is calculated to be 0.49 nm, which is similar to values of another fullerene derivative, $PC_{61}BM$.[40, 41]

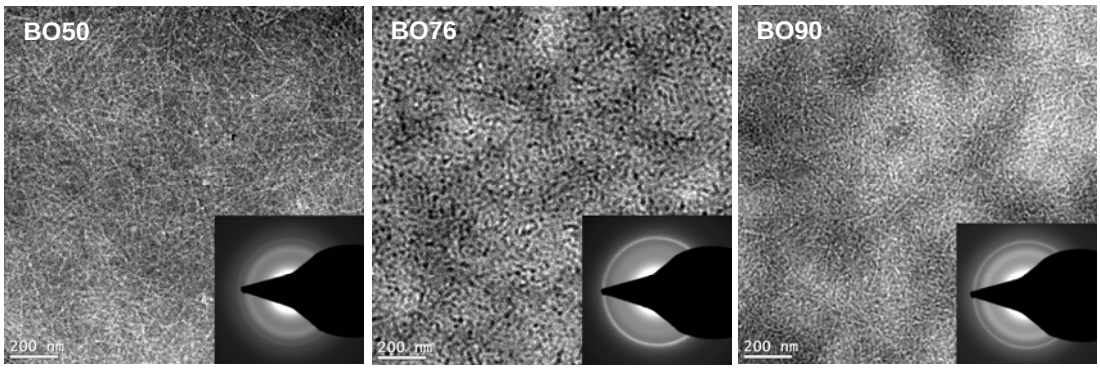

Figure 2.16 TEM images of BO*x* NWs:$PC_{71}BM$ thin films peeled from solar cells and their SAED patterns (inset).

The charge-carrier mobility of the NWs and the BO*x* NWs:$PC_{71}BM$ nanocomposites were evaluated by the space charge limited current (SCLC) method. The dark-current density (*J*) versus voltage (*V*) curves in the hole-only devices are shown in Figure 2.17. Zero-field mobilities of holes were extracted from the *J–V* curves by non-linear least-square fit to the modified

Mott-Gurney equation.[14, 36] The hole mobility in films of the neat BO50, BO76 and BO90 NWs was calculated to be 1.61×10^{-4}, 0.87×10^{-4}, and 1.26×10^{-4} cm^2/V s, respectively. The corresponding β values, which show the electric field dependence of mobility, were -2.10×10^{-4} $(m/V)^{1/2}$, -1.89×10^{-4} $(m/V)^{1/2}$, and -1.63×10^{-4} $(m/V)^{1/2}$, respectively. The SCLC mobility of holes in the BO*x* NW:$PC_{71}BM$ nanocomposites, which is collected in Table 2.3, showed very similar values as the films of the neat NWs. This means that the aspect ratio of the NWs does not influence the SCLC carrier mobility in the vertical direction of the thin films. The observed independence of SCLC carrier mobility as a function of aspect ratio is in line with the fact that the NWs in the BHJ thin films are largely parallel to the substrate. These SCLC hole mobilities are comparable to that of P3HT in annealed P3HT:$PC_{61}BM$ (1:1) blends (2×10^{-4} cm^2/V s)[47] and are one- or two-order of magnitude higher than those in P3OT:$PC_{71}BM$ (2.91×10^{-5} cm^2/V s) and P3BT:$PC_{71}BM$ (4.26×10^{-6} cm^2/V s) blends, respectively.[21] We note that, similar to P3BT NW:$PC_{61}BM$ solar cells, the hole mobility of these BO*x* NWs:$PC_{71}BM$ blends shows a negative electric field dependence.[14] These β values are comparable among BO*x* NWs and BO*x* NWs:$PC_{71}BM$ thin films, regardless of block composition and aspect ratio of NWs. The lack of dependence of SCLC hole mobility on aspect ratio in both neat BO*x* NWs and BO*x* NWs:$PC_{71}BM$ thin films means that the aspect-ratio-dependent photovoltaic properties is not likely to be caused by variation in hole transport.

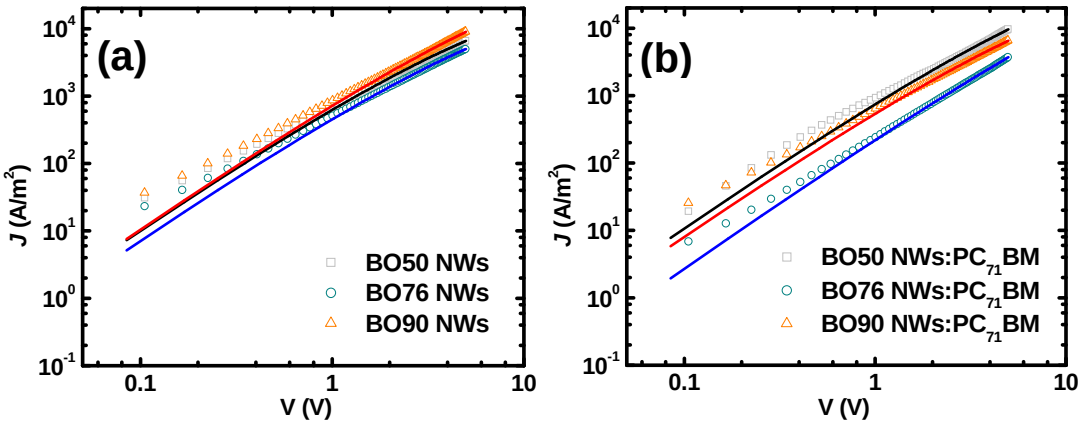

Figure 2.17 (a) *J-V* curves and the corresponding non-linear least-square fitting of films of BO*x* NWs (a) and BHJ BO*x* NWs:$PC_{71}BM$ films (b). The thickness of BO*x* NW (x = 50, 76, 90) films is 73 nm, 66 nm, and 68 nm, respectively, and 81 nm, 93 nm, and 79 nm for BO*x* NWs:$PC_{71}BM$ films.

In summary, we have found that the performance (PCE, IPCE) of BHJ solar cells based on diblock copolythiophene NWs increases with increasing aspect ratio of the nanowires. Although the absorption (and thus light harvesting) and charge carrier (SCLC) mobility of holes are enhanced in these nanowire-based BHJ devices, compared to similar blend or homopolymer devices, these factors could not explain the observed dependence of power conversion efficiency and IPCE on aspect ratio of the block copolymer NWs. In the light of the observed morphology, although the NWs have similar widths within the nanocomposites with $PC_{71}BM$, the variation in the aspect ratio seems to influence performance of the BHJ solar cells in subtle ways. The introduction of donor materials in the form of polymer nanowires also allows a more uniform nanoscale mixing between donors and acceptors in the BHJ thin films. Since long nanowires facilitate the formation of interconnected network and bicontinuous, percolated phase separation, NWs with high aspect ratios would facilitate a higher rate of exciton generation and dissociation,

and subsequent charge transport and collection. Additional studies of exciton dissociation and charge recombination rates in polymer nanowire-based BHJ solar cells are necessary to fully understand the observed aspect ratio dependence of photovoltaic efficiency.

2.2.4 Conclusions

We have synthesized NWs with tunable aspect ratio from a series of block copoly(3-alkylthiophene)s through solution phase self-assembly. TEM imaging of the morphology of these NWs showed that the one-dimensional polymer nanostructures had a width of 13 – 16 nm and average aspect ratio of 48 ± 13, 80 ± 27 and 263 ± 46 for BO50, BO76, and BO90 NWs, respectively. The results show that the diblock copolymer composition provides a facile and powerful means of tuning the aspect ratio of polymer semiconductor nanowires. Bulk heterojunction solar cells based on BO*x* NWs/$PC_{71}BM$ nanocomposites showed a dependence of photovoltaic efficiency (2.9 - 3.4 % PCE) on aspect ratio of the NWs. TEM imaging showed that an interconnected network of polymer NWs with nanoscale donor/acceptor phase separation was achieved. The crystallinity of both copolymer and $PC_{71}BM$ phases was revealed by SAED, as indicated by the intensity of reflection peaks from polymer π-stacking in the copolymer phase and $PC_{71}BM$. The SCLC charge mobility of holes in the BHJ solar cells was invariant with the aspect ratio of the nanowires because of the parallel orientation of the NWs to the substrate. The observed aspect-ratio-dependent photovoltaic properties of the BO*x* NWs are attributed to enhanced charge separation, transport, and collection in the BHJ devices. We conclude that polymer semiconductor NWs with high aspect ratio (length/width = 125 – 350) are desirable for improving the performance of BHJ solar cells.

2.2.5 References

1. Gunes, S.; Neugebauer, H.; Sariciftci, N. S. *Chem. Rev.* **2007,** *107*, 1324-1338.

2. Coakley, K. M.; McGehee, M. D. *Chem. Mater.* **2004,** *16*, 4533-4542.

3. Thompson, B. C.; Frechet, J. M. J. *Angew. Chem. Int. Ed.* **2008,** *47*, 58-77.

4. Dennler, G.; Scharber, M. C.; Brabec, C. J. *Adv. Mater.* **2009,** *21*, 1323-1338.

5. Blom, P. W. M.; Mihailetchi, V. D.; Koster, L. J. A.; Markov, D. E. *Adv. Mater.* **2007,** *19*, 1551-1566.

6. Alam, M. M.; Jenekhe, S. A. *J. Phys. Chem. B* **2001,** *105*, 2479-2482.

7. Yu, G.; Gao, J.; Hummelen, J. C.; Wudl, F.; Heeger, A. J. *Science* **1995,** *270*, 1789-1792.

8. Liang, Y.; Wu, Y.; Feng, D.; Tsai, S.-T.; Son, H.-J.; Li, G.; Yu, L. *J. Am. Chem. Soc.* **2009,** *131*, 56-57.

9. Liang, Y.; Xu, Z.; Xia, J.; Tsai, S.-T.; Wu, Y.; Li, G.; Ray, C.; Yu, L. *Adv. Mater.* **2010,** *22*, E135-E138.

10. Lee, J. K.; Ma, W. L.; Brabec, C. J.; Yuen, J.; Moon, J. S.; Kim, J. Y.; Lee, K.; Bazan, G. C.; Heeger, A. J. *J. Am. Chem. Soc.* **2008,** *130*, 3619-3623.

11. Peet, J.; Kim, J. Y.; Coates, N. E.; Ma, W. L.; Moses, D.; Heeger, A. J.; Bazan, G. C. *Nat Mater* **2007,** *6*, 497-500.

12. Xin, H.; Kim, F. S.; Jenekhe, S. A. *J. Am. Chem. Soc.* **2008,** *130*, 5424-5425.

13. Xin, H.; Reid, O. G.; Ren, G.; Kim, F. S.; Ginger, D. S.; Jenekhe, S. A. *ACS Nano* **2010,** *4*, 1861–1872.

14. Xin, H.; Ren, G.; Kim, F. S.; Jenekhe, S. A. *Chem. Mater.* **2008,** *20*, 6199-6207.

15. Wu, P.-T.; Xin, H.; Kim, F. S.; Ren, G.; Jenekhe, S. A. *Macromolecules* **2009,** *42*, 8817-8826.

16. Berson, S.; Bettignies, R. D.; Bailly, S.; Guillerez, S. *Adv. Funct. Mater.* **2007,** *17*, 1377-1384.

17. Kim, F. S.; Ren, G.; Jenekhe, S. A. *Chem. Mater.* **2011,** *23*, 682–732.

18. Botiz, I.; Darling, S. B. *Mater. Today* **2010,** *13*, 42-51.

19. Wu, P.-T.; Ren, G.; Li, C.; Mezzenga, R.; Jenekhe, S. A. *Macromolecules* **2009,** *42*, 2317-2320.

20. Wu, P.-T.; Ren, G.; Kim, F. S.; Li, C.; Mezzenga, R.; Jenekhe, S. A. *J. Polym. Sci. A: Polym. Chem.* **2010,** *48*, 614-626.

21. Ren, G.; Wu, P.-T.; Jenekhe, S. A. *Chem. Mater.* **2010,** *22*, 2020-2026.

22. He, M.; Zhao, L.; Wang, J.; Han, W.; Yang, Y.; Qiu, F.; Lin, Z. *ACS Nano* **2010,** *4*, 3241-3247.

23. Botiz, I.; Darling, S. B. *Macromolecules* **2009,** *42*, 8211-8217.

24. Segalman, R. A.; McCulloch, B.; Kirmayer, S.; Urban, J. J. *Macromolecules* **2009,** *42*, 9205-9216.

25. Lindner, S. M.; Huttner, S.; Chiche, A.; Thelakkat, M.; Krausch, G. *Angew. Chem. Int. Ed.* **2006,** *45*, 3364-3368.

26. Sommer, M.; Huttner, S.; Wunder, S.; Thelakkat, M. *Adv. Mater.* **2008,** *20*, 2523-2527.

27. Zhang, Q.; Cirpan, A.; Russell, T. P.; Emrick, T. *Macromolecules* **2009,** *42*, 1079-1082.

28. Darling, S. B. *Energy Environ. Sci.* **2009,** *2*, 1266 - 1273.

29. Ihn, K. J.; Moulton, J.; Smith, P. *J. Polym. Sci. B* **1993,** *31*, 735-742.

30. Oosterbaan, W. D.; Vrindts, V.; Berson, S.; Guillerez, S.; Douhéret, O.; Ruttens, B.; D'Haen, J.; Adriaensens, P.; Manca, J.; Lutsen, L.; Vanderzande, D. *J. Mater. Chem.* **2009,** *19*, 5424-5435.

31. Samitsu, S.; Shimomura, T.; Heike, S.; Hashizume, T.; Ito, K. *Macromolecules* **2008,** *41*, 8000-8010.

32. Merlo, J. A.; Frisbie, C. D. *J. Phys. Chem. B* **2004,** *108*, 19169-19179.

33. Samitsu, S.; Shimomura, T.; Ito, K. *Thin Solid Films* **2008,** *516*, 2478-2486.

34. Liu, J.; Arif, M.; Zou, J.; Khondaker, S. I.; Zhai, L. *Macromolecules* **2009,** *42*, 9390-9393.

35. Lu, G.; Li, L.; Yang, X. *Macromolecules* **2008,** *41*, 2062-2070.

36. Murgatroyd, P. N. *J. Phys. D: Appl. Phys.* **1970,** *3*, 151-156.

37. Blom, P. W. M.; de Jong, M. J. M.; van Munster, M. G. *Phys. Rev. B* **1997,** *55*, R656-R659.

38. Domercq, B.; Yu, J. S.; Kaafarani, B. R.; Kondo, T.; Yoo, S.; Haddock, J. N.; Barlow, S.; Marder, S. R.; Kippelen, B. *Mol. Cryst. Liq. Cryst.* **2008,** *481*, 80-93.

39. Bendersky, L. A.; Gayle, F. W. *J. Res. Natl. Inst. Stand. Technol.* **2001,** *106*, 997-1012.

40. van Bavel, S. S.; Sourty, E.; de With, G.; Loos, J. *Nano Lett.* **2009,** *9*, 507-513.

41. Yang, X.; van Duren, J. K. J.; Rispens, M. T.; Hummelen, J. C.; Janssen, R. A. J.; Michels, M. A. J.; Loos, J. *Adv. Mater.* **2004,** *16*, 802-806.

42. Wu, P.-T.; Ren, G.; Jenekhe, S. A. *Macromolecules* **2010,** *43*, 3306-3313.

43. Li, G.; Yao, Y.; Yang, H.; Shrotriya, V.; Yang, G.; Yang, Y. *Adv. Funct. Mater.* **2007,** *17*, 1636-1644.

44. Padinger, F.; Rittberger, R. S.; Sariciftci, N. S. *Adv. Funct. Mater.* **2003,** *13*, 85-88.

45. Ma, W.; Yang, C.; Gang, X.; Lee, K.; Heeger, A. J. *Adv. Funct. Mater.* **2005,** *15*, 1617-1622.

46. Chu, C.-W.; Yang, H.; Hou, W.-J.; Huang, J.; Li, G.; Yang, Y. *Appl. Phys. Lett.* **2008,** *92*, 103306.

47. Mihailetchi, V. D.; Xie, H.; de Boer, B.; Koster, L. J. A.; Blom, P. W. M. *Adv. Funct. Mater.* **2006,** *16*, 699-708.

Chapter 3 Benzobisthiazole Copolymer/Fullerene Bulk Heterojunction Solar Cells: Driving Force of Hole Transfer

3.1 Introduction

Organic semiconductors are finding increasing applications in optoelectronic and electronic devices, such as organic solar cells (OSCs)[1-5] and organic field-effect transistors (OFETs).[6,7] For example, the power conversion efficiency (PCE) of bulk heterojunction (BHJ) solar cells made from organic semiconductors is approaching 10%,[3] demonstrating the potential of organic solar cells as a means of utilizing solar energy.

Oxidation-resistant conjugated polymers, typically those with very negative ionization energies, have attracted increased attention in OFET research, due to their enhanced durability and lengthened operation lifetime in air. For instance, using benzobisthiazole as the electron deficient building block and various other electron rich moieties (dithienosilole, dithienopyrrole, carbazole, and bithiophene), the ionization energy can be tuned by nearly 900 meV, yielding OFETs with remarkably stable (over 2 years in air) hole mobility, threshold voltage, and on/off current ratio.[4i] Further exploring such oxidation-resistant conjugated copolymers for use in organic solar cells with extended operation lifetime is highly desirable. However, making the donor material more difficult to oxidize can complicate device operation as it can decrease the free energy available for driving photoinduced hole transfer from the acceptor material.

Fullerene derivatives have been widely used as the electron acceptors in organic solar cells and have yielded the highest power conversion efficiencies so far.[3] High performance fullerene materials include [6,6]-phenyl-C_{71}-butyric acid methyl ester ($PC_{71}BM$), [6,6]-phenyl-C_{61}-butyric acid methyl ester ($PC_{61}BM$), and indene-C_{60} *bis*-adduct ($IC_{60}BA$).

However, chemical modification of fullerenes usually results in modified ionization energy (*IE*) and electron affinity (*EA*) values, as well as changes in film morphology, both of which can affect the photovoltaic properties of solar cells. For example, in $PC_{71}BM$, $PC_{61}BM$ and $IC_{60}BA$, the value of *EA* varies between 3.8 - 4.0 eV.[8]

In this paper, we study the use of an oxidation-resistant conjugated copolymer, poly[(4,8-bis(2-hexyldecyl)oxy)benzo[1,2-b:4,5-b']dithiophene)-2,6-diyl-alt-(2,5-bis(3-dodecylthiophen-2-yl)benzo[1,2-d;4,5-d']bisthiazole)] (PBTHDDT)[4i] in a series of polymer/fullerene blend solar cells. In addition to the technological interest associated with the use of polymers with increased oxidative stability, the use of PBTHDDT is of interest for fundamental studies because the ionization energy (*IE*) of the polymer is quite negative relative to vacuum, and is similar to the energy released when transferring an electron to the half-filled HOMO of the fullerene exciton (the excited state electron affinity). We can thus use PBTHDDT/fullerene blends to examine the effects of modulating the driving force for photoinduced hole transfer on the photovoltaic behavior of BHJ polymer solar cells. We find that solar cells based on PBTHDDT:PCBM have much higher power conversion efficiencies (2.70-3.75% PCE) compared with that of ICBA-based devices (1.52% PCE). The photoinduced absorption (PIA) spectra of all the PBTHDDT:fullerene blends exhibit long-lived positive polarons in PBTHDDT and negative polarons on the fullerene when exciting the polymer. However, no induced absorption features are observed when selectively exciting $IC_{60}BA$ blended with PBTHDDT, suggesting that $IC_{60}BA$ excitons do not efficiently generate long-lived charges at the D/A interface. On the other hand, selective excitation of $PC_{71}BM$ or $PC_{61}BM$ blended with PBTHDDT does generate long-lived polarons. We explain these results by using the offset between the ionization energy of the polymer and the electron affinity of the fullerene *in its*

singlet excited state as the measure of the driving force for charge separation via photoinduced hole transfer. Specifically, we find the driving force for photoinduced hole transfer to be insufficient to sustain long-lived charge separation from $IC_{60}BA$ excitons when paired with PBTHDDT.

3.2 Experimental Section

3.2.1 Materials: The synthesis and characterization of poly[(4,8-bis(2-hexyldecyl)oxy)benzo[1,2-b:4,5-b']dithiophene)-2,6-diyl-alt-(2,5-bis(3-dodecylthiophen-2-yl)benzo[1,2-d;4,5-d']bisthiazole)] (PBTHDDT, M_n = 19.94 kDa, PDI = 2.84) were reported elsewhere.[4i] Regioregular poly(3-hexylthiophene) (P3HT) (M_w = 35.40 kDa, PDI = 2.45) was purchased from Rieke Metals. The fullerenes, [6,6]-phenyl-C_{71}-butyric acid methyl ester ($PC_{71}BM$, >99.0%), [6,6]-phenyl-C_{61}-butyric acid methyl ester ($PC_{61}BM$, >99.5%), and indene− C_{60} bisadduct ($IC_{60}BA$, >99%) were purchased from Nano-C, American Dye Sources, Inc., and Luminescence Technology Corp., respectively. Anhydrous *ortho*-dichlorobenzene (ODCB), and 1,8-diiodooctane (DIO) were obtained from Sigma Aldrich. All commercial products were used without further purification.

3.2.2 Characterization of Energy Levels: Cyclic voltammetry (CV) was carried out on an EG&G Princeton Applied Research potentiostat/galvanostat (Model 273A), and the data were analyzed using a Model 270 electrochemical analysis system software. A three-electrode cell was used, with platinum wires as both counter and working electrodes, and Ag/Ag^+ (Ag in 0.1 M $AgNO_3$ solution, Bioanalytical System, Inc.) as a reference electrode. A thin film of each semiconductor was coated onto a platinum electrode from a concentrated solution in chloroform and dried in vacuum. Solution CV was performed with 10 mg of solute in a 0.1 M solution of $TBAPF_6$ in benzene/acetonitrile (11.3mL/3.8mL) under N_2. Using the ferrocenium/ferrocene

(Fc^+/Fc) redox couple as an internal standard, the redox potential values were obtained in reference to a Ag/Ag^+ electrode. All solutions were purged with N_2 for 20 min before each experiment. Solid state ionization energy (*IE*) and electron affinity (*EA*) values were estimated from cyclic voltammetry (relative to SCE) using the relationship of, $EA = eE_{red}^{onset} + 4.4\ eV$ and *IE* using the relationship $IE = eE_{ox}^{onset} + 4.4\ eV$.[26]

UV photoemission spectroscopy measurements (UPS) were performed under ultra-high vacuum conditions using the He(I) photon line (21.22 eV) from a He discharge lamp. The energy resolution of the measurement was 0.15 eV. A -5V bias was applied to the sample to facilitate the observation of the slow electron cutoff. Inverse photoemission spectroscopy (IPES) measurements were conducted in the isochromat mode, detecting photons with an energy of ~10eV. For the measurements, the energy of the exciting electrons produced by a low energy electron gun was swept from ~ 5 to 15 eV. Degradation of the sample was minimized by varying the position of the electron beam on the surface, so that no single spot was exposed for longer than 2 min. The overall IPES instrumental resolution is 450 meV, estimated from the width of a metal Fermi edge. The substrates prepared for UPS and IPES measurements consisted of ozone treated indium tin oxide (Thin Film Technology) covered by approximately 20 nm of PBTHDDT or each fullerene derivative. The ionization energy and electron affinity were derived by fitting the onset of the density of states by a linear slope and measuring the intersection of this fit with the background signal.

3.2.3 Device Fabrication and Characterization: ODCB solutions of 10 mg/mL PBTHDDT, 20 mg/mL P3HT, and 60 mg/mL fullerene ($PC_{71}BM$, $PC_{61}BM$, or $IC_{60}BA$) were prepared and stirred until complete dissolution. All solutions were passed through 0.45 μm filters before use. Blend solutions of PBTHDDT:fullerene and P3HT:fullerene were prepared by mixing respective

solutions at desired weight ratio.

Solar cells were fabricated on ITO-coated glass substrates (10 Ω/square, Shanghai B. Tree Tech, China). The substrates were cleaned sequentially with acetone, deionized water, isopropyl alcohol in an ultrasonic bath, and dried in a vacuum oven. A 40 nm PEDOT:PSS (Clevios P VP AI 4083) layer was spin-coated on top of the ITO and dried at 150 ° C for 10 min under vacuum. The blend solution, which is either PBTHDDT:fullerene (containing 2.5 vol% DIO) or P3HT:fullerene blend, was spin-coated on top of PEDOT:PSS to make a BHJ active layer of ~80 nm in the glovebox. The active layer was then dried in vacuum for 2 hours (PBTHDDT:fullerene) or aged in a Petri dish for 30 min and annealed at 175 ° C for 10 min (P3HT:fullerene). The substrates were then loaded in a thermal evaporator (BOC Edwards, model 306) to deposit a cathode composed of 1.0 nm LiF and 80 nm Al under high vacuum (8×10^{-7} Torr). Four solar cells, each with an active area of 9 mm^2, were fabricated per ITO substrate.

Current–voltage characteristics of the non-encapsulated solar cells were obtained using an HP4155A semiconductor parameter analyzer in ambient laboratory air. The 1 Sun illumination (AM1.5 at 100 mW/cm^2) was provided by a filtered Xe lamp and calibrated by using a Si diode calibrated at the National Renewable Energy Lab (NREL, USA). Incident photon-to-current efficiency (IPCE) was measured using a QEX10 solar cell quantum efficiency measurement system (PV Measurements, Inc.).

3.2.4 Characterization of Morphology. Atomic force microscopy (AFM) imaging was performed on the same solar cell devices using a Dimension 3100 SPM (Veeco) instrument operating in tapping mode. Thin films of the active layers were obtained by scratching edges of the thin films, soaking with water, and peeling them off from the device substrates, and they were then supported on TEM grids (Electron Microscopy Sciences) for bright-field transmission

electron microscopy (BF-TEM) imaging. An FEI Tecnai G^2 F20 TEM at 200 kV was employed. Images were slightly defocused to enhance the phase contrast between the polymer and fullerene, and were acquired with a CCD camera and recorded with Gatan DigitalMicrograph software.

3.2.5 UV-vis Absorption and Photoinduced Absorption (PIA) Spectra: UV-vis absorption spectra of neat polymer or fullerene films were recorded with a Perkin-Elmer model Lambda 900 UV/vis/near-IR spectrophotometer using glass substrate. UV− vis absorption spectra of blend films were recorded on the blend films spin-coated on top of PEDOT/ITO substrates, following the same processing conditions as the solar cells. PIA spectra were collected as previously described[27] using conventional lock-in detection methods[28] employing either a 455 nm or 630 nm LED excitation source modulated at 200 Hz. Measurements were performed in transmission mode on glass substrates in a Janis cryostat at 80K. Spectroelectrochemical measurements were performed at room temperature on PBTHDDT films deposited on ITO substrates immersed in acetonitrile:tetrabutylammonium perchlorate solution with a silver reference electrode in a Cary UV-Vis-NIR spectrophotometer.

3.3 Results and Discussion

3.3.1. Photovoltaic Properties

We show the molecular structures of poly[(4,8-bis(2-hexyldecyl)oxy)benzo[1,2-b:4,5-b']dithiophene)-2,6-diyl-alt-(2,5-bis(3-dodecylthiophen-2-yl)benzo[1,2-d;4,5-d']bisthiazole)] (PBTHDDT) and the three different fullerene derivatives, including $PC_{71}BM$, $PC_{61}BM$, and $IC_{60}BA$, in Figure 5.1. PBTHDDT contains a benzobisthiazole as the electron deficient moiety and a benzodithiophene as the electron rich moiety in the repeating unit.

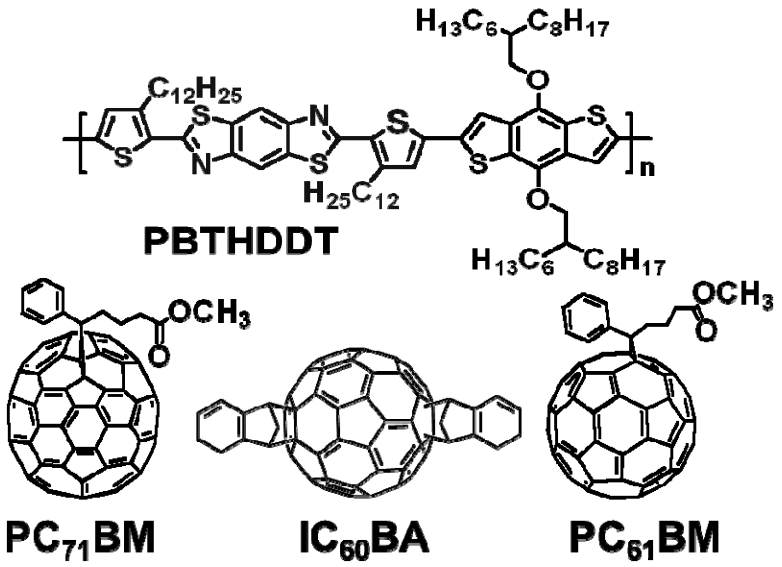

Figure 3.1 Molecular structures of PBTHDDT donor polymer and three fullerene acceptors ($PC_{71}BM$, $IC_{60}BA$, and $PC_{61}BM$) used this study.

We first investigated the photovoltaic properties of BHJ solar cells made from PBTHDDT:fullerene blends, where the fullerene acceptor is either $PC_{71}BM$, $PC_{61}BM$, or $IC_{60}BA$. The solar cells have the basic device structure of ITO/PEDOT:PSS/active layer/LiF/Al, where the active layer is a spin-cast film composed of PBTHDDT:fullerene blend with an optimal weight ratio of 1:2, and processed with 2.5 vol% 1,8-diiodooctane (DIO). The solar cells were fabricated in a glovebox and tested under AM1.5 solar illumination at 1 sun (100 mW/cm^2) in ambient air. The current density (*J*)–voltage (*V*) curves for these devices are shown in Figure 3.2a. The photovoltaic parameters of devices made from PBTHDDT:fullerene blends, including the open circuit voltage (V_{oc}), the short-circuit current density (J_{sc}), and fill factors (*FF*) are collected in Table 3.1. V_{oc} increased slightly from 0.64 V in PBTHDDT:$PC_{71}BM$ devices to 0.69 V in PBTHDDT:$PC_{61}BM$ devices, but increased dramatically to 0.95 V in PBTHDDT:$IC_{60}BA$ solar cells. However, we observe a significant reduction in J_{sc} and slight losses in *FF* as well in the $IC_{60}BA$-based solar cells, compared with the $PC_{71}BM$ and $PC_{61}BM$ based devices. For

example, a J_{sc} of 3.45 mA/cm^2 in PBTHDDT:IC$_{60}$BA solar cells represents a 64% and 46% decrease compared to that of PBTHDDT:PC$_{71}$BM (9.60 mA/cm^2) and PBTHDDT:PC$_{61}$BM (6.39 mA/cm^2) solar cells, respectively. We observe a small decrease in *FF* to 0.50 for PBTHDDT:IC$_{60}$BA solar cells (~20% lower than that of PCBM-based devices). As a result, average power conversion efficiency (PCE) decreased from 3.75 ± 0.06% for PBTHDDT:PC$_{71}$BM, and 2.70 ± 0.05% for PBTHDDT:PC$_{61}$BM, to 1.52 ± 0.07% in PBTHDDT:IC$_{60}$BA solar cells, with the major efficiency loss due to comparatively low photocurrent generation.

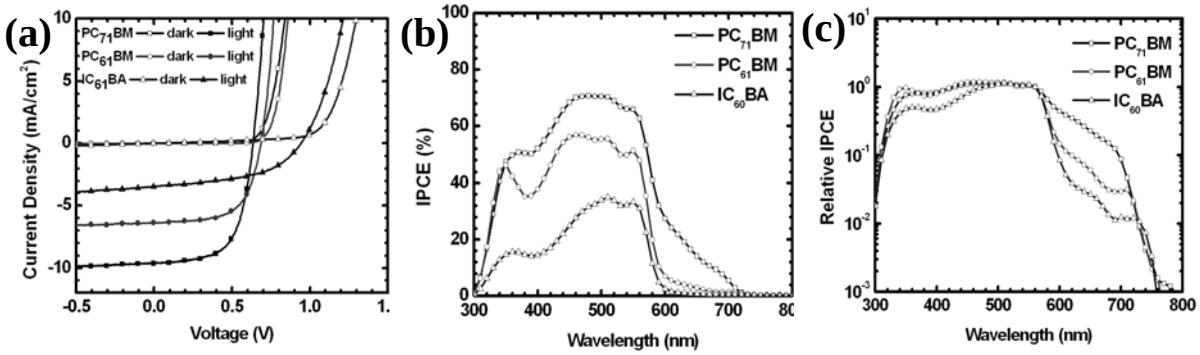

Figure 3.2 a) Current density (*J*) – voltage (*V*) characteristics, b) IPCE spectra of the PBTHDDT:fullerene (1:2) blend solar cells and c) Semi-log scale IPCE spectra normalized to PBTHDDT absorption at 560 nm.

The incident photon-to-electron efficiency (IPCE) or photocurrent action spectrum of each PBTHDDT:fullerene solar cell system is shown in Figure 3.2b. The photoresponse of PBTHDDT:PC$_{71}$BM turns on at about 720 nm and peaks at 460-510 nm. The response above 600 nm is due almost entirely to the fullerene, as PBTHDDT has negligible absorbance beyond 600 nm (Figure 3.3). The photoresponse of PBTHDDT:PC$_{61}$BM also begins at ~720 nm, but is much weaker over the region from ~720-580 nm due to the reduced absorption in the spherically

symmetric fullerene relative to the $PC_{71}BM$. Finally, the PBTHDDT:$IC_{60}BA$ solar cells exhibit the lowest overall photocurrent, and show less than 1% IPCE over the region where only the fullerene absorbs (λ = 600 – 720 nm). To more clearly illustrate the low photoresponse from the $IC_{60}BA$ acceptor in this spectral region, Figure 3.2c shows the IPCE values normalized to the PBTHDDT absorption at ca. 560 nm.

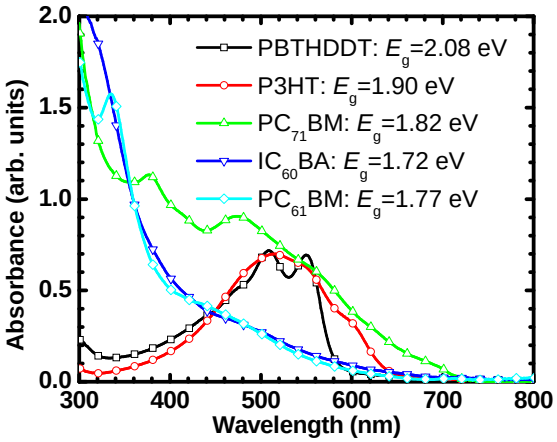

Figure 3.3 UV-vis absorption spectra of neat films of PBTHDDT, P3HT, $PC_{71}BM$, $PC_{61}BM$, and $IC_{60}BA$, and their optical bandgap.

The maximum IPCE was 70% for PBTHDDT:$PC_{71}BM$, 57% for PBTHDDT:$PC_{61}BM$, and 33% for PBTHDDT:$IC_{71}BA$ devices. The expected J_{sc} (calculated from the IPCE spectrum) is 9.00 mA/cm^2 for PBTHDDT:$PC_{71}BM$, 6.13 mA/cm^2 for PBTHDDT:$PC_{61}BM$, and 3.25 mA/cm^2 for PBTHDDT:$IC_{71}BA$, respectively. These J_{sc} values calculated from the IPCE spectra are slightly (4.1-6.3%) lower than the J_{sc} obtained in *J-V* measurements. This small discrepancy could be due to spectral mismatch between the simulated light source and the AM1.5 solar spectrum or to degradation of the solar cells during measurement since the IPCE data was collected following the *J-V* measurement.

Table 3.1 Device Metrics and Energies Offsets of PBTHDDT:Fullerene Blend Solar Cells.[a]

Blend[b]	V_{oc} [V]	J_{sc} [mA/cm^2]	FF	η_{max} [% PCE]	η_{ave} [% PCE]	ΔE_{Hole}[c]	ΔE_{Elec}[c]	ΔE_{DA}[d]
PBTHDDT:$PC_{71}BM$	0.64	9.60	0.63	3.83	3.75±0.06	-0.133	-0.403	-1.68
PBTHDDT:$PC_{61}BM$	0.69	6.39	0.62	2.72	2.70±0.05	-0.066	-0.376	-1.70
PBTHDDT:$IC_{60}BA$	0.95	3.45	0.50	1.62	1.52±0.07	0.110	-0.250	-1.83

[a] Energy difference calculated in eV from average of film CV, solution, CV and PES data. [b] 1:2 wt:wt blend ratio. [c] See Equation 3.2. [d] $\Delta E_{DA} = IE$[Donor] – EA[Acceptor].

Table 3.2 Photovoltaic Properties of P3HT:Fullerene Blend Solar Cells.

Blend[a]	V_{oc} [V]	J_{sc} [mA/cm^2]	FF	η_{max} [% PCE]	η_{ave} [% PCE]
P3HT:$PC_{71}BM$	0.61	9.54	0.64	3.73	3.70±0.04
P3HT:$PC_{61}BM$	0.61	8.29	0.63	3.19	3.15±0.05
P3HT:$IC_{60}BA$	0.79	9.12	0.61	4.40	4.32±0.09

[a] 1:1 wt:wt blend ratio.

For comparison with the PBTHDDT devices, we fabricated BHJ solar cells based on P3HT:fullerene (1:1 wt/wt) blends, and characterized their photovoltaic performance under similar conditions. We present the *J-V* characteristics of our P3HT:fullerene BHJ solar cells in Figure 3.4 and summarize their photovoltaic properties in Table 3.2. Average PCEs of 3.70± 0.04%, 3.15±0.05%, and 4.32±0.09% were achieved in P3HT:$PC_{71}BM$, P3HT:$PC_{61}BM$, and P3HT:$IC_{60}BA$ solar cells, respectively. The increasing trend in PCE as $PC_{61}BM$, $PC_{71}BM$, and $IC_{60}BA$ are used as electron acceptor in BHJ solar cells agrees well with previous observations.[4f, 4k] Briefly, the enhancement in PCE in P3HT:$PC_{71}BM$ compared to that of P3HT:$PC_{61}BM$ is primarily due to the enhanced absorption in the visible region and optimized nanoscale morphology in P3HT:$PC_{71}BM$ films.[9] P3HT:$IC_{60}BA$ solar cells have a higher V_{oc} (0.79 V) than that of P3HT:PCBM devices (0.61 V), while the other photovoltaic parameters (J_{sc} and FF) are similar to those of P3HT:PCBM devices, resulting in higher overall power conversion efficiency.[4f, 8b]

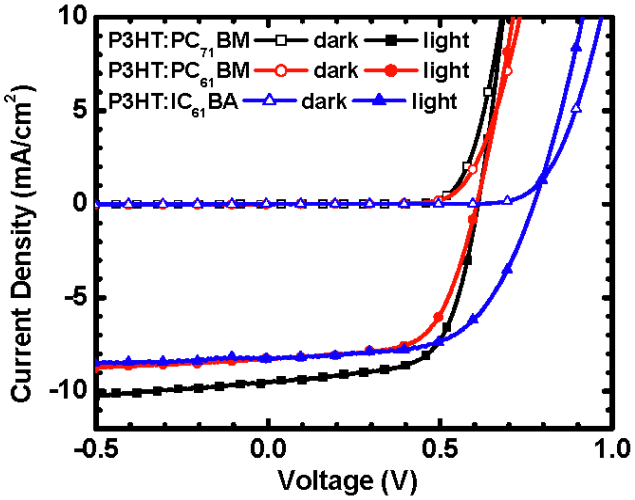

Figure 3.4 Current density (J) – voltage (V) characteristics of P3HT:fullerene (1:1) solar cells.

We further compared the photovoltaic properties of BHJ solar cells based on the same fullerene acceptor. PBTHDDT:$PC_{71}BM$ and P3HT:$PC_{71}BM$ solar cells showed similar photovoltaic parameters (V_{oc}, J_{sc}, and FF), and similar photovoltaic efficiency (3.75% vs. 3.70%). Using $PC_{61}BM$ as the acceptor in BHJ solar cells, we observe a 14% decrease in PCE for PBTHDDT:$PC_{61}BM$ devices, compared with that of P3HT:$PC_{61}BM$ solar cells, with the slight decrease in PCE being largely attributable to a comparable decrease in the J_{sc} due to the slightly bluer absorption onset of PBTHDDT relative to P3HT. The observed increase in V_{oc} in PBTHDDT:$IC_{60}BA$ devices is understandable considering the increased diagonal energy offset $\Delta E_{DA} = IE[\text{Donor}] - EA[\text{Acceptor}]$ of that blend.[10] The decrease of J_{sc} and FF in PBTHDDT:$IC_{60}BA$ solar cells, compared with those of P3HT:$IC_{60}BA$ solar cells, is critical in explaining the observed difference in photovoltaic properties. We therefore focused a detailed study on the morphology, optical and photophysical properties of PBTHDDT:fullerene blend films to look for the reason for the reduction in J_{sc} and FF when ICBA is used as the electron acceptor instead of PCBM.

3.3.2. Morphology

Figure 3.5 shows bright-field transmission electron microscope (BF-TEM) images of the nanomorphology of PBTHDDT:fullerene blend films (~80 nm thick) directly peeled off from the solar cells. The images were taken at a slightly defocused condition to enhance the phase contrast between polymer and fullerene, with fullerene-rich domains often appearing darker under BF-TEM due to their higher density than the polymer-rich domains.[11] The TEM images of PBTHDDT:$PC_{61}BM$ and PBTHDDT:$IC_{60}BA$ blends showed similar nanomorphology (Figure 3.5c, d), containing long fibrillar nanostructures. A low density of bright features were observed in the PBTHDDT:$IC_{60}BA$ blend films (Figure 3.5e, f), possibly suggesting the presence of larger aggregates in this blend. Similar aggregates were not observed in either P3HT:$IC_{60}BA$ (Figure 3.6e, f) or PBTHDDT:PCBM (Figure 3.5a-d) blend films. Overall, however we observe similar morphology by TEM imaging among all three of our PBTHDDT:fullerene blends. We also used atomic force microscopy (AFM) to characterize the surface topography of the active layer on the actual solar cells. We present topographical AFM images for a 5 μm × 5 μm region of each PBTHDDT:fullerene blend film in Figure 3.7. All the blend films showed similar surface topography with surface features less than 50 nm in height. The root-mean-square roughness (R_q) among these blend films was comparable, with values as follows: PBTHDDT:$PC_{71}BM$ (3.89 nm), PBTHDDT:$PC_{61}BM$ (4.05 nm), and PBTHDDT:$IC_{60}BA$ (3.54 nm). From these data we are unable to identify an obvious large-scale source of morphological variation that could explain the large efficiency differences between the different PBTHDDT/fullerene blends. Therefore, as we discuss in the following sections, we turned to optical spectroscopy to examine the photophysical and energetic differences between the films.

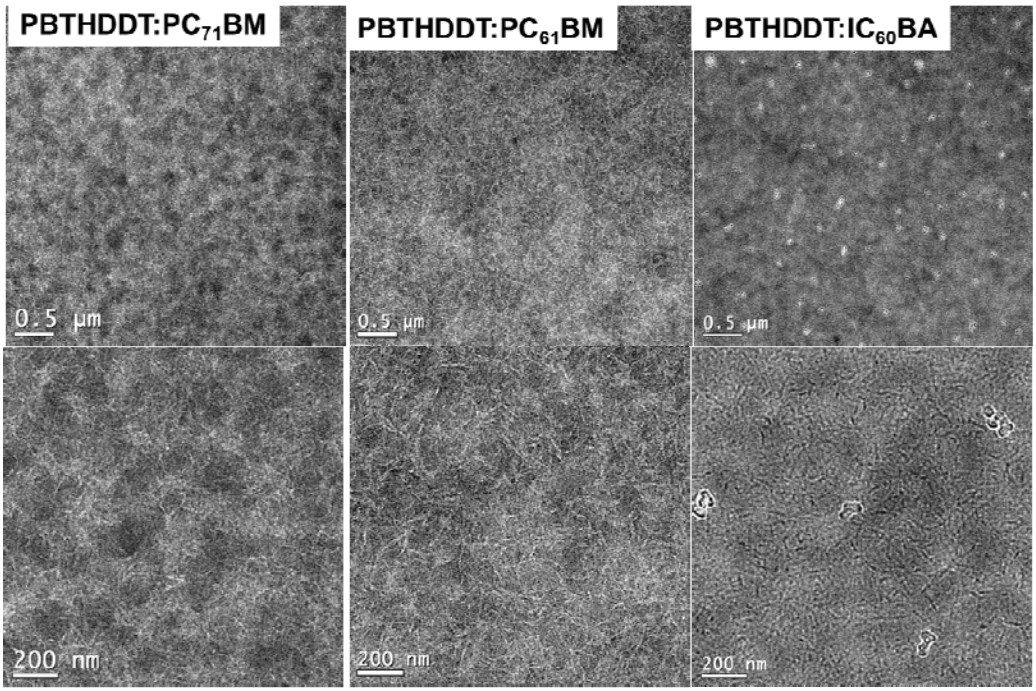

Figure 3.5 TEM images of PBTHDDT:fullerene (1:2) blend films. (a,b) PBTHDDT:$PC_{71}BM$, (c,d) PBTHDDT:$PC_{61}BM$, and (e,f) PBTHDDT:$IC_{60}BA$.

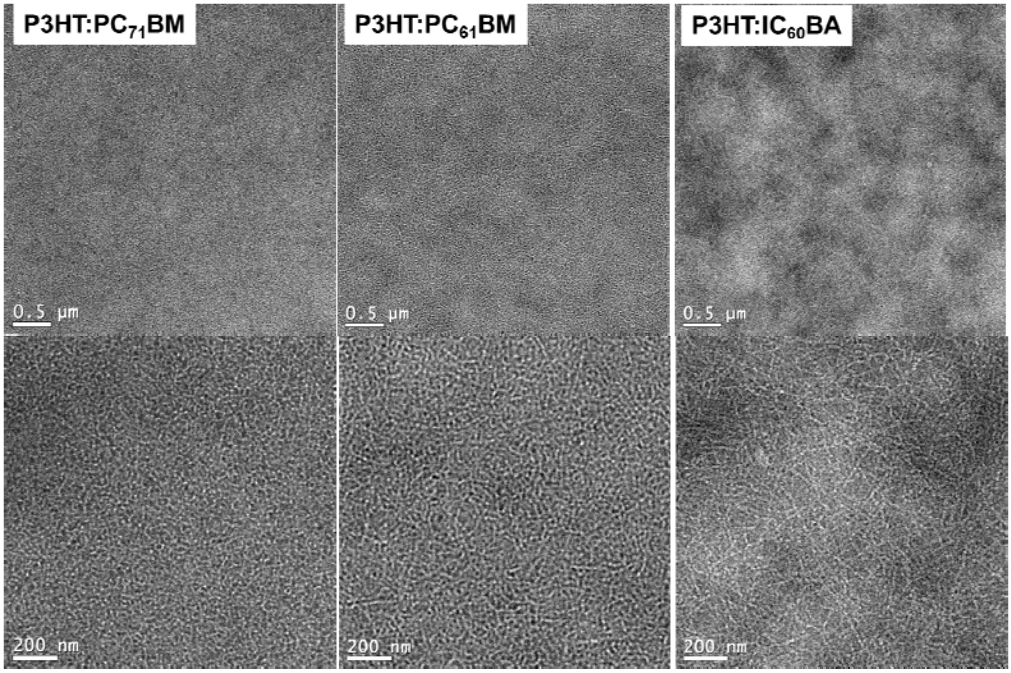

Figure 3.6 TEM images of P3HT:fullerene (1:1) blend films. (a,b) P3HT:$PC_{71}BM$, (c,d) P3HT:$PC_{61}BM$, and (e,f) P3HT:$IC_{60}BA$.

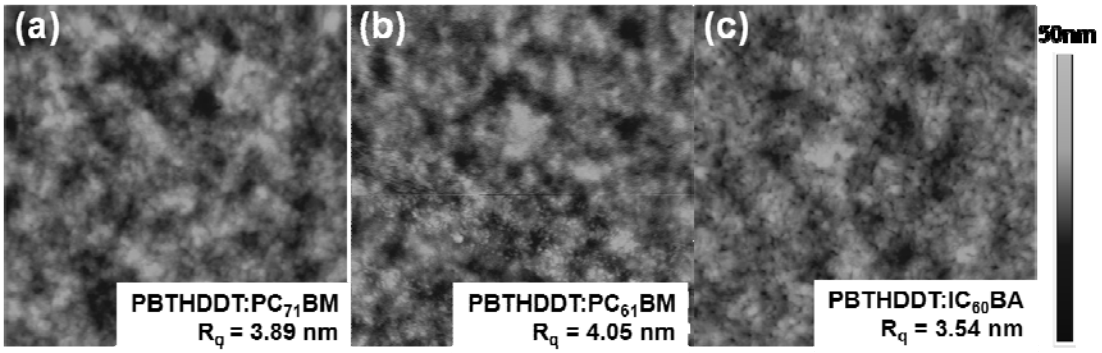

Figure 3.7 AFM topographical images (5×5 μm) of PBTHDDT:fullerene blend solar cells.

3.3.3 Photophysical Properties of Polymer:Fullerene Blends

Figure 3.8 compares the absorption spectra of PBTHDDT:$PC_{71}BM$, PBTHDDT:$PC_{61}BM$, and PBTHDDT:$IC_{60}BA$ blend films. The optical densities near 450 nm for the PBTHDDT:$IC_{60}BA$ and PBTHDDT:$PC_{61}BM$ blends are comparable (ca. OD = 0.24). As expected, they are both lower than that of PBTHDDT:$PC_{71}BM$ blends (ca. OD = 0.35). The difference in optical density between the $PC_{71}BM$ blend and the $PC_{61}BM$ or $IC_{60}BA$ blends is due to the enhanced absorbance of $PC_{71}BM$ in the visible region of the spectrum (Figure 3.4). However, despite the similar optical density in PBTHDDT:$PC_{61}BM$ and PBTHDDT:$IC_{60}BA$ blend solar cells, the measured IPCE for the $IC_{60}BA$ device in this spectral region is 75% lower than that of the $PC_{61}BM$ device.

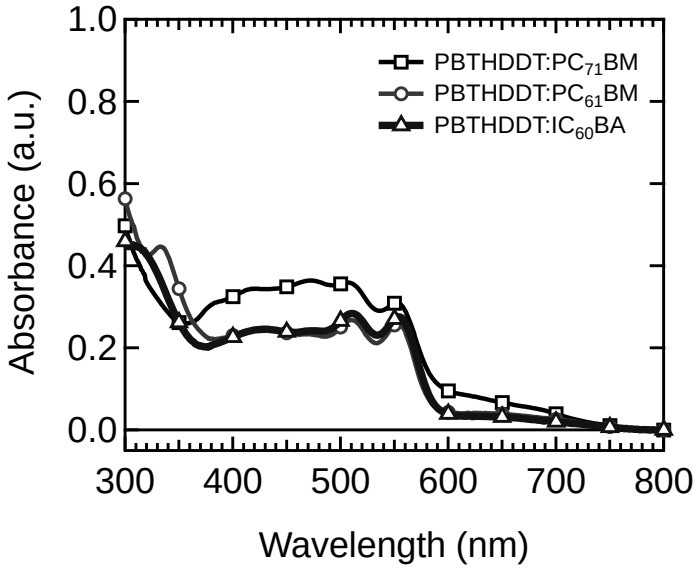

Figure 3.8 UV-vis absorption spectra of PBTHDDT:fullerene blend films.

We employed spectroelectrochemical measurements and photoinduced absorption (PIA) spectroscopy to understand the different photocurrent responses in our PBTHDDT:$IC_{60}BA$ solar cells. Polaron optical signatures arising from photoinduced radicals are commonly observable in the PIA spectra for polymer:fullerene blends.[12] To identify the expected spectral signature for $PBTHDDT^+$ radical cation (polaron spectrum) Figure 3.9a shows a differential absorption ($\Delta OD = OD_{Oxidized} - OD_{Neutral}$) spectrum for an electrochemically-oxidized neat film of PBTHDDT on ITO (open circle trace in Figure 3.9a). The ΔOD spectrum exhibits a distinct oxidatively induced absorption feature corresponding to absorption by the polymer cation at λ = 790 nm labeled $PBTHDDT^+$.

The PIA experiment is a pump-probe technique that measures the optical absorption of long-lived excited states (e.g. polarons or triplets with lifetime, τ, on the order of ~ μs – ms) resulting from excitation by a frequency modulated monochromatic excitation source. We plot the normalized differential transmittance data (ΔT/T) in terms of the differential thin film absorption coefficient as $\Delta\alpha d = -\ln[1+\Delta T/T]$. The solid black trace in Figure 3.9a representing

the PIA spectrum (right y-axis) for a neat film of PBTHDDT (excitation at λ = 455 nm), exhibits a significantly different spectral fingerprint than the oxidized form of the polymer collected by spectroelectrochemical methods, suggesting that few if any polarons are formed upon photoexcitation of the neat film. At 80 K, the neat film exhibits a broad PIA feature that peaks at ca. λ = 1180 nm. The intensity of this NIR feature increases by two orders of magnitude upon cooling from room temperature to T = 80K and exhibits non-dispersive decay with increasing modulation frequency. Based on the temperature dependence, frequency dependence, and the absence of any such feature in the spectroelectrochemical data in Figure 3.9a we assign this PIA signal at λ = 1180 nm to T_1-T_n absorption by PBTHDDT triplet excitons, probably generated via intersystem crossing from the S_1 singlet state excited by 455 nm light.

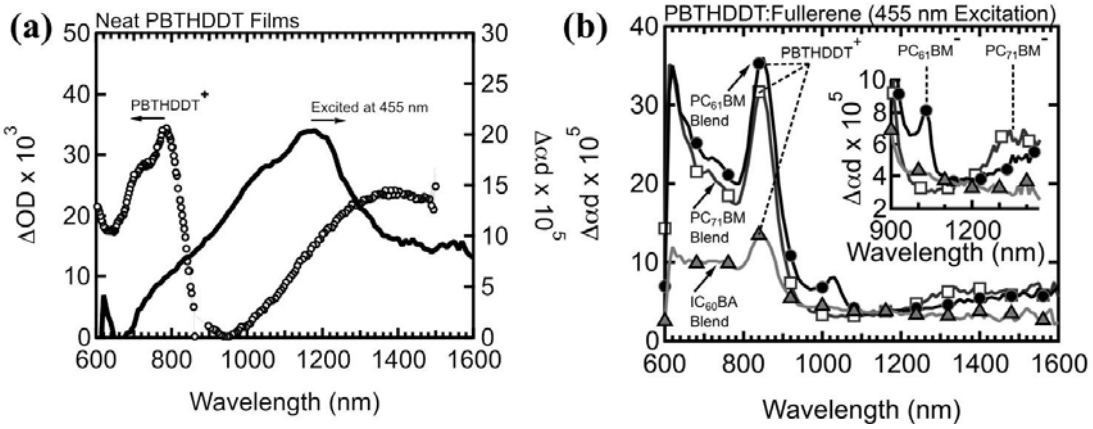

Figure 3.9 a) Spectroelectrochemical differential absorption (open circles) of a PBTHDDT film ($\Delta OD = OD_{Oxidized} - OD_{Neutral}$) showing an electrochemically induced $PBTHDDT^+$ polaron absorption peak at λ = 790 nm. The photoinduced absorption (PIA) spectrum (solid line, Excited at 455 nm) on the right ordinate ($\Delta\alpha d = -\ln[1+\Delta T/T]$) for a pristine film of PBTHDDT exhibits a peak at λ = 1170 nm consistent with polymer triplet absorption. ΔOD measured in transmission mode on ITO in CH_3CN:$(C_4H_9)_4N(ClO_4)$. b) PIA spectra for PBTHDDT:Fullerene blends ($PC_{61}BM$ blend = filled circles, $PC_{71}BM$ blend = open squares, and $IC_{60}BA$ blend = filled triangles) when both components are excited at 455 nm. Peaks consistent with PBTHDDT polarons at λ = 850 nm are labeled $PBTHDDT^+$. Inset depicts the spectral region for λ > 900 nm, where peaks consistent with fullerene anion generation are observed at λ = 1030 nm ($PC_{61}BM^-$, filled circles) and λ = 1340 nm ($PC_{71}BM^-$, open squares). The weak feature at λ = 1010 nm (filled triangles) is consistent with $IC_{60}BA^-$ generation. All Δαd recorded at 80K under 455 nm excitation modulated at 200 Hz.

The PIA spectra for PBTHDDT:fullerene blends under 455 nm excitation are presented in Figure 3.9b. Note that the polymer and each of the fullerenes absorb 455 nm light. Thus, the resulting PIA features arise from processes involving excitons created on either the donor or the acceptor. Between the wavelength range λ = 700 nm – 900 nm the PIA signals for each blend are qualitatively similar, exhibiting sharp induced absorption features peaking at λ = 850 nm (slightly red shifted from the PBTHDDT^{+} peak we observe by spectroelectrochemistry). Given the resemblance of the PIA signals observed in this spectral region to that obtained for the electrochemically oxidized polymer in Figure 3.9a, we assign this feature to a positive PBTHDDT^{+} polaron on the polymer backbone. Fullerene anion peaks are also apparent in the PIA spectra for $PC_{71}BM$ (1340 nm)[13] and $PC_{61}BM$ (1030 nm)[14] (see inset Figure 3.9b). In the $IC_{60}BA$-based blend an extremely weak feature near 1010 nm may also suggest the presence of fullerene anion resulting when the sample is illuminated with 455 nm excitation. We note that no discernible polymer triplet features appear at 1180 nm in any of the blends examined in Figure 3.9b, suggesting that polymer excitons are quenched prior to intersystem crossing and charge recombination to the polymer triplet state is negligible.

Although the optical densities (Figure 3.8) are nearly equivalent at the excitation wavelength (λ = 455 nm) for the PBTHDDT:$IC_{60}BA$ blend and the PBTHDDT:$PC_{61}BM$ blend, the PIA signature corresponding to PBTHDDT^{+} polarons in the $IC_{60}BA$ blend ($\Delta\alpha d = 1.3 \times 10^{-4}$) is more than a factor of 2.5 lower than that observed for the analogous fullerene methyl ester blend (PBTHDDT:$PC_{61}BM$, $\Delta\alpha d = 3.6 \times 10^{-4}$). This result suggests fewer long lived charges are being formed per absorbed photon, and is in qualitative agreement with the lower photocurrent density and IPCE measured for the corresponding $IC_{60}BA$ devices.

Upon direct excitation of the fullerene, the PBTHDDT:$IC_{60}BA$ blends produce less

photocurrent than the PBTHDDT:$PC_{61}BM$ blend (Figure 3.2c), despite the fact that the two different active layers show nearly equal absorption amplitude at 630 nm (Figure 3.8). Based on this observation we hypothesized that photoinduced hole transfer from $IC_{60}BA$ singlet excitons to PBTHDDT may not be occurring, which would indicate that charge generation in the PBTHDDT:$IC_{60}BA$ may primarily involve polymer exciton dissociation, with minimal harvesting of fullerene excitons.

To test this hypothesis, we compared the PIA signal measured for PBTHDDT:$IC_{60}BA$ to that measured for PBTHDDT:$PC_{61}BM$ *while selectively exciting the fullerene component at 630 nm*. The PBTHDDT polymer is completely transparent at this wavelength; therefore, PIA signals in the blend measured under 630 nm excitation originate uniquely from photoexcitation of the fullerene. Figure 3.10a shows the resulting PIA data, with the signal magnitudes scaled by the absorbed photon flux at the excitation wavelength (Φ_{Abs} with unit of mol cm^{-2} s^{-1}). Importantly, selectively exciting $PC_{61}BM$ in the polymer blend leads to a significant population of $PBTHDDT^{+}$ polarons ($\Delta\alpha d/\Phi_{Abs} \sim 2000$ cm^2 s mol^{-1} at 850 nm) in the PIA spectrum, indicating that $PC_{61}BM$ excitons reaching the PBTHDDT interface can undergo efficient charge transfer quenching. However, when we selectively excite the fullerene in the PBTHDDT:$IC_{60}BA$ blend at 630 nm (triangles in Figure 3.10a) we observe no discernible induced absorption features. For comparison, we have plotted $\Delta\alpha d/\Phi_{Abs}$ in Figure 3.10b for the PBTHDDT:$PC_{61}BM$ blend collected using 455 nm (circles) and note that the $PBTHDDT^{+}$ polaron signal magnitude obtained from selectively exciting $PC_{61}BM$ is comparable to that obtained from concomitant excitation of both blend components. Assuming a similar peak intensity ratio for excitation of the fullerene in the PBTHDDT:$IC_{60}BA$ blend, we would expect to observe a $PBTHDDT^{+}$ PIA feature with signal magnitude $\Delta\alpha d/\Phi_{Abs} \approx 720$ cm^2 s mol^{-1} appearing at 850 nm when the

$IC_{60}BA$ in the blend is excited with 630 nm light. However, we observe instead an extremely weak and poorly resolved feature in Figure 3.10a (triangles) at 850 nm ($\Delta\alpha d/\Phi_{Abs} \approx 315$ cm^2 s mol^{-1}) approaching the noise floor of our instrumentation ($\Delta\alpha d/\Phi_{Abs} \approx 100$ cm^2 s mol^{-1}). We may take this as an upper limit for the relative dissociation efficiency of $IC_{60}BA$ excitons compared to $PC_{61}BM$ excitons at the PBTHDDT interface, suggesting that the photoinduced hole transfer efficiency of $IC_{60}BA$ excitons is less than 20% that of $PC_{61}BM$ excitons.

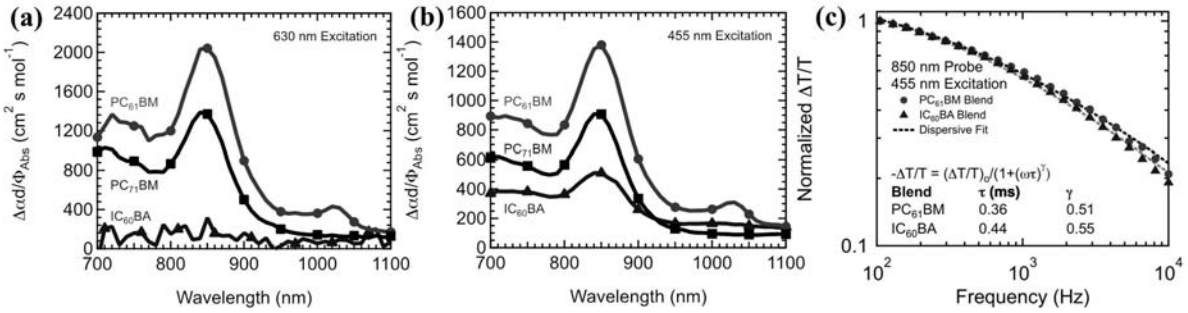

Figure 3.10 a) Photoinduced absorption ($\Delta\alpha d$) spectra scaled by the photon flux absorbed (Φ_{Abs}) by selectively exciting the fullerene at 630 nm in PBTHDDT:Fullerene blends ($PC_{61}BM$ blend = circles, $IC_{60}BA$ blend = triangles, $PC_{71}BM$ = squares). b) $\Delta\alpha d/\Phi_{Abs}$ spectra collected when both blend components are simultaneously excited at 455 nm for each PBTHDDT:fullerne blend using the same illustration as in a). c) Modulation frequency dependence of the differential transmittance ($-\Delta T/T \approx \Delta\alpha d$) monitored at 850 nm ($PBTHDDT^+$ polaron peak) for the $PC_{61}BM$ (circles) and $IC_{60}BA$ (triangles) blends in a) under 455 nm excitation. Decay parameters (τ) according to the inset model were obtained from dispersive fits (dashed lines) to the data as a function of modulation frequency $f = \omega/(2\pi)$. All PIA data collected at 80K.

Finally, we plot the dependence of the normalized $PBTHDDT^+$ PIA signal intensity as a function of modulation frequency in Figure 3.10c for PBTHDDT:$IC_{60}BA$ (triangles) and PBTHDDT:$PC_{61}BM$ (circles). The two traces exhibit nearly identical characteristic roll-off behavior that may be fit using the simple dispersive decay model[15] presented in the inset of Figure 3.10c, with nearly equivalent lifetime fitting parameters of $\tau \approx 0.40$ ms in both blends.[16] Thus, the significantly lower $PBTHDDT^+$ signal obtained when exciting the PBTHDDT:$IC_{60}BA$ blend at 455 nm in Figure 3.10a cannot be attributed to faster recombination in the

PBTHDDT:$IC_{60}BA$ compared to the PBTHDDT:$PC_{61}BM$ blend.

These data suggest that a portion of the polymer excitons in all of the polymer:fullerene blends examined here leads to long-lived positive polarons on the polymer and negative polarons on the fullerene. While $PC_{71}BM$ and $PC_{61}BM$ excitons appear to undergo hole transfer at the D/A interface, generating long-lived charges in the PBTHDDT:PCBM blends, excitons on the $IC_{60}BA$ do not appear to efficiently produce long-lived charges at the D/A interface. We next examine this result in the context of the expected driving forces for photoinduced charge separation via electron and hole transfer in these blends.

3.3.4 Driving Force for Photoinduced Charge Transfer

To identify qualitative trends in the energy landscape resulting from PBTHDDT with different fullerene acceptors we compare energies tabulated from cyclic voltammetry (CV for thin film and solution samples measured in this work and compared against solution values taken from literature)[8b,17] with those derived from photoemission spectroscopy (PES).

Importantly, rather than using the common approximation of frontier orbital energies[18] to estimate the driving force for photoinduced charge separation we instead follow the established electrochemical convention[19] of calculating the exited state oxidation potential (the potential required to oxidize the material in its excited state) of the donor and the excited state reduction potential (the potential required to reduce the material in its excited state) of the acceptor. We extend this convention to the solid state ionization energy (*IE*), and the electron affinity (*EA*) of ground state materials compared to those in the excited state as previously proposed.[20] Using the value of the singlet exciton energy E_g^{Opt} we estimate the electron affinity of the excited state ($EA_{(M^*/M^-)}$) as given by Equation 3.1a. Similarly, we calculate the excited state ionization energy ($IE_{(M^+/M^*)}$) of the donor according to Equation 3.1b. We note that this convention is similar to the

effective HOMO and effective LUMO convention used by Veldmann et al.[21] in that it accounts for the binding energy of the exciton. However, our convention differs with regard to the driving force for generating separated charges being defined as the energy associated with a particular exciton undergoing dissociation with a ground-state charge acceptor rather than splitting the exciton binding energy between the HOMO and LUMO of each material and adding the coulomb energy to calculate the energy of the bound charge transfer state.

$$EA_{(M^*/M^-)} = EA_{(M/M^-)} - E_g^{Opt} \quad (3.1a)$$

$$IE_{(M^+/M^*)} = IE_{(M^+/M)} + E_g^{Opt} \quad (3.1b)$$

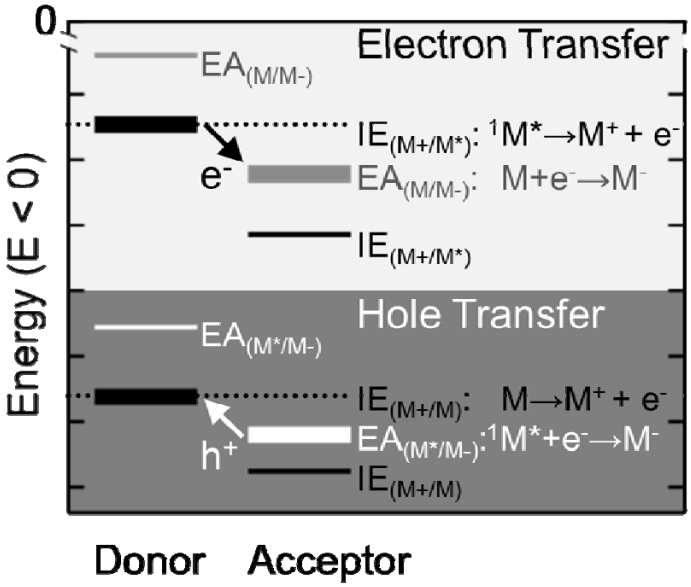

Scheme 3.1 The driving force for charge separation proceeding through photoinduced hole transfer indicated by the large white arrow labeled h^+ from the acceptor to the donor is related to the difference in the excited state electron affinity ($EA_{(M^*/\ M^-)}$ = white lines) of the acceptor exciton (heavy-weight white line) and the ground state ionization energy ($IE_{(M^+/M)}$ = black lines in lower 'Hole Transfer' panel) of the donor (heavy-weight black line in lower 'Hole Transfer' panel). Charge separation via hole transfer will occur spontaneously in donor/acceptor pairs for which $IE_{(M^+/M)}$[Donor] is more positive than $EA_{(M^*/\ M^-)}$[Acceptor]. The analogous electron transfer process indicated by the large black arrow labeled e^- will be spontaneous when the excited state ionization energy ($IE_{(M^+/M^*)}$ = black lines in upper 'Electron Transfer' panel) of the donor (heavy-weight black line) is more positive than the ground state electron affinity ($EA_{(M/M^-)}$ = dark grey lines) of the acceptor (heavy-weight dark grey line). Light-weight solid lines follow the same shading scheme, with the black light-weight lines in the upper and lower panels

depicting $IE_{(M+/M*)}$ and $IE_{(M+/M)}$, respectively. The grey light-weight lines in the upper and lower panels depict $EA_{(M/M-)}$ and $EA_{(M*/M-)}$, respectively.

Following this convention, in Scheme 3.1 we illustrate that an acceptor material under illumination with energy $hv \geqslant E_g^{Opt}$ will engage in spontaneous charge separation via hole transfer to the donor if the value of $EA_{(M*/M-)}$ for the acceptor is more negative than the value of *IE* for the donor material. We assume the energy difference ΔE_{Hole} calculated from Equation 3.2a to satisfactorily approximate the change in free energy (ΔG)[22] for charge separation via photoinduced hole transfer. A similar analysis can be applied using Equation 3.2b to calculate ΔE_{Elec} to assess whether a given donor exciton is likely to undergo charge separation via electron transfer to a given acceptor:

$$\Delta E_{\text{Hole}} = EA_{(M*/M-)}[\text{Acceptor}] - IE_{(M+/M)}[\text{Donor}] \quad (3.2a)$$

$$\Delta E_{\text{Elec}} = EA_{(M/M-)}[\text{Acceptor}] - IE_{(M+/M*)}[\text{Donor}] \quad (3.2b)$$

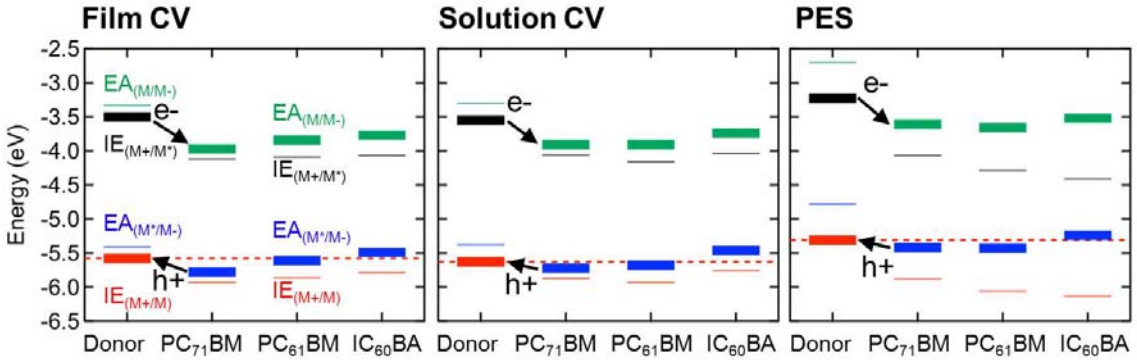

Figure 3.11 Excited state electron affinity values ($EA_{(M*/M-)}$ = heavy-weight blue lines) relevant for estimating whether photoinduced hole transfer (h^+) from each fullerene exciton to the "Donor" polymer PBTHDDT (ground state ionization energy *IE* = heavy-weight red lines) will occur spontaneously (*IE*[Donor] more positive than $EA_{(M*/M-)}$[Acceptor]). The analogous electron transfer process (e^-) will be spontaneous when the excited state ionization energy ($IE_{(M+/M*)}$ = black lines and defined numerically in the text) of the donor is more positive than the ground state electron affinity (*EA* = green lines) of the acceptor. "Film CV" denotes energies tabulated from thin film cyclic voltammetry, "Solution CV" denotes energies tabulated from solution cyclic voltammetry with $PC_{71}BM$ from Ref. [17a], and $PC_{61}BM$, $IC_{60}BA$ from Ref. [8b]), and "PES" denotes energies tabulated from ultraviolet photoemission spectroscopy (UPS) and

inversion photoemission spectroscopy (IPES). Light-weight black and red lines depict $IE_{(M+/M^*)}$ and $IE_{(M+/M)}$, respectively, green and blue light-weight lines depict $EA_{(M/M-)}$ and $EA_{(M^*/M-)}$, respectively.

Using this convention, in Figure 3.11 we plot the estimated energies related to the driving forces for photoinduced charge separation in our different PBTHDDT/fullerene blends. The CV oxidation/reduction waves, ultra-violet photoemission spectroscopy (UPS), and inverse photoemission spectroscopy (IPES) traces used to estimate energies relative to vacuum in Figure 3.11 are presented in Figure 3.12 and Figure 3.13, respectively, in Supporting Information. As previously observed[4i] PBTHDDT exhibits an irreversible oxidation wave in thin film as well as solution, thus we must regard the *IE* plotted in Figure 3.11 based on the CV data as a lower limit, with the true value possibly being slightly more positive. Photoelectron spectroscopy measurements yielded a featureless spectrum for PBTHDDT where the density of states showed an exponential decay into the band gap. Therefore an onset of the density of states is very hard to place. The reason for this lies most likely in the long hydrocarbon side chains attached to the polymer that commonly dominate the photoemission spectra and tend to shield the *IE* and *EA* features. Given the potential inaccuracies in estimating absolute *IE* values for PBTHDDT using a single method, we present self-consistent estimates for each material using three methods (film CV, solution CV and film PES) in Figure 3.11, arriving at qualitatively equivalent conclusions based on each method. We calculated the energy changes relevant for charge separation (ΔE_{Hole} *and* ΔE_{Elec} calculated from Equation 3.2 and tabulated in Table 3.1) in PBTHDDT solar cells from the *IE* and *EA* values in Tables 3.3 and 3.4.

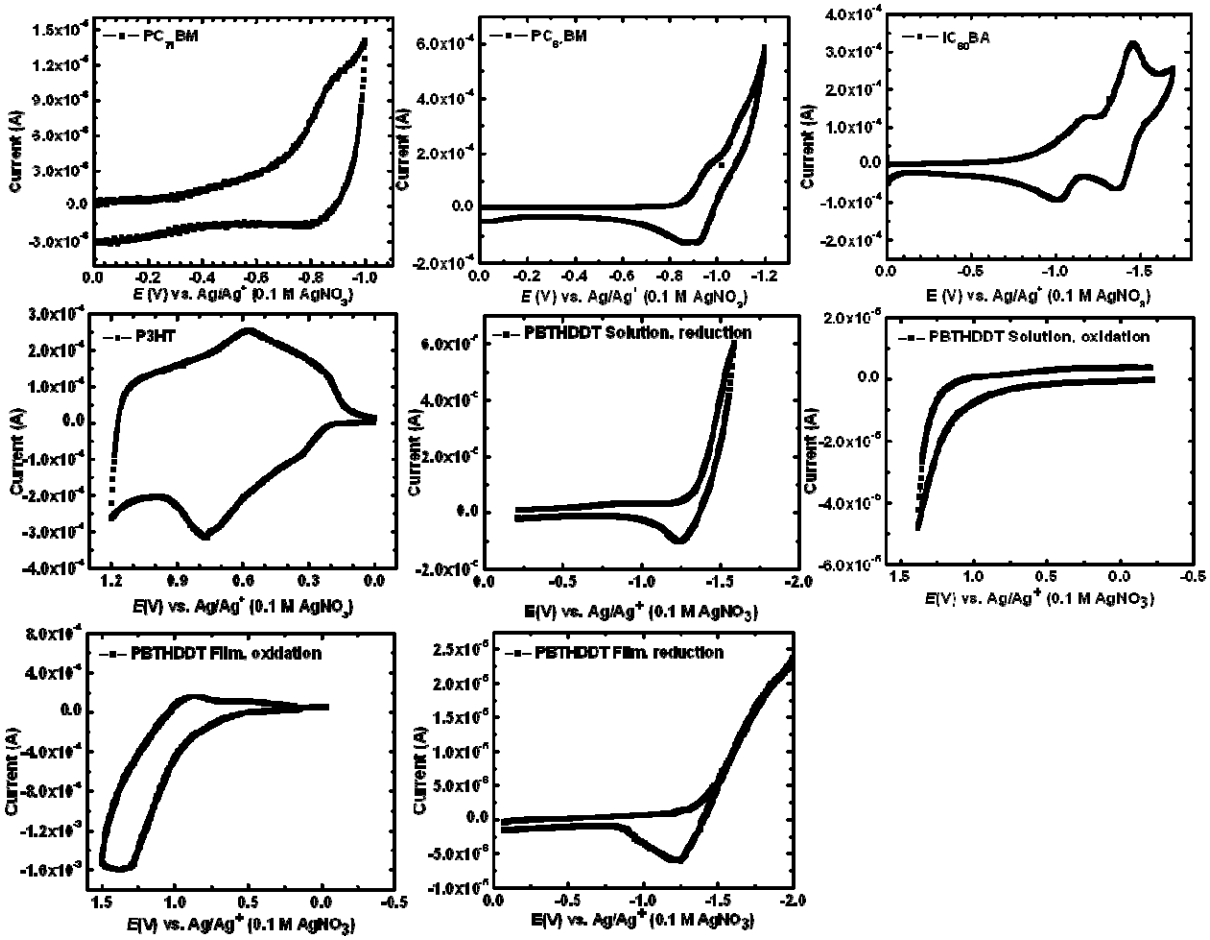

Figure 3.12 Solid-state cyclic voltammograms of fullerene derivatives and P3HT. Reduction curves of $PC_{71}BM$, $PC_{61}BM$, and $IC_{60}BA$, and oxidation curve of P3HT are shown. Reduction and oxidation curves of thin film and solution cyclic voltammograms of PBTHDDT are also shown. Scan rate = 100 mV/s.

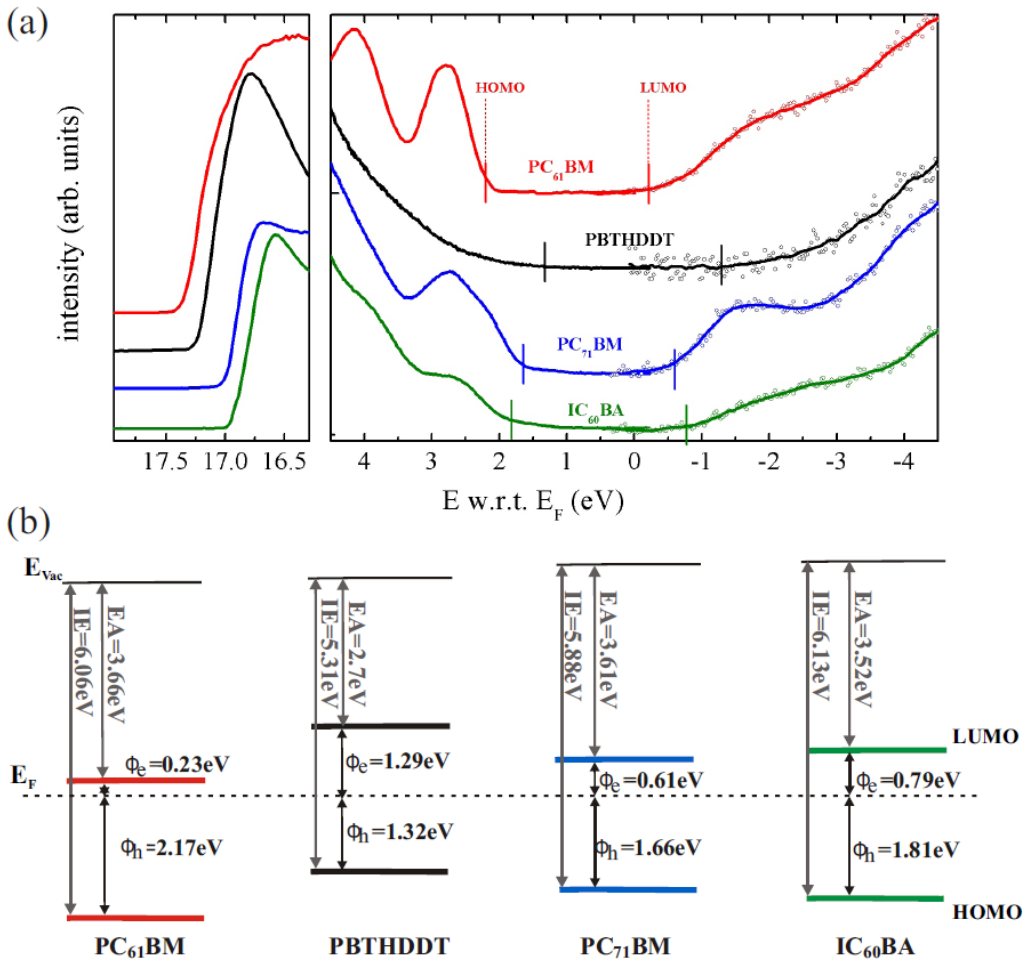

Figure 3.13 a) Combined UPS and IPES spectra of films of pure $PC_{61}BM$, PBTHDDT, $PC_{71}BM$, and $IC_{60}BA$ deposited on ITO. The curves are shifted in vertical direction for clarity. b) The resulting energy level alignment diagram from the UPS and IPES measurements.

Table 3.3 Energies relevant to charge separation via hole transfer.

Material	*$IE_{(M+/M)}$ from Film CV*	*$EA_{(M*/M-)}$ from Film CV [b]*	*$IE_{(M+/M)}$ from Solution CV*	*$EA_{(M*/M-)}$ from Solution CV[a] [b]*	*$IE_{(M+/M)}$ from PES*	*$EA_{(M*/M-)}$ from PES [b]*
PBTHDDT	-5.58	--	-5.63	--	-5.31	--
$PC_{71}BM$	--	-5.78	--	-5.72	--	-5.42
$PC_{61}BM$	--	-5.61	--	-5.68	--	-5.43
$IC_{60}BA$	--	-5.49	--	-5.46	--	-5.24

[a] Energies in eV tabulated based on Ref. [17a]. [b] Excited state EA calculated based on Equation 3.1a.

Table 3.4 Energies relevant to charge separation via electron transfer.

Material	$IE_{(M+/M*)}$ *from Film CV [b]*	$EA_{(M/M-)}$ *from Film CV*	$IE_{(M+/M*)}$ *from Solution CV [b]*	$EA_{(M/M-)}$ *from Solution CV[a]*	$IE_{(M+/M*)}$ *from PES [b]*	$EA_{(M/M-)}$ *from PES*
PBTHDDT	-3.50	--	-3.55	--	-3.23	--
$PC_{71}BM$	--	-3.97	--	-3.91	--	-3.61
$PC_{61}BM$	--	-3.84	--	-3.91	--	-3.66
$IC_{60}BA$	--	-3.77	--	-3.74	--	-3.52

[a] Energies in eV tabulated based on Refs. [8b] and [17a]. [b] Excited state IE calculated based on Equation 3.1b.

From the values plotted in Figure 3.11 we conclude that charge separation by forward electron transfer from photoexcited PBTHDDT to each of the fullerenes should be spontaneous, ($IE_{(M+/M*)}$[Donor] > $EA_{(M/M-)}$[Acceptor] giving $\Delta E_{Elec} < 0$ based on Equation 3.2b). On the other hand, we anticipate spontaneous hole transfer from photoexcited $PC_{71}BM$ to PBTHDDT ($IE_{(M+/M)}$[Donor] > $EA_{(M*/M-)}$[Acceptor] giving $\Delta E_{Hole} < 0$), but not from $IC_{60}BA$ to PBTHDDT ($IE_{(M+/M)}$[Donor] < $EA_{(M*/M-)}$[Acceptor] giving $\Delta E_{Hole} > 0$). Since the value of $IE_{(M+/M)}$[Donor] is nearly equal to $EA_{(M*/M-)}$[Acceptor] for $PC_{61}BM$ paired with PBTHDDT, the energy difference for hole transfer among each method is negative, with an average value of only $\Delta E_{Hole} = -0.070$ eV, suggesting that, while photoinduced hole transfer will be spontaneous, the driving force is relatively small. We arrive at qualitatively identical conclusions based on the solution electrochemical data for PBTHDDT (Figure 3.12) compared against the solution reduction potentials of $PC_{71}BM$, $PC_{61}BM$, and $IC_{60}BA$ previously reported literature values.[8a]

Importantly, the CV and PES data can account for the experimental device and PIA data (dramatically reduced photocurrent and PIA signal when selectively exciting $IC_{60}BA$) only when the state conventions are used. As seen from the positions of the thin lines in Figure 3.11, a simple analysis based on the position of the ground state *EA*/*IE* values (or HOMO/LUMO levels as is sometimes casually referred to in the OPV literature), suggests that each of the fullerene

blends examined here should form a staggered type-II heterojunction with PBTHDDT and thus should support both excited-polymer-to-fullerene electron transfer, and excited-fullerene-to-polymer hole transfer. In contrast, use of the *excited state EA*/*IE* values also predicts that the photoexcited polymer should transfer an electron to all three fullerenes, but correctly predicts that only the photoexcited $PC_{61}BM$ and $PC_{71}BM$ (but not $IC_{60}BA$) should transfer a photoexcited hole back to the polymer.

While we have focused on the primary loss in EQE above, there is also a difference in *FF* between the $PC_{61}BM$ and $IC_{60}BA$ blends. There are several possible origins for this *FF* difference in the context of our findings. First, the value of $EA_{(M^*/M^-)}$ for $IC_{60}BA$ is slightly more positive than that of $IE_{(M^+/M)}$ for PBTHDDT, suggesting that photogenerated charges in the $IC_{60}BA$ blend might have an additional thermodynamically plausible pathway for charge recombination (i.e. free charges may recombine to form $IC_{60}BA$ singlet excitons). Free charges engaging in this additional recombination process would lead to diminished FF for PBTHDDT:$IC_{60}BA$ devices compared with PCBM devices. However, attempts to test this hypothesis via photoluminescence have been inconclusive, since we observe overlapping fluorescence from both blend components in all three PBTHDDT blends that we have examined. Moreover, as discussed above, in both $PC_{61}BM$ and $IC_{60}BA$ blends we observe a nearly identical polaron lifetime (based on the modulation frequency dependence in our photoinduced absorption measurements). These results could thus also be consistent with the result of differences in field dependent charge carrier separation/geminate recombination rates arising from the lower driving force for electron transfer from the polymer to $IC_{60}BA$ compared to $PC_{61}BM$.

Finally, we note that Förster resonant excitation transfer (FRET) from the donor polymer to the fullerene has been observed for many polymer:fullerene systems,[23] when the singlet excited

state of the donor is higher in energy than that of the acceptor. Since the S_1 energy of the PBTHDDT is roughly 360 meV above that of $IC_{60}BA$, it is likely that the FRET process from PBTHDDT to $IC_{60}BA$ competes with exciton dissociation from the polymer. Although we cannot observe distinct transient species indicative of this FRET process in our quasi-steady state photoinduced absorption measurement, we believe it is likely that the origin of the poor overall polaron generation and low photocurrent in these $IC_{60}BA$ devices arises from singlet excitation transfer from the polymer to the fullerene and extremely poor fullerene exciton dissociation. This is reflected in the IPCE of PBTHDDT:$IC_{60}BA$ being 53% lower and the PIA signal being 63% lower than the PBTHDDT:$PC_{61}BM$ when both the polymer and the fullerene are excited at 455 nm, despite the two blends exhibiting identical decays with increasing modulation frequency.

3.4. Conclusions

We have investigated the impact that modulating the driving force for photoinduced hole transfer has on the photovoltaic properties of bulk heterojunction solar cells using an oxidation-resistant copolymer semiconductor, PBTHDDT, and various fullerene derivatives. We found that solar cells based on PBTHDDT:$PC_{71}BM$, PBTHDDT:$PC_{61}BM$ and PBTHDDT:$IC_{60}BA$ blends showed average efficiency of 3.75%, 2.70%, and 1.52% PCE, respectively. At a coarse level we observe similar nanoscale features among the different PBTHDDT:fullerene blends by TEM and AFM imaging. While these data do not address molecular level packing and orientation effects, they suggest that large-scale morphological changes are unlikely to be the source of the significant observed variation in photovoltaic performance. Photophysical studies of the PBTHDDT:fullerene blends showed that all the PBTHDDT:fullerene blends generated long-lived positive polarons in PBTHDDT and negative polarons on the fullerene upon photoexcitation of the polymer. While fullerene excitons in

PBTHDDT:$PC_{71}BM$ and PBTHDDT:$PC_{61}BM$ blends appear to undergo photoinduced hole transfer at the donor/acceptor interface to generate long-lived polarons, *selective excitation of the fullerene in PBTHDDT:$IC_{60}BA$ blends does not efficiently produce long-lived charges*. Thus, at least part of the low photocurrent observed in the PBTHDDT:$IC_{60}BA$ blend solar cells is attributable to the low quantum yield for charge generation/separation of $IC_{60}BA$ excitons. We attribute this low dissociation efficiency to the small driving force for hole transfer at the polymer/$IC_{60}BA$ interface being insufficient to sustain efficient charge separation. Comparing these results with the CV and PES data, we find they are consistent in a state energy level picture but not a simplified frontier orbital picture. While our analysis is based purely on thermodynamic parameters, we point out that kinetic factors can also play an important role in determining overall charge separation efficiency in some systems, as previous authors have suggested.[22, 24]

Although the fullerene itself is not responsible for the bulk of the light absorption in this blend, energy transfer from the polymer to the fullerene has been proposed in many systems,[25] and poor fullerene exciton dissociation could thus represent a significant loss mechanism. Neglecting undetected morphological changes, our results would suggest that the efficiency of fullerene exciton dissociation at the polymer/fullerene interface drops by ~ 80% when $PC_{61}BM$ is replaced with $IC_{60}BA$ in PBTHDDT:fullerene blends. These results provide an important guide for materials design and device engineering in bulk heterojunction polymer solar cells.

3.5 References

1. a) Coakley, K. M.; McGehee, M. D. *Chem. Mater.* **2004**, *16*, 4533-4542; b) Gunes, S.; Neugebauer, H.; Sariciftci, N. S. *Chem. Rev.* **2007**, *107*, 1324-1338; c) Thompson, B. C.; Fréchet, J. M. J. *Angew. Chem. Int. Ed.* **2008**, *47*, 58-77; d) Dennler, G.; Scharber, M. C.; Brabec, C. J. *Adv. Mater.* **2009**, *21*, 1323-1338; e) Brunetti, F. G.; Kumar, R.; Wudl, F. *J. Mater. Chem.* **2010**, *20*, 2934-2948; f) Boudreault, P.-L. T.; Najari, A.; Leclerc, M. *Chem. Mater.* **2010**, *23*, 456-469; g) Li, G.; Zhu, R.; Yang, Y. *Nat. Photon.* **2012**, *6*, 153-161.

2. Yu, G.; Gao, J.; Hummelen, J. C.; Wudl, F.; Heeger, A. J. *Science* **1995**, *270*, 1789-1791.

3. a) Liang, Y.; Xu, Z.; Xia, J.; Tsai, S. T.; Wu, Y.; Li, G.; Ray, C.; Yu, L. *Adv. Mater.* **2010**, *22*, E135− E138; b) Small, C. E.; Chen, S.; Subbiah, J.; Amb, C. M.; Tsang, S.-W.; Lai, T.-H.; Reynolds, J. R.; So, F. *Nat. Photon.* **2012**, *6*, 115-120; c) He, Z.; Zhong, C.; Su, S.; Xu, M.; Wu, H.; Cao, Y. *Nat. Photon.* **2012**, 6, 593–597.

4. a) Peet, J.; Kim, J. Y.; Coates, N. E.; Ma, W. L.; Moses, D.; Heeger, A. J.; Bazan, G. C. *Nat. Mater.* **2007**, *6*, 497-500; b) Lee, J. K.; Ma, W. L.; Brabec, C. J.; Yuen, J.; Moon, J. S.; Kim, J. Y.; Lee, K.; Bazan, G. C.; Heeger, A. J. *J. Am. Chem. Soc.* **2008**, *130*, 3619-3623; c) Ahmed, E.; Kim, F. S.; Xin, H.; Jenekhe, S. A. *Macromolecules* **2009**, *42*, 8615-8618; d) Krebs, F. C. *Sol. Energy Mater. Sol. Cells* **2009**, *93*, 394-412; e) Ren, G.; Wu, P.-T.; Jenekhe, S. A. *Chem. Mater.* **2010**, *22*, 2020-2026; f) Zhao, G.; He, Y.; Li, Y. *Adv. Mater.* **2010**, *22*, 4355-4358; g) Ren, G.; Wu, P.-T.; Jenekhe, S. A. *ACS Nano* **2011**, *5*, 376-384; h) Sonar, P.; Ng, G.-M.; Lin, T. T.; Dodabalapur, A.; Chen, Z.-K. *J. Mater. Chem.* **2010**, *20*, 3626-3636; i) Ahmed, E.; Subramaniyan, S.; Kim, F. S.; Xin, H.; Jenekhe, S. A. *Macromolecules* **2011**, *44*, 7207-7219; j) Subramaniyan, S.; Xin, H.; Kim, F. S.; Shoaee, S.; Durrant, J. R.; Jenekhe, S. A. *Adv. Energy. Mater.* **2011**, *1*, 854-860; k) Xin, H.; Subramaniyan, S.; Kwon, T.-W.; Shoaee, S.; Durrant, J. R.; Jenekhe, S. A. *Chem. Mater.* **2012**, *24*, 1995–2001; l) Ren, G.; Ahmed, E.; Jenekhe, S. A. *J. Mater. Chem.* **2012**, *22*, 24373-24379.

5. a) Ren, G.; Ahmed, E.; Jenekhe, S. A. *Adv. Energy. Mater.* **2011**, *1*, 946-953; b) Schwenn, P. E.; Gui, K.; Nardes, A. M.; Krueger, K. B.; Lee, K. H.; Mutkins, K.; Rubinstein-Dunlop, H.; Shaw, P. E.; Kopidakis, N.; Burn, P. L.; Meredith, P. *Adv. Energy. Mater.* **2011**, *1*, 73-81; c) Ahmed, E.; Ren, G.; Kim, F. S.; Hollenbeck, E. C.; Jenekhe, S. A. *Chem. Mater.* **2011**, *23*, 4563–4577; d) Wu, P.-T.; Xin, H.; Kim, F. S.; Ren, G.; Jenekhe, S. A. *Macromolecules* **2009**, *42*, 8817-8826; e) Wu, P.-T.; Ren, G.; Jenekhe, S. A. *Macromolecules* **2010**, *43*, 3306-3313.

6. Zaumseil, J.; Sirringhaus, H. *Chem. Rev.* **2007**, *107*, 1296-1323.

7. a) Babel, A.; Jenekhe, S. A. *J. Am. Chem. Soc.* **2003**, *125*, 13656-13657; b) Babel, A.; Wind, J. D.; Jenekhe, S. A. *Adv. Funct. Mater.* **2004**, *14*, 891–898; c) Singh, T. B.; Senkarabacak, P.; Sariciftci, N. S.; Tanda, A.; Lackner, C.; Hagelauer, R.; Horowitz, G. *Appl. Phys. Lett.* **2006**, *89*, 033512-033513; d) Usta, H.; Facchetti, A.; Marks, T. J. *J. Am. Chem. Soc.* **2008**, *130*, 8580-8581; e) Kim, F. S.; Guo, X.; Watson, M. D.; Jenekhe, S. A. *Adv. Mater.* **2010**, *22*, 478–482.

8. a) He, Y.; Li, Y. *Phys. Chem. Chem. Phys.* **2011**, *13*, 1970-1983; b) He, Y.; Chen, H.-Y.; Hou, J.; Li, Y. *J. Am. Chem. Soc.* **2010**, *132*, 1377-1382; c) Guan, Z.-L.; Kim, J. B.; Wang, H.; Jaye, C.; Fischer, D. A.; Loo, Y.-L.; Kahn, A. *Org. Electron.* **2010**, *11*, 1779-1785.

9. a) Boland, P.; Sunkavalli, S. S.; Chennuri, S.; Foe, K.; Abdel-Fattah, T.; Namkoong, G. *Thin Solid Films* **2010**, *518*, 1728-1731; b) Xin, H.; Kim, F. S.; Jenekhe, S. A. *J. Am. Chem. Soc.* **2008**, *130*, 5424-5542.

10. a) Vandewal, K.; Tvingstedt, K.; Gadisa, A.; Inganas, O.; Manca, J. V. *Nat. Mater.* **2009**,

8, 904-909; b) Brabec, C. J.; Cravino, A.; Meissner, D.; Sariciftci, N. S.; Fromherz, T.; Rispens, M. T.; Sanchez, L.; Hummelen, J. C. *Adv. Funct. Mater.* **2001**, *11*, 374-380.

11. van Bavel, S. S.; Sourty, E.; de With, G.; Loos, J. *Nano Lett.* **2009**, *9*, 507-513.

12. Sariciftci, N. S.; Smilowitz, L.; Heeger, A. J.; Wudl, F. *Science* **1992**, *258*, 1474-1476.

13. Sperlich, A.; Liedtke, M.; Kern, J.; Kraus, H.; Deibel, C.; Filippone, S.; Delgado, J. L.; Martín, N.; Dyakonov, V. *Phys. Status Solidi. Rapid Res. Lett.,* **2011**, *5*, 128-130.

14. Guldi, D. M.; Prato, M. *Acc. Chem. Res.* **2000**, *33*, 695-703.

15. Heinemann, M. D.; von Maydell, K.; Zutz, F.; Kolny-Olesiak, J.; Borchert, H.; Riedel, I.; Parisi, J. *Adv. Funct. Mater.* **2009**, *19*, 3788-3795.

16. Noone, K. M.; Subramaniyan, S.; Zhang, Q.; Cao, G.; Jenekhe, S. A.; Ginger, D. S. *J. Phys. Chem. C* **2011**, *115*, 24403-24410.

17. a) He, Y.; Zhao, G.; Peng, B.; Li, Y. *Adv. Funct. Mater.* **2010**, *20*, 3383-3389; b) Deibel, C.; Mack, D.; Gorenflot, J.; Schöll, A.; Krause, S.; Reinert, F.; Rauh, D.; Dyakonov, V. *Phys. Rev. B* **2010**, *81*, 085202.

18. a) Sun, S.-S.; Sariciftci, N. S. *Organic Photovoltaics: Mechanisms, Materials, and Devices*, CRC Press: Boca Raton, **2005**; b) Gong, X.; Tong, M.; Brunetti, F. G.; Seo, J.; Sun, Y.; Moses, D.; Wudl, F.; Heeger, A. J. *Adv. Mater.* **2011**, *23*, 2272-2277; c) He, Y.; Chen, C.; Richard, E.; Dou, L.; Wu, Y.; Li, G.; Yang, Y. *J. Mater. Chem.* **2012**, *22*, 13391-13394.

19. a) Crabtree, R. H. *Energy Production and Storage: Inorganic Chemical Strategies for a Warming World;* , John Wiley & Sons Ltd., Chichester, UK, **2010**; b) Delcamp, J. H.; Yella, A.; Nazeeruddin, M. K.; Grätzel, M. *Chem. Commun.* **2012**, *48*, 2295-2297.

20. Schlenker, C. W.; Thompson, M. E. *Top. Curr. Chem.* **2012**, *312*, 175-213.

21. Veldman, D.; Meskers, S. C. J.; Janssen, R. A. J. *Adv. Funct. Mater.* **2009**, *19*, 1939-1948.

22. Cook, S.; Katoh, R.; Furube, A. *J. Phys. Chem. C* **2009**, *113*, 2547-2552.

23. Benson-Smith, J. J.; Ohkita, H.; Cook, S.; Durrant, J. R.; Bradley, D. D. C.; Nelson, J. *Dalton Trans.* **2009**, 10000-10005.

24. Bakulin, A. A.; Rao, A.; Pavelyev, V. G.; van Loosdrecht, P. H. M.; Pshenichnikov, M. S.; Niedzialek, D.; Cornil, J.; Beljonne, D.; Friend, R. H. *Science* **2012**, *335*, 1340-1344.

25. a) Coffey, D. C.; Ferguson, A. J.; Kopidakis, N.; Rumbles, G. *ACS Nano* **2010**, *4*, 5437-5445; b) Soon, Y. W.; Clarke, T. M.; Zhang, W.; Agostinelli, T.; Kirkpatrick, J.; Dyer-Smith, C.; McCulloch, I.; Nelson, J.; Durrant, J. R. *Chem. Sci.* **2011**, *2*, 1111-1120.

26. a) Kulkarni, A. P.; Tonzola, C. J.; Babel, A.; Jenekhe, S. A. *Chem. Mater.* **2004**, *16*, 4556-4573; b) Ahmed, E.; Earmme, T.; Ren, G.; Jenekhe, S. A. *Chem. Mater.* **2010**, *22*, 5786-5796.

27. Noone, K. M.; Anderson, N. C.; Horwitz, N. E.; Munro, A. M.; Kulkarni, A. P.; Ginger, D. S. *ACS Nano* **2009**, *3*, 1345-1352.

28. Ginger, D. S.; Greenham, N. C. *Phys. Rev. B* **1999**, *59*, 10622-10629.

Chapter 4 Optimization of the Nanoscale Morphology of Non-Fullerene Acceptor-Based Bulk Heterojunction Polymer Solar Cells via Processing Additives

4.1 Introduction

Organic photovoltaic cells are of growing interest because they offer a potential low cost alternative to current solar energy technologies.[1-3] Considerable advances have recently been made in increasing the efficiency of bulk heterojunction (BHJ) polymer solar cells,[3] in which an electron-donor polymer and an electron-acceptor material are blended to make the active photovoltaic layer.[2a,b] The most commonly employed electron-acceptor materials are fullerene derivatives, including [6,6]-phenyl C61-butyric acid methyl ester (PCBM)[4] and [6,6]-phenyl C71-butyric acid methyl ester (C71-PCBM).[5] These fullerene-based electron acceptors have many advantages in photovoltaic devices, including a deep-lying lowest unoccupied molecular orbital (LUMO, ~3.8-4.2 eV),[6] reversible reduction with ability to accept up to six electrons,[4a] ultra-fast three-dimensional charge transfer,[1a] and high electron mobility.[7] However, the almost negligible absorption of fullerene acceptors in the solar spectrum region dictates that the light-harvesting of BHJ solar cells using them is limited by the optical absorption of the donor materials. In addition, fullerene acceptors have poor photochemical stability in air and their spherical geometry leads to morphological instability of blends with linear polymers. The development of new non-fullerene acceptor materials is thus an important goal in organic photovoltaics.

Several non-fullerene n-type small molecules have been synthesized and studied as acceptors in bulk heterojunction solar cells.[1f, 8] Perylene diimide derivatives, are among the most

studied non-fullerene acceptors, and have yielded photovoltaic properties as high as 1.87% power conversion efficiency (PCE).[9,10] Other n-type small-molecule acceptors include vinazene derivatives,[11] cyanopentacenes,[1f, 12] bifluorenylidene,[13] and diketopyrrolopyrrole derivatives.[14] The highest efficiency achieved with typical classes of small-molecule acceptors are 1.29% PCE in cyanopentacene,[12b] 1.4% PCE in vinazene derivatives,[11b] and 1% PCE in diketyopyrrolopyrrole derivatives.[14] In addition to the design and synthesis of new n-type small molecules for more efficient polymer solar cells, new methods for the processing and optimization of non-fullerene BHJ solar cells are equally needed.

Towards the optimization of the photovoltaic properties of fullerene-based BHJ solar cells, various approaches have been proposed to manipulate the morphology of polymer blend films,[15] including slow-drying (film aging and solvent annealing),[16] thermal annealing,[17] self-assembled polymer nanowires,[18,19] and processing additives.[20] The use of processing additives in the optimization of the photovoltaic properties of polymer/fullerene blends has been shown to be effective in many systems including P3HT/PCBM,[20c, 21] and low-bandgap polymer/PCBM blends.[2b, 20a,b] In the case of P3HT/PCBM blends, the processing additive appears to enhance the photoresponsivity in the blend films, increase the charge carrier mobility, and increase the crystallinity of the P3HT phase.[20a,c] In the case of low-bandgap polymer/PCBM blends, the enhancement in photovoltaic properties is attributed to the increased charge carrier generation efficiency as a result of the formation of a bicontinuous nanomorphology.[20a,b] However, these approaches, especially the use of processing additives, are yet to be fully explored in the optimization of the photovoltaic properties of non-fullerene BHJ polymer solar cells.

In this chapter, we report the use of a processing additive in the optimization of bulk heterojunction (BHJ) polymer solar cells based on a non-fullerene acceptor,

N,*N*'-bis(2-ethylhexyl)-2,6-bis(5"-hexyl-[2,2';5',2"]terthiophen-5yl)-1,4,5,8-naphthalene diimide (NDI-3TH),[22] whose molecular structure and HOMO/LUMO energy levels are shown in Figure 4.1a. We show that the power conversion efficiency of BHJ solar cells based on blends of poly(3-hexylthiophene) (P3HT) and NDI-3TH can be enhanced 10-fold by using a 1,8-diiodooctane processing additive in conjunction with a P3HT electron-blocking layer and a 1,3,5-tris(1-phenyl-1H-benzimidazol-2-yl)benzene (TPBI) hole-blocking layer. The optimum concentration of the processing additive was found to be 0.2 vol%, which is substantially lower than the 2-3 vol% optimum concentration previously found in polymer/fullerene systems. It is shown that the nanomorphology and photovoltaic properties of the P3HT:NDI-3TH blend films are optimized at the 0.2 vol% concentration of the processing additive whereas micrometer-sized NDI-3TH domains with poor connectivity are found at high concentrations (>0.5 vol%) of the processing additive. The results demonstrate for the first time that processing additives can be profitably used to improve the nanomorphology and power conversion efficiency of BHJ polymer solar cells based on non-fullerene acceptors.

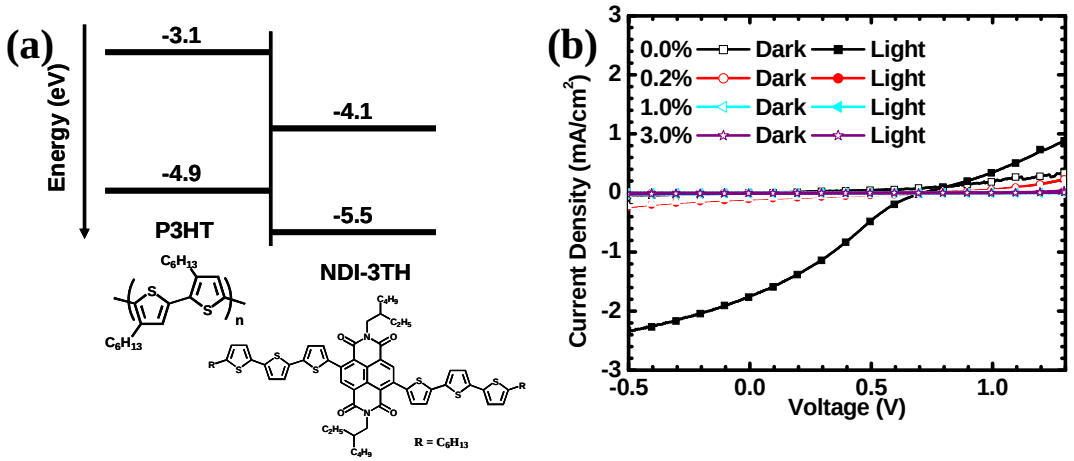

Figure 4.1 (a) Molecular structures and HOMO/LUMO energy levels of BHJ solar cell materials: donor P3HT and acceptor NDI-3TH. (b) Current density – Voltage characteristics of P3HT:NDI-3TH (1:3 wt/wt) blend solar cells fabricated with different concentrations of the processing additive DIO (in volume%).

4.2 Experimental Section

4.2.1 Materials. Regioregular poly(3-hexylthiophene) (P3HT) (M_w = 35.40 kDa, PDI = 2.45) was purchased from Rieke Metals. The synthesis and characterization of *N*,*N*'-bis(2-ethylhexyl)-2,6-bis(5"-hexyl-[2,2';5',2"]terthiophen-5yl)-1,4,5,8-naphthalene diimide (NDI-3TH) was reported elsewhere, and the HOMO/LUMO energy levels were determined by cyclic voltammetry.[22] 1,3,5-tris(1-phenyl-1H-benzimidazol-2-yl)benzene (TPBI, sublimed) was purchased from SynTec, a division of Sensient Imaging Technologies GmbH. Anhydrous dichloromethane (DCM, ≥ 99.8%, contains 50-150 ppm amylene stabilizer), anhydrous chloroform (≥99%) and 1,8-diiodooctane (DIO) were obtained from Sigma Aldrich and used without further purification.

4.2.2 Fabrication and Characterization of Solar Cells. A P3HT:NDI-3TH (6 mg mL^{-1}, 1:1 wt/wt) solution in DCM was prepared and stirred at 80 ℃ overnight until complete dissolution. The resulting solution was cooled to room temperature (20 ℃) and stored undisturbed for two days before device fabrication.

Solar cells were fabricated on indium tin oxide (ITO) glass substrates. ITO substrates (10 Ω/□, Shanghai B. Tree Tech. Consult Co., Ltd, Shanghai, China) were cleaned sequentially with acetone, deionized water and isopropyl alcohol in an ultrasonic bath, and blown with nitrogen until dried. A 40 nm PEDOT:PSS (Clevios P VP AI 4083) layer was spin-coated on top of the ITO and dried at 150 ℃ for 10 min under vacuum. For solar cells with a P3HT electron-blocking buffer layer, P3HT (8 mg mL^{-1}) in *ortho*-dichlorobenzene (ODCB) solution was spin-coated on top of the PEDOT:PSS layer, aged in a Petri dish for 5 min and thermally annealed at 150 ℃ for 5 min. The thickness of the P3HT buffer layer was 15 nm. The

P3HT:NDI-3TH blend solution was then spin-coated on top of the P3HT buffer layer for 18 s in a glovebox to make a BHJ active layer of ~70 nm. For solar cells without a P3HT buffer layer, the blend solution was spin-coated directly on top of the PEDOT:PSS layer. The active layer was then dried in vacuum for 2 hours or annealed at 100 ℃ for 10 min. The substrates were then loaded in a thermal evaporator (BOC Edwards, 306) to deposit a cathode composed of 1.0 nm LiF (or 3 nm TPBI) and 80 nm Al under high vacuum (8×10^{-7} torr). Five solar cells, each with an active area of 4 mm^2, were fabricated per ITO substrate.

Current – voltage characteristics of the non-encapsulated solar cells were obtained using an HP4155A semiconductor parameter analyzer in ambient laboratory air. The illumination (AM1.5 at 100 mW/cm^2) was provided by a filtered Xe lamp and calibrated by using a calibrated Si diode from the National Renewable Energy Lab (NREL, USA).

4.2.3 Characterization of Morphology and Absorption Spectra. Atomic force microscopy (AFM) imaging (5×5 μm area) was done using a Dimension 3100 SPM (Veeco) instrument operating in tapping mode. To obtain a thin film of P3HT:NDI-3TH active layer for bright field transmission electron microscope (BF-TEM) imaging, the substrate was first scratched, and soaked in deionized water. The active layer was then peeled-off the substrate, supported on a TEM grid (Electron Microscopy Sciences, Inc.), and dried. An FEI Tecnai G^2 F20 TEM operated at 200 kV was employed for BF-TEM imaging. Images were slightly defocused to enhance the phase contrast between the P3HT and NDI-3TH, and were acquired with a CCD camera and recorded with Gatan DigitalMicrograph software.

UV-vis absorption spectra were recorded with a Perkin-Elmer model Lambda 900 UV/vis/near-IR spectrophotometer on P3HT:NDI-3TH blend films spin-coated on top of ITO/PEDOT:PSS/(P3HT) substrates, following the same processing conditions as for the solar

cells. The film thickness was determined by using an Alpha-Step 500 profilometer (KLA-Tencor).

4.3 Results and Discussion

4.3.1 Effects of Processing Additives on Morphology and Photovoltaic Properties

We investigated the photovoltaic properties of P3HT:NDI-3TH blends (1:3 wt/wt) in BHJ solar cells processed from chloroform solutions without and with various concentrations of DIO additive. The solar cells have the basic device structure of ITO/PEDOT:PSS/P3HT:NDI-3TH (1:3)/LiF/Al and were fabricated and tested under AM1.5 solar illumination at 1 sun (100 mW/cm^2) in ambient air. The current density (J) – voltage (V) curves for these devices are shown in Figure 4.1b. The photovoltaic parameters, of devices fabricated without and with a processing additive, including the open circuit voltage (V_{oc}), the short-circuit current density (J_{sc}), and fill factors (FF) are collected in Table 4.1. A power conversion efficiency (PCE) of 0.34% was obtained without a processing additive. However, the use of a processing additive in fabricating devices from chloroform led to a large decrease in performance. For example, the use of 0.2 vol% DIO already led to a reduction of the photovoltaic efficiency of P3HT:NDI-3TH (1:3) devices from 0.34% to 0.01% PCE. The use of DIO seemed to increase the V_{oc} while dramatically reducing J_{sc} by a factor of 10. The photovoltaic efficiency of P3HT:NDI-3TH devices progressively decreased with increasing DIO concentration (Table 4.1), reaching 0.001% PCE at a 3.0 vol% DIO. We note that 2.0-3.0 vol% DIO is the optimal concentration range that has yielded the best photovoltaic properties in many polymer:fullerene (PCBM) blends.[2b, 20a,b, 21, 23] Clearly, the present results imply that a processing additive functions differently in processing P3HT:NDI-3TH blend devices compared to conventional polymer:fullerene solar cells.

Table 4.1 Photovoltaic properties of P3HT:NDI-3TH (1:3 wt/wt) blend solar cells: ITO/PEDOT:PSS/active layer/LiF/Al.

DIO additive (vol%)	V_{oc} [V]	J_{sc} [mA/cm^2]	*FF*	PCE_{max} [%]	PCE_{ave} [%]
0	0.69	1.76	0.29	0.34	0.32±0.03
0.2	0.87	0.10	0.21	0.02	0.013±0.006
0.5	0.86	0.17	0.23	0.03	0.02±0.01
0.8	0.75	0.011	0.26	0.002	0.002±0.00
1.0	0.70	0.013	0.24	0.002	0.002±0.00
3.0	0.56	0.007	0.39	0.001	0.001±0.00

The devices were processed from chloroform solvent containing DIO additive (vol%).

To better understand the large negative effect of a processing additive (DIO) on the photovoltaic properties of P3HT:NDI-3TH blends, we have investigated the photophysics and morphology of the BHJ solar cell films. The normalized UV-vis absorption spectra of the P3HT:NDI-3TH blend films were recorded prior to the deposition of the LiF/Al cathode (Figure 4.2). Only a small progressive red-shift of the absorption maxima around ~400 nm and ~700 nm was observed, which is consistent with previous observation of the optical properties of polymer:PCBM blends processed via additives.[20a,b, 21] However, the observed huge decrease in PCE cannot be explained by the observed absorption spectra.

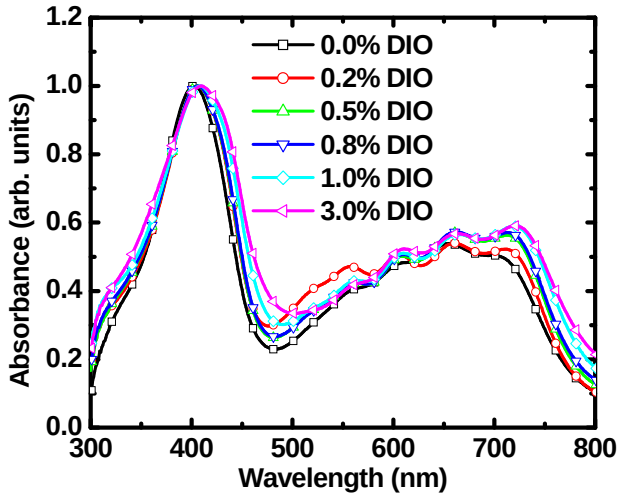

Figure 4.2 Normalized UV-vis spectra of P3HT:NDI-3TH (1:3 wt/wt) blend films processed from chloroform with various DIO concentrations.

Bright-field transmission electron microscope (BF-TEM) imaging was used to investigate the nanomorphology of the BHJ P3HT:NDI-3TH blend films directly peeled off from the solar cells and the results are shown in Figure 4.3. The pristine P3HT:NDI-3TH blend obtained without a processing additive showed a well-mixed nanomorphology (Figure 4.3a). P3HT:NDI-3TH blend films processed from a solution containing 0.2 vol% DIO show a phase-separated morphology (Figure 4.3b), with domains of aggregated NDI-3TH molecules on the scale of >400 nm. Such large domains would result in a decrease in interfacial area between donor and acceptor and thus reduction in charge carrier photogeneration and PCE. As the volume percentage of DIO in solution increased, NDI-3TH domains in the P3HT:NDI-3TH blend films increased as well. Processing from a solution containing 0.8 vol% DIO resulted in visible NDI-3TH nanorods with ~400 nm in diameter and several μm in length (Figure 4.3d). The efficiency of the corresponding solar cells was only 0.002% PCE, a factor of 170 reduction compared to devices processed without DIO. As the amount of DIO in solution increased further, the number density and dimension of the NDI-3TH nanorods increased, resulting in macrophase separated films with negligible photovoltaic properties (Figure 4.3f). We conclude that the deterioration in photovoltaic properties when DIO was used as a processing additive is a result of the large domains of the phase-separated P3HT:NDI-3TH blend, caused by the DIO-induced aggregation of NDI-3TH molecules. The large NDI-3TH aggregates present in DIO-processed P3HT:NDI-3TH blends are likely to have direct contact with the anode (PEDOT:PSS), which would negatively impact the performance of the solar cells. We note that simply reducing the NDI-3TH weight ratio in the P3HT:NDI-3TH blend did not help to prevent the processing additive - induced aggregation of the NDI-3TH acceptor molecules.

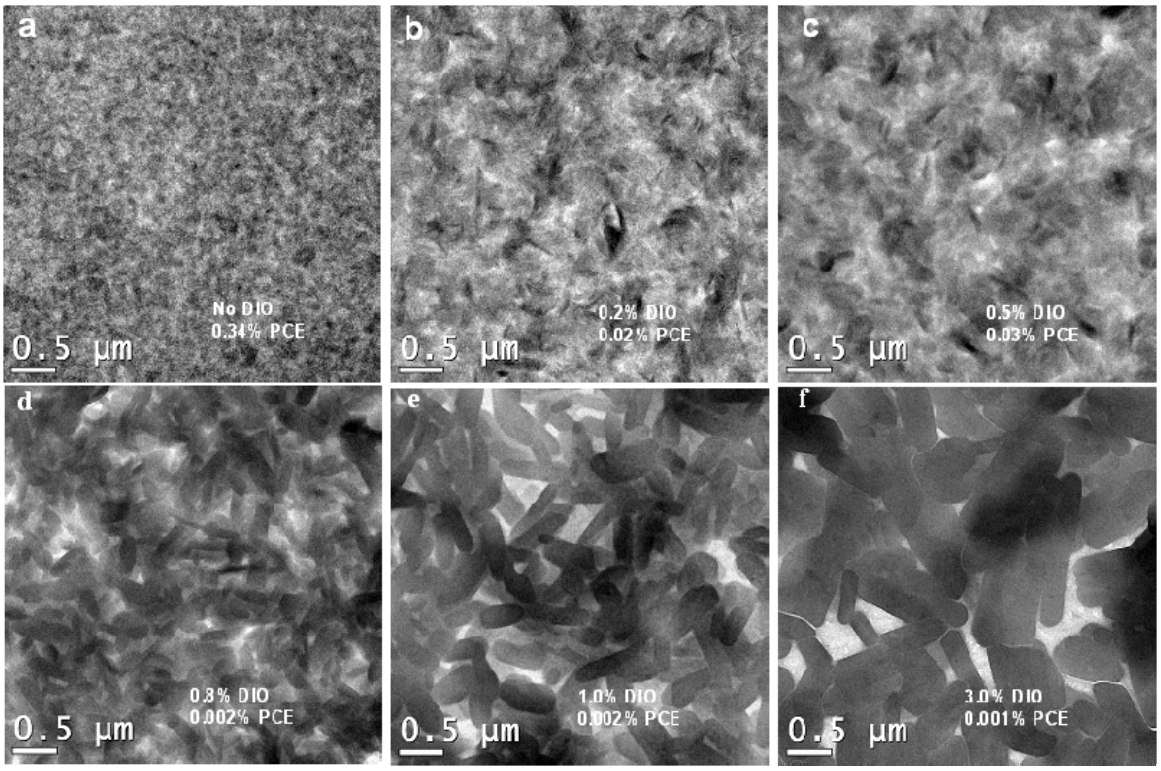

Figure 4.3 BF-TEM images of P3HT:NDI-3TH (1:3) blend solar cell films prepared by using different concentrations of the processing additive DIO in chloroform solutions: a) 0 vol% DIO; b) 0.2 vol% DIO; c) 0.5 vol% DIO; d) 0.8 vol% DIO; e)1.0 vol% DIO; f) 3.0 vol% DIO.

4.3.2 P3HT:NDI-3TH Blend Solar Cells Using Dichloromethane as Solvent

We explored dichloromethane (DCM, boiling point = 40 ℃) as an alternative processing solvent to chloroform (b.p. = 62 ℃). Although both are good solvents for NDI-3TH, dichloromethane is a poorer solvent for P3HT than chloroform. DCM has been found to be a marginal solvent for the growth of nanowires of poly(3-alkylthiophene)s.[18,19b-d] Initial investigation of three P3HT:NDI-3TH blend ratios (1:1, 1:2, and 1:3 wt/wt) showed that unlike chloroform-processed blends in which 1:3 weight ratio gave the best PCE, the 1:1 blend ratio showed the best photovoltaic properties in DCM-processed BHJ solar cells. We therefore focused a detailed investigation of the photovoltaic properties and morphology of P3HT:NDI-3TH (1:1 wt/wt) blends.

P3HT:NDI-3TH (1:1 wt/wt) solar cells were fabricated from DCM solutions without and with various DIO concentrations. Figure 4.4 shows the *J-V* curves of the P3HT:NDI-3TH (1:1 wt/wt) blend solar cell without a processing additive. The diode characteristics, such as the rectification ratio, are enhanced compared with those of the chloroform-processed diodes. A maximum efficiency of 0.16% PCE and an average of 0.14±0.01% PCE were achieved (Table 4.2). P3HT:NDI-3TH (1:1) blend solar cells processed from DCM solutions containing different DIO concentrations (0.1, 0.2, 0.5, 1.0 and 2.0 vol%) were fabricated and characterized and the *J-V* curves are shown in Figure 4.4b. The photovoltaic parameters are summarized in Table 4.2. Compared with the device processed without an additive, P3HT:NDI-3TH (1:1) blend solar cells processed using DIO additive showed that the V_{oc} increased from 0.61 V to 0.80 V at 2.0% DIO. However, both J_{sc} and FF exhibited maxima at 0.2% DIO, with peak values of 2.52 mA/cm^2 and 0.35, respectively. These photovoltaic parameters translate to an average efficiency of 0.58± 0.04% PCE. The photovoltaic properties decreased as the concentration of DIO progressively increases to 2.0 vol%.

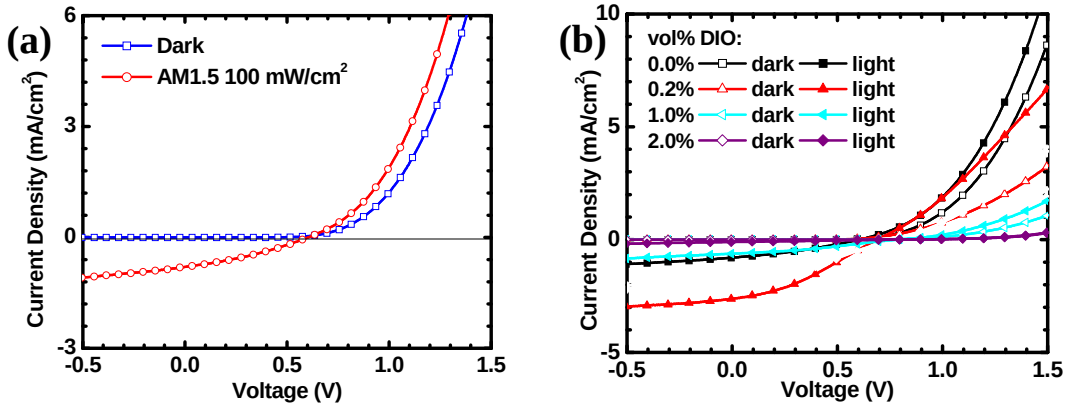

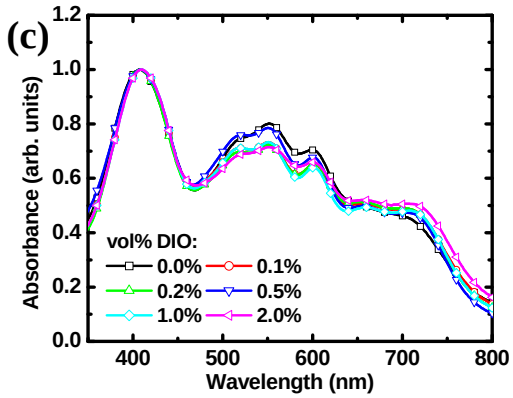

Figure 4.4 (a) Current density – Voltage curves of P3HT:NDI-3TH (1:1) blend solar cells processed from DCM. (b) Current density – Voltage characteristics of P3HT:NDI-3TH (1:1) blend solar cells processed from DCM solutions of various DIO concentrations (vol%). (c) UV-vis absorption spectra of P3HT:NDI-3TH (1:1) blend films processed from solutions of various DIO concentrations (vol%).

Table 4.2 Effects of DIO concentrations on the photovoltaic properties of P3HT:NDI-3TH (1:1 wt/wt) blend solar cells: ITO/PEDOT:PSS/active layer/LiF/Al.

DIO additive (vol%)	V_{oc} [V]	J_{sc} [mA/cm^2]	*FF*	PCE_{max} [%]	PCE_{ave} [%]
0	0.61	0.80	0.32	0.16	0.14±0.01
0.1	0.73	1.43	0.31	0.32	0.26±0.04
0.2	0.70	2.52	0.35	0.61	0.58±0.04
0.5	0.77	1.92	0.32	0.46	0.41±0.04
1.0	0.79	0.78	0.26	0.16	0.14±0.02
2.0	0.80	0.11	0.25	0.02	$(9\pm8)\times10^{-3}$

The devices were processed from dichloromethane solvent containing DIO additive (vol%).

In an effort to understand the effect of DIO additive in P3HT:NDI-3TH blend devices processed from DCM, we investigated the absorption spectra and morphology of P3HT:NDI-3TH blend films. The normalized UV-vis absorption spectra recorded from the actual solar cells are shown in Figure 4.4c. The line shape of the spectra and absorption maxima vary only slightly with the DIO concentration in the processing solution. Absorption peaks in the range of 500-600 nm are seen to decrease in intensity as the amount of DIO increases to above 1.0 vol%. Because NDI-3TH has no absorption peaks in this spectral region,[22] this decrease is likely caused by the disruption of the P3HT phase due to aggregation of NDI-3TH molecules.

The absorption edge around ~710 nm in the blend processed without DIO additive red-shifts with increasing amount of DIO in solution, indicating an increased order in NDI-3TH phase[20a] as P3HT has negligible absorption in this region.

Bright-field transmission electron microscope (BF-TEM) images of the P3HT:NDI-3TH (1:1) blend films processed from DCM solutions without and with DIO additive are shown in Figure 4.5 and Figure 4.6. The images were taken at a slightly defocused condition to enhance the phase contrast, which originates from density difference.[24] The TEM image of the P3HT:NDI-3TH blend film processed without DIO additive, as shown in Figure 4.5a, reveals a well-mixed, bicontinuous, percolated morphology, with P3HT nanowires dispersed evenly in the NDI-3TH matrix. Some aggregated NDI-3TH domains of ~500 nm are visible. As the amount of DIO in solution increases to 0.2 vol%, NDI-3TH forms interconnected, well-woven pathways for charge transport, while P3HT domains remain in nanowire network (Figure 4.5c and 4.6c). The enhanced photovoltaic properties observed for this processing condition may result from better charge carrier photogeneration and transport facilitated by this morphology. Clear large-scale phase separation is seen in blends processed with 0.5% and 1.0% DIO. The connectivity between these large domains is limited, resulting in loss of efficient charge photogeneration and transport. In the case of P3HT:NDI-3TH blends processed with 2.0% DIO (Figure 4.5f and 4.6f), large "flakes" of NDI-3TH with disrupted boundaries are observed, which could explain the rather poor photovoltaic efficiency (0.02% PCE).

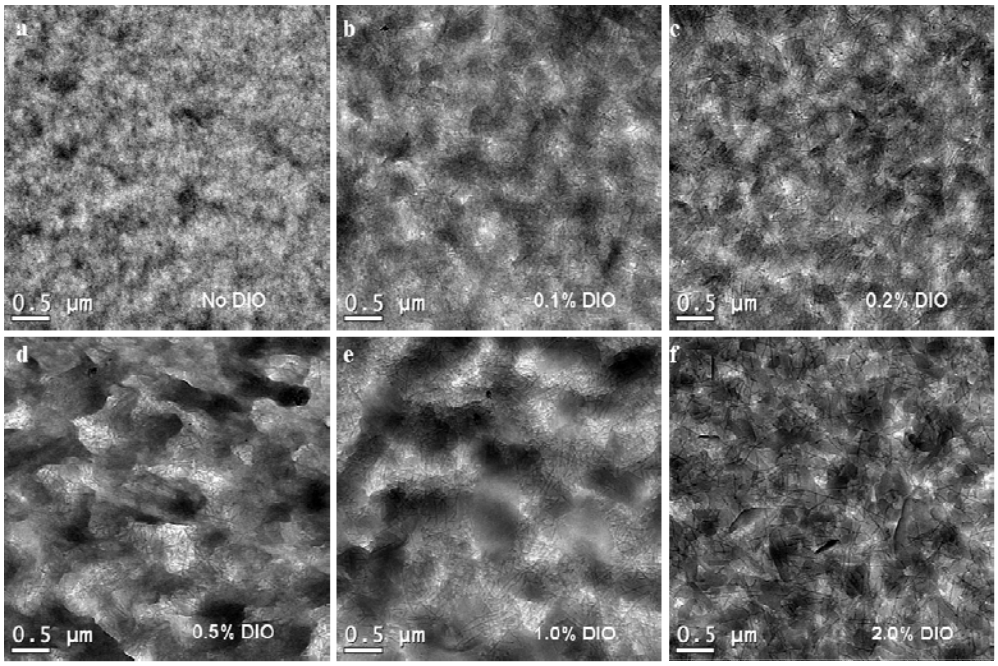

Figure 4.5 TEM images of P3HT:NDI-3TH (1:1 wt/wt) blend films processed from dichloromethane solutions containing different DIO concentrations (vol%).

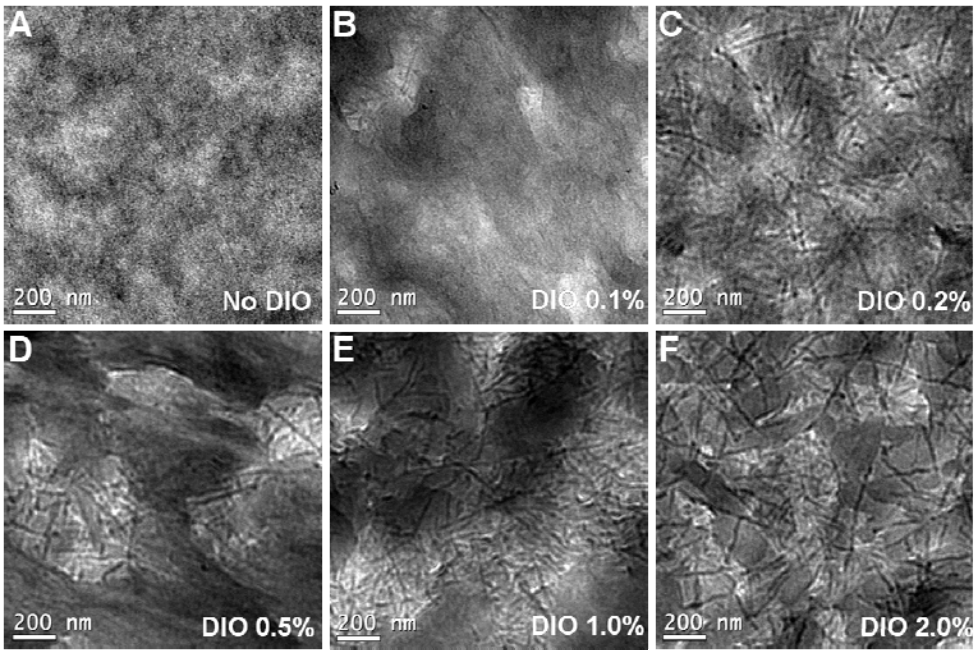

Figure 4.6 TEM images of P3HT:NDI-3TH (1:1) blend films processed from dichloromethane with various DIO concentrations.

We suspected that the surface morphology may also be modified as the concentration of DIO additive increases, and therefore used atomic force microscope (AFM) to study the surface morphology of the actual solar cells. The topographical AFM images with size of 5 × 5 μm are shown in Figure 4.7. The root-mean-square (RMS) surface roughness of each device was measured, and a clear increase of surface roughness (from 4.89 nm to 16.5 nm) with increasing DIO concentration in the processing solution was observed. The increase in surface roughness is due to the aggregation of molecules at the surface. AFM phase images, shown in Figure 4.8, indicated that the surface aggregates are primarily NDI-3TH small molecules. Combining the information from both TEM and AFM imaging, we can say that the use of DIO in processing P3HT:NDI-3TH blends modifies the phase distribution in the blends in the horizontal as well as on the surface of blend films. Furthermore, processing with 0.2 vol% DIO gives the best photovoltaic properties of P3HT:NDI-3TH blends. It is well-known that for PCBM-based polymer solar cells, the best concentration of a processing additive is in the range 2.0-3.0 vol%,[2b, 20a,b, 21, 23] which is significantly different from our finding of 0.2 vol% DIO in the case of P3HT:NDI-3TH blend solar cells. The exact reason for the reduced optimal amount of a processing additive in non-fullerene small-molecule/polymer solar cells remains unknown. Possible reasons include the different molar mass, solubility, and mode of interaction between the acceptor and polymer chains.

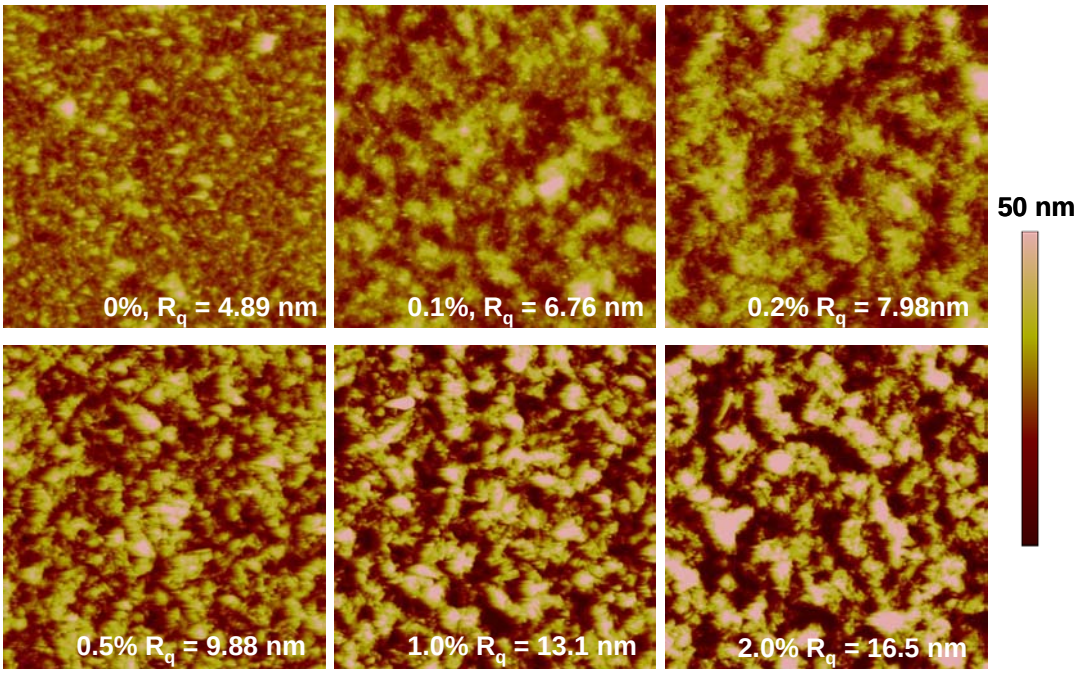

Figure 4.7 AFM topographical images of P3HT:NDI-3TH (1:1) processed from dichloromethane with various DIO concentrations. The size of image is 5 × 5 μm.

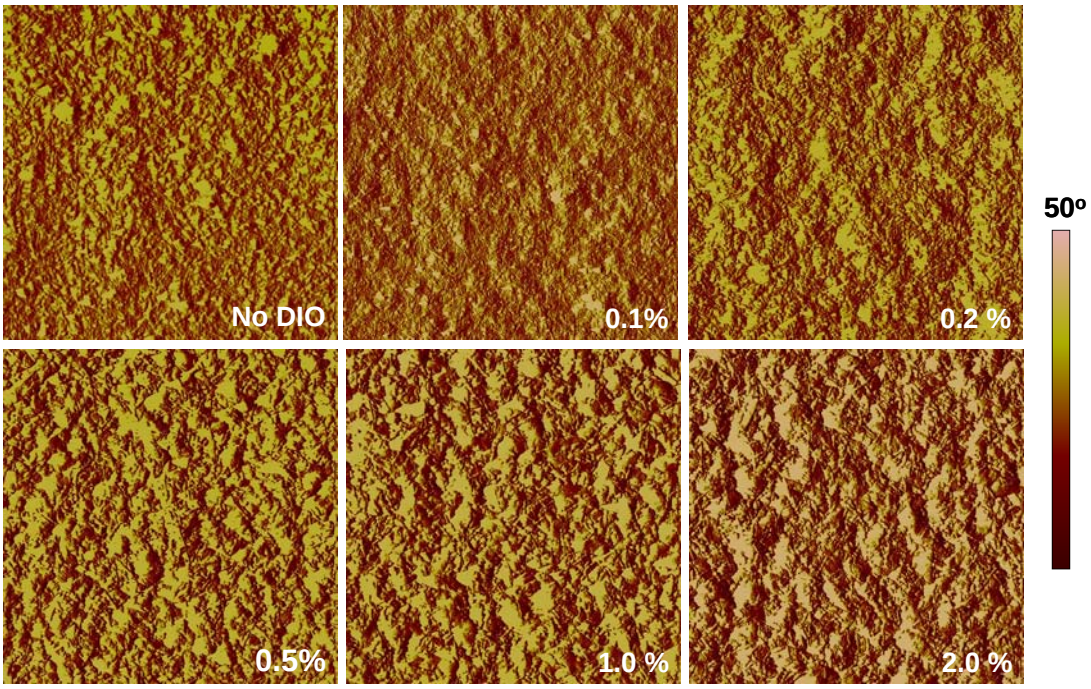

Figure 4.8 AFM phase images of P3HT:NDI-3TH (1:1) processed from dichloromethane with various DIO concentrations. The size of image is 5 × 5 μm.

4.3.3 Effects of an Electron-Blocking Buffer Layer

Because of the ambipolar charge transport nature of NDI-3TH,[22] we suspected that unintentional loss of charge carrier could take place at the interface between active layer and electrodes. We thus investigated the effects of an electron blocking layer or a p-type buffer layer on the photovoltaic properties of P3HT:NDI-3TH (1:1) blend solar cells processed with 0.2 vol% DIO additive. We selected P3HT as a suitable p-type semiconductor that can function as an electron blocking layer while enabling orthogonal fabrication of the P3HT:NDI-3TH active layer. Solar cells processed without and with a DIO additive were fabricated with the device structure of ITO/PEDOT:PSS/P3HT/P3HT:NDI-3TH (1:1)/LiF/Al and a 15 nm P3HT electron-blocking (buffer) layer. *J-V* curves of solar cells processed with various DIO concentrations are shown in Figure 4.9a. The associated photovoltaic parameters are summarized in Table 4.3. Incorporation of a P3HT electron-blocking layer without processing with a DIO additive results in a decrease in efficiency (0.09% PCE) compared with devices without an electron blocking layer. However, an increase in PCE was seen in P3HT/P3HT:NDI-3TH (1:1) blend solar cells when processed via a DIO additive (0.1 – 0.5 vol%). P3HT:NDI-3TH blend solar cells incorporating an electron blocking layer and processed with 0.2 vol% DIO had a maximum efficiency of 0.77% PCE, representing a 26% increase compared with devices without the P3HT electron blocking layer (0.61% PCE). In this case, the primary contributing factor is an increase in J_{sc}, although V_{oc} and *FF* also increased slightly. We note that as the concentration of DIO in the processing solution increased further to 1.0 - 2.0 vol%, the efficiency of the P3HT:NDI-3TH blend devices containing P3HT electron-blocking layer decreased significantly (Table 4.3). The observed decrease of the photovoltaic properties of P3HT:NDI-3TH blend solar cells containing P3HT electron-blocking layer when processed from solutions containing higher amounts (>0.2 vol%) of DIO can be explained by the previously discussed morphological changes associated with

NDI-3TH aggregation (Figure 4.3 and 4.5).

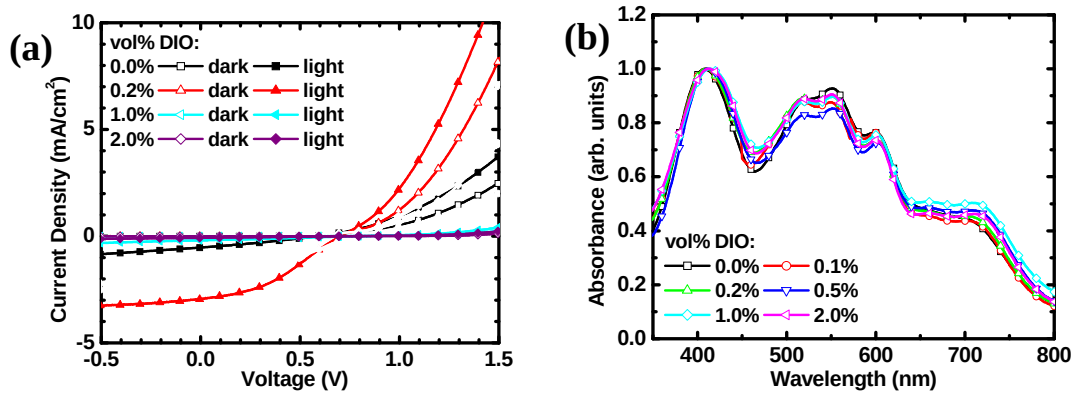

Figure 4.9 (a) Current density – Voltage curves of P3HT/P3HT:NDI-3TH (1:1) blend solar cells processed from DCM with various DIO concentrations (vol%). (b) UV-vis absorption spectra of P3HT/P3HT:NDI-3TH (1:1) blend films processed from solutions of various DIO concentrations (vol%).

Table 4.3 Effects of P3HT buffer layer on the photovoltaic properties of P3HT:NDI-3TH (1:1 wt/wt) blend solar cells: ITO/PEDOT:PSS/P3HT/active layer/LiF/Al.

DIO additive (vol%)	V_{oc} [V]	J_{sc} [mA/cm^2]	*FF*	PCE_{max} [%]	PCE_{ave} [%]
0	0.59	0.53	0.29	0.09	0.08±0.005
0.1	0.70	1.73	0.27	0.33	0.32±0.01
0.2	0.71	2.93	0.37	0.77	0.72±0.04
0.5	0.76	1.87	0.37	0.52	0.43±0.05
1.0	0.81	0.20	0.27	0.042	0.02±0.01
2.0	0.78	0.08	0.26	0.015	$(9\pm4)\times10^{-3}$

The devices were processed from dichloromethane solvent containing DIO additive (vol%).

The UV-vis absorption spectra of P3HT/P3HT:NDI-3TH (1:1) blend films processed with various DIO concentrations are shown in Figure 4.9b. Compared with P3HT/P3HT:NDI-3TH blend films processed without a DIO additive, the absorption intensity in the 500-600 nm region is seen to decrease with various amount of DIO concentration, reaching the lowest intensity when 0.5 vol% DIO is used. The absorption peak at ~710 nm in the blend films processed without an additive red-shifts to ~730 nm as the amount of DIO in solution increases. Comparing the UV-vis spectra of P3HT:NDI-3TH blend films processed with DIO additive and with (Figure

4.9b) or without (Figure 4.4c) a P3HT buffer layer, only absorption intensity in the region of 500-600 nm increases, attributable to the absorption of the P3HT buffer layer. It is possible that the small increase in photon harvesting can contribute to the slight increase in the efficiency of P3HT/P3HT:NDI-3TH blend solar cells processed with 0.1-0.5 vol% DIO additives, but the enhancement is offset by the largely negative effect on the morphology when higher DIO concentrations (1.0 – 2.0 vol%) were used.

4.3.4 Effects of a Hole Blocking Layer

To further improve the photovoltaic properties of P3HT:NDI-3TH (1:1) blend solar cells processed with the optimal amount of DIO additive (0.2 vol%) and incorporating a P3HT electron-blocking layer, we introduced a thin (3 nm) evaporated 1,3,5-tris(1-phenyl-1H-benzimidazol-2-yl)benzene (TPBI) hole blocking layer between the active layer and cathode. TPBI has a dendritic molecular structure with a moderate electron affinity (EA = 2.7 eV) and a high ionization potential (IP = 6.2-6.7eV).[25,26] The active blend layers of the resulting BHJ solar cells, ITO/PEDOT:PSS/P3HT/P3HT:NDI-3TH (1:1)/TPBI/Al, were either dried in vacuum or thermally annealed at 100 ^{o}C for 10 min. The *J-V* curves of these devices are shown in Figure 4.10a, and the calculated photovoltaic parameters are summarized in Table 4.4. A comparison of the vacuum-dried devices without and with a TPBI layer showed increase in both the V_{oc} and FF, while the J_{sc} is similar. A maximum efficiency of 1.15% PCE was achieved in devices with a TPBI hole-blocking layer, which represents a 49% increase compared with devices without a TPBI layer. After thermal annealing, the device performance was greatly enhanced, resulting in improved photovoltaic parameters, V_{oc} (0.82V), J_{sc} (3.51 mA/cm^2), and *FF* (0.52), and an efficiency of 1.50% PCE, which represents one of the highest efficiencies achieved in BHJ polymer solar cells based on non-fullerene small-molecule

acceptors. Additionally, annealed devices incorporating P3HT and TPBI layers processed without DIO showed a photovoltaic efficiency of 0.78% PCE, with reduced photovoltaic parameters, V_{oc} (0.73V), J_{sc} (2.51 mA/cm^2), and *FF* (0.43). These results further confirm the critical role of 0.2 vol% DIO processing additive in enhancing the photovoltaic properties of P3HT:NDI-3TH blends.

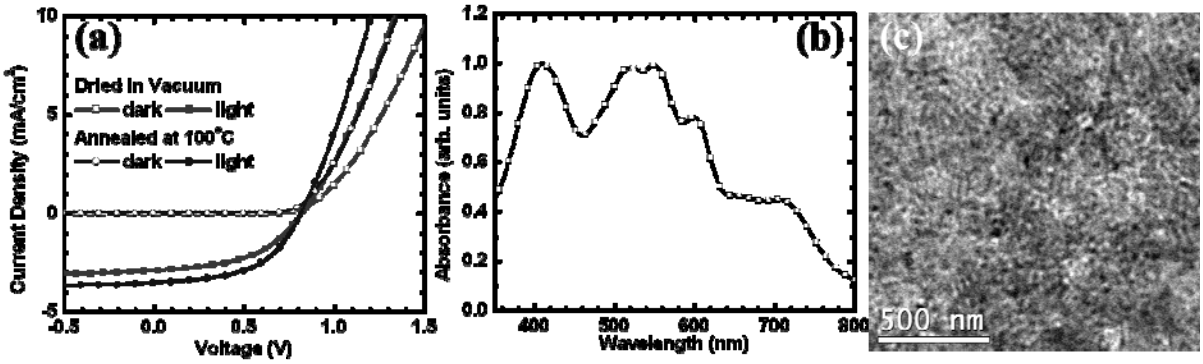

Figure 4.10 (a) Current density – Voltage curves of vacuum-dried or thermally annealed (100 ^{o}C) P3HT/P3HT:NDI-3TH (1:1)/TPBI/Al solar cells processed from DCM solution containing 0.2 vol% DIO. (b) UV-vis spectra of thermally annealed P3HT/P3HT:NDI-3TH (1:1) thin films. (c) BF-TEM image of a thermally annealed P3HT/P3HT:NDI-3TH (1:1) blend film.

We studied the optical absorption and morphology of the thermally annealed devices to gain an insight into the enhanced performance. The UV-vis spectrum of the actual solar cells is shown in Figure 4.10b. The absorption of P3HT:NDI-3TH blend in the spectral region of 500 – 600 nm is enhanced by thermal annealing, facilitating improved light harvesting. The BF-TEM image of the P3HT/P3HT:NDI-3TH bilayer is shown in Figure 4.10c. A bicontinuous nanoscale morphology containing NDI-3TH phase and P3HT nanowires is observed.

Table 4.4 Photovoltaic Properties of P3HT:NDI-3TH (1:1 wt/wt) Blend Solar Cells.

Devices [a]	V_{oc} [V]	J_{sc} [mA/cm^2]	*FF*	PCE_{max} [%]	PCE_{ave} [%]
P3HT:NDI-3TH/LiF [b]	0.61	0.80	0.32	0.16	0.14±0.01
P3HT/NDI-3TH:P3HT/LiF [b]	0.59	0.53	0.29	0.09	0.08±0.005
P3HT:NDI-3TH/LiF [b, d]	0.70	2.52	0.35	0.61	0.58±0.04
P3HT/P3HT:NDI-3TH/LiF [b, d]	0.71	2.93	0.37	0.77	0.72±0.04
P3HT/P3HT:NDI-3TH/TPBI [b, d]	0.83	2.85	0.49	1.15	1.12±0.04
P3HT/P3HT:NDI-3TH/TPBI [c, d]	0.82	3.51	0.52	1.50	1.45±0.05
P3HT/P3HT:NDI-3TH/TPBI [c]	0.73	2.51	0.43	0.78	0.77±0.02

[a] Devices processed from dichloromethane. Anode: ITO/PEDOT:PSS. Cathode: Al. [b] Devices were dried in vacuum at room temperature. [c] Devices were thermally annealed at 100 °C for 10 min. [d] Devices were processed from dichloromethane with 0.2 vol% DIO.

4.4 Conclusions

We have investigated the processing additive strategy in the optimization of BHJ polymer solar cells based on a non-fullerene small-molecule acceptor. It is found that the average power conversion efficiency of P3HT:NDI-3TH solar cells is improved from 0.14% to 1.5% by use of a 1,8-diiodooctane (DIO) processing additive along with a P3HT electron-blocking layer and a TPBI hole-blocking layer. The underlying mechanism for the enhancement in performance is that the processing additive regulates the aggregation and domain size and connectivity of the NDI-3TH phase in the BHJ blends. The optimum concentration of the DIO processing additive was found to be 0.2 vol%, which is significantly less than the 2.0-3.0 vol% optimum concentrations previously reported for polymer/fullerene systems. Results of TEM and AFM imaging of P3HT:NDI-3TH blends revealed that the size of NDI-3TH domains rapidly increased from the nanoscale at the optimum additive concentration (0.2 vol%) to the micrometer scale at higher concentrations (>0.5 vol%). The present results show for the first time that processing additives can be used to optimize the nanomorphology and enhance the performance of bulk

heterojunction polymer solar cells based on non-fullerene acceptors.

4.5 References

1. a) Thompson, B. C.; Frechet, J. M. J. *Angew. Chem. Int. Ed.* **2008**, *47*, 58-77; b) Dennler, G.; Scharber, M. C.; Brabec, C. J. *Adv. Mater.* **2009**, *21*, 1323-1338; c) Coakley, K. M.; McGehee, M. D. *Chem. Mater.* **2004**, *16*, 4533-4542; d) Brunetti, F. G.; Kumar, R.; Wudl, F. *J. Mater. Chem.* **2010**, *20*, 2934-2948; e) Cheng, Y.-J.; Yang, S.-H.; Hsu, C.-S. *Chem. Rev.* **2009**, *109*, 5868-5923; f) Anthony, J. E. *Chem. Mater.* **2011**, *23*, 583-590; g) Boudreault, P.-L. T.; Najari, A.; Leclerc, M. *Chem. Mater.* **2011**, *23*, 456-469; h) Roncali, J. *Adv. Energy Mater.* **2011**, *1*, 147-160.

2. a) Zhou, H.; Yang, L.; Stuart, A. C.; Price, S. C.; Liu, S.; You, W. *Angew. Chem. Int. Ed.* **2011**, *50*, 2995-2998; b) Liang, Y.; Xu, Z.; Xia, J.; Tsai, S.-T.; Wu, Y.; Li, G.; Ray, C.; Yu, L.P. *Adv. Mater.* **2010**, *22*, E135-E138; c) Alam, M. M.; Jenekhe, S. A. *Chem. Mater.* **2004**, *16*, 4647-4656; d) Wu, P.-T.; Xin, H.; Kim, F. S.; Ren, G.; Jenekhe, S. A. *Macromolecules* **2009**, *42*, 8817-8826; e) Wu, P.-T.; Ren, G.; Jenekhe, S. A. *Macromolecules* **2010**, *43*, 3306-3313; f) Ren, G.; Wu, P.-T.; Jenekhe, S. A. *Chem. Mater.* **2010**, *22*, 2020-2026; g) Xin, H.; Guo, X.; Kim, F. S.; Ren, G.; Watson, M. D.; Jenekhe, S. A. *J. Mater. Chem.* **2009**, *19*, 5303-5310.

3. Yu, G.; Gao, J.; Hummelen, J. C.; Wudl, F.; Heeger, A. J. *Science* **1995**, *270*, 1789-1791.

4. a) Hummelen, J. C.; Knight, B. W.; LePeq, F.; Wudl, F.; Yao, J.; Wilkins, C. L. *J. Org. Chem.* **1995**, *60*, 532-538; b) Wudl, F. *Acc. Chem. Res.* **1992**, *25*, 157-161.

5. Wienk, M. M.; Kroon, J. M.; Verhees, W. J. H.; Knol, J.; Hummelen, J. C.; v. Hal, P. A.; Janssen, R. A. *Angew. Chem. Int. Ed.* **2003**, *42*, 3371-3375.

6. a) Allemand, P. M.; Koch, A.; Wudl, F.; Rubin, Y.; Diederich, F.; Alvarez, M. M.; Anz, S. J.; Whetten, R. L. *J. Am. Chem. Soc.* **1991**, *113*, 1050-1051; b) Brabec, C. J.; Cravino, A.; Meissner, D.; Sariciftci, N. S.; Fromherz, T.; Rispens, M. T.; Sanchez, L.; Hummelen, J. C. *Adv. Funct. Mater.* **2001**, *11*, 374-380; c) Guan, Z.-L.; Kim, J. B.; Wang, H.; Jaye, C.; Fischer, D. A.; Loo, Y.-L.; Kahn, A. *Org. Electron.* **2010**, *11*, 1779-1785.

7. Singh, T. B.; Marjanovic, N.; Matt, G. J.; Günes, S.; Sariciftci, N. S.; Montaigne Ramil, A.; Andreev, A.; Sitter, H.; Schwödiauer, R.; Bauer, S. *Org. Electron.* **2005**, *6*, 105-110.

8. Sonar, P.; Lim, J. P. F.; Chan, K. L. *Energy Environ. Sci.* **2011**, *4*, 1558-1574.

9. a) Dittmer, J. J.; Marseglia, E. A.; Friend, R. H. *Adv. Mater.* **2000**, *12*, 1270-1274; b) Schmidt-Mende, L.; Fechtenkötter, A.; Müllen, K.; Moons, E.; Friend, R. H.; MacKenzie, J. D. *Science* **2001**, *293*, 1119-1122; c) Li, J.; Dierschke, F.; Wu, J.; Grimsdale, A. C.; Müllen, K. *J. Mater. Chem.* **2006**, *16*, 96-100; d) Rajaram, S.; Armstrong, P. B.; Kim, B. J.; Frechet, J. M. J. *Chem. Mater.* **2009**, *21*, 1775-1777; e) Schwenn, P. E.; Gui, K.; Nardes, A. M.; Krueger, K. B.; Lee, K. H.; Mutkins, K.; Rubinstein-Dunlop, H.; Shaw, P. E.; Kopidakis, N.; Burn, P. L.; Meredith, P. *Adv. Energy Mater.* **2011**, *1*, 73-81.

10. Sharma, G. D.; Suresh, P.; Mikroyannidis, J. A.; Stylianakis, M. M. *J. Mater. Chem.* **2010**, *20*, 561-567.

11. a) Shin, R. Y. C.; Kietzke, T.; Sudhakar, S.; Dodabalapur, A.; Chen, Z.-K.; Sellinger, A. *Chem. Mater.* **2007**, *19*, 1892-1894; b) Woo, C. H.; Holcombe, T. W.; Unruh, D. A.; Sellinger, A.; Fréchet, J. M. J. *Chem. Mater.* **2010**, *22*, 1673-1679; c) Inal, S.; Castellani, M.; Sellinger, A.; Neher, D. *Macromol. Rapid Commun.* **2009**, *30*, 1263-1268.

12. a) Lloyd, M. T.; Anthony, J. E.; Malliaras, G. G. *Mater. Today* **2007**, *10*, 34-41; b) Shu, Y.; Lim, Y.-F.; Li, Z.; Purushothaman, B.; Hallani, R.; Kim, J. E.; Parkin, S. R.; Malliaras, G. G.; Anthony, J. E. *Chem. Sci.* **2011**, *2*, 363-368.

13. Brunetti, F. G.; Gong, X.; Tong, M.; Heeger, A. J.; Wudl, F. *Angew. Chem. Int. Ed.* **2010**, *49*, 532-536.

14. a) Sonar, P.; Ng, G.-M.; Lin, T. T.; Dodabalapur, A.; Chen, Z.-K. *J. Mater. Chem.* **2010**, *20*, 3626-3636; b) Karsten, B. P.; Bijleveld, J. C.; Janssen, R. A. J. *Macromol. Rapid Commun.* **2010**, *31*, 1554-1559.

15. Peet, J.; Senatore, M. L.; Heeger, A. J.; Bazan, G. C. *Adv. Mater.* **2009**, *21*, 1521-1527.

16. a) Li, G.; Yao, Y.; Yang, H.; Shrotriya, V.; Yang, G.; Yang, Y. *Adv. Funct. Mater.* **2007**, *17*, 1636-1644; b) Arnautov, S. A.; Nechvolodova, E. M.; Bakulin, A. A.; Elizarov, S. G.; Khodarev, A. N.; Martyanov, D. S.; Paraschuk, D. Y. *Synth. Met.* **2004**, *147*, 287-291; c) Mihailetchi, V. D.; Xie, H.; de Boer, B.; Popescu, L. M.; Hummelen, J. C.; Blom, P. W. M.; Koster, L. J. A. *Appl. Phys. Lett.* **2006**, *89*, 012107.

17. a) Camaioni, N.; Ridolfi, G.; Casalbore-Miceli, G.; Possamai, G.; Maggini, M. *Adv. Mater.* **2002**, *14*, 1735-1738; b) Janssen, G.; Aguirre, A.; Goovaerts, E.; Vanlaeke, P.; Poortmans, J.; Manca, J. *Eur. Phys. J. Appl. Phys.* **2007**, *37*, 287-290.

18. Kim, F. S.; Ren, G.; Jenekhe, S. A. *Chem. Mater.* **2011**, *23*, 682-732.

19. a) Xin, H.; Kim, F. S.; Jenekhe, S. A. *J. Am. Chem. Soc.* **2008**, *130*, 5424-5425; b) Xin, H.; Reid, O. G.; Ren, G.; Kim, F. S.; Ginger, D. S.; Jenekhe, S. A. *ACS Nano* **2010**, *4*, 1861-1872; c) Xin, H.; Ren, G.; Kim, F. S.; Jenekhe, S. A. *Chem. Mater.* **2008**, *20*, 6199-6207; d) Ren, G.; Wu, P.-T.; Jenekhe, S. A. *ACS Nano* **2011**, *5*, 376-384.

20. a) Peet, J.; Kim, J. Y.; Coates, N. E.; Ma, W. L.; Moses, D.; Heeger, A. J.; Bazan, G. C. *Nat. Mater.* **2007**, *6*, 497-500; b) Lee, J. K.; Ma, W. L.; Brabec, C. J.; Yuen, J.; Moon, J. S.; Kim, J. Y.; Lee, K.; Bazan, G. C.; Heeger, A. J. *J. Am. Chem. Soc.* **2008**, *130*, 3619-3623; c) Peet, J.; Soci, C.; Coffin, R. C.; Nguyen, T. Q.; Mikhailovsky, A.; Moses, D.; Bazan, G. C. *Appl. Phys. Lett.* **2006**, *89*, 252105.

21. Chen, H. Y.; Yang, H. C.; Yang, G. W.; Sista, S.; Zadoyan, R. B.; Li, G.; Yang, Y. *J. Phys. Chem. C* **2009**, *113*, 7946-7953.

22. Ahmed, E.; Ren, G.; Kim, F. S.; Hollenbeck, E. C.; Jenekhe, S. A. *Chem. Mater.* **2011**, *23*, 4563-4577.

23. Moon, J. S.; Takacs, C. J.; Cho, S.; Coffin, R. C.; Kim, H.; Bazan, G. C.; Heeger, A. J. *Nano Lett.* **2010**, *10*, 4005-4008.

24. van Bavel, S. S.; Sourty, E.; de With, G.; Loos, J. *Nano Lett.* **2009**, *9*, 507-513.

25. a) Gao, Z.; Lee, C. S.; Bello, I.; Lee, S. T.; Chen, R.-M.; Luh, T.-Y.; Shi, J.; Tang, C. W. *Appl. Phys. Lett.* **1999**, *74*, 865; b) Anthopoulos, T. D.; Markham, J. P. J.; Namdas, E. B.; Samuel, I. D. W.; Lo, S.-C.; Burn, P. L. *Appl. Phys. Lett.* **2003**, *82*, 4824.

26. a) Kulkarni, A. P.; Tonzola, C. J.; Babel, A.; Jenekhe, S. A. *Chem. Mater.* **2004**, *16*, 4556-4573; b) Lo, S. C.; Burn, P. L. *Chem. Rev.* **2007**, *107*, 1097-1116.

Chapter 5 Nanowires of Oligothiophene-Functionalized Naphthalene Diimides: Self Assembly, Morphology, and All-Nanowire Bulk Heterojunction Solar Cells

5.1 Introduction

Organic photovoltaic cells have been demonstrated as a promising new class of solar energy conversion devices and therefore of broad current interest.[1-20] The active layer of the typical organic solar cell is composed of a phase-separated blend of two components – a polymer semiconductor that acts as an electron donor (p-type) and hole-conducting phase, and a fullerene-based semiconductor that serves as an electron acceptor (n-type) and electron-conducting phase – necessary for efficient photoinduced charge transfer and separation.[21] Because of the relative small exciton diffusion lengths in organic semiconductors (10-20 nm), control and fine-tuning of the nanoscale morphology of the active layer blend or bulk heterojunction (BHJ) film have been critical to improving photoconversion efficiency in organic photovoltaics.[1-6, 22-25] Various approaches have been demonstrated in the control of the nanomorphology of BHJ films, including thermal/solvent annealing,[26-30] processing additives,[10, 31-35] and the use of polymer semiconductor nanowires.[12, 36-39] The concept of using organic semiconductor nanowires as either the donor or acceptor component of BHJ solar cells has been explored and demonstrated to have several advantages.[40] Self-assembled nanowires (NWs) offer a rational approach to the control of the nanoscale morphology of the phase-separated BHJ film. The typical dimensions of assembled polymer semiconductor NWs have widths of 10-30 nm

(and lengths of μm) which are perfectly matched to the exciton diffusion lengths. Assembled, π-stacked, organic semiconductors generally have high carrier mobilities and high absorption coefficients due to the increased crystallinity and supramolecular order.[40] The use of self-assembled nanowires allows avoidance of the difficulties of controlling blend phase separation kinetics, thermodynamics, and related phenomena such as domain coarsening and time-dependent instability.

p-Type polymer semiconductor nanowires have been extensively studied as the donor components of BHJ polymer solar cells. Examples include the use of NWs assembled from poly(3-butylthiophene) (P3BT),[12, 37, 38] poly(3-pentylthiophene) (P3PT),[41] poly(3-hexylthiophene) (P3HT),[36] and block copolymers[11, 42-44] (e.g. poly(3-butylthiophene)-*b*-poly(3-octylthiophene) (P3BT-*b*-P3OT),[11, 43] and poly(3-hexylthiophene)-*b*-poly(3-cyclohexylthiophene) (P3HT-*b*-P3cHT)[44]). Typical dimensions of these p-type polymer nanowires are 10-18 nm in width and >10 μm in length. The length of these polymer nanowires has been varied from 200 nm to >5 μm while the width is in the range of 13-16 nm using block copolymers with different block compositions.[11]

Non-fullerene n-type organic semiconductors are actively being pursued as an alternative class of electron acceptors to replace fullerene derivatives in organic solar cells.[45-47] Polymer semiconductors have been demonstrated as electron acceptors in organic solar cells with efficiencies of about 1-2% PCE.[48-53] Self-assembly of n-type polymer semiconductor has been exemplified with poly(benzobisimidazobenzophenanthroline) (BBL) nanoribbons with average widths of ~200nm to ~1 μm and thicknesses of ~10-50 nm.[54] In the case of small-molecule

organic semiconductors, various molecular structures have been synthesized and used in organic solar cells,[45, 46] such as perylene diimides[55-58] and naphthalene diimides.[10, 47] Self-assembled small molecule nanostructures have also been explored,[40] but their dimensions are usually quite large (>500 nm) in width to be useful in BHJ solar cells. Although NWs have been assembled from various n-type organic semiconductors,[40, 54] however, only one example of the use of NWs of an n-type organic semiconductor as the acceptor in BHJ solar cells has been reported.[59] Nanoribbons of N,N'-dioctyl-3,4,9,10-perylenedicarboximide (PTCDI-C_8) of widths 100–200 nm and length several μm when blended with P3HT could give BHJ devices with an efficiency of 1.03% PCE.[59] To date BHJ solar cells incorporating organic semiconductor nanowires as both the electron donor and the electron acceptor components have not been explored or demonstrated.

In this paper we report a systematic study of the solution-phase self-assembly of nanowires, morphology, and photovoltaic properties of a series of n-type organic semiconductors, oligothiophene-functionalized naphthalene diimides (NDI-nTH, NDI-nT), whose molecular structures are shown in Figure 5.1a. We show that highly crystalline nanowires (NWs) with width of 80-250 nm can be readily assembled from all naphthalene diimides, NDI-nTH and NDI-nT, in dichloromethane (DCM) solution. The morphology of the n-type organic semiconductor NWs was investigated by transmission electron microscopy (TEM) imaging, electron diffraction, and AFM imaging. By utilizing the n-type organic semiconductor NWs as acceptor and poly(3-hexylthiophene) (P3HT) NWs as donor, we could explore the new concept of an *all-nanowire* BHJ solar cell (Fig. 1b). Such all-nanowire BHJ solar cells comprised of

P3HT NWs:NDI-3THs NW blends had a power conversion efficiency of 1.15% and external quantum efficiency (EQE) spectra that demonstrate light harvesting by both donor (P3HT) and acceptor (NDI-3TH) nanowires.

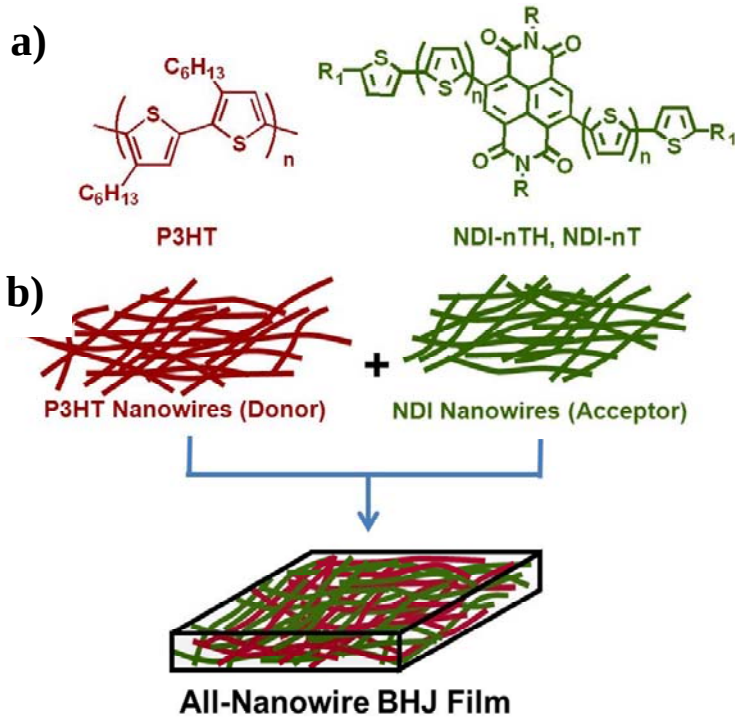

Figure 5.1 a) Molecular structures of P3HT and oligothiophene-functionalized naphthalene diimides (NDI-nTH, NDI-nT). NDI-2TH: n = 1, R_1 = C_6H_{13}; NDI-3TH: n = 2, R_1 = C_6H_{13}; NDI-4TH: n = 3, R_1 = C_6H_{13}; NDI-2T: n = 1, R_1 = H; NDI-3T: n = 2, R_1 = H; NDI-4T: n = 3, R_1 = H. R = ethylhexyl. b) Schematic of all-nanowire bulk heterojunction (BHJ) film for organic photovoltaics.

5.2 Experimental Section

5.2.1 Materials. The synthesis and characterization of the series of oligothiophene-functionalized naphthalene diimides (NDI-nTH and NDI-nT) were reported elsewhere. [47] Six NDI-nTH and NDI-nT samples were investigated, including NDI-2TH, NDI-3TH, NDI-4TH, NDI-2T, NDI-3T, and NDI-4T. Regioregular poly(3-hexylthiophene) (P3HT) (M_w = 35.4 kDa, PDI = 2.45) was purchased from Rieke Metals.

1,3,5-Tris(1-phenyl-1H-benzimidazol-2-yl)benzene (TPBI, sublimed) was purchased from Luminescence Technology Corp. (Taiwan). Anhydrous dichloromethane (DCM, ≥99.8%, contains 50-150 ppm amylene stabilizer) and methanol (≥99.8%) were obtained from Sigma Aldrich and used as received.

5.2.2 Assembly of Organic Semiconductor Nanowires. P3HT NWs and NDI-nTH (or NDI-nT) NWs were prepared separately via solution-phase self-assembly approaches.[40] To assemble P3HT NWs, 3 mg/mL P3HT was dissolved in DCM at 80 ^{o}C under vigorous stirring overnight. The solution was then cooled at room temperature and left for two days to allow undisturbed assembly of P3HT NWs. The 1D nanostructures of NDI-nTH or NDI-nT semiconductors were prepared via solvent exchange by adding a non-solvent (methanol) into solutions of the n-type organic semiconductor. Briefly, 1 mg/mL NDI in dichloromethane (DCM) solution was prepared and stirred until complete dissolution at room temperature (20^{o}C). Methanol was then added into the NDI solution in DCM drop by drop by using a pipette under vigorous stirring. The addition of methanol ceased when aggregates of nanostructures were visually observed. The quantity of methanol added into each NDI solution varied with different NDIs. For example, 0.2 mL of methanol was added to 1 mL of 1 mg/mL NDI-3TH solution in DCM. The resulting suspension of NDI NWs was centrifuged to obtain a precipitate of NDI NWs. The NWs were dried and re-dispersed in a mixed solvent of DCM/methanol with the same volume ratio as that of the mixed solvent used for the assembly of NWs.

5.2.3 Fabrication and Characterization of Solar Cells. Blends of P3HT NWs and NDI-nTH (NDI-nT) NWs were prepared by mixing the respective suspensions at 1:1 wt:wt. Solar cells

were fabricated on indium tin oxide (ITO) glass substrates. ITO substrates (10 Ω/□, Shanghai B. Tree Tech. Consult Co., Ltd, Shanghai, China) were cleaned sequentially with acetone, deionized water and isopropyl alcohol in an ultrasonic bath, and blown with nitrogen until dried. A 40 nm PEDOT:PSS (Clevios P VP AI 4083) layer was spin-coated on top of the ITO and dried at 150 °C for 10 min under vacuum. A 15 nm P3HT electron-blocking buffer layer was spin-coated onto the PEDOT:PSS from a 8 mg/mL P3HT/*ortho*-dichlorobenzene (ODCB) solution. The P3HT buffer layer was aged in a Petri dish for 5 min and thermally annealed at 150 °C for 5 min. The P3HT NWs:NDI-nTH (or NDI-nT) NWs blend suspension was then spin-coated on top of the P3HT buffer layer for 18 s in a glovebox to make a BHJ active layer of ~80 nm. The active layer was annealed at 150 °C for 10 min. The substrates were then loaded in a thermal evaporator (BOC Edwards, Model 306) to deposit a 3 nm TPBI hole blocking layer and a 80 nm Al cathode layer under high vacuum (8×10^{-7} Torr). Four solar cells, each with an active area of 9 mm^2, were fabricated per ITO substrate.

Current–voltage characteristics of the non-encapsulated solar cells were obtained using an HP4155A semiconductor parameter analyzer in ambient laboratory air. The illumination (AM1.5 at 100 mW/cm^2) was provided by a filtered Xe lamp and calibrated using a calibrated Si diode from the National Renewable Energy Lab (NREL, USA). External quantum efficiency (EQE) was measured using a QEX10 solar cell quantum efficiency measurement system (PV Measurements, Inc.), and was calibrated with a NREL-certified Si diode before measurement.

5.2.4 Characterization of Morphology and Absorption Spectra. Samples for atomic force microscopy (AFM) imaging (5 × 5 μm area) were prepared by spin-coating a dilute suspension

of NDI-3TH NWs onto silicon wafer. A dimension 3100 SPM (Veeco Instruments Inc.) instrument operating in tapping mode was used to for the AFM imaging. Samples for bright-field transmission electron microscope (BF-TEM) imaging were prepared by drop-casting suspensions of the NWs in DCM/methanol onto TEM grids (Electron Microscope Sciences, Inc.) and drying in vacuum. An FEI Tecnai G^2 F20 TEM operated at 200 kV was employed, with a 0.031 mm^2 aperture for selected area electron diffraction (SAED). Images were slightly defocused to enhance the phase contrast and were acquired with a CCD camera and recorded with Gatan DigitalMicrograph software.

UV−vis absorption spectra were recorded with a Perkin-Elmer model Lambda 900 UV/vis/near-IR spectrophotometer from both suspensions of the NWs and the neat films of the NWs spin-coated on top of glass substrates.

5.3 Results and Discussion

5.3.1 Assembly and Morphology of n-Type Organic Semiconductor Nanowires. We have previously demonstrated that one of the n-type organic semiconductors investigated here, NDI-3TH, can self-assemble into single-crystalline nano/microwires via the solvent exchange method,[40] in which methanol (a non-solvent) is added into a solution of NDI-3TH in dichloromethane and the resulting mixture is left for an extended period of time (2 weeks).[47] The resulting NDI-3TH nano/microwire had widths of 100 nm to 20 μm and equally polydisperse length (1-300 μm), making them not ideal for bulk heterojunction solar cells. In the present study we investigated the self-assembly of nanowires from all 6 NDI-nTH and NDI-nT materials and aimed to achieve narrower widths. We thus reduced the concentration of the NDI solutions in

dichloromethane (DCM), applied vigorous stirring during the assembly process, and shortened the assembly time. For instance, a 1 mg/mL NDI-3TH solution in DCM was prepared at room temperature (20^{o}C). Under magnetic stirring, methanol was added into the same solution drop by drop by using a pipette. The addition of methanol ceased when aggregates of nanowires were visually observed. This solution was set aside for one day and used for further investigation. We note that the conditions were different from previously reported for the assembly of NDI-3TH nano/microwires, in which a more concentrated solution (5 mg/mL) and longer assembly time were used.

Bright-field transmission electron microscope (BF-TEM) imaging was used to investigate the morphology of the NDI nanowire suspensions drop-cast on copper grids. A representative TEM image of NDI-3TH NWs is shown in Figure 5.2a. The NDI-3TH nanostructures are seen to have well-defined 1D nanowire morphology with 80-250 nm (average 168 ± 45 nm) width and 2-10 μm length as measured from the magnified image shown in Figure 5.2b. To obtain the thickness of NDI-3TH NWs, a diluted suspension of NWs was spin-coated on top of silicon wafer and an AFM height image was obtained (Figure 5.2c). An average thickness of 14.2-15.3 nm was measured for the NDI-3TH NWs, indicating these NDI-3TH nanowires are actually belt-like.

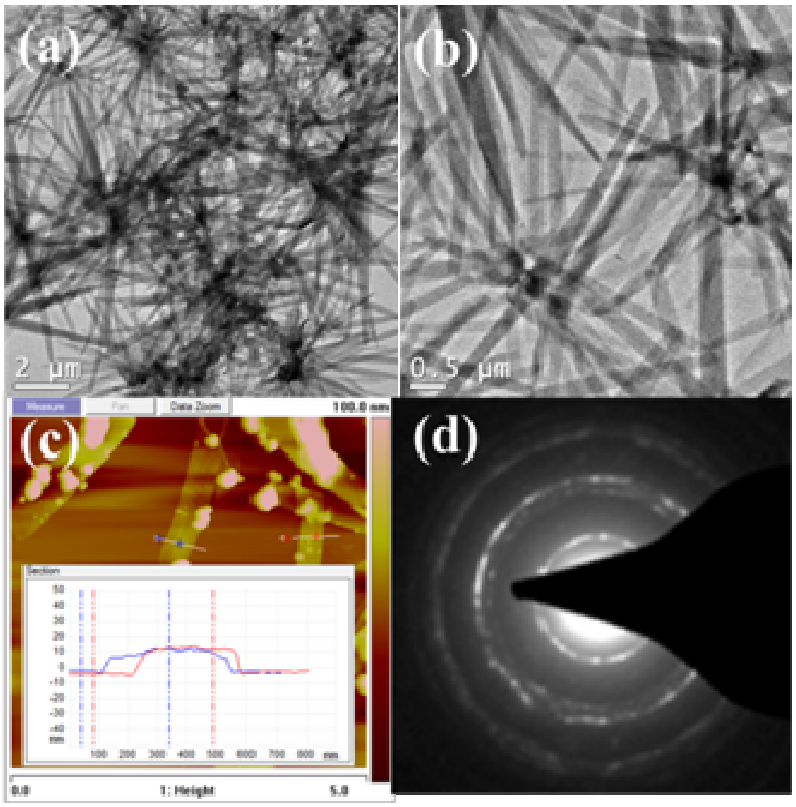

Figure 5.2 TEM images of pure block copolymer nanowire films.

The selected area electron diffraction (SAED) pattern of a collection of NDI-3TH NWs showed three strong Debye-Scherrer diffraction rings, corresponding to *d*-spacings of 0.90 nm, 0.46 nm and 0.34 nm, respectively. (Figure 5.2d) We note that the *d*-spacing of 0.34 nm matches the observed slipped π-stacking distance (*d*-spacing of 0.335 nm) between two NDI-3TH molecules along the *a*-axis in the single-crystal X-ray diffraction structure.[47] This confirms the fact that the formation of NDI-3TH NWs is driven by π-stacking. The *d*-spacing distance of 0.90 nm is very close to the distance of b/2 (b = 1.8779(3) nm).[47] However, further attempt to determine the molecular packing details of these NDI-3TH NWs failed due to the inability to obtain single-wire SAED pattern and the significant electron beam damage of the nanowires.

Nevertheless, these NDI-3TH NWs are highly crystalline in nature and may be beneficial for device applications.

The effects of solution concentration and the amount of non-solvent added on the morphology of NWs were also explored (Figure 5.3). NDI-3TH NWs prepared from 5 mg/mL NDI-3TH solution (with 0.3 mL methanol added into 1 mL solution) had width of 250 – 600 nm, and these NWs appeared polycrystalline as observed from both TEM image and the SAED (Figure 5.3a). NWs prepared from 1 mg/mL NDI-3TH solution in DCM with high methanol addition (0.6 mL methanol added to 1 mL solution) showed even broader width range of 100 nm – 1500 nm, with polycrystalline morphology (Figure 5.3b). In both cases, these NWs are bundled together and are hard to separate from each other. We note that the morphology of NDI NWs assembled via solvent exchange is largely dependent on the assembly conditions, as contrasted with polymer NWs assembled from solution-phase self-assembly whose morphology is usually insensitive to temperature and concentrations.[40, 60] We also note that the large difference in the morphology of NDI NWs obtained under different conditions is likely to affect their optical and photovoltaic properties.

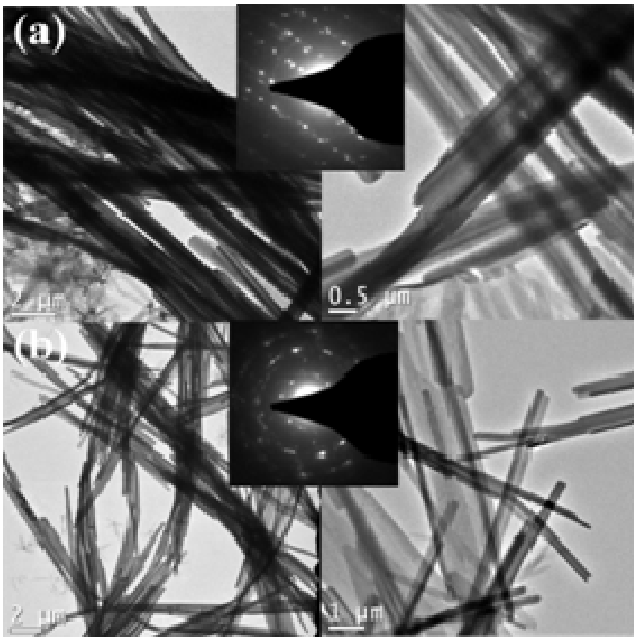

Figure 5.3 TEM images of NDI-3TH nanowires obtained at different conditions. (a) NDI-3TH nanowires obtained from 5 mg/mL NDI-3TH solution (0.3 mL methanol was added into 1 mL NDI-3TH/DCM solution). (b) NDI-3TH nanowires obtained from 1 mg/mL NDI-3TH solution with excessive methanol (0.3 mL methanol added to 0.5 mL NDI-3TH solution in DCM).

Nanowires of other NDI-nTH and NDI-nT materials were assembled by following the same approach as described above for NDI-3TH NWs and TEM images of NDI-2TH (Figure 5.4a), NDI-4TH (Figure 5.4b), NDI-2T (Figure 5.5a), NDI-3T (Figure 5.5b), and NDI-4T (Figure 5.5c) were recorded. The width of NDI-2TH and NDI-4TH NWs are 0.5 – 1.0 μm and 160 nm – 560 nm, respectively. In the case of NDI-nT NWs, the width varied from 80 – 660 nm in NDI-2T NWs to 180 – 500 nm in NDI-4T NWs. In the case of NDI-3T, although NWs with sharp needles are commonly observed, a rare nanosheet with width larger than 3 μm is seen as well. Based on the TEM images of these NDI NWs, we conclude that the size of oligothiophene unit appended to the naphthalene diimide core also plays a critical role in the control of the morphology of assembled nanostructures.

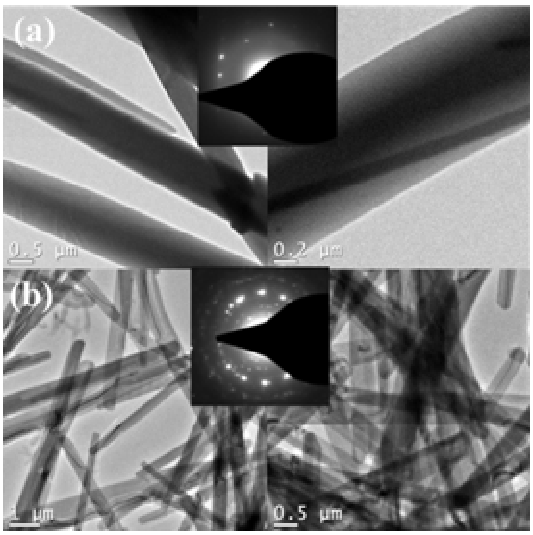

Figure 5.4 TEM images of NDI-nTH nanowires and their SAED (inset). (a) NDI-2TH; (b) NDI-4TH.

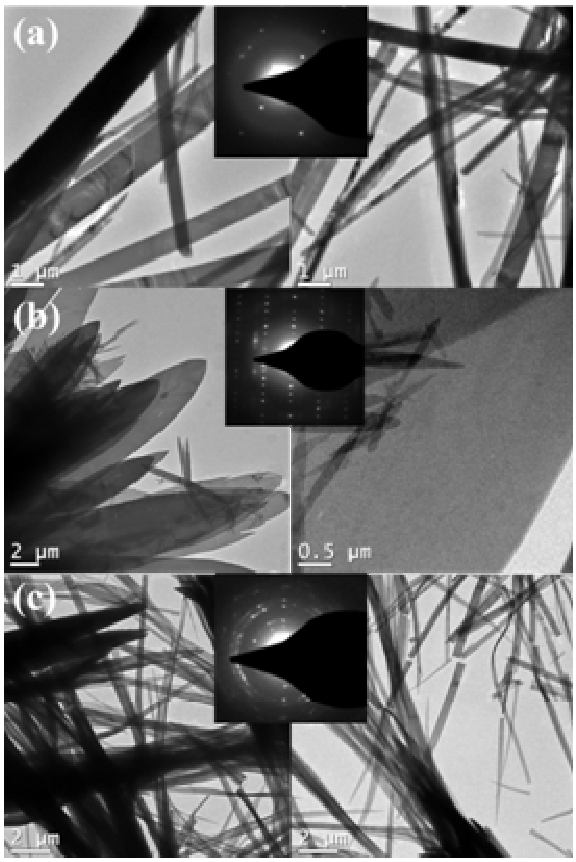

Figure 5.5 TEM images of NDI-nT nanowires and SAED (inset). (a) NDI-2T; (b) NDI-3T; (c) NDI-4T.

5.3.2 Assembly of Poly(3-hexylthiophene) Nanowires. To prepare poly(3-hexylthiophene) (P3HT) NWs, we adopted the whisker method by which polymer semiconductor nanowires with well-defined morphology can be readily assembled from a selective marginal solvent.[61] At elevated temperature (80 ^{o}C), the solvent is a good solvent for the polymer and polymer solution can be made. Upon cooling, the solvent becomes a poor solvent for the polymer and nanowires self-assemble spontaneously in solution. The P3HT nanowires assembled in this way have typical dimensions of ~15-18 nm in width, 3-7 nm in thickness, and >10 μm in length.[10]

5.3.3 Optical Properties. We used optical absorption spectroscopy to characterize the optical properties of the NDI-nTH and NDI-nT NWs. The normalized absorption spectra of NDI-3TH solution in DCM, neat thin film, suspension of NWs in DCM/methanol, and thin film of NWs are compared in Figure 5.6a. Two absorption peaks (~380 nm and 610 nm) are observed in the UV-vis spectrum of NDI-3TH in dilute DCM solution (~1×10^{-6} mol/L), and they are respectively red-shifted to 400 nm and ~680 nm in the thin film. The absorption intensity of the low-energy band in the range of 600 – 800 nm significantly increases in the solid state, indicating strong π-π stacking between NDI molecules. When NWs are formed, both the high-energy and low-energy absorption peaks in the absorption spectra of the nanowire suspension and nanowire film are further red-shifted compared with those of the NDI-3TH neat film. The relative intensity of the low-energy band to that of the high-energy band in the nanowire suspension and nanowire film increases to near unity, indicating enhanced ability to absorb photons of the solar spectrum. The increase in the absorption intensity of low-energy band may be attributed to the increased molecular order and preferential molecular alignment in NWs.

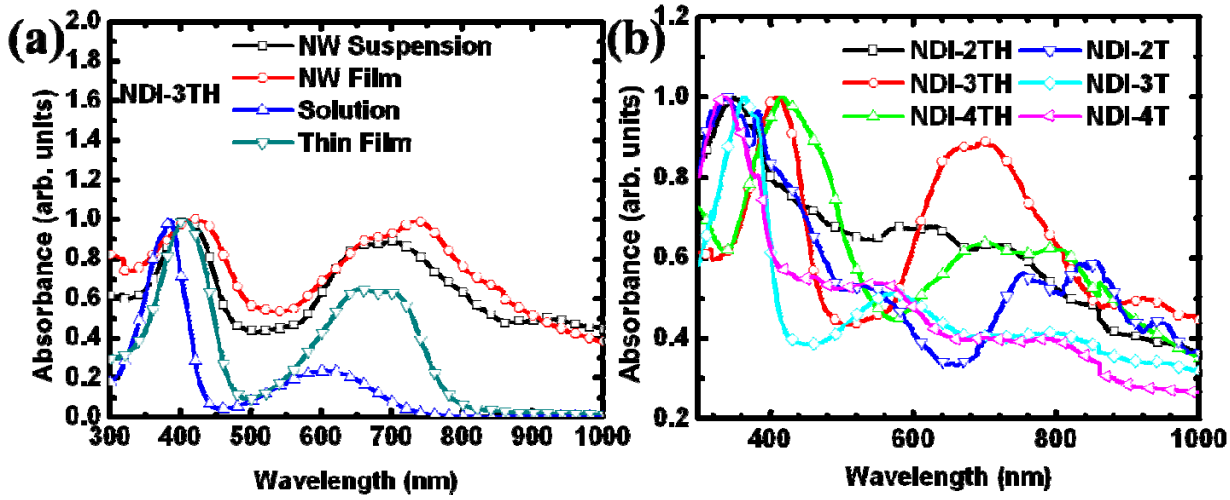

Figure 5.6 (a) Optical absorption spectra of NDI-3TH: nanowire suspension in DCM/methanol, nanowire film, thin film and solution (~1×10^{-6} mol/L) in DCM. (b) Optical absorption spectra of nanowire suspensions of various NDI materials in DCM/methanol.

The absorption spectrum of suspensions of NWs of each NDI-nTH and NDI-nT is summarized in Figure 5.6b and the spectra are normalized with respect to the high-energy peak in the range of 340 – 410 nm. In the case of NDI-nTH NWs, the high-energy absorption peak is in the 340 to 410 nm region. This high-energy peak red-shifts from 340 nm in NDI-2TH NWs, to 400 nm in NDI-3TH NWs and 410 nm in NDI-4TH NWs, respectively. In the case of NDI-nT NWs, the high-energy absorption peak ranges from 330 nm in both NDI-2T NWs and NDI-4T NWs to 360 nm in NDI-3T NWs. An additional absorption feature at ~380 nm shows up in the optical absorption spectrum of each NDI-nT nanowire suspension. A sharp peak is observed in the optical absorption spectrum of NDI-2T nanowire suspension, but the peak diminishes into an absorption shoulder in the absorption spectra of suspensions of NDI-3T NWs and NDI-4T NWs. The low-energy absorption peak above 600 nm varied significantly for NWs of each NDI material. In the 600 – 1000 nm spectral region, NDI-3T and NDI-4T NWs show similar absorption profile and

intensity, but NDI-2T NWs show much enhanced absorption with two peaks located at 760 and 860 nm. In the case of NDI-nTH NWs, their absorption intensity is generally higher than that of NDI-nT NWs. In particular, NDI-3TH NWs showed the most prominent absorption peak in the low-energy region. We note that the observed difference in the absorption spectra of NDI NWs may result from the different morphology (width and length) of NWs, in addition to the intrinsic absorption properties of the NDI molecules. We expect the observed difference in the absorption spectra of NWs of the series of NDI materials, especially the absorption bands in the low-energy region, will affect the photovoltaic properties of solar cells made from such NWs.

5.3.4 All-Nanowire Bulk Heterojunction Solar Cells. We fabricated and investigated all-nanowire bulk heterojunction (BHJ) solar cells comprised of P3HT NWs as the donor component and NDI NWs as the acceptor component. The device structure was: ITO/PEDOT:PSS (40 nm)/P3HT (15 nm)/active layer (~80 nm)/TPBI (3 nm)/Al (80 nm), where the P3HT and TPBI thin films acted as the electron-blocking and hole-blocking buffer layers, respectively, and the active layer was composed of P3HT NWs:NDI NWs (1:1 wt/wt) blend films. We note that the nanowire morphology of P3HT and NDI components of the active layer survived the blending as a suspension, as exemplified by the TEM images of the drop-cast P3HT NWs:NDI-3TH NWs blend thin films (Figure 5.7). Four unencapsulated solar cells with an area of 9 mm^2 each were fabricated and tested under AM1.5 solar illumination at 1 sun (100 mW/cm^2) in ambient air. The current density (J)–voltage (V) curves in the dark and under illumination are shown in Figure 5.8a for the P3HT NWs:NDI NWs devices. The photovoltaic parameters of the solar cells, including the open circuit voltage (V_{oc}), the short-circuit current density (J_{sc}), fill

factors (FF), and maximum/average power conversion efficiency (η, % PCE) are collected in Table 5.1.

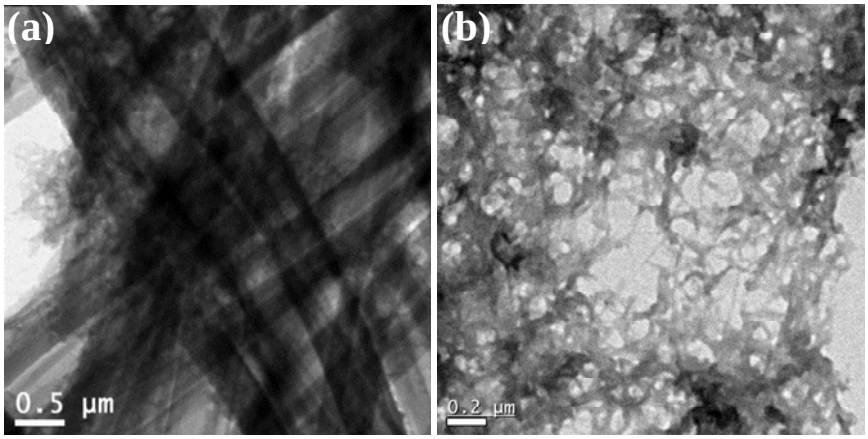

Figure 5.7 (a) Optical absorption spectra of NDI-3TH: nanowire suspension in DCM/methanol, nanowire film, thin film and solution (~1×10^{-6} mol/L) in DCM. (b) Optical absorption spectra of nanowire suspensions of various NDI materials in DCM/methanol.

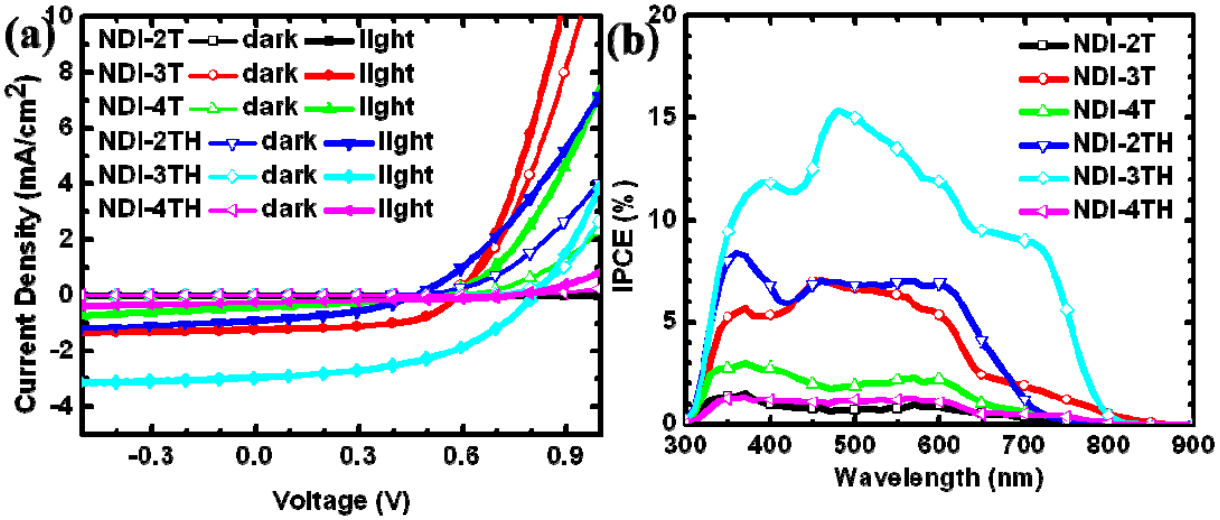

Figure 5.8 (a) Current density (*J*) – voltage (*V*) characteristics of P3HT NWs:NDI NWs solar cells, and (b) their corresponding EQE spectra.

Table 5.1 Photovoltaic Properties of P3HT NWs:NDI NWs BHJ Solar Cells

Acceptor*	V_{oc} (V)	J_{sc} (mA/cm^2)	FF	η_{max} (PCE %)	η_{ave} (PCE %)
NDI-2T	0.65	0.0076	0.20	0.001	0.001±0.000
NDI-3T	0.59	1.25	0.56	0.41	0.407±0.006
NDI-4T	0.52	0.44	0.33	0.075	0.069±0.007
NDI-2TH	0.47	0.89	0.41	0.17	0.12±0.03
NDI-3TH	0.81	2.95	0.48	1.15	1.11 ±0.05
NDI-4TH	0.74	0.27	0.37	0.07	0.05±0.02

* Solar cells were made from blends of P3HT NWs and NDI NWs with 1:1 wt:wt.

Among all the NDI NWs, NDI-3TH NWs and NDI-3T NWs showed the best photovoltaic properties. In the case of P3HT NWs:NDI-3TH NWs solar cells, a high V_{oc} of 0.81 V, J_{sc} of 2.95 mA/cm^2, and FF of 0.48 were observed, which translate to an average PCE of 1.11%. We note that this efficiency represents a 54% enhancement in photovoltaic efficiency compared with previously reported conventional BHJ blend film of P3HT:NDI-3TH with identical device structure (0.72% PCE).[10] The observed improved power conversion efficiency of the all-nanowire BHJ solar cells can be understood to result from a combination of factors, including the formation of a well-defined nanomorphology consisting of a bicontinuous, percolated nanowire network of donor and acceptor nanowires, increased surface area, and high crystallinity, which facilitate the charge separation, transport and collection.[11, 12, 37, 38] In the case of P3HT NWs:NDI-3T NWs photodiodes, an average PCE of 0.41% was calculated from a V_{oc} of 0.59 V, a J_{sc} of 1.25 mA/cm^2, and a FF of 0.56. Notably, NDI-2TH showed an average PCE of 0.12% in the all-nanowire BHJ solar cells whereas a photovoltaic effect was not observed in conventional P3HT:NDI-2TH BHJ solar cells due to the unusual macrophase-separated morphology with

dendritic NDI-2TH phase.[47] All-nanowire BHJ devices based on NDI-2T, NDI-4T, or NDI-4TH showed very poor photovoltaic efficiencies (<0.1% PCEs). The reason for the poor photovoltaic properties of some of these NDI-nT and NDI-nTH is probably because of ambipolar charge transport properties, which could make the majority carrier in some of them holes.[47] We note that the power conversion efficiency of the P3HT NWs:NDI NWs BHJ solar cells may be further improved by optimization of the electronic energy levels and electron mobility of the NDI molecules as well as via device optimization techniques such as solvent/thermal annealing and/or film aging.[12]

The external quantum efficiency (EQE) or action spectrum of each of the all-nanowire BHJ (P3HT NWs:NDI NWs) solar cell is presented in Figure 5.8b. A maximum EQE of 16% and 7% was obtained in the NDI-3TH NWs and NDI-3T NWs solar cells, respectively. The J_{sc} calculated by integration of the IPCE spectrum over the solar spectrum shows values of 2.79 mA/cm^2 and 1.13 mA/cm^2 for NDI-3TH NWs and NDI-3T NWs devices, respectively. The slight difference between the measured and calculated J_{sc} may be attributable to the spectral mismatch between the solar simulator and the actual solar spectrum, and the possible degradation of unencapsulated devices during measurement in air. The EQE spectrum of P3HT NWs:NDI-3TH NWs solar cells shows that photons with wavelength up to ~800 nm in the near-IR region of the solar spectrum are harvested; this clearly demonstrates that the non-fullerene acceptor, NDI NWs, harvests photons in the near IR and generates excitons which dissociate at the interface with P3HT NWs.

5.4 Conclusions

We have investigated the solution-phase self-assembly and morphology of nanowires of a series of 6 oligothiophene-functionalized naphthalene diimides (NDI-nTH and NDI-nT). Well-defined nanowires, whose size and detailed morphology varied with the molecular structure of the NDIs, the solution concentration, and solvent/non-solvent ratio, were successfully assembled. In the case of NDI-3TH, NWs with 80 – 250 nm width, 2 – 10 μm length, and 14.2 – 15.3 nm thickness were obtained. A comparison of the optical absorption spectra of neat thin films and nanowire films of NDI-3TH showed a significant red-shift and enhancement of intensity of the low energy absorption band (~600 nm) in the nanowire films, indicating a stronger molecular order in the nanowires. Bulk heterojunction (BHJ) solar cells made from blends P3HT NWs as the donor and NDI-3TH NWs as the acceptor showed a power conversion efficiency (PCE) of 1.15%, and a broad EQE spectrum ranging from 300 to 800 nm. Our results demonstrate, for the first time, that all-nanowire organic solar cells can be fabricated by using nanowires of p-type and n-type organic semiconductor as building blocks.

5.5 References

1. Coakley, K. M.; McGehee, M. D. *Chem. Mater.*, **2004**, *16*, 4533-4542.
2. Gunes, S.; Neugebauer, H.; Sariciftci, N. S. *Chem. Rev.*, **2007**, *107*, 1324-1338.
3. Blom, P. W. M.; Mihailetchi, V. D.; Koster, L. J. A.; Markov, D. E. *Adv. Mater.*, **2007**, *19*, 1551-1566.
4. Thompson, B. C.; Fréchet, J. M. J. *Angew. Chem. Int. Ed.*, **2008**, *47*, 58-77.
5. Dennler, G.; Scharber, M. C.; Brabec, C. J. *Adv. Mater.*, **2009**, *21*, 1323-1338.
6. Chen, L. M.; Hong, Z.; Li, G.; Yang, Y. *Adv. Mater.*, **2009**, *21*, 1434-1449.

7. Brunetti, F. G.; Kumar, R.; Wudl, F. *J. Mater. Chem.*, **2010**, *20*, 2934-2948.

8. Liang, Y.; Xu, Z.; Xia, J.; Tsai, S. T.; Wu, Y.; Li, G.; Ray, C.; Yu, L. *Adv. Mater.*, **2010**, *22*, E135−E138.

9. Small, C. E.; Chen, S.; Subbiah, J.; Amb, C. M.; Tsang, S.-W.; Lai, T.-H.; Reynolds, J. R.; So, F. *Nat. Photon.*, **2012**, *6*, 115-120.

10. Ren, G.; Ahmed, E.; Jenekhe, S. A. *Adv. Energy. Mater.*, **2011**, *1*, 946-953.

11. Ren, G.; Wu, P.-T.; Jenekhe, S. A. *ACS Nano*, **2011**, *5*, 376-384.

12. Xin, H.; Reid, O. G.; Ren, G.; Kim, F. S.; Ginger, D. S.; Jenekhe, S. A. *ACS Nano*, **2010**, *4*, 1861-1872.

13. Xin, H.; Subramaniyan, S.; Kwon, T.-W.; Shoaee, S.; Durrant, J. R.; Jenekhe, S. A. *Chem. Mater.*, **2012**, *24*, 1995–2001.

14. Subramaniyan, S.; Xin, H.; Kim, F. S.; Shoaee, S.; Durrant, J. R.; Jenekhe. S. A. *Adv. Energy. Mater.*, **2011**, *1*, 854-860.

15. Subramaniyan, S.; Xin, H.; Kim, F. S.; Jenekhe, S. A. *Macromolecules*, **2011**, *44*, 6245-6248.

16. Kietzke, T.; Hörhold, H.-H.; Neher, D. *Chem. Mater.*, **2005**, *17*, 6532-6537.

17. Holcombe, T. W.; Woo, C. H.; Kavulak, D. F. J.; Thompson, B. C.; Fréchet, J. M. J. *J. Am. Chem. Soc.*, **2009**, *131*, 14160-14161.

18. Bloking, J. T.; Han, X.; Higgs, A. T.; Kastrop, J. P.; Pandey, L.; Norton, J. E.; Risko, C.; Chen, C. E.; Brédas, J.-L.; McGehee, M. D.; Sellinger, A. *Chem. Mater.*, **2011**, *23*, 5484-5490.

19. Zhou, T.; Jia, T.; Kang, B.; Li, F.; Fahlman, M.; Wang, Y. *Adv. Energy. Mater.*, **2011**, *1*, 431-439.

20. Walker, B.; Han, X;. Kim, C.; Sellinger, A.; Nguyen, T.-Q. *ACS Appl. Mater. Interfaces*, **2011**, *4*, 244-250.

21. Yu, G.; Gao, J.; Hummelen, J. C.; Wudl, F.; Heeger, A. J. *Science*, **1995**, *270*, 1789-1791.

22. Yang, X.; Loos, J. *Macromolecules*, **2007**, *40*, 1353-1362.

23. Wang, D. H.; Moon, J. S.; Seifter, J.; Jo, J.; Park, J. H.; Park, O. O.; Heeger, A. J. *Nano Lett.*, **2011**, *11*, 3163-3168.

24. Nagarjuna, G.; Venkataraman, D. *J. Polym. Sci. B: Polym. Phys.*, **2012**, *50*, 1045–1056.

25. Liu, F.; Gu, Y.; Jung, J. W.; Jo, W. H.; Russell, T. P. *J. Polym. Sci. B: Polym. Phys.*, **2012**, *50*, 1018–1044.

26. Ma, W.; Yang, C.; Gang, X.; Lee, K.; Heeger, A. J. *Adv. Funct. Mater.*, **2005**, *15*, 1617-1622.

27. Li, G.; Shrotriya, V.; Huang, J.; Yao, Y.; Moriarty, T.; Emery, K.; Yang, Y. *Nat. Mater.*, **2005**, *4*, 864-868.

28. Erb, T.; Zhokhavets, U.; Hoppe, H.; Gobsch, G.; Al-Ibrahim, M.; Ambacher, O. *Thin Solid Films*, **2006**, *511−512*, 483-485.

29. Nguyen, L. H.; Hoppe, H.; Erb, T.; Gunes, S.; Gobsch, G.; Sariciftci, N. S. *Adv. Funct. Mater.*, **2007**, *17*, 1071-1078.

30. Ren, G.; Wu, P.-T.; Jenekhe, S. A. *Chem. Mater.*, **2010**, *22*, 2020-2026.

31. Peet, J.; Kim, J. Y.; Coates, N. E.; Ma, W. L.; Moses, D.; Heeger, A. J.; Bazan, G. C. *Nat. Mater.*, **2007**, *6*, 497-500.

32. Lee, J. K.; Ma, W. L.; Brabec, C. J.; Yuen, J.; Moon, J. S.; Kim, J. Y.; Lee, K.; Bazan, G. C.; Heeger, A. J. *J. Am. Chem. Soc.*, **2008**, *130*, 3619-3623.

33. Peet, J.; Senatore, M. L.; Heeger, A. J.; Bazan, G. C. *Adv. Mater.*, **2009**, *21*, 1521-1527.

34. Mayer, A. C.; Michael, F. T.; Shawn, R. S.; Jonathan, R.; Christoph, J. B.; Marcus, S.; Marcus, K.; Martin, H.; Iain, M.; Michael, D. M. *Adv. Funct. Mater.*, **2009**, *19*, 1173-1179.

35. Xin, H.; Guo, X.; Ren, G.; Watson, M. D.; Jenekhe, S. A. *Adv. Energy. Mater.*, **2012**, *2*, 575–582.

36. Berson, S.; Bettignies, R. D.; Bailly, S.; Guillerez, S. *Adv. Funct. Mater.*, **2007**, *17*, 1377-1384.

37. Xin, H.; Kim, F. S.; Jenekhe, S. A. *J. Am. Chem. Soc.*, **2008**, *130*, 5424-5542.

38. Xin, H.; Ren, G.; Kim, F. S.; Jenekhe, S. A. *Chem. Mater.*, **2008**, *20*, 6199-6207.

39. Salim, T.; Sun, S.; Wong, L. H.; Xi, L.; Foo, Y. L.; Lam, Y. M. *J. Phys. Chem. C*, **2010**, *114*, 9459-9468.

40. Kim, F. S.; Ren, G.; Jenekhe, S. A. *Chem. Mater.*, **2011**, *23*, 682-732.

41. Wu, P. T.; Xin, H.; Kim, F. S.; Ren, G.; Jenekhe, S. A. *Macromolecules*, **2009**, *42*, 8817-8826.

42. Botiz, I.; Darling, S. B. *Macromolecules*, **2009**, *42*, 8211-8217.

43. Wu, P. T.; Ren, G.; Li, C.; Mezzenga, R.; Jenekhe, S. A. *Macromolecules*, **2009**, *42*, 2317-2320.

44. Wu, P. T.; Ren, G.; Kim, F. S.; Li, C.; Mezzenga, R.; Jenekhe, S. A. *J. Polym. Sci., A: Polym. Chem.*, **2010**, *48*, 614-626.

45. Sonar, P.; Lim, J. P. F.; Chan, K. L. *Energy Environ. Sci.*, **2011**, *4*, 1558-1574.

46. Anthony, J. E. *Chem. Mater.*, **2011**, *23*, 583-590.

47. Ahmed, E.; Ren, G.; Kim, F. S.; Hollenbeck, E. C.; Jenekhe, S. A. *Chem. Mater.*, **2011**, *23*, 4563–4577.

48. Jenekhe, S. A.; Yi, S. *Appl. Phys. Lett.*, **2000**, *77*, 2635-2637.

49. Alam, M. M.; Jenekhe, S. A. *Chem. Mater.*, **2004**, *16*, 4647-4656.

50. Zhou, E.; Cong, J.; Wei, Q.; Tajima, K.; Yang, C.; Hashimoto, K. *Angew. Chem. Int. Ed.*, **2011**, *50*, 2799-2803.

51. He, X.; Gao, F.; Tu, G.; Hasko, D.; Hüttner, S.; Steiner, U.; Greenham, N. C.; Friend, R. H.; Huck, W. T. S. *Nano Lett.*, **2010**, *10*, 1302-1307.

52. Holcombe, T. W.; Norton, J. E.; Rivnay, J.; Woo, C. H.; Goris, L.; Piliego, C.; Griffini, G.; Sellinger, A.; Brédas, J.-L.; Salleo, A.; Fréchet, J. M. J. *J. Am. Chem. Soc.*, **2011**, *133*, 12106-12114.

53. Schubert, M.; Dolfen, D.; Frisch, J.; Roland, S.; Steyrleuthner, R.; Stiller, B.; Chen, Z.; Scherf, U.; Koch, N.; Facchetti, A.; Neher, D. *Adv. Energy. Mater.*, **2012**, *2*, 369-380.

54. Briseno, A. L.; Mannsfeld, S. C. B.; Shamberger, P. J.; Ohuchi, F. S.; Bao, Z.; Jenekhe, S. A.; Xia, Y. *Chem. Mater.*, 2008, **20**, 4712-4719.

55. Dittmer, J. J.; Marseglia, E. A.; Friend, R. H. *Adv. Mater.*, **2000**, *12*, 1270-1274.

56. Schmidt-Mende, L.; Fechtenkötter, A.; Müllen, K.; Moons, E.; Friend, R. H.; MacKenzie, J. D. *Science*, **2001**, *293*, 1119-1122.

57. Li, J.; Dierschke, F.; Wu, J.; Grimsdale, A. C.; Müllen, K. *J. Mater. Chem.*, **2006**, *16*, 96-100.

58. Schwenn, P. E.; Gui, K.; Nardes, A. M.; Krueger, K. B.; Lee, K. H.; Mutkins, K.; Rubinstein-Dunlop, H.; Shaw, P. E.; Kopidakis, N.; Burn, P. L.; Meredith, P. *Adv. Energy. Mater.*, **2011**, *1*, 73-81.

59. Karak, S.; Ray, S. K.; Dhar, A. *Appl. Phys. Lett.*, **2010**, *97*, 043306-043303.

60. Liu, J.; Arif, M.; Zou, J.; Khondaker, S. I.; Zhai, L. *Macromolecules*, **2009**, *42*, 9390-9393.

61. Ihn, K. J.; Moulton, J.; Smith, P. *J. Polym. Sci., Part B*, **1993**, *31*, 735-742.

Chapter 6 All-Polymer Bulk Heterojunction Solar Cells

6.1 Introduction

The morphology of organic bulk heterojunction (BHJ) solar cells plays a critical role in maximizing the power conversion efficiency of the blend devices.[1-5] Characterization of the morphology of BHJ polymer thin films with high spatial resolution, high chemical specificity and sensitivity, however, remains an important challenge for fully understanding the photovoltaic performance of BHJ polymer solar cells. Among the limited techniques currently employed to investigate the morphology of BHJ polymer films, bright-field transmission electron microscopy (BF-TEM),[3,6] energy-filtered TEM (EFTEM),[7,8] scanning transmission electron microscopy (STEM),[9] and electron tomography,[10] have been extensively used to varying degrees of success. Each of these techniques has its own drawbacks that prevent a complete understanding of the morphology of organic photovoltaic systems. BF-TEM shows low phase contrast for organic materials at focusing condition due to low mass-thickness and diffraction contrast resulting from the low density of the materials.[11] Although the contrast can be enhanced by defocusing, the size of the features in the resulting images can change and sometimes the phase contrast can be reversed.[11] EFTEM provides a better phase contrast at focusing condition by generating contrast using differences in the energy-loss spectra of the pure components, but it suffers from a low signal-to-noise ratio arising from the low yield of inelastically scattered electrons.[9,11] STEM utilizing a high-angle annular dark field (HAADF) detector is capable of providing atomic resolution images with excellent elemental contrast better than BF-TEM due to

atomic-number-related Z-contrast,[12] but it is unable to accurately distinguish the phase distribution within a blend film with high chemical specificity and sensitivity. Electron tomography, which when coupled with S/TEM can enable 3D reconstruction of morphology, is limited by the associated electron microscopy.[9,10,13] Although non-electron microscopy based imaging techniques such as atomic force microscopy (AFM) are related scanning probe techniques have high spatial resolution they are limited to surface imaging. Scanning near-field optical microscopy (SNOM) on the other hand has low spatial resolution and thus cannot resolve information about bulk films at high resolution.[14]

Energy dispersive X-ray spectroscopy (EDS) is a widely used microanalysis technique in electron microscopy.[15] In STEM, when the high energy electron beam interacts with the sample, the inelastic scattering of the incident electrons leads to two classes of X-rays – Bremsstrahlung and characteristic radiation. Bremsstrahlung or braking radiation is a result of deceleration of the incident electrons caused by the Coulombic field of the atoms (both nucleus and electrons) and therefore constitutes the continuous electromagnetic spectrum (background radiation).[15] The characteristic X-ray radiation, which is emitted by deactivation of excited atom due to inner-shell ionization by ejection of a bound electron can be used to identify the corresponding element. The spatial resolution of EDS is largely defined by a bell-shaped interaction volume in bulk sample. However, in S/TEM analysis, due to the small thickness of the specimen (~100 nm) and the high acceleration voltage (100-200 kV), the spatial resolution is only limited by the size of the microprobe (electron beam).[15] This can enable high resolution imaging using EDS. The coupling of HAADF-STEM with EDS could in principle facilitate the combination of the high spatial

resolution (sub-nanometer) of STEM with the high chemical specificity and sensitivity of EDS analysis. The combination of STEM, EDS, and EFTEM techniques was recently used to study the morphology of aged poly(3-hexylthiophene)/fullerene (P3HT/$PC_{61}BM$) blend solar cells.[16] EDS performed on the cross-sectioned blend film was used as an elemental analysis tool to generate line profile of elemental distribution (such as sulfur, carbon, oxygen, and metals) in the vertical direction of the active layer. The relative abundance of sulfur and carbon was compared in different vertical positions and the diffusion of electrode materials (ytterbium) into the active layer was investigated. Discrete maps of sulfur and carbon were obtained based on zero-loss peak filtered EFTEM but not by EDS mapping.[16] The great potential to use EDS to achieve high spatial resolution and high chemical specificity imaging of bulk heterojunction polymer solar cells thus remains to be explored.

In this work, we propose and demonstrate the use of energy dispersive X-ray spectroscopy (EDS) coupled with HAADF-STEM in characterizing the blend morphology of BHJ polymer solar cells with high spatial resolution and high chemical specificity for the first time. The BHJ polymer blend devices investigated are composed of poly[(4,4'-bis(3-(2-ethyl-hexyl)dithieno[3,2-b:",3'-d]silole)-2,6-diyl-alt-(2,5-bis(3-(2-ethyl-hexyl)thiophen-2yl)thiazolo[5,4-d]thiazole)] (PSEHTT) donor[17] and poly[[N,N'-bis(2-decyltetradecyl)naphthalene-1,4,5,8-bis(dicarboximide)-2,6-diyl]-alt-5,5'-(2,2' -biselenophene)] (PNDIBS) acceptor.[18,19] The molecular structures and HOMO/LUMO energy levels of these conjugated polymers are shown in Figure 6.1. The photovoltaic properties of the all-polymer BHJ solar cells were investigated as a function of blend composition, showing that

the optimum composition was 1:2 PSEHTT:PNDIBS weight ratio. For comparison purposes we also investigated the morphology of the PSEHTT:PNDIBS BHJ blends by conventional imaging techniques of AFM, TEM, and STEM. High spatial resolution EDS images of the PSEHTT:PNDIBS BHJ blends were obtained by use of ImageJ software to analyze the sulfur- and selenium-distribution maps as a function of blend composition.

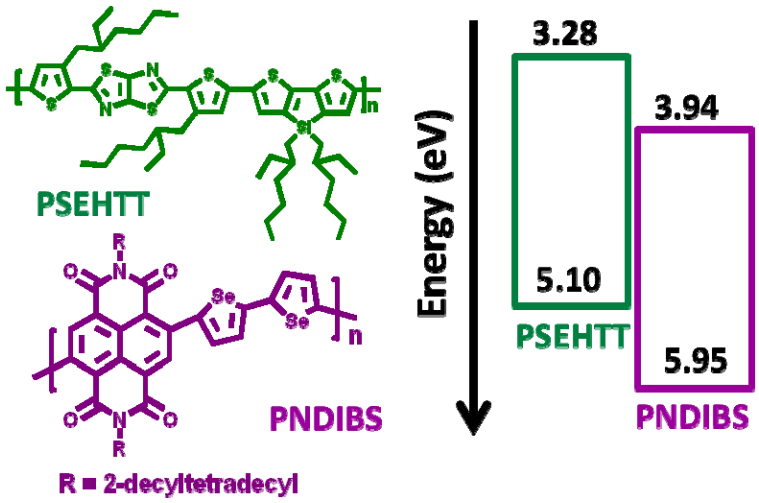

Figure 6.1 Molecular structures and energy level diagram of PSEHTT and PNDIBS.

6.2 Experimental Section

6.2.1 Materials.

The synthesis of the donor polymer PSEHTT[17] (M_n = 33.9 kDa, PDI = 3.9) and the acceptor polymer PNDIBS[18] (M_n = 42.4 kDa, PDI = 2.6) were previously reported and their HOMO/LUMO energy levels were determined by cyclic voltammetry.[17,18] Anhydrous chlorobenzene (99.8%) was obtained from Sigma Aldrich and used without further purification. Aluminum shots and LiF were purchased from Sigma Aldrich.

Poly(3,4-ethylenedioxythiophene):Poly(styrenesulfonate) (PEDOT:PSS) (Clevios P VP AI 4083, Heraeus) was passed through a 0.45 μm filter before use.

6.2.2 Fabrication and Characterization of Solar Cells.

PSEHTT and PNDIBS solutions in chlorobenzene (10 mg mL^{-1}, respectively) were prepared, stirred until complete dissolution and filtered with 0.45 μm syringe filter.

Solar cells with the device structure of ITO/PEDOT:PSS/active layer/LiF/Al were fabricated. ITO substrates (10 Ω/□, Shanghai B. Tree Tech. Consult Co., Ltd, Shanghai, China) were cleaned sequentially with acetone, deionized water and isopropyl alcohol in an ultrasonic bath, and blown with nitrogen until dried. A 40 nm PEDOT:PSS layer was spin-coated on top of the ITO and dried at 150 °C for 10 min under vacuum. The active layer was then spin-coated from PSEHTT:PNDIBS blend solutions with different ratios to make a thin film of ~110 nm thickness and thermally annealed at 150 °C for 10 min in a glovebox. The substrates were then loaded in a thermal evaporator (BOC Edwards, 306) to deposit a cathode composed of 1.0 nm LiF and 90 nm Al under high vacuum (8×10^{-7} Torr). Five solar cells, each with an active area of 4 mm^2, were fabricated per ITO substrate.

The current density–voltage (*J*–*V*) curves of the solar cells were measured using a HP4155A semiconductor parameter analyzer under laboratory ambient air conditions. An AM1.5 illumination at 100 mW/cm^2 was provided by a filtered Xe lamp and calibrated by using an NREL-calibrated Si photodiode. The external quantum efficiency (EQE) was measured by using a QEX10 solar cell quantum efficiency measurement system (PV Measurements, Inc.) and was calibrated with a NREL-certified Si photodiode before measurement.

6.2.3 Characterization of Morphology.

Atomic force microscopy (AFM) imaging (5 × 5 μm area) was done using a Dimension 3100 SPM (Veeco) instrument operating in tapping mode. To obtain a thin film of the active layer for scanning/transmission electron microscope (S/TEM) imaging, the substrate was first scratched and then soaked in deionized water. The active layer was then peeled-off from the substrate, supported on a TEM grid (300 mesh, Electron Microscopy Sciences, Inc.), and dried. An FEI Tecnai G^2 F20 S/TEM operated at 200 kV was employed for imaging. For the bright-field TEM (BF-TEM) imaging, images were slightly defocused to enhance the phase contrast between the two polymers, and were acquired with a CCD camera and recorded with Gatan DigitalMicrograph software. For STEM imaging, a high angle annular dark field (HAADF) detector (point resolution: 0.18nm) was used and images were acquired at proper focus with TEM Imaging & Analysis (TIA) software. To perform the elemental mapping of selenium and sulfur, an energy-dispersive X-ray spectroscopy (EDS) was used to record a drift corrected spectrum image for each blend thin film (dwell time of 250 ms). An ImageJ software (National Institutes of Health, USA, version 1.46r)[20] was used for the image analysis and processing. Phase distribution maps were obtained from the EDS maps by adjusting the color threshold using the MinError threshold method which assumes the shade level of objects follows a normal distribution and removes the corresponding background.[20] EDS map of sulfur in P3HT:PC_{71}BM (1:1 wt/wt) blend film was acquired and processed in a similar way.

6.3 Results and Discussion

6.3.1 Bulk Heterojunction (BHJ) Solar Cells.

We investigated the blend composition dependence of the photovoltaic properties of the all-polymer BHJ solar cells by fabricating devices with the structure ITO/PEDOT:PSS/blend/LiF/Al and PSEHTT:PNDIBS blends with weight ratios of 1:1, 1:2, and 1:3. The solar cells were tested under AM1.5 solar illumination at 1 Sun (100 mW/cm^2) in ambient air. The current density (J) – voltage (V) curves of these devices are shown in Figure 6.2a. The photovoltaic parameters, including the open circuit voltage (V_{oc}), the short-circuit current density (J_{sc}), and fill factors (FF), are collected in Table 1. The average power conversion efficiency (PCE) is found to be 0.64±0.02%, 1.58±0.03%, and 0.93±0.03% for PSEHTT:PNDIBS blend ratios of 1:1, 1:2, and 1:3, respectively. The variation of the PCE with blend composition is largely due to the blend composition dependence of J_{sc} and FF since the V_{oc} is unchanged. A maximum 1.62% PCE was obtained from the 1:2 blend devices. The external quantum efficiency (EQE) spectra of the PSEHTT:PNDIBS devices (Figure 6.2b) show that the photoresponse begins at near 900 nm for each of the blend. The maximum EQE of 11.4-19.2% was reached in the 590 – 640 nm wavelength range. The J_{sc} calculated by integrating the EQE spectrum over the AM1.5G solar spectrum is 1.63 mA/cm^2, 3.38 mA/cm^2, and 2.31 mA/cm^2, respectively for the 1:1, 1:2, and 1:3 blends. Possible reasons for the 4-7% difference between the directly measured J_{sc} under simulated illumination and those calculated from the EQE spectrum include a spectral mismatch between simulated illumination and AM1.5G solar spectrum and degradation of devices during measurement in ambient air. These results clearly

show that the best photovoltaic properties are obtained at the 1:2 PSEHTT:PNDIBS blend weight ratio.

Table 6.1 Photovoltaic and Electrical Properties of PSEHTT:PNDIBS Blend Solar Cells.

Blend [wt/wt][a)]	Rectification Ratio[b)]	r_s [Ωcm^2]	r_p [Ωcm^2]	V_{oc} [V]	J_{sc} [mA/cm^2]	FF	PCE_{max} [%]	PCE_{ave} [%][c)]
1:1	132	81	1250	0.76	1.75	0.50	0.66	0.64±0.02
1:2	496	29	1240	0.77	3.58	0.59	1.62	1.58±0.03
1:3	270	50	1400	0.77	2.41	0.52	0.96	0.93±0.03

[a)] PSEHTT:PNDIBS blend film processed from chlorobenzene; [b)] Rectification ratio calculated at ±2 V; [c)] PCE values averaged from 5 devices.

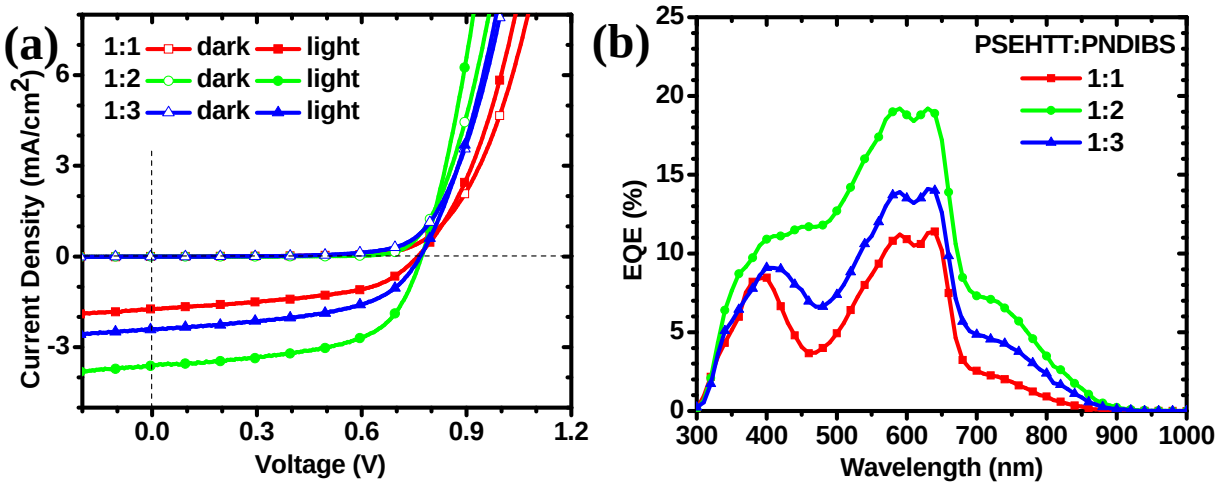

Figure 6.2 (a) Current density (J) – voltage (V) characteristics of PSEHTT:PNDIBS blend solar cells with different blend ratios and (b) their corresponding EQE spectra.

The observed 1.62% PCE in the all-polymer PSEHTT:PNDIBS BHJ solar cells represents an 84% improvement in performance compared to similar all-polymer BHJ devices based on PNDIBS acceptor and poly(3-hexylthiophene) (P3HT) donor.[18] Among the likely reasons for the superior performance of PSEHTT/PNDIBS BHJ devices compared to similar P3HT/PNDIBS devices include the better near infrared absorption of PSEHTT, high hole mobility (0.03 cm^2/V

s),[17] and its generally more crystalline morphology.[21] We also note that the present photovoltaic efficiency (1.62% PCE) is among the highest achieved so far for all-polymer BHJ solar cells based on various naphthalene diimide-based copolymer acceptors. [14,18,22-25]

6.3.2 Morphology via AFM and TEM

We investigated the morphology of PSEHTT:PNDIBS blend films using the conventional techniques of atomic force microscopy (AFM) and transmission electron microscopy (TEM). Figure 6.3 shows the topographical and phase images obtained by scanning 5 μm × 5 μm areas of the actual BHJ solar cells. The AFM height images of all the PSHETT:PNDIBS blend films clearly show a two-phase morphology reminiscent of one obtained by a spinodal decomposition.[26] The surface roughness (R_a) decreases from 11.4 nm to 5.17 nm as the amount of PNDIBS in the blend is increased from 50 wt% (1:1) to 75 wt% (1:3). The decrease in surface roughness is a result of the decrease in the size of the bright domains, which constitute the elevated phase and have widths varying from 200 – 500 nm in the 1:1 blend to 50 – 300 nm in the 1:3 blend. The bright domains can be assigned to the PSEHTT-rich phase while the dark domains or valleys are thus assigned to the PNDIBS-rich phase, as will be confirmed later by transmission electron microscopy. In the phase images of the blend films (Figure 6.3b), a clear microscale phase separated film is observed on the same scale as that of corresponding height image and dense polymer nanofibrils with width of 20-35 nm are visible. Although these AFM images show high spatial resolution in both topographical and phase images of the surface, it is difficult to assign the phase information by itself and of course the imaging is only limited to the

surface whereas morphological information about the bulk film is more relevant for understanding BHJ solar cells.

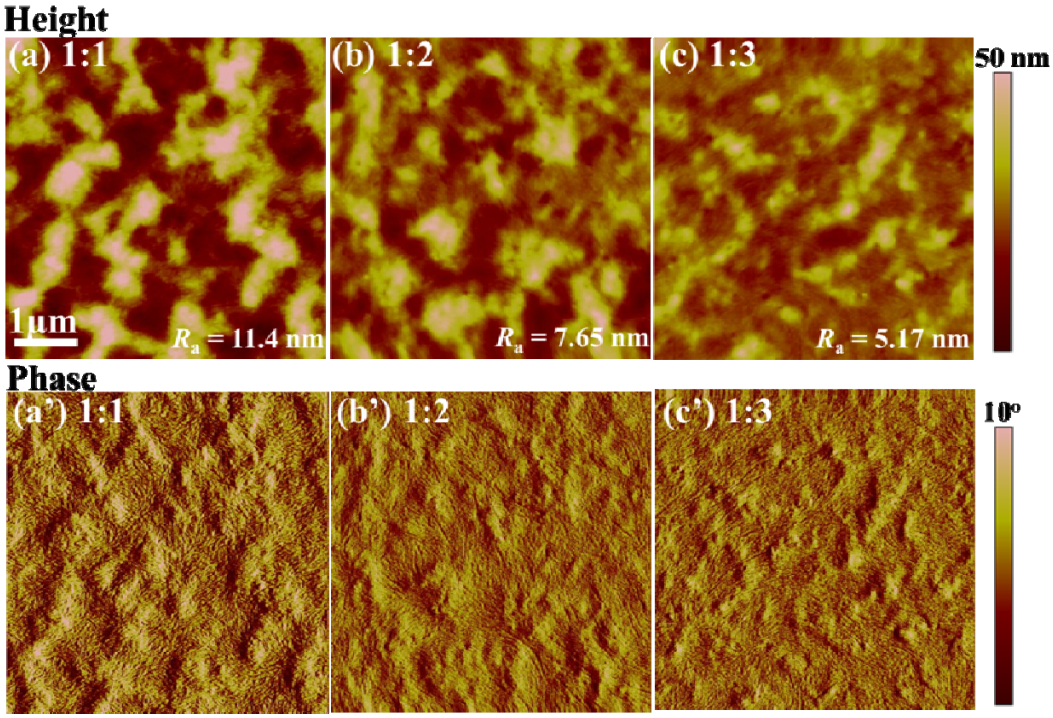

Figure 6.3 AFM height and phase images of PSEHTT:PNDIBS blend films with different blend ratios.

Figure 6.4 shows bright-field transmission electron microscope (BF-TEM) images of the PSEHTT:PNDIBS blend films directly peeled off from the solar cells. The images were taken at a slightly defocused condition to enhance the phase contrast between the two polymers without the occurrence of phase reversal. Based on the facts that phases with higher density appear darker than those with lower density[6] and PSEHTT tends to form aggregated domains, we tentatively assign the dark domains to PSEHTT and bright domains to PNDIBS. The TEM image of PSEHTT:PNDIBS (1:1) shown in Figure 6.4a displays dense PSEHTT domains with widths of 200 – 500 nm and lengths of 0.5 to several μm. As the PSEHTT concentration in the blend is

decreased, PSEHTT domain size gets smaller, indicating a higher uniformity and better mixing in the blend film. However, the phase contrast between PSEHTT and PNDIBS diminishes, resulting in poor spatial resolution that prevents a better understanding of the phase separation in the blend films. This is especially the case of the 1:2 blend ratio found to give optimum photovoltaic performance. Moreover, the contrast in BF-TEM as a result of density difference is not a characteristic of specific material because of the possibility that a mixed phase may exist in the blend.[27]

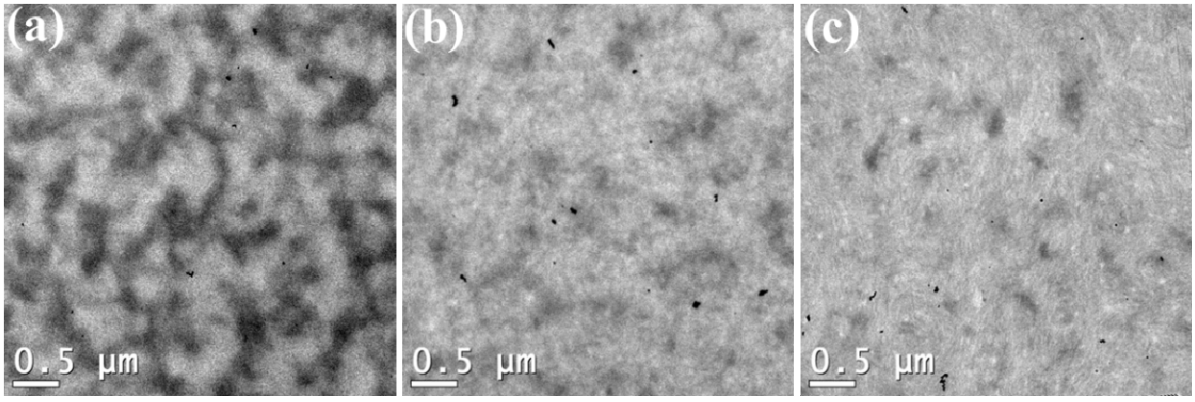

Figure 6.4 TEM images of PSEHTT:PNDIBS blend films with different blend ratios: (a) 1:1; (b) 1:2; and (c) 1:3.

We used X-ray diffraction (XRD) to examine whether PSEHTT and PNDIBS formed crystalline domains in the blend films (Figure 6.5). A single weak (100) diffraction peak (d ~ 2.09 nm), which lies between those characteristic of the lamellar structures of pure PSEHTT (d = 1.65 nm)[17] and pure PNDIBS (d = 2.595 nm),[18] was observed. The observed XRD patterns of PSEHTT:PNDIBS blend films are in contrast to those of crystalline conjugated diblock copolymers[28] and other binary blends of conjugated polymers such as P3HT and poly(9,9-dioctylfluorene-co-benzothiadiazole) (F8BT),[29] in which two distinct lamellar

crystalline (100) peaks of the pure polymers were seen. A possible reason for the observed single diffraction peak in the binary blend films is the formation of a miscible phase of PSEHTT and PNDIBS with an intermediate *d*-spacing. Similar XRD pattern as evidence of miscibility in binary blends of rigid-rod polymers with flexible side chains that form lamellar crystalline structures are known in the literature.[30,31]

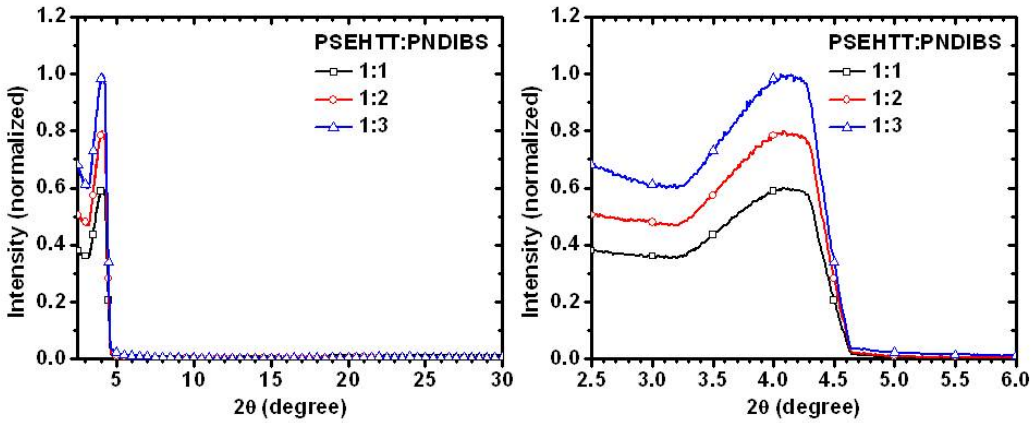

Figure 6.5 XRD spectra of PSEHTT:PNDIBS blend films taken from actual devices. Blend ratios. (a) 1:1, 2θ = 4.22°, *d* = 2.092 nm 1:2, 2θ = 4.23°, *d* = 2.087 nm; (c) 1:3, 2θ = 4.22°, *d* = 2.092 nm.

6.3.3 Scanning Transmission Electron Microscopy (STEM) and Energy Dispersive X-ray Spectroscopy (EDS)

We have used a combination of high-angle annular dark-field scanning TEM (HAADF-STEM) and energy dispersive spectroscopy (EDS) to investigate the morphology of PSEHTT:PNDIBS blend films to overcome the disadvantages of conventional AFM and BF-TEM imaging (low spatial resolution and poor chemical specificity). The combination of these two techniques (STEM and EDS) allows us to simultaneously image the nanomorphology and map the chemical composition in the *same* area of interest. Representative HAADF-STEM

images of PSEHTT:PNDIBS blend films of various compositions are shown in Figure 6.6a-c. The PNDIBS domains appear dark and PSEHTT domains appear bright in the dark-field STEM images of Figure 6.6a-c in contrast to the BF-TEM images shown in Figure 6.4. PSEHTT and PNDIBS have similar domain sizes of width of 200 – 500 nm in the 1:1 blend. The bright PSEHTT domains decreased significantly in size to 50 – 200 nm and were uniformly distributed in the PNDIBS phase as the blend composition was changed to 1:3. Although these STEM images (Figure 6.6a-c) are grey-scaled images similar to BF-TEM images, they show better contrast with distinct two-phase morphology due to atomic-number-related Z-contrast.[11] However, definitive assignment of the phase distribution of each polymer in the blend and the possibility of a miscible phase cannot be made based solely on STEM imaging.

Elemental mapping by EDS analysis of selected areas in each STEM image (marked with square) was performed to further identify the nanoscale phase distribution of each polymer in the PSEHTT:PNDIBS blends. The characteristic K-shell X-rays from sulfur (S) and selenium (Se), which are found respectively in PSEHTT and PNDIBS, were monitored. The resulting EDS maps of S and thus PSEHTT phase distribution in the blend film are shown in Figure 6.6d-f. Similar EDS maps of Se and thus PNDIBS phase distribution in the blend films are given in Figure 6.6g-i. We note that the overall morphology shown in the EDS map is similar to that of the corresponding HAADF-STEM image, which implies that the high-energy electron beam does not alter the phase distribution significantly. The EDS S-maps in Figure 6.6d-f clearly show in green the regions where PSEHTT exists and the dark background where PSEHTT is absent. It is also seen that although PSEHTT has large domain sizes (200-500 nm in width in Figure 6.6d and

50-300 nm in width in Figure 6.6f), the large domains are composed of aggregates of smaller PSEHTT domains of 20 – 35 nm in size. The EDS Se-maps in Figure 6.6g-i show that PNDIBS in purple has a relatively uniform distribution. The observed large PNDIBS domains (50-100 nm in width) are similarly made up (i.e. aggregates) of smaller nanostructures.

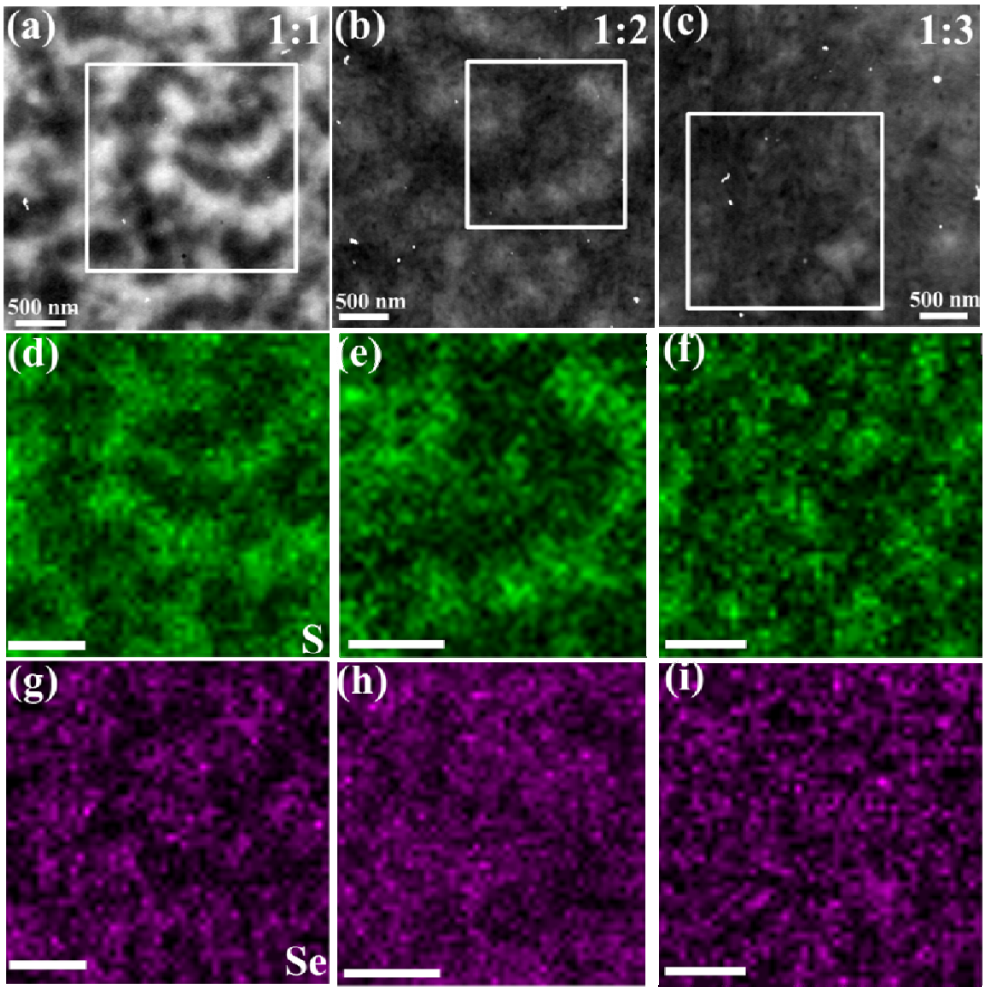

Figure 6.6 (a-c) STEM images of PSEHTT:PNDIBS blend film and the corresponding EDS maps of the square regions in the STEM images, showing (d-f) S element (indicating PSEHTT) and (g-i) Se element (indicating PNDIBS) phases. The blend ratios are (a, d, g) 1:1, (b, e, h) 1:2, and (c, f, i) 1:3. The scale bar is 500 nm.

Wormlike and fibrillar fine nanostructures with widths of 20-35 nm are observed embedded in the dark backgrounds of the EDS elemental maps of both PSEHTT and PNDIBS (Figure 6.7).

These fine fibrillar nanostructures of PSEHTT and PNDIBS were not observed in either TEM or STEM but are similar in size and features to those seen in AFM phase images. On the other hand, AFM could not distinguish between the nanofibrils of PSEHTT and PNDIBS whereas EDS mapping does. We conclude that EDS mapping enables the characterization of the nanoscale morphology of photovoltaic bulk heterojunction films with superior spatial resolution and chemical specificity than current techniques (BF-TEM, STEM, and AFM). However, we emphasize that EDS imaging reveals the structure/composition of the bulk thin film projected onto a 2D image, similar to standard TEM and STEM. Nevertheless, EDS coupled with STEM clearly offers new morphological information and insights into BHJ polymer solar cells.

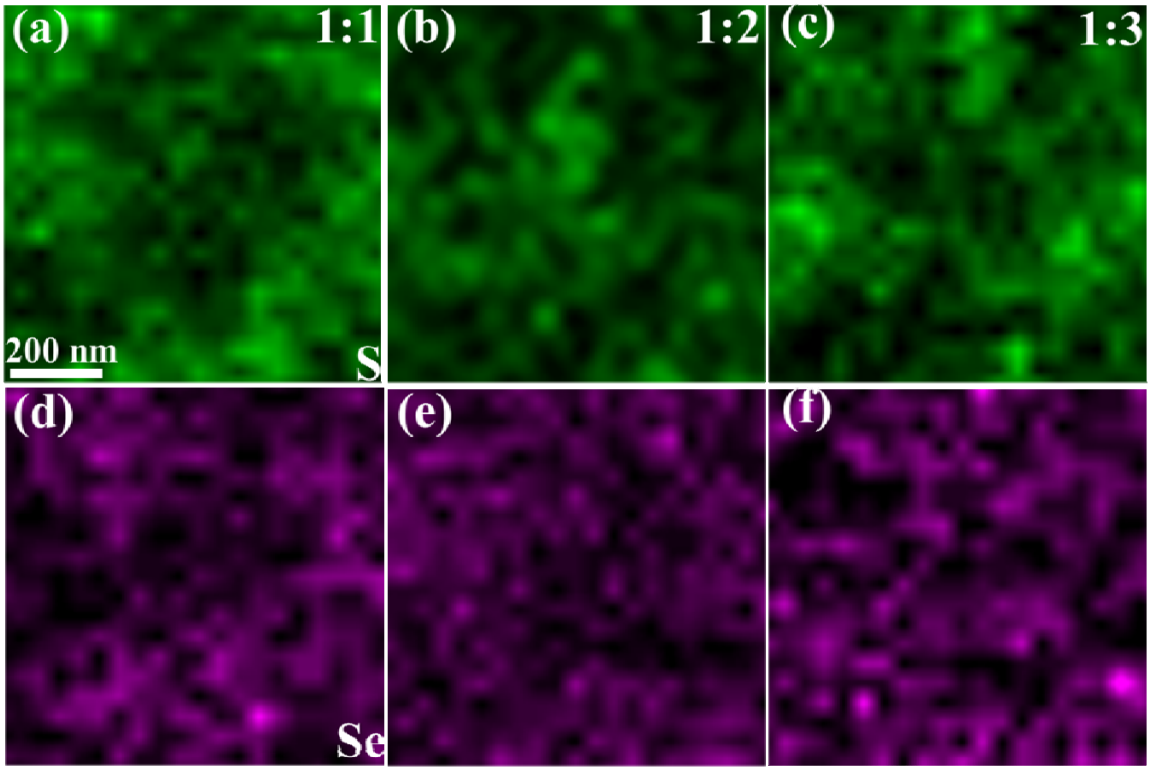

Figure 6.7 Wormlike and fibrillar nanostructures embedded in the dark background. (a-c) S-maps (indicating PSEHTT) and (d-f) Se-maps (indicating PNDIBS) of PSEHTT:PNDIBS

blend films with blend ratios of (a, d) 1:1, (b, e) 1:2, and (c, f) 1:3. The scale bar is the same for each image.

6.3.4 Blend Morphology via EDS Imaging

The image processing software ImageJ[20] was used to perform pattern recognition to generate the relative S- and Se-distribution maps and thus phase separation and distribution images of the binary PSEHTT:PNDIBS binary blends. We accomplished this by using the MinError threshold method of ImageJ in which the background weak characteristic X-ray emission below a certain threshold in an area is removed. The resulting threshold-adjusted S-maps and thus PSEHTT distribution in the blend are shown in Figure 6.8a-c. Similar threshold-adjusted Se-maps and thus PNDIBS distribution in the blend are shown in Figure 6.8d-f. These threshold-adjusted S- and Se-maps only show the polymer phases that exhibit relatively high level of X-ray emission in the blend. A consequence of this is that some wormlike and fibrillar nanostructures with weak X-ray emission (Figure 6.7) in both PSEHTT and PNDIBS EDS elemental maps are removed, which thereby reduces the spatial resolution achievable. We note that the morphology (spatial distribution and topology) of each polymer in the blend revealed by these EDS elemental maps (Figure 6.8) is significantly different and is roughly complementary. PSEHTT forms large domains (100-500 nm) that are not uniformly distributed in the blends. PNDIBS domains are smaller (50-100 nm) and are more uniformly distributed and interconnected in the blends.

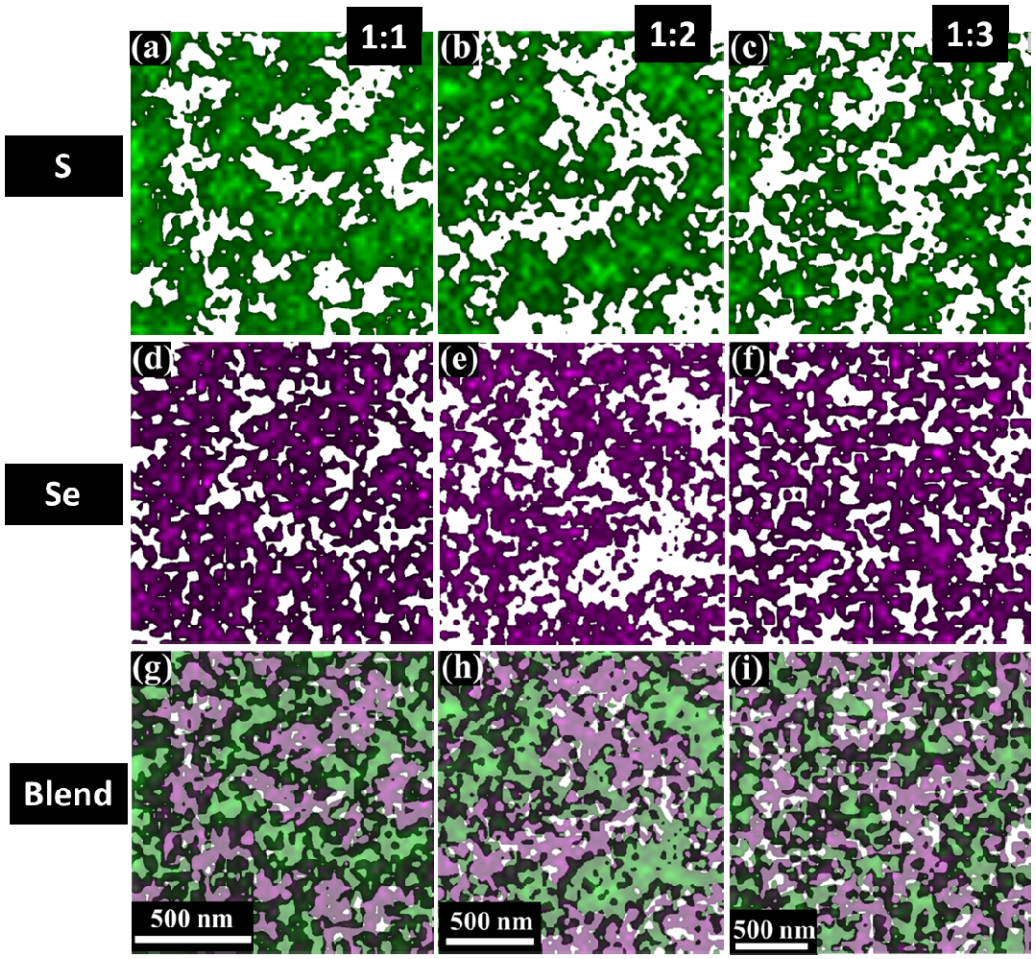

Figure 6.8 EDS sulfur (S) and selenium (Se) maps generated by the MinError threshold method. (a-c) PSEHTT phase distribution and (d-f) PNDIBS phase distribution from the respective S- and Se-maps in Figure 6.6. (g-i) PSEHTT:PNDIBS blend morphology revealed by superposition of the corresponding PSEHTT and PNDIBS EDS maps. The blend ratios are (a,d,g) 1:1, (b,e,h) 1:2, (c,f,i) 1:3. The scale bar is the same for each column and represents 500 nm.

The overall blend morphology revealed by EDS elemental mapping was obtained by the superposition of the individual PSEHTT and PNDIBS maps as shown in Figure 6.8g-i. It is observed that the PSEHTT and PNDIBS phases in the blend are complementary to each other, demonstrating that the blend films exhibit bicontinuous, percolated, phase separation. The remaining white areas in Figure 6.8g-i indicate a low level of existence of both polymers whose

color shade level was below the threshold. There are some places with overlapping colors (shown in black), indicating the co-existence of both polymers and can be regarded as a miscible phase. Blend maps thus show three distinct phases, a PSEHTT phase, a PNDIBS phase, and a miscible PSEHTT/PNDIBS phase. We note that EDS imaging cannot distinguish between if the miscible phase is a result of vertical overlap or a result of co-existence in the same plane since the images are 2D in nature. Nevertheless, this result is consistent with similar observations of three phases, i.e. pure polymer phase, fullerene-rich phase, and a mixed polymer/fullerene phase, in polymer/fullerene BHJ films.[9,32,33] We believe that the observed miscible phase likely plays a very important role in the charge transfer, separation, and recombination process. These EDS imaging results reveal critical information on the nanomorphology of all-polymer BHJ films and thus may provide guidelines for the optimization of the photovoltaic properties through control of the morphology.

We examined the morphology of poly(3-hexylthiophene) (P3HT): [6,6]-phenyl-C_{71}-butyric acid methyl ester ($PC_{71}BM$) (1:1 wt/wt) blend films by STEM/EDS to assess feasibility of applying the method to polymer/small molecule blend systems. Solar cells based on such P3HT:$PC_{71}BM$ blend films had a previously reported power conversion efficiency of 3.70 % (V_{oc} = 0.61 V; J_{sc} = 9.54 mA/cm^2; FF = 0.64).[34] Our observed typical TEM image (Figure 6.9) of the P3HT:$PC_{71}BM$ blend films shows a phase contrast (PCBM-rich areas appear dark and P3HT bright) that agrees well with previously reported TEM images of P3HT:PCBM blend films.[6] STEM image, EDS map for sulfur, and phase distribution map of P3HT of the same area are shown in Figure 6.9b-d. The bright areas in the STEM image are P3HT-rich domains (aggregates

of nanowires) and the dark areas are PCBM-rich. A well interconnected network of P3HT donor with embedded PCBM phases is observed. Although the fullerene ($PC_{71}BM$) phase distribution in the blend could not be mapped directly by EDS because fullerene lacks a high Z element, the threshold-adjusted sulfur map and thus phase distribution of P3HT (Figure 6.9d) in the blend also gives some indication of the expected complementary phase of fullerene. An important possible limitation of the accuracy and spatial resolution of EDS mapping of polymer blends containing fullerene or other small-molecule materials is the much greater molecular mobility (diffusion) of small molecules under intense electron beam irradiation.

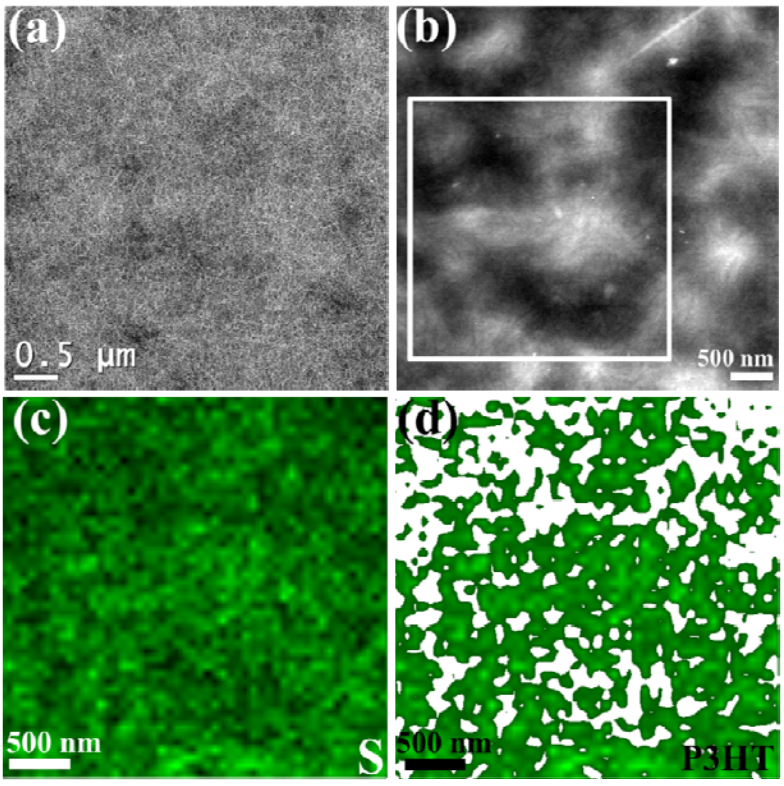

Figure 6.9 Images of P3HT:$PC_{71}BM$ (1:1 wt/wt) blend film by: (a) TEM, (b) STEM, (c) EDS map of sulfur, and (d) threshold-adjusted P3HT phase distribution map. Note: TEM image and STEM image show images for different area of the same film; STEM image and EDS map show image of the same area.

Our present results on PSEHTT/PNDIBS all-polymer and polymer/fullerene (P3HT/$PC_{71}BM$) BHJ solar cells clearly demonstrate that EDS imaging can provide important new information on the nanoscale morphology of organic solar cells. In addition to sulfur and selenium, other high Z elements such as Si, Ge, and Pt[35] found in current organic photovoltaic (OPV) materials could enable the use of high resolution EDS imaging to understand the morphology of BHJ OPV systems. We also envision that EDS imaging as demonstrated here could potentially be combined with electron tomography[10] towards the detailed determination of the 3D nanoscale morphology of BHJ OPV systems.

6.4 Conclusions

Energy dispersive X-ray spectroscopy (EDS) coupled with scanning transmission electron microscopy (STEM) has been successfully used to characterize the nanoscale morphology of BHJ polymer solar cells for the first time. The model all-polymer BHJ solar cells were composed of a sulfur-containing thiazolothiazole copolymer (PSEHTT) donor and a selenium-containing naphthalene diimide-biselenophene copolymer (PNDIBS) acceptor, facilitating high Z-contrast chemical imaging. The use of EDS coupled with STEM combines the high spatial resolution of STEM imaging and the high chemical specificity of EDS and therefore, can provide important information on composition and phase distribution in BHJ blends beyond what is achievable by current techniques of AFM, BF-TEM, and STEM. EDS imaging showed that the domain size of PSEHTT decreased as the blend composition changed from 1:1 to 1:3 PSEHTT:PNDIBS weight ratio. Both PSEHTT and PNDIBS phases consisted of small domains with size of 20-35 nm. EDS images showed that the blend films were composed of three phases, including a PSEHTT

phase, a PNDIBS phase, and a miscible PSEHTT/PNDIBS phase. These results demonstrate that the nanoscale morphology of BHJ polymer solar cells can be determined with high spatial resolution and chemical specificity by the use of EDS coupled with STEM.

6.5 References

1. Yang, X.; Loos, J. *Macromolecules* **2007**, *40*, 1353-1362.
2. McNeill, C. R. *Energy Environ. Sci.* **2012**, *5*, 5653-5667.
3. Oosterhout, S. D.; Wienk, M. M.; van Bavel, S. S.; Thiedmann, R.; Jan Anton Koster, L.; Gilot, J.; Loos, J.; Schmidt, V.; Janssen, R. A. J. *Nat. Mater.* **2009**, *8*, 818-824.
4. Liu, F.; Gu, Y.; Jung, J. W.; Jo, W. H.; Russell, T. P. *J. Polym. Sci. B: Polym. Phys.* **2012**, *50*, 1018–1044.
5. Nagarjuna, G.; Venkataraman, D. *J. Polym. Sci. B: Polym. Phys.* **2012**, *50*, 1045–1056.
6. van Bavel, S. S.; Sourty, E.; de With, G.; Loos, J. *Nano Lett.* **2009**, *9*, 507-513.
7. Herzing, A. A.; Richter, L. J.; Anderson, I. M. *J. Phys. Chem. C* **2010**, *114*, 17501-17508.
8. Drummy, L. F.; Davis, R. J.; Moore, D. L.; Durstock, M.; Vaia, R. A.; Hsu, J. W. P. *Chem. Mater.* **2010**, *23*, 907-912.
9. Roehling, J. D.; Batenburg, K. J.; Swain, F. B.; Moulé, A. J.; Arslan, I. *Adv. Funct. Mater.* **2013**, *23*, 2115–2122.
10. Arslan, I.; Yates, T. J. V.; Browning, N. D.; Midgley, P. A. *Science* **2005**, *309*, 2195-2198.
11. Williams, D. B.; Carter, C. B. *Transmission Electron Microscopy: A Textbook for Materials Science*; Springer Science + Business Media, LLC: New York, NY, USA, 2009.
12. Loos, J.; Sourty, E.; Lu, K.; de With, G.; van Bavel, S. S. *Macromolecules* **2009**, *42*, 2581-2586.
13. van Bavel, S. S.; Bärenklau, M.; de With, G.; Hoppe, H.; Loos, J. *Adv. Funct. Mater.* **2010**, *20*, 1458-1463.
14. Schubert, M.; Dolfen, D.; Frisch, J.; Roland, S.; Steyrleuthner, R.; Stiller, B.; Chen, Z.; Scherf, U.; Koch, N.; Facchetti, A.; Neher, D. *Adv. Energy. Mater.* **2012**, *2*, 369-380.

15. Garratt-Reed, A. J.; Bell, D. C. *Energy Dispersive X-ray Analysis in the Electron Microscope* BIOS Scientific Publishers Ltd: Oxford, UK, 2003.

16. Favia, P.; Voroshazi, E.; Heremans, P.; Bender, H. *J. Mater. Sci.* **2013**, *48*, 2908-2919.

17. Subramaniyan, S.; Xin, H.; Kim, F. S.; Shoaee, S.; Durrant, J. R.; Jenekhe, S. A. *Adv. Energy. Mater.* **2011**, *1*, 854-860.

18. Hwang, Y.-J.; Ren, G.; Murari, N. M.; Jenekhe, S. A. *Macromolecues* **2012**, *45*, 9056–9062.

19. Hwang, Y.-J.; Murari, N. M.; Jenekhe, S. A. *Polym. Chem.* **2013**, DOI: 10.1039/C3PY00325F.

20. T. Ferreira and W. Rasband, ImageJ User Guide IJ1.46r, http://rsbweb.nih.gov/ij/docs/guide/146.html, accessed March 5, 2013.

21. Shoaee, S.; Subramaniyan, S.; Xin, H.; Keiderling, C.; Tuladhar, P. S.; Jamieson, F.; Jenekhe, S. A.; Durrant, J. R. *Adv. Funct. Mater.* **2013**, DOI: 10.1002/adfm.201203148.

22. Moore, J. R.; Albert-Seifried, S.; Rao, A.; Massip, S.; Watts, B.; Morgan, D. J.; Friend, R. H.; McNeill, C. R.; Sirringhaus, H. *Adv. Energy. Mater.* **2011**, *1*, 230-240.

23. Nakabayashi, K.; Mori, H. *Macromolecules* **2012**, *45*, 9618-9625.

24. Zhou, E.; Cong, J.; Zhao, M.; Zhang, L.; Hashimoto, K.; Tajima, K. *Chem. Commun.* **2012**, *48*, 5283-5285.

25. Fabiano, S.; Chen, Z.; Vahedi, S.; Facchetti, A.; Pignataro, B.; Loi, M. A. *J. Mater. Chem.* **2011**, *21*, 5891-5896.

26. Alam, M. M.; Tonzola, C. J.; Jenekhe, S. A. *Macromolecules* **2003**, *36*, 6577-6587.

27. Mayer, A. C.; Michael, F. T.; Shawn, R. S.; Jonathan, R.; Christoph, J. B.; Marcus, S.; Marcus, K.; Martin, H.; Iain, M.; Michael, D. M. *Adv. Funct. Mater.* **2009**, *19*, 1173-1179.

28. Wu, P. T.; Ren, G.; Li, C.; Mezzenga, R.; Jenekhe, S. A. *Macromolecules* **2009**, *42*, 2317-2320.

29. Nam, S.; Shin, M.; Park, S.; Lee, S.; Kim, H.; Kim, Y. *Phys. Chem. Chem. Phys.* **2012**, *14*, 15046-15053.

30. Zhang, X.; Kale, D. M.; Jenekhe, S. A. *Macromolecules* **2002**, *35*, 382-393.

31. Duran, R.; Ballauff, M.; Wenzel, M.; Wegner, G. *Macromolecules* **1988**, *21*, 2897-2899.

32. Moulé, A. J.; Tsami, A.; Bünnagel, T. W.; Forster, M.; Kronenberg, N. M.; Scharber, M.; Koppe, M.; Morana, M.; Brabec, C. J.; Meerholz, K.; Scherf, U. *Chem. Mater.* **2008**, *20*, 4045-4050.

33. Pfannmöller, M.; Flügge, H.; Benner, G.; Wacker, I.; Sommer, C.; Hanselmann, M.; Schmale, S.; Schmidt, H.; Hamprecht, F. A.; Rabe, T.; Kowalsky, W.; Schröder, R. R. *Nano Lett.* **2011**, *11*, 3099-3107.

34. Ren, G.; Schlenker, C. W.; Ahmed, E.; Subramaniyan, S.; Olthof, S.; Kahn, A.; Ginger, D. S.; Jenekhe, S. A. *Adv. Funct. Mater.* **2013**, *23*, 1238–1249.

35. Wu, P. T.; Bull, T.; Kim, F. S.; Luscombe, C. K.; Jenekhe, S. A. *Macromolecules* **2009**, *42*, 671-681.

Chapter 7 Conclusions and Outlook

7.1 Conclusions

In the studies presented in this dissertation, I have primarily focused on the control of the nanoscale morphology of organic bulk heterojunction solar cells to enhance the photovoltaic properties of given blends. Specifically, I studied how the block composition of block copolymers affects their photovoltaic performance, the use of processing additives in benzobisthiazole-copolymer/fullerene and P3HT/non-fullerene acceptor solar cells, the fabrication of efficient all-nanowire BHJ solar cells, and the morphology of all-polymer BHJ solar cells.

I have investigated the photovoltaic, charge transport properties, and morphology of bulk heterojunction solar cells based on a series of diblock copoly(3-alkylthiophene)s, poly(3-butylthiophene)-*b*-poly(3-octylthiophene) (P3BT-*b*-P3OT). The results have shown that crystalline block copoly(3-alkylthiophene)s have substantially enhanced photovoltaic properties compared to the parent homopolymers. On the one hand, BHJ solar cells based on P3BT-*b*-P3OT with varying block compositions (17 - 90 mol% P3BT block) and fullerene derivative ($PC_{71}BM$) showed that the power conversion efficiency strongly depends on the block composition, reaching a maximum value of 3.0% PCE at 50 mol % P3BT. This efficiency is about a factor of 1.6−9 times higher than the corresponding homopolymer devices made under similar conditions.[1] On the other hand, study of solution-phase self-assembly of polymer nanowires from P3BT-*b*-P3OT revealed that the aspect ratio (length/width) can vary significantly according to the block composition. Bulk heterojunction solar cells based on nanowires/$PC_{71}BM$ nanocomposites showed a dependence of photovoltaic efficiency (2.9−3.4% PCE) on aspect ratio of the nanowires. The observed aspect-ratio-dependent photovoltaic properties of the nanowires

are attributed to enhanced charge separation, transport, and collection in the BHJ devices.[2] These results demonstrate that block composition is a facile means of tuning the photovoltaic properties of block copolymer semiconductors.

I have studied the optimization of BHJ solar cells based on a novel benzobisthiazole copolymer (PBTHDDT) donor and three fullerene acceptors, $PC_{71}BM$, $PC_{61}BM$, and $IC_{60}BA$, using a processing additive.[3] The impact of modulating the driving force for photoinduced hole transfer on the photovoltaic properties of BHJ solar cells was investigated. Solar cells based on PBTHDDT:$PC_{71}BM$, PBTHDDT:$PC_{61}BM$ and PBTHDDT:$IC_{60}BA$ blends showed average efficiency of 3.75%, 2.70%, and 1.52% PCE, respectively. The observed significant variation in the photovoltaic performance is unlikely a results of blend morphology. Photophysical studies of the PBTHDDT:fullerene blends showed that all the PBTHDDT:fullerene blends generated long-lived positive polarons in PBTHDDT and negative polarons on the fullerene upon photoexcitation of the polymer. While fullerene excitons in PBTHDDT:$PC_{71}BM$ and PBTHDDT:$PC_{61}BM$ blends appear to undergo photoinduced hole transfer at the donor/acceptor interface to generate long-lived polarons, selective excitation of the fullerene in PBTHDDT:$IC_{60}BA$ blends does not efficiently produce long-lived charges. This low dissociation efficiency is attributable to the small driving force for hole transfer at the polymer/IC60BA interface being insufficient to sustain efficient charge separation. A minimum driving force of ~70 meV between donor and acceptor materials is identified. These results provide an important guide for materials design and device engineering in bulk heterojunction polymer solar cells.

The processing additive strategy in the optimization of BHJ polymer solar cells based on a non-fullerene small-molecule acceptor was also explored.[4] It is found that the average power conversion efficiency of P3HT:NDI-3TH solar cells is improved from 0.14% to 1.5% by use of a

1,8-diiodooctane (DIO) processing additive along with a P3HT electron-blocking layer and a TPBI hole-blocking layer. The underlying mechanism for the enhancement in performance is that the processing additive regulates the aggregation and domain size and connectivity of the NDI-3TH phase in the BHJ blends. The optimum concentration of the DIO processing additive was found to be 0.2 vol%, which is significantly less than the 2.0-3.0 vol% optimum concentrations previously reported for polymer/fullerene systems. The present results show for the first time that processing additives can be used to optimize the nanomorphology and enhance the performance of bulk heterojunction polymer solar cells based on non-fullerene acceptors.

In addition, I have investigated the solution-phase self-assembly and morphology of nanowires of a series of 6 oligothiophene-functionalized naphthalene diimides (NDI-nTH and NDI-nT).[5,6] Well-defined nanowires, whose size and detailed morphology varied with the molecular structure of the NDIs, the solution concentration, and solvent/non-solvent ratio, were successfully assembled. A comparison of the optical absorption spectra of neat thin films and nanowire films of NDI-3TH showed a significant red-shift and enhancement of intensity of the low energy absorption band (600 nm) in the nanowire films, indicating a stronger molecular order in the nanowires. Bulk heterojunction (BHJ) solar cells made from blends P3HT NWs as the donor and NDI-3TH NWs as the acceptor showed a power conversion efficiency (PCE) of 1.15%, and a broad EQE spectrum ranging from 300 to 800 nm. These results demonstrate, for the first time, that all-nanowire organic solar cells can be fabricated by using nanowires of p-type and n-type organic semiconductor as building blocks.

Finally, energy dispersive X-ray spectroscopy (EDS) coupled with scanning transmission electron microscopy (STEM) has been successfully used to characterize the nanoscale morphology of BHJ polymer solar cells for the first time.[7] The model all-polymer BHJ solar cells

were composed of a sulfur-containing thiazolothiazole copolymer (PSEHTT) donor and a selenium-containing naphthalene diimide-biselenophene copolymer (PNDIBS) acceptor, facilitating high Z-contrast chemical imaging. The use of EDS coupled with STEM combines the high spatial resolution of STEM imaging and the high chemical specificity of EDS and therefore, can provide important information on composition and phase distribution in BHJ blends beyond what is achievable by current techniques of AFM, BF-TEM, and STEM. EDS imaging showed that the domain size of PSEHTT decreased as the blend composition changed from 1:1 to 1:3 PSEHTT:PNDIBS weight ratio. Both PSEHTT and PNDIBS phases consisted of small domains with size of 20-35 nm. EDS images showed that the blend films were composed of three phases, including a PSEHTT phase, a PNDIBS phase, and a miscible PSEHTT/PNDIBS phase. These results demonstrate that the nanoscale morphology of BHJ polymer solar cells can be determined with high spatial resolution and chemical specificity by the use of EDS coupled with STEM.

Overall, researches presented here have shed new light on the optimization of organic solar cells. New device physics has been revealed to guide materials selection in device fabrication, new morphology characterization techniques have been proposed and demonstrated to better understand the limiting factors of device performance, and new device processing techniques have been developed to significantly enhance the photovoltaic properties of known materials. Knowledge obtained from these studies provides additional guidelines in the design of new materials with greater photovoltaic performance. With the collective efforts of researchers in the organic solar cell community, another breakthrough in the power conversion efficiency of organic solar cells is achievable in the near future.

7.2 Outlook

Research on organic solar cells is an ongoing hot topic in both academia and industry. The following are possible future directions in this field.

The richness in the chemistry, physics, materials science, and engineering of π-conjugated organic semiconductors continues to unfold despite the considerable interdisciplinary advances in scientific understanding and technological applications of the materials in the past two decades. The increasing ability to assemble π-conjugated molecular building blocks (small molecules, oligomers, and polymers) into well-defined crystalline 1D nanostructures is opening new opportunities for discoveries and interdisciplinary research in many areas as well as for applications. The various approaches developed for producing organic semiconductor nanowires, nanoribbons/nanobelts, and nanotubes and the range of accessible dimensions (diameter or width *d*, length *L*) have been demonstrated. Collectively, these strategies can offer a wide range of 1D nanomaterials and nanostructures with readily tunable electronic, optoelectronic, and photonic properties, suggesting ways toward high-volume, low-cost, affordable nanotechnologies. However, the degree of precision achievable in the control of dimensions, composition, shape, and crystal structure of organic semiconductor nanostructures is still low compared with inorganic semiconductors. In addition, a better control of the diameter/width, aspect ratio, and single-crystallinity of organic semiconductor nanostructures is needed to facilitate systematic basic studies that can be expected to uncover the fundamental limits on properties ranging from charge and exciton transport to photovoltaic properties. Methods for the facile alignment of organic nanowires in a preferred direction, beyond templated strategies are also needed since such an alignment is beneficial for enhanced charge transport, production of polarized light

emission, and improved absorption and photovoltaic properties, especially when dealing with an ensemble of nanowires used for various device applications.

Organic solar cells based on a vast variety of non-fullerene n-type materials (polymers, oligomers, and small molecules) represent another opportunity of technology breakthrough. Recent advances in organic synthesis have made a variety of novel n-type materials avaialbe in simple chemistry and low cost compared with fullerenes. These novel electron acceptors have tunable molecular structures that enable tunable electronic and optoelectronic properties, allow better photon harvesting in a wider range of solar spectrum, and higher charge carrier mobility. In addition, a better control of the energy levels of n-type materials allows a systematic explore and an indepth understanding of the impact of energy level offset on exciton generation and dissociation, charge transfer, and photovoltaic properties, unachievable in fullerene-based devices.[8,9] For solar cells based on n-type small molecules and oligomers, one of the major challenges is lack of new morphology control approaches beyond those used for fullerene-based devices. Another issue is the possible different photophysics involved in these molecules with linear geometry compared with spherical fullerenes. In the case of all-polymer solar cells, as seen from literature, the molecular weight of polymer semiconductors plays a very important role in determining the photovoltaic properties.[10,11] The morphology control of all-polymer solar cells is much less flexible compared with small-molecule-based polymer solar cells in which molecular diffusion is possible by control of evaporation rate. The other effective method for morphology optimization of all-polymer BHJ solar cell is the use of solvent mixtures with different ratios.[12,13] But the selection of proper solvent is based solely on trial-and-error. The photophysical process of all-polymer solar cells is much less understood as well. In one word, there are still a lot of

opportunities in non-fullerene polymer solar cells that potentially have a high impact on organic solar cells.

7.3 References

1. Ren, G.; Wu, P.-T.; Jenekhe, S. A. *Chem. Mater.* **2010**, *22*, 2020-2026.

2. Ren, G.; Wu, P.-T.; Jenekhe, S. A. *ACS Nano* **2011**, *5*, 376-384.

3. Ren, G.; Schlenker, C. W.; Ahmed, E.; Subramaniyan, S.; Olthof, S.; Kahn, A.; Ginger, D. S.; Jenekhe, S. A. *Adv. Funct. Mater.* **2013**, *23*, 1238–1249.

4. Ren, G.; Ahmed, E.; Jenekhe, S. A. *Adv. Energy. Mater.* **2011**, *1*, 946-953.

5. Ahmed, E.; Ren, G.; Kim, F. S.; Hollenbeck, E. C.; Jenekhe, S. A. *Chem. Mater.* **2011**, *23*, 4563–4577.

6. Ren, G.; Ahmed, E.; Jenekhe, S. A. *J. Mater. Chem.* **2012**, *22*, 24373 - 24379.

7. Ren, G.; Hwang, Y.-J.; Subramanian, S.; Jenekhe, S. A. *Energy Environ. Sci.* **2013**, *submitted*.

8. Sonar, P.; Lim, J. P. F.; Chan, K. L. *Energy Environ. Sci.* **2011**, *4*, 1558-1574.

9. Anthony, J. E. *Chem. Mater.* **2011**, *23*, 583-590.

10. Mori, D.; Benten, H.; Ohkita, H.; Ito, S.; Miyake, K. *Acs Appl. Mater. Inter.* **2012**, *4*, 3325-3329.

11. Mori, D.; Benten, H.; Kosaka, J.; Ohkita, H.; Ito, S.; Miyake, K. *ACS Appl. Mater. Interfaces* **2011**, *3*, 2924-2927.

12. Moore, J. R.; Albert-Seifried, S.; Rao, A.; Massip, S.; Watts, B.; Morgan, D. J.; Friend, R. H.; McNeill, C. R.; Sirringhaus, H. *Adv. Energy. Mater.* **2011**, *1*, 230-240.

13. Zhou, E.; Cong, J.; Wei, Q.; Tajima, K.; Yang, C.; Hashimoto, K. *Angew. Chem. Int. Ed.* **2011**, *50*, 2799-2803.

Bibliography

1. Shirakawa, H.; Louis, E. J.; MacDiarmid, A. G.; Chiang, C. K.; Heeger, A. J. *J. Chem. Soc., Chem. Commun.* **1977**, 578-580.

2. Shirakawa, H. *Angew. Chem. Int. Ed.* **2001**, *40*, 2574-2580.

3. MacDiarmid, A. G. *Angew. Chem. Int. Ed.* **2001**, *40*, 2581-2590.

4. Heeger, A. J. *Angew. Chem. Int. Ed.* **2001**, *40*, 2591-2611.

5. Kim, F. S.; Ren, G.; Jenekhe, S. A. *Chem. Mater.* **2011**, *23*, 682-732.

6. Xin, H.; Kim, F. S.; Jenekhe, S. A. *J. Am. Chem. Soc.* **2008**, *130*, 5424-5425.

7. Peet, J.; Kim, J. Y.; Coates, N. E.; Ma, W. L.; Moses, D.; Heeger, A. J.; Bazan, G. C. *Nat. Mater.* **2007**, *6*, 497-500.

8. Briseno, A. L.; Mannsfeld, S. C. B.; Jenekhe, S. A.; Bao, Z.; Xia, Y. *Mater.Today* **2008**, *11*, 38-47.

9. Ihn, K. J.; Moulton, J.; Smith, P. *J. Polym. Sci., Part B* **1993**, *31*, 735-742.

10. Liang, Y.; Xu, Z.; Xia, J.; Tsai, S. T.; Wu, Y.; Li, G.; Ray, C.; Yu, L. *Adv. Mater.* **2010**, *22*, E135−E138.

11. Zhou, H.; Yang, L.; Stuart, A. C.; Price, S. C.; Liu, S.; You, W. *Angew. Chem. Int. Ed.* **2011**, *50*, 2995-2998.

12. Small, C. E.; Chen, S.; Subbiah, J.; Amb, C. M.; Tsang, S.-W.; Lai, T.-H.; Reynolds, J. R.; So, F. *Nat. Photon.* **2012**, *6*, 115-120.

13. Dou, L.; You, J.; Yang, J.; Chen, C.-C.; He, Y.; Murase, S.; Moriarty, T.; Emery, K.; Li, G.; Yang, Y. *Nat. Photon.* **2012**, *6*, 180-185.

14. He, Z.; Zhong, C.; Su, S.; Xu, M.; Wu, H.; Cao, Y. *Nat. Photon.* **2012**, *6*, 593-597.

15. Gunes, S.; Neugebauer, H.; Sariciftci, N. S. *Chem. Rev.* **2007**, *107*, 1324-1338.

16. Thompson, B. C.; Fréchet, J. M. J. *Angew. Chem. Int. Ed.* **2008**, *47*, 58-77.

17. Coakley, K. M.; McGehee, M. D. *Chem. Mater.* **2004**, *16*, 4533-4542.

18. Jong, D.; Friedlein, M. P.; Osikowicz, R. W.; Salaneck, W. R.; Fahlman, M. *Mol. Cryst. Liq. Cryst.* **2006**, *455*, 193-203.

19. Brabec, C. J.; Shaheen, S. E.; Winder, C.; Sariciftci, N. S.; Denk, P. *Appl. Phys. Lett.* **2002**, *80*, 1288-1290.

20. Shrotriya, V.; Li, G.; Yao, Y.; Moriarty, T.; Emery, K.; Yang, Y. *Adv. Funct. Mater.* **2006**, *16*, 2016-2023.

21. Marks, R. N.; Halls, J. J. M.; Bradley, D. D. C.; Friend, R. H.; Holmes, A. B. *J. Phys. Condens. Matter* **1994**, *6*, 1379-1394.

22. Antoniadis, H.; Hsieh, B. R.; Abkowitz, M. A.; Jenekhe, S. A.; Stolka, M. *Synth. Met.* **1994**, *62*, 265-271.

23. Tang, C. W. *Appl. Phys. Lett.* **1986**, *48*, 183-185.

24. Alam, M. M.; Jenekhe, S. A. *Chem. Mater.* **2004**, *16*, 4647-4656.

25. Sariciftci, N. S.; Braun, D.; Zhang, C.; Srdanov, V. I.; Heeger, A. J.; Stucky, G.; Wudl, F. *Appl. Phys. Lett.* **1993**, *62*, 585-587.

26. Yu, G.; Gao, J.; Hummelen, J. C.; Wudl, F.; Heeger, A. J. *Science* **1995**, *270*, 1789-1791.

27. Ma, W.; Yang, C.; Gang, X.; Lee, K.; Heeger, A. J. *Adv. Funct. Mater.* **2005**, *15*, 1617-1622.

28. Li, G.; Shrotriya, V.; Huang, J.; Yao, Y.; Moriarty, T.; Emery, K.; Yang, Y. *Nat. Mater.* **2005**, *4*, 864-868.

29. Blom, P. W. M.; Mihailetchi, V. D.; Koster, L. J. A.; Markov, D. E. *Adv. Mater.* **2007**, *19*, 1551-1566.

30. Moliton, A.; Nunzi, J.-M. *Polym. Int.* **2006**, *55*, 583-600.

31. Pivrikas, A.; Neugebauer, H.; Sariciftci, N. S. *IEEE J. Sel. Top. Quant. Electron.* **2010**, *16*, 1746-1758.

32. Mihailetchi, V. D.; Xie, H.; de Boer, B.; Koster, L. J. A.; Blom, P. W. M. *Adv. Funct. Mater.* **2006**, *16*, 699-708.

33. Gong, X.; Tong, M.; Brunetti, F. G.; Seo, J.; Sun, Y.; Moses, D.; Wudl, F.; Heeger, A. J. *Adv. Mater.* **2011**, *23*, 2272-2277.

34. Tiwari, S.; Greenham, N. *Opt. Quant. Electron.* **2009**, *41*, 69-89-89.

35. Bredas, J.-L.; Beljonne, D.; Coropceanu, V.; Cornil, J. *Chem. Rev.* **2004**, *104*, 4971-5004.

36. Shirota, Y.; Kageyama, H. *Chem. Rev.* **2007**, *107*, 953-1010.

37. Sze, S. M. *Physics of Semiconductor Devices (2nd ed.)*; Wiley: New York, 1981.

38. Mihailetchi, V. D.; Wildeman, J.; Blom, P. W. M. *Phys. Rev. Lett.* **2005**, *94*, 126602-4.

39. Murgatroyd, P. N. *J. Phys. D: Appl. Phys.* **1970**, *3*, 151.

40. Domercq, B.; Yu, J. S.; Kaafarani, B. R.; Kondo, T.; Yoo, S.; Haddock, J. N.; Barlow, S.; Marder, S. R.; Kippelen, B. *Mol. Cryst. Liq. Cryst.* **2008**, *481*, 80-93.

41. Haber, K. S.; Albrecht, A. C. *J. Phys. Chem. C* **1984**, *88*, 6025-6030.

42. Sirringhaus, H. *Adv. Mater.* **2005**, *17*, 2411-2425.

43. Brabec, C. J.; Cravino, A.; Meissner, D.; Sariciftci, N. S.; Fromherz, T.; Rispens, M. T.; Sanchez, L.; Hummelen, J. C. *Adv. Funct. Mater.* **2001**, *11*, 374-380.

44. Mihailetchi, V. D.; Blom, P. W. M.; Hummelen, J. C.; Rispens, M. T. *J. Appl. Phys.* **2003**, *94*, 6849-6854.

45. Gomez, E. D.; Loo, Y.-L. *J. Mater. Chem.* **2010**, *20*, 6604-6611.

46. Nagarjuna, G.; Venkataraman, D. *J. Polym. Sci. B: Polym. Phys.* **2012**, *50*, 1045–1056.

47. Liu, F.; Gu, Y.; Jung, J. W.; Jo, W. H.; Russell, T. P. *J. Polym. Sci. B: Polym. Phys.* **2012**, *50*, 1018–1044.

48. Ren, G.; Ahmed, E.; Jenekhe, S. A. *Adv. Energy. Mater.* **2011**, *1*, 946-953.

49. Shaheen, S. E.; Brabec, C. J.; Sariciftci, N. S.; Padinger, F.; Fromherz, T.; Hummelen, J. C. *Appl. Phys. Lett.* **2001**, *78*, 841-843.

50. Chen, L. M.; Hong, Z.; Li, G.; Yang, Y. *Adv. Mater.* **2009**, *21*, 1434-1449.

51. Mayer, A. C.; Michael, F. T.; Shawn, R. S.; Jonathan, R.; Christoph, J. B.; Marcus, S.; Marcus, K.; Martin, H.; Iain, M.; Michael, D. M. *Adv. Funct. Mater.* **2009**, *19*, 1173-1179.

52. Li, G.; Yao, Y.; Yang, H.; Shrotriya, V.; Yang, G.; Yang, Y. *Adv. Funct. Mater.* **2007**, *17*, 1636-1644.

53. Xu, T.; Qiao, Q. *Energy Environ. Sci.* **2011**, *4*, 2700-2720.

54. Oosterhout, S. D.; Wienk, M. M.; van Bavel, S. S.; Thiedmann, R.; Jan Anton Koster, L.; Gilot, J.; Loos, J.; Schmidt, V.; Janssen, R. A. J. *Nat. Mater.* **2009**, *8*, 818-824.

55. Padinger, F.; Rittberger, R. S.; Sariciftci, N. S. *Adv. Funct. Mater.* **2003**, *13*, 85-88.

56. Kim, Y.; Choulis, S. A.; Nelson, J.; Bradley, D. D. C.; Cook, S.; Durrant, J. R. *Appl. Phys. Lett.* **2005**, *86*, 063502-3.

57. Savenije, T. J.; Kroeze, J. E.; Yang, X.; Loos, J. *Adv. Funct. Mater.* **2005**, *15*,

1260-1266.

58. Bertho, S.; Janssen, G.; Cleij, T. J.; Conings, B.; Moons, W.; Gadisa, A.; D'Haen, J.; Goovaerts, E.; Lutsen, L.; Manca, J.; Vanderzande, D. *Sol. Energy Mater. Sol. Cells* **2008**, *92*, 753-760.

59. Xin, H.; Ren, G.; Kim, F. S.; Jenekhe, S. A. *Chem. Mater.* **2008**, *20*, 6199-6207.

60. Shrotriya, V.; Yao, Y.; Li, G.; Yang, Y. *Appl. Phys. Lett.* **2006**, *89*, 063505-3.

61. Campoy-Quiles, M.; Ferenczi, T.; Agostinelli, T.; Etchegoin, P. G.; Kim, Y.; Anthopoulos, T. D.; Stavrinou, P. N.; Bradley, D. D. C.; Nelson, J. *Nat. Mater.* **2008**, *7*, 158-164.

62. Bates, F. S.; Fredrickson, G. H. *Physics Today* **1999**, *52*, 32-38.

63. Bates, F. S.; Fredrickson, G. H. *Annu. Rev. Phys. Chem.* **1990**, *41*, 525-57.

64. Darling, S. B. *Energy Environ. Sci.* **2009**, *2*, 1266-1273.

65. Segalman, R. A.; McCulloch, B.; Kirmayer, S.; Urban, J. J. *Macromolecules* **2009**, *42*, 9205-9216.

66. Lindner, S. M.; Huttner, S.; Chiche, A.; Thelakkat, M.; Krausch, G. *Angew. Chem., Int. Ed.* **2006**, *45*, 3364-3368.

67. Zhang, Q.; Cirpan, A.; Russell, T. P.; Emrick, T. *Macromolecules* **2009**, *42*, 1079-1082.

68. Sivula, K.; Ball, Z. T.; Watanabe, N.; Frechet, J. M. J. *Adv. Mater.* **2006**, *18*, 206-210.

69. Xin, H.; Reid, O. G.; Ren, G.; Kim, F. S.; Ginger, D. S.; Jenekhe, S. A. *ACS Nano* **2010**, *4*, 1861-1872.

70. Berson, S.; Bettignies, R. D.; Bailly, S.; Guillerez, S. *Adv. Funct. Mater.* **2007**, *17*, 1377-1384.

71. Chen, H.-Y.; Yang, H.; Yang, G.; Sista, S.; Zadoyan, R.; Li, G.; Yang, Y. *J. Phys. Chem. C* **2009**, *113*, 7946-7953.

72. Peet, J.; Soci, C.; Coffin, R. C.; Nguyen, T. Q.; Mikhailovsky, A.; Moses, D.; Bazan, G. C. *Appl. Phys. Lett.* **2006**, *89*, 252105.

73. Lee, J. K.; Ma, W. L.; Brabec, C. J.; Yuen, J.; Moon, J. S.; Kim, J. Y.; Lee, K.; Bazan, G. C.; Heeger, A. J. *J. Am. Chem. Soc.* **2008**, *130*, 3619-3623.

74. Peet, J.; Senatore, M. L.; Heeger, A. J.; Bazan, G. C. *Adv. Mater.* **2009**, *21*, 1521-1527.

75. Peet, J.; Heeger, A. J.; Bazan, G. C. *Acc. Chem. Res.* **2009**, *42*, 1700-1708.

76. The National Center for Photovoltaics (NCPV) at the National Renewable Energy Laboratory, http://www.nrel.gov/ncpv/images/efficiency_chart.jpg, accessed May 2013.

77. Dennler, G.; Scharber, M. C.; Brabec, C. J. *Adv. Mater.* **2009**, *21*, 1323-1338.

78. Kim, Y.; Cook, S.; Tuladhar, S. M.; Choulis, S. A.; Nelson, J.; Durrant, J. R.; Bradley, D. D. C.; Giles, M.; McCulloch, I.; Ha, C.-S.; Ree, M. *Nat. Mater.* **2006**, *5*, 197-203.

79. Halls, J. J. M.; Walsh, C. A.; Greenham, N. C.; Marseglia, E. A.; Friend, R. H.; Moratti, S. C.; Holmes, A. B. *Nature* **1995**, *376*, 498-500.

80. Nguyen, L. H.; Hoppe, H.; Erb, T.; Gunes, S.; Gobsch, G.; Sariciftci, N. S. *Adv. Funct. Mater.* **2007**, *17*, 1071-1078.

81. Zhou, E.; Yamakawa, S.; Tajima, K.; Yang, C.; Hashimoto, K. *Chem. Mater.* **2009**, *21*, 4055-4061.

82. Liang, Y.; Wu, Y.; Feng, D.; Tsai, S. T.; Son, H. J.; Li, G.; Yu, L. *J. Am. Chem. Soc.* **2009**, *131*, 56-57.

83. Bull, T. A.; Pingree, L. S. C.; Jenekhe, S. A.; Ginger, D. S.; Luscombe, C. K. *ACS Nano* **2009**, *3*, 627-636.

84. Wu, P. T.; Bull, T.; Kim, F. S.; Luscombe, C. K.; Jenekhe, S. A. *Macromolecules* **2009**, *42*, 671-681.

85. Blouin, N.; Michaud, A.; Gendron, D.; Wakim, S.; Blair, E.; Neagu-Plesu, R.; Belletete, M.; Durocher, G.; Tao, Y.; Leclerc, M. *J. Am. Chem. Soc.* **2008**, *130*, 732-742.

86. Gadisa, A.; Oosterbaan, W. D.; Vandewal, K.; Bolsee, J. C.; Bertho, S.; D'Haen, J.; Lutsen, L.; Vanderzande, D.; Manca, J. V. *Adv. Funct. Mater.* **2009**, *19*, 3300-3306.

87. Babel, A.; Jenekhe, S. A. *Synth. Met.* **2005**, *148*, 169-173.

88. Eckert, J. F.; Nicoud, J. F.; Nierengarten, J. F.; Liu, S. G.; Echegoyen, L.; Barigelletti, F.; Armaroli, N.; Ouali, L.; Krasnikov, V.; Hadziioannou, G. *J. Am. Chem. Soc.* **2000**, *122*, 7467-7479.

89. Jenekhe, S. A.; Chen, X. L. *Science* **1998**, *279*, 1903.

90. Chen, X. L.; Jenekhe, S. A. *Macromolecules* **1996**, *29*, 6189-6192.

91. Sommer, M.; Huttner, S.; Wunder, S.; Thelakkat, M. *Adv. Mater.* **2008**, *20*, 2523-2527.

92. Rajaram, S.; Armstrong, P. B.; Kim, B. J.; Frechet, J. M. J. *Chem. Mater.* **2009**, *21*, 1775-1777.

93. Crossland, E. J. W.; Kamperman, M.; Nedelcu, M.; Ducati, C.; Wiesner, U.; Smilgies, D. M.; Toombes, G. E. S.; Hillmyer, M. A.; Ludwigs, S.; Steiner, U.; Snaith, H. J. *Nano Lett.* **2009**, *9*, 2807-2812.

94. Crossland, E. J. W.; Nedelcu, M.; Ducati, C.; Ludwigs, S.; Hillmyer, M. A.; Steiner, U.; Snaith, H. J. *Nano Lett.* **2009**, *9*, 2813-2819.

95. Botiz, I.; Darling, S. B. *Macromolecules* **2009**, *42*, 8211-8217.

96. Wu, P. T.; Ren, G.; Kim, F. S.; Li, C.; Mezzenga, R.; Jenekhe, S. A. *J. Polym. Sci., A: Polym. Chem.* **2010**, *48*, 614-626.

97. Heeny, M.; Zhang, W.; Duffy, W.; McCulloch, I.; Koller, G. *World Patent Application* **2007**, WO2007/059838.

98. Wu, P. T.; Ren, G.; Li, C.; Mezzenga, R.; Jenekhe, S. A. *Macromolecules* **2009**, *42*, 2317-2320.

99. Xin, H.; Guo, X.; Kim, F. S.; Ren, G.; Watson, M. D.; Jenekhe, S. A. *J. Mater. Chem.* **2009**, *19*, 5303-5310.

100. Erb, T.; Zhokhavets, U.; Hoppe, H.; Gobsch, G.; Al-Ibrahim, M.; Ambacher, O. *Thin Solid Films* **2006**, *511−512*, 483-485.

101. van Bavel, S. S.; Sourty, E.; de With, G.; Loos, J. *Nano Lett.* **2009**, *9*, 507-513.

102. Yang, X.; van Duren, J. K. J.; Rispens, M. T.; Hummelen, J. C.; Janssen, R. A. J.; Michels, M. A. J.; Loos, J. *Adv. Mater.* **2004**, *16*, 802-806.

103. Alam, M. M.; Jenekhe, S. A. *J. Phys. Chem. B* **2001**, *105*, 2479-2482.

104. Wu, P. T.; Xin, H.; Kim, F. S.; Ren, G.; Jenekhe, S. A. *Macromolecules* **2009**, *42*, 8817-8826.

105. Botiz, I.; Darling, S. B. *Mater. Today* **2010**, *13*, 42-51.

106. Ren, G.; Wu, P.-T.; Jenekhe, S. A. *Chem. Mater.* **2010**, *22*, 2020-2026.

107. He, M.; Zhao, L.; Wang, J.; Han, W.; Yang, Y.; Qiu, F.; Lin, Z. *ACS Nano* **2010**, *4*, 3241-3247.

108. Oosterbaan, W. D.; Vrindts, V.; Berson, S.; Guillerez, S.; Douhéret, O.; Ruttens, B.; D'Haen, J.; Adriaensens, P.; Manca, J.; Lutsen, L.; Vanderzande, D. *J. Mater. Chem.* **2009**, *19*, 5424-5435.

109. Samitsu, S.; Shimomura, T.; Heike, S.; Hashizume, T.; Ito, K. *Macromolecules* **2008**, *41*, 8000-8010.

110. Merlo, J. A.; Frisbie, C. D. *J. Phys. Chem. B* **2004**, *108*, 19169-19179.

111. Samitsu, S.; Shimomura, T.; Ito, K. *Thin Solid Films* **2008**, *516*, 2478-2486.

112. Liu, J.; Arif, M.; Zou, J.; Khondaker, S. I.; Zhai, L. *Macromolecules* **2009**, *42*, 9390-9393.

113. Lu, G.; Li, L.; Yang, X. *Macromolecules* **2008**, *41*, 2062-2070.

114. Blom, P. W. M.; de Jong, M. J. M.; van Munster, M. G. *Phys. Rev. B* **1997**, *55*, R656.

115. Bendersky, L. A.; Gayle, F. W. *J. Res. Natl. Inst. Stand. Technol.* **2001**, *106*, 997-1012.

116. Wu, P. T.; Ren, G.; Jenekhe, S. A. *Macromolecules* **2010**, *43*, 3306-3313.

117. Chu, C. W.; Yang, H.; Hou, W. J.; Huang, J.; Li, G.; Yang, Y. *Appl. Phys. Lett.* **2008**, *92*, 103306.

118. Brunetti, F. G.; Kumar, R.; Wudl, F. *J. Mater. Chem.* **2010**, *20*, 2934-2948.

119. Boudreault, P.-L. T.; Najari, A.; Leclerc, M. *Chem. Mater.* **2010**, *23*, 456-469.

120. Li, G.; Zhu, R.; Yang, Y. *Nat. Photon.* **2012**, *6*, 153-161.

121. Ahmed, E.; Kim, F. S.; Xin, H.; Jenekhe, S. A. *Macromolecules* **2009**, *42*, 8615-8618.

122. Krebs, F. C. *Sol. Energy Mater. Sol. Cells* **2009**, *93*, 394-412.

123. Zhao, G.; He, Y.; Li, Y. *Adv. Mater.* **2010**, *22*, 4355-4358.

124. Ren, G.; Wu, P.-T.; Jenekhe, S. A. *ACS Nano* **2011**, *5*, 376-384.

125. Sonar, P.; Ng, G.-M.; Lin, T. T.; Dodabalapur, A.; Chen, Z.-K. *J. Mater. Chem.* **2010**, *20*, 3626-3636.

126. Ahmed, E.; Subramaniyan, S.; Kim, F. S.; Xin, H.; Jenekhe, S. A. *Macromolecules* **2011**, *44*, 7207-7219.

127. Subramaniyan, S.; Xin, H.; Kim, F. S.; Shoaee, S.; Durrant, J. R.; Jenekhe, S. A. *Adv. Energy. Mater.* **2011**, *1*, 854-860.

128. Xin, H.; Subramaniyan, S.; Kwon, T.-W.; Shoaee, S.; Durrant, J. R.; Jenekhe, S. A. *Chem. Mater.* **2012**, *24*, 1995–2001.

129. Ren, G.; Ahmed, E.; Jenekhe, S. A. *J. Mater. Chem.* **2012**, *22*, 24373 - 24379.

130. Schwenn, P. E.; Gui, K.; Nardes, A. M.; Krueger, K. B.; Lee, K. H.; Mutkins, K.; Rubinstein-Dunlop, H.; Shaw, P. E.; Kopidakis, N.; Burn, P. L.; Meredith, P. *Adv. Energy. Mater.* **2011**, *1*, 73-81.

131. Ahmed, E.; Ren, G.; Kim, F. S.; Hollenbeck, E. C.; Jenekhe, S. A. *Chem. Mater.* **2011**, *23*, 4563–4577.

132. Zaumseil, J.; Sirringhaus, H. *Chem. Rev.* **2007**, *107*, 1296-1323.

133. Babel, A.; Jenekhe, S. A. *J. Am. Chem. Soc.* **2003**, *125*, 13656-13657.

134. Babel, A.; Wind, J. D.; Jenekhe, S. A. *Adv. Funct. Mater.* **2004**, *14*, 891–898.

135. Singh, T. B.; Senkarabacak, P.; Sariciftci, N. S.; Tanda, A.; Lackner, C.; Hagelauer, R.; Horowitz, G. *Appl. Phys. Lett.* **2006**, *89*, 033512-3.

136. Usta, H.; Facchetti, A.; Marks, T. J. *J. Am. Chem. Soc.* **2008**, *130*, 8580-8581.

137. Kim, F. S.; Guo, X.; Watson, M. D.; Jenekhe, S. A. *Adv. Mater.* **2010**, *22*, 478–482.

138. He, Y.; Chen, H.-Y.; Hou, J.; Li, Y. *J. Am. Chem. Soc.* **2010**, *132*, 1377-1382.

139. He, Y.; Li, Y. *Phys. Chem. Chem. Phys.* **2011**, *13*, 1970-1983.

140. Guan, Z.-L.; Kim, J. B.; Wang, H.; Jaye, C.; Fischer, D. A.; Loo, Y.-L.; Kahn, A. *Org. Electron.* **2010**, *11*, 1779-1785.

141. Boland, P.; Sunkavalli, S. S.; Chennuri, S.; Foe, K.; Abdel-Fattah, T.; Namkoong, G. *Thin Solid Films* **2010**, *518*, 1728-1731.

142. Vandewal, K.; Tvingstedt, K.; Gadisa, A.; Inganas, O.; Manca, J. V. *Nat. Mater.* **2009**, *8*, 904-909.

143. Sariciftci, N. S.; Smilowitz, L.; Heeger, A. J.; Wudl, F. *Science* **1992**, *258*, 1474-1476.

144. Sperlich, A.; Liedtke, M.; Kern, J.; Kraus, H.; Deibel, C.; Filippone, S.; Delgado, J. L.; Martín, N.; Dyakonov, V. *Phys. Status Solidi. Rapid Res. Lett.,* **2011**, *5*, 128-130.

145. Guldi, D. M.; Prato, M. *Acc. Chem. Res.* **2000**, *33*, 695-703.

146. Heinemann, M. D.; von Maydell, K.; Zutz, F.; Kolny-Olesiak, J.; Borchert, H.; Riedel, I.; Parisi, J. *Adv. Funct. Mater.* **2009**, *19*, 3788-3795.

147. Noone, K. M.; Subramaniyan, S.; Zhang, Q. F.; Cao, G. Z.; Jenekhe, S. A.; Ginger, D. S. *J. Phys. Chem. C* **2011**, *115*, 24403-24410.

148. He, Y.; Zhao, G.; Peng, B.; Li, Y. *Adv. Funct. Mater.* **2010**, *20*, 3383-3389.

149. Deibel, C.; Mack, D.; Gorenflot, J.; Schöll, A.; Krause, S.; Reinert, F.; Rauh, D.;

Dyakonov, V. *Phys. Rev. B* **2010**, *81*, 085202.

150. Sun, S.-S.; Sariciftci, N. S. *Organic Photovoltaics: Mechanisms, Materials, and Devices*; CRC Press: Boca Raton, 2005.

151. He, Y.; Chen, C.; Richard, E.; Dou, L.; Wu, Y.; Li, G.; Yang, Y. *J. Mater. Chem.* **2012**, *22*, 13391-13394.

152. Crabtree, R. H. *Energy Production and Storage: Inorganic Chemical Strategies for a Warming World;* ; John Wiley & Sons Ltd., 2010.

153. Delcamp, J. H.; Yella, A.; Nazeeruddin, M. K.; Grätzel, M. *Chem. Commun.* **2012**, *48*, 2295-2297.

154. Schlenker, C. W.; Thompson, M. E. *Top. Curr. Chem.* **2012**, *312*, 175-213.

155. Veldman, D.; Meskers, S. C. J.; Janssen, R. A. J. *Adv. Funct. Mater.* **2009**, *19*, 1939-1948.

156. Cook, S.; Katoh, R.; Furube, A. *J. Phys. Chem. C* **2009**, *113*, 2547-2552.

157. Benson-Smith, J. J.; Ohkita, H.; Cook, S.; Durrant, J. R.; Bradley, D. D. C.; Nelson, J. *Dalton Trans.* **2009**, 10000-10005.

158. Bakulin, A. A.; Rao, A.; Pavelyev, V. G.; van Loosdrecht, P. H. M.; Pshenichnikov, M. S.; Niedzialek, D.; Cornil, J.; Beljonne, D.; Friend, R. H. *Science* **2012**, *335*, 1340-1344.

159. Coffey, D. C.; Ferguson, A. J.; Kopidakis, N.; Rumbles, G. *ACS Nano* **2010**, *4*, 5437-5445.

160. Soon, Y. W.; Clarke, T. M.; Zhang, W.; Agostinelli, T.; Kirkpatrick, J.; Dyer-Smith, C.; McCulloch, I.; Nelson, J.; Durrant, J. R. *Chem. Sci.* **2011**, *2*, 1111-1120.

161. Kulkarni, A. P.; Tonzola, C. J.; Babel, A.; Jenekhe, S. A. *Chem. Mater.* **2004**, *16*, 4556-4573.

162. Ahmed, E.; Earmme, T.; Ren, G.; Jenekhe, S. A. *Chem. Mater.* **2010**, *22*, 5786-5796.

163. Noone, K. M.; Anderson, N. C.; Horwitz, N. E.; Munro, A. M.; Kulkarni, A. P.; Ginger, D. S. *ACS Nano* **2009**, *3*, 1345-1352.

164. Ginger, D. S.; Greenham, N. C. *Phys. Rev. B* **1999**, *59*, 10622-10629.

165. Cheng, Y.-J.; Yang, S.-H.; Hsu, C.-S. *Chem. Rev.* **2009**, *109*, 5868-5923.

166. Anthony, J. E. *Chem. Mater.* **2011**, *23*, 583-590.

167. Roncali, J. *Adv. Energy. Mater.* **2011**, *1*, 147-160.

168. Hummelen, J. C.; Knight, B. W.; LePeq, F.; Wudl, F.; Yao, J.; Wilkins, C. L. *J. Org. Chem.* **1995**, *60*, 532-538.

169. Wudl, F. *Acc. Chem. Res.* **1992**, *25*, 157-161.

170. Wienk, M. M.; Kroon, J. M.; Verhees, W. J. H.; Knol, J.; Hummelen, J. C.; van Hal, P. A.; Janssen, R. A. J. *Angew. Chem. Int. Ed.* **2003**, *42*, 3371-3375.

171. Allemand, P. M.; Koch, A.; Wudl, F.; Rubin, Y.; Diederich, F.; Alvarez, M. M.; Anz, S. J.; Whetten, R. L. *J. Am. Chem. Soc.* **1991**, *113*, 1050-1051.

172. Singh, T. B.; Marjanović, N.; Matt, G. J.; Günes, S.; Sariciftci, N. S.; Montaigne Ramil, A.; Andreev, A.; Sitter, H.; Schwödiauer, R.; Bauer, S. *Org. Electron.* **2005**, *6*, 105-110.

173. Sonar, P.; Lim, J. P. F.; Chan, K. L. *Energy Environ. Sci.* **2011**, *4*, 1558-1574.

174. Dittmer, J. J.; Marseglia, E. A.; Friend, R. H. *Adv. Mater.* **2000**, *12*, 1270-1274.

175. Schmidt-Mende, L.; Fechtenkötter, A.; Müllen, K.; Moons, E.; Friend, R. H.; MacKenzie, J. D. *Science* **2001**, *293*, 1119-1122.

176. Li, J.; Dierschke, F.; Wu, J.; Grimsdale, A. C.; Müllen, K. *J. Mater. Chem.* **2006**, *16*, 96-100.

177. Sharma, G. D.; Suresh, P.; Mikroyannidis, J. A.; Stylianakis, M. M. *J. Mater. Chem.* **2010**, *20*, 561-567.

178. Shin, R. Y. C.; Kietzke, T.; Sudhakar, S.; Dodabalapur, A.; Chen, Z.-K.; Sellinger, A. *Chem. Mater.* **2007**, *19*, 1892-1894.

179. Woo, C. H.; Holcombe, T. W.; Unruh, D. A.; Sellinger, A.; Fréchet, J. M. J. *Chem. Mater.* **2010**, *22*, 1673-1679.

180. Inal, S.; Castellani, M.; Sellinger, A.; Neher, D. *Macromol. Rapid Commun.* **2009**, *30*, 1263-1268.

181. Lloyd, M. T.; Anthony, J. E.; Malliaras, G. G. *Mater. Today* **2007**, *10*, 34-41.

182. Shu, Y.; Lim, Y.-F.; Li, Z.; Purushothaman, B.; Hallani, R.; Kim, J. E.; Parkin, S. R.; Malliaras, G. G.; Anthony, J. E. *Chem. Sci.* **2011**, *2*, 363-368.

183. Brunetti, F. G.; Gong, X.; Tong, M.; Heeger, A. J.; Wudl, F. *Angew. Chem. Int. Ed.* **2010**, *49*, 532-536.

184. Karsten, B. P.; Bijleveld, J. C.; Janssen, R. A. J. *Macromol. Rapid Commun.* **2010**, *31*,

1554-1559.

185. Arnautov, S. A.; Nechvolodova, E. M.; Bakulin, A. A.; Elizarov, S. G.; Khodarev, A. N.; Martyanov, D. S.; Paraschuk, D. Y. *Synth. Met.* **2004**, *147*, 287-291.

186. Mihailetchi, V. D.; Xie, H.; de Boer, B.; Popescu, L. M.; Hummelen, J. C.; Blom, P. W.; Koster, L. J. *Appl. Phys. Lett.* **2006**, *89*, 012107.

187. Camaioni, N.; Ridolfi, G.; Casalbore-Miceli, G.; Possamai, G.; Maggini, M. *Adv. Mater.* **2002**, *14*, 1735-1738.

188. Janssen, G.; Aguirre, A.; Goovaerts, E.; Vanlaeke, P.; Poortmans, J.; Manca, J. *Eur. Phys. J. Appl. Phys.* **2007**, *37*, 287–290.

189. Moon, J. S.; Takacs, C. J.; Cho, S.; Coffin, R. C.; Kim, H.; Bazan, G. C.; Heeger, A. J. *Nano Lett.* **2010**, *10*, 4005-4008.

190. Gao, Z.; Lee, C.; Bello, I.; Lee, S.; Chen, R.; Luh, T.; Shi, J.; Tang, C. *Appl. Phys. Lett.* **1999**, *74*, 865.

191. Anthopoulos, T.; Markham, J.; Namdas, E.; Samuel, I.; Lo, S.; Burn, P. *Appl. Phys. Lett.* **2003**, *82*, 4824.

192. Lo, S.-C.; Burn, P. L. *Chem. Rev.* **2007**, *107*, 1097-1116.

193. Subramaniyan, S.; Xin, H.; Kim, F. S.; Jenekhe, S. A. *Macromolecules* **2011**, *44*, 6245-6248.

194. Kietzke, T.; Hörhold, H.-H.; Neher, D. *Chem. Mater.* **2005**, *17*, 6532-6537.

195. Holcombe, T. W.; Woo, C. H.; Kavulak, D. F. J.; Thompson, B. C.; Fréchet, J. M. J. *J. Am. Chem. Soc.* **2009**, *131*, 14160-14161.

196. Bloking, J. T.; Han, X.; Higgs, A. T.; Kastrop, J. P.; Pandey, L.; Norton, J. E.; Risko, C.; Chen, C. E.; Brédas, J.-L.; McGehee, M. D.; Sellinger, A. *Chem. Mater.* **2011**, *23*, 5484-5490.

197. Zhou, T.; Jia, T.; Kang, B.; Li, F.; Fahlman, M.; Wang, Y. *Adv. Energy. Mater.* **2011**, *1*, 431-439.

198. Walker, B.; Han, X.; Kim, C.; Sellinger, A.; Nguyen, T.-Q. *ACS Appl. Mater. Interfaces* **2011**, *4*, 244-250.

199. Yang, X.; Loos, J. *Macromolecules* **2007**, *40*, 1353-1362.

200. Wang, D. H.; Moon, J. S.; Seifter, J.; Jo, J.; Park, J. H.; Park, O. O.; Heeger, A. J. *Nano Lett.* **2011**, *11*, 3163-3168.

201. Xin, H.; Guo, X.; Ren, G.; Watson, M. D.; Jenekhe, S. A. *Adv. Energy. Mater.* **2012**, *2*, 575–582.

202. Salim, T.; Sun, S.; Wong, L. H.; Xi, L.; Foo, Y. L.; Lam, Y. M. *J. Phys. Chem. C* **2010**, *114*, 9459-9468.

203. Jenekhe, S. A.; Yi, S. *Appl. Phys. Lett.* **2000**, *77*, 2635-2637.

204. He, X.; Gao, F.; Tu, G.; Hasko, D.; Hüttner, S.; Steiner, U.; Greenham, N. C.; Friend, R. H.; Huck, W. T. S. *Nano Lett.* **2010**, *10*, 1302-1307.

205. Holcombe, T. W.; Norton, J. E.; Rivnay, J.; Woo, C. H.; Goris, L.; Piliego, C.; Griffini, G.; Sellinger, A.; Brédas, J.-L.; Salleo, A.; Fréchet, J. M. J. *J. Am. Chem. Soc.* **2011**, *133*, 12106-12114.

206. Schubert, M.; Dolfen, D.; Frisch, J.; Roland, S.; Steyrleuthner, R.; Stiller, B.; Chen, Z.; Scherf, U.; Koch, N.; Facchetti, A.; Neher, D. *Adv. Energy. Mater.* **2012**, *2*, 369-380.

207. Briseno, A. L.; Mannsfeld, S. C. B.; Shamberger, P. J.; Ohuchi, F. S.; Bao, Z.; Jenekhe, S. A.; Xia, Y. *Chem. Mater.* **2008**, *20*, 4712-4719.

208. Karak, S.; Ray, S. K.; Dhar, A. *Appl. Phys. Lett.* **2010**, *97*, 043306-3.

209. McNeill, C. R. *Energy Environ. Sci.* **2012**, *5*, 5653-5667.

210. Herzing, A. A.; Richter, L. J.; Anderson, I. M. *J. Phys. Chem. C* **2010**, *114*, 17501-17508.

211. Drummy, L. F.; Davis, R. J.; Moore, D. L.; Durstock, M.; Vaia, R. A.; Hsu, J. W. P. *Chem. Mater.* **2010**, *23*, 907-912.

212. Roehling, J. D.; Batenburg, K. J.; Swain, F. B.; Moulé, A. J.; Arslan, I. *Adv. Funct. Mater.* **2013**, *23*, 2115–2122.

213. Arslan, I.; Yates, T. J. V.; Browning, N. D.; Midgley, P. A. *Science* **2005**, *309*, 2195-2198.

214. Williams, D. B.; Carter, C. B. *Transmission Electron Microscopy: A Textbook for Materials Science*; Springer Science + Business Media, LLC: New York, NY, USA, 2009.

215. Loos, J.; Sourty, E.; Lu, K.; de With, G.; van Bavel, S. S. *Macromolecules* **2009**, *42*, 2581-2586.

216. van Bavel, S. S.; Bärenklau, M.; de With, G.; Hoppe, H.; Loos, J. *Adv. Funct. Mater.* **2010**, *20*, 1458-1463.

217. Garratt-Reed, A. J.; Bell, D. C. *Energy Dispersive X-ray Analysis in the Electron*

Microscope BIOS Scientific Publishers Ltd: Oxford, UK, 2003.

218. Favia, P.; Voroshazi, E.; Heremans, P.; Bender, H. *J. Mater. Sci.* **2013**, *48*, 2908-2919.

219. Hwang, Y.-J.; Ren, G.; Murari, N. M.; Jenekhe, S. A. *Macromolecues* **2012**, *45*, 9056–9062.

220. Hwang, Y.-J.; Murari, N. M.; Jenekhe, S. A. *Polym. Chem.* **2013**, DOI: 10.1039/C3PY00325F.

221. T. Ferreira and W. Rasband, ImageJ User Guide IJ1.46r, http://rsbweb.nih.gov/ij/docs/guide/146.html, accessed March 5, 2013.

222. Shoaee, S.; Subramaniyan, S.; Xin, H.; Keiderling, C.; Tuladhar, P. S.; Jamieson, F.; Jenekhe, S. A.; Durrant, J. R. *Adv. Funct. Mater.* **2013**, DOI: 10.1002/adfm.201203148.

223. Moore, J. R.; Albert-Seifried, S.; Rao, A.; Massip, S.; Watts, B.; Morgan, D. J.; Friend, R. H.; McNeill, C. R.; Sirringhaus, H. *Adv. Energy. Mater.* **2011**, *1*, 230-240.

224. Nakabayashi, K.; Mori, H. *Macromolecules* **2012**, *45*, 9618-9625.

225. Zhou, E.; Cong, J.; Zhao, M.; Zhang, L.; Hashimoto, K.; Tajima, K. *Chem. Commun.* **2012**, *48*, 5283-5285.

226. Fabiano, S.; Chen, Z.; Vahedi, S.; Facchetti, A.; Pignataro, B.; Loi, M. A. *J. Mater. Chem.* **2011**, *21*, 5891-5896.

227. Alam, M. M.; Tonzola, C. J.; Jenekhe, S. A. *Macromolecules* **2003**, *36*, 6577-6587.

228. Nam, S.; Shin, M.; Park, S.; Lee, S.; Kim, H.; Kim, Y. *Phys. Chem. Chem. Phys.* **2012**, *14*, 15046-15053.

229. Zhang, X.; Kale, D. M.; Jenekhe, S. A. *Macromolecules* **2002**, *35*, 382-393.

230. Duran, R.; Ballauff, M.; Wenzel, M.; Wegner, G. *Macromolecules* **1988**, *21*, 2897-2899.

231. Moulé, A. J.; Tsami, A.; Bünnagel, T. W.; Forster, M.; Kronenberg, N. M.; Scharber, M.; Koppe, M.; Morana, M.; Brabec, C. J.; Meerholz, K.; Scherf, U. *Chem. Mater.* **2008**, *20*, 4045-4050.

232. Pfannmöller, M.; Flügge, H.; Benner, G.; Wacker, I.; Sommer, C.; Hanselmann, M.; Schmale, S.; Schmidt, H.; Hamprecht, F. A.; Rabe, T.; Kowalsky, W.; Schröder, R. R. *Nano Lett.* **2011**, *11*, 3099-3107.

233. Ren, G.; Schlenker, C. W.; Ahmed, E.; Subramaniyan, S.; Olthof, S.; Kahn, A.; Ginger, D. S.; Jenekhe, S. A. *Adv. Funct. Mater.* **2013**, *23*, 1238–1249.

234. Ren, G.; Hwang, Y.-J.; Subramanian, S.; Jenekhe, S. A. *Energy Environ. Sci.* **2013**, *submitted*.

235. Mori, D.; Benten, H.; Ohkita, H.; Ito, S.; Miyake, K. *Acs Appl. Mater. Inter.* **2012**, *4*, 3325-3329.

236. Mori, D.; Benten, H.; Kosaka, J.; Ohkita, H.; Ito, S.; Miyake, K. *ACS Appl. Mater. Interfaces* **2011**, *3*, 2924-2927.

VITA

Guoqiang Ren was born in Taiyuan, China. He entered Southern Yangtze University, China and received the B.S. degree in Chemical Engineering. Then he came to the USA for graduate study in the University of Missouri and obtained the M.S. degree in Chemical Engineering. He earned a Doctor of Philosophy (Ph.D.) at the University of Washington under the guidance of Professor Samson A. Jenekhe in 2013. During his Ph.D. study, he received two University of Washington Initiatives Fund (UIF) Fellowships in 2008-2010 from College of Engineering, the 2010 Chinese Government Award for Outstanding Ph.D. Students Abroad from the Education Ministry of China, and 2012 High Impact Factor Publication Award from UW Department of Chemical Engineering. He also received several awards from Business Plan Competitions in 2011, including the Davis Wright Tremaine Honorable Mention in UW Environmental Innovation Challenge and the Best Idea Prize in UW Business Plan Competition.

Below is a list of the author's publications during Ph.D. study:

1. **Ren, G.**; Hwang, Y.-J.; Subramaniyan, S.; Jenekhe, S. A. "Nanoscale Morphology of Polymer Solar Cells by Use of Energy Dispersive X-ray Spectroscopy Imaging," *Energy Environ. Sci.*, submitted.

2. **Ren, G.**; Schlenker, C. W.; Ahmed, E.; Subramaniyan, S.; Olthof, S.; Kahn, A.; Ginger, D. S.; Jenekhe, S. A. "Photoinduced Hole Transfer is Suppressed with Diminished Driving Force in Polymer-Fullerene Solar Cells, While Electron Transfer Remains Active," *Adv. Funct. Mater.* **2013**, *23*, 1238-1249.

3. **Ren, G.**; Ahmed, E.; Jenekhe, S. A. "Nanowires of oligothiophene-functionalized naphthalene diimides: self assembly, morphology, and all-nanowire bulk heterojunction solar cells", *J. Mater. Chem.* **2012**, *22*, 24373 – 24379.

4. **Ren, G.**; Ahmed, E.; Jenekhe, S. A. "Non-Fullerene Acceptor-Based Bulk Heterojunction Polymer Solar Cells: Engineering the Nanomorphology via Processing Additives," *Adv. Energy Mater.* **2011**, *1*, 946–953.

5. **Ren, G.**; Wu, P.-T.; Jenekhe, S. A. "Solar Cells Based on Block Copolymer Semiconductor Nanowires: Effects of Nanowire Aspect Ratio," *ACS Nano* **2011**, *5*, 376-384.

6. **Ren, G.**; Wu, P.-T.; Jenekhe, S. A. "Enhanced Performance of Bulk Heterojunction Solar Cells Using Block Copoly(3-alkylthiophene)s," *Chem. Mater*. **2010**, *22*, 2020-2026.

7. Li, H.; Kim, F. S.; **Ren, G.**; Earmme, T.; Jenekhe, S. A. "Two-dimensional nanoribbon electron-transport polymers for organic electronics and photovoltaics," *submitted*.

8. Li, H.; Kim, F. S.; **Ren, G.**; Hollenbeck, E. C.; Subramaniyan, S.; Jenekhe, S. A. "Tetraazabenzodifluoranthene Diimides: New Building Blocks for Solution Processable N-Type Organic Semiconductors," *Angew. Chem. Int. Ed.* **2013**, *125*, 5623-5627.

9. Hwang, Y.-J.; **Ren, G.**; Murari, N. M.; Jenekhe, S. A. "n-Type Naphthalene Diimide-Biselenophene Copolymer for All-polymer Bulk Heterojunction Solar Cells," *Macromolecules*, **2012**, *45*, 9056–9062.

10. Subramaniyan, S.; Kim, F. S.; **Ren, G.**; Murari, N.; Li, H.; Jenekhe, S. A. "High Mobility Thiazole-Diketopyrrolopyrrole Copolymer Semiconductors for High Performance Field-Effect Transistors and Photovoltaic Devices," *Macromolecules* **2012**, *45*, 9029–9037.

11. Xin, H.; Guo, X.; **Ren, G.**; Watson, M. D.; Jenekhe, S. A. "Efficient Phthalimide Copolymer-Based Bulk Heterojunction Solar Cells: How the Processing Additive Influences Nanoscale Morphology and Photovoltaic Properties," *Adv. Energy Mater.* **2012**, *2*, 575–582.

12. Ahmed, E. A.; **Ren, G.**; Kim, F. S.; Hollenbeck**,** E. C.; Jenekhe, S. A. "Design of New Electron Acceptor Materials for Organic Photovoltaics: Synthesis, Electron Transport, Photophysics, and Photovoltaic Properties of Oligothiophene-Functionalized Naphthalene Diimides," *Chem. Mater.* **2011**, *23*, 4563–4577.

13. Kim, F. S.; **Ren, G.**; Jenekhe, S. A. "One-Dimensional Nanostructures of π-Conjugated Molecular Systems: Assembly, Properties, and Applications from Photovoltaics, Sensors, and Nanophotonics to Nanoelectronics," *Chem. Mater.* **2011**, *23*, 682–732.

14. Ahmed, E.; Earmme, T.; **Ren, G.**; Jenekhe, S. A. "Novel n-Type Conjugated Ladder Heteroarenes: Synthesis, Self-Assembly of Nanowires, Electron Transport, and Electroluminescence of Bisindenoanthrazolines," *Chem. Mater.* **2010**, *22*, 5786–5796.

15. Wang, C.; Kim, F. S.; **Ren, G.**; Xu, Y. Q.; Pang, Y.; Jenekhe, S. A.; Jia, L. "Regioregular Poly(3-alkanoylthiophene): Synthesis and Electrochemical, Photophysical, Charge Transport, and Photovoltaic Properties," *J. Polym. Sci. A - Polym. Chem.* **2010**, *48*, 4681–4690.

16. Xin, H.; Reid, O.; **Ren, G.**; Kim, F. S.; Ginger, D. S.; Jenekhe, S. A. "Polymer

Nanowire/Fullerene Bulk Heterojunction Solar Cells: How Nanostructure Determines Photovoltaic Properties," *ACS Nano* **2010**, *4*, 1861-1872.

17. Wu, P.-T.; **Ren, G.**; Jenekhe, S. A. "Crystalline Random Conjugated Copolymers with Multiple Side Chains: Tunable Intermolecular Interactions and Enhanced Charge Transport and Photovoltaic Properties," *Macromolecules* **2010**, *43*, 3306-3313.

18. Wu, P.-T.; **Ren, G.**; Kim, F. S.; Li, C.; Mezzenga, R.; Jenekhe, S. A. "Poly(3-hexylthiophene)-b-poly(3-cyclohexylthiophene): Synthesis, Microphase Separation, Thin Film Transistors, and Photovoltaic Applications," *J. Polym. Sci. A* **2010**, *48*, 614-626.

19. Wu, P.-T.; Xin, H.; Kim, F. S.; **Ren, G.**; Jenekhe, S. A. "Regioregular Poly(3-pentylthiophene): Synthesis, Self-Assembly of Nanowires, High-Mobility Field-Effect Transistors, and Efficient Photovoltaic Cells," *Macromolecules* **2009**, *42*, 8817-8826.

20. Xin, H.; Guo, X.; Kim, F. S.; **Ren**, G.; Watson, M. D.; Jenekhe, S. A. "Efficient Solar Cells Based on a New Phthalimide-Based Donor–Acceptor Copolymer Semiconductor: Morphology, Charge-Transport, and Photovoltaic Properties," *J. Mater. Chem.* **2009**, *19*, 5303-5310.

21. Wu, P.-T.; **Ren, G.**; Li, C.; Mezzenga, R.; Jenekhe, S. A. "Crystalline Diblock Conjugated Copolymers: Synthesis, Self-Assembly, and Microphase Separation of Poly(3-butylthiophene)-b-poly(3-octylthiophene) ," *Macromolecules* **2009**, *42*, 2317-2320.

22. Xin, H.; **Ren**, G.; Kim, F. S.; Jenekhe, S. A. "Bulk Heterojunction Solar Cells from Poly(3-butylthiophene)/Fullerene Blends: In-Situ Self-Assembly of Nanowires, Morphology and Photovoltaic Properties," *Chem. Mater.* **2008**, *20*, 6199-6207.